Corrosion in Molten Fluoride Salt: Environmental Effects

By

Cody James Falconer

A dissertation submitted in partial fulfillment of
the requirements for the degree of

Doctor of Philosophy
(Materials Science and Engineering)

at the

UNIVERSITY OF WISCONSIN-MADISON
2022

Date of final oral examination: 6 July 2022

The dissertation is approved by the following members of the Final Oral Committee:

Adrien Couet, Associate Professor, Engineering Physics

Kumar Sridharan, Professor, Engineering Physics

Dane Morgan, Professor, Materials Science and Engineering

Yongfeng Zhang, Assistant Professor, Engineering Physics

Stephen Raiman, Assistant Professor, Texas A&M University, Nuclear Engineering

Executive Summary

As the concentration of greenhouse gases in the environment continues to reach levels that have never been recorded in history, the demand for low greenhouse gas emitting forms of energy are reaching an all-time high. With current public opinion and geopolitical changes occurring, Generation IV nuclear energy systems are ready to help transition energy production away from the consumption of fossil fuels. While not necessarily a new idea, the Generation IV Molten Salt Reactor (MSR) design has garnered a significant amount of interest from both government agencies and private companies alike, making it a critical reactor design for research.

Originally developed in the mid-twentieth century, the MSR was successfully demonstrated by Oak Ridge National Laboratory, but little interest has been expressed for MSR designs until recently. In order for the development and deployment of MSRs to be successful today, there is a need for understanding how code certified alloys, as well as new materials, are going to perform in a molten salt environment. A prototypical approach in literature at investigating the performance of materials in molten salt environments has become the use of static isothermal salt exposure testing cells. Unfortunately, there exists no standard method for these tests which has resulted in a large scattering of material data coming out of research efforts. Literature has suggested that this scattering is a direct result of variations in the design of the static isothermal salt exposure test cell. In this dissertation, several aspects that go into the design of static isothermal salt exposure test cells are studied to see how variations in the test cell can affect the materials behavior in these tests. The size of the test cell effectively creates a limit on a test parameter referred to as the volume of salt to exposed surface area ratio (Vol/SA). In this work, it is shown that adjusting this ratio results in dramatically different rates of corrosion in 316H stainless steel (316HSST) samples

exposed to a LiF-NaF-KF salt mixture known as FLiNaK. At small ratios, the corrosion rate of 316HSST actually appears to plateau after only 500 hrs of salt exposure whereas a higher ratio continues corroding 316HSST beyond 1000 hrs. This result shows an obvious challenge then for determine the true behavior of 316HSST in FLiNaK salt. It is then speculated that a new way of ranking materials performance in salt qualitatively could be by determine the corrosion plateau time for a given material in a given Vol/SA ratio at a given temperature.

Intimately tied to the Vol/SA ratio is the affect that the purity of the FLiNaK salt has on the material performance. Molten salts are highly sensitive to the levels of impurities in them and changes to the impurity levels can dramatically change how aggressive the salts are towards materials in them. In this dissertation 316HSST was exposed to purified and as-received FLiNaK salt and it can clearly be observed that the purification process for the FLiNaK salt improved the corrosion rate of the 316HSST as a result of impurity removal.

The final area of investigation in this dissertation was the effects that dissimilar materials have on one another when coexisting in the same FLiNaK salt. Traditional interaction mechanisms between dissimilar materials like galvanic coupling were shown to have little if no effect on the interaction of dissimilar metals submerged in FLiNaK. The main driving force for interaction of dissimilar materials in FLiNaK was demonstrated to be through a mechanism referred to as activity gradient driven mass transportation which is primarily enabled through the disproportionation reaction of corrosion products. Activity gradient driven mass transportation is accurately predicted through computational tools and is shown to dramatically alter how 304SST samples behave in FLiNaK. Additionally, this mechanism is expected to have a large effect on materials interactions with graphite in MSR designs and a novel design for eliminating this interaction is investigated.

Acknowledgments

First and foremost I would like to thank my Ph.D. advisor Dr. Adrien Couet, as well as my co-advisor Dr. Kumar Sridharan. Without whom I would not have had the incredible opportunity of studying molten salts at the University of Wisconsin-Madison. It was often through their wisdom and experiences that I was able to continue many of the projects that I worked on. I would also like to thank my Ph.D. committee for their advice and attention through my preliminary examinations which undoubtedly made this research successful.

I want to thank my colleagues and mentors both past and present at the University of Wisconsin. A special thanks goes to Dr. William H. Doniger for his support in all of the molten salt equipment that we designed, built, and operated together. Thank you Dr. Mohamed Elbakhshwan, Dr. Yafei Wang, Dr. Taeho Kim, and Dr. Iman Abdallah for your support and guidance. Dr. Karl Britsch, Dr. Lazarus German, Dr. Patrick Strohbeen, Dr. Zefeng Yu, Nathan Curtis, Matthew Weinstein, Leo Borrel, Louis Bailly-Salins, Calvin Parkin, Raphelle David, Bonita Goh and Evan Buxton for their friendship and availability to take a break once in a while.

A special thanks goes out to my follow group secretary Dr. Michael Moorehead for showing me how to navigate the department.

My family has always provided an inconceivable amount of support and love. I am forever grateful for their support of my education and push to pursue every opportunity that I was able to pursue.

Finally, I would like to thank my partner Hannah Richardson who followed me to Wisconsin knowing that this journey was going to be long and challenging, but was always by my side with unwavering support.

Table of Contents

List of Tables

List of Figures

Nomenclature

Acronyms and Abbreviations

304SST	304 Stainless Steel
316HSST	316H Stainless Steel
316LSST	316L Stainless Steel
AHF	Anhydrous Hydrogen Fluoride
ARE	Aircraft Reactor Experiment
DI	Deionized
EDM	Electrical Discharge Machining
EDS	Energy Dispersive X-ray Spectroscopy
FEP	Fluorinated Ethylene Propylene
FHR	Fluoride High temperature salt-cooled Reactor
FIB	Focused Ion Beam
FLiBE	$LiF\text{-}BeF_2$ (66-34 mol%)
FLiNaK	LiF-NaF-KF (46.5-11.5-42 mol%)
GDOES	Glow Discharge Optical Emission Spectroscopy
GTAW	Gas Tungsten Arc Welding
ICP-MS	Inductively Coupled Plasma Mass Spectrometry
LWR	Light-Water Reactor
MSBR	Molten Salt Breeder Reactor
MSR	Molten Salt Reactor
MSRE	Molten Salt Reactor Experiment
NC	Natural Circulation
OCP	Open Circuit Potential
ORNL	Oak Ridge National Laboratory
PG	Pyrolytic Graphite
PyBN	Pyrolytic Boron Nitride
SEM	Scanning Electron Microscope
SiC	Silicon Carbide
TEM	Tranmission Electron Microscope
TRISO	Tristructural Isotropic
TZM	Titanium-Zirconium-Molybdenum alloy
Vol/SA	Volume of salt to exposed surface area
WSLH	Wisconsin State Laboratory of Hygiene
XPS	X-ray Photoelectron Spectroscopy
XRD	X-Ray Diffraction
ZRA	Zero-Resistance Ammeter

Chapter 1

Introduction and Molten Salt Use for Nuclear Applications

Over the last century greenhouse gas emissions, particular the emission of CO_2, have reached a level that the world's natural global carbon cycle can no longer compensate for resulting in increased levels of greenhouse gases remaining in the environment [1]. Of the many sources of greenhouse gas production, the energy sector has become one of the largest generators of greenhouse gases. The burning of fossil fuels for energy production is estimated to account for approximately 92% of human related greenhouse gas emissions [2]. In 2002 (updated in 2014), a subcommittee on Generation IV Technology Planning outlined sustainability goals for Generation IV nuclear reactor systems. These Generation IV systems were specifically targeted to help advance nuclear energy as a source of clean air energy and reduce the dependence of energy on fossil fuels [3, 4]. In addition to establishing the Generation IV systems as clean energy systems, a primary goal for the Generation IV nuclear systems is to dramatically improve nuclear energies safety and reduce the need for offsite emergency response [4].

Of the several reactor systems outlined by the committee, one of the promising Generation IV nuclear systems identified was the Molten Salt Reactor (MSR) system. A generic schematic of an MSR is shown in Figure 1-1. One of the primary deviations of the MSR design away from current Light-Water Reactors (LWRs) is the use of a halide-based salt to keep the reactor operating at a reasonable temperature. This shift in coolant provides the MSR concept with several key safety benefits including (i) higher operating temperatures which in turn improves the thermodynamic efficiency of the reactor, (ii) lower pressure operations due to the high boiling point of molten

halide salts, and (iii) increased fission product solubility which limits the possibility of fission products escaping the salt in case of an accident [3, 5, 6].

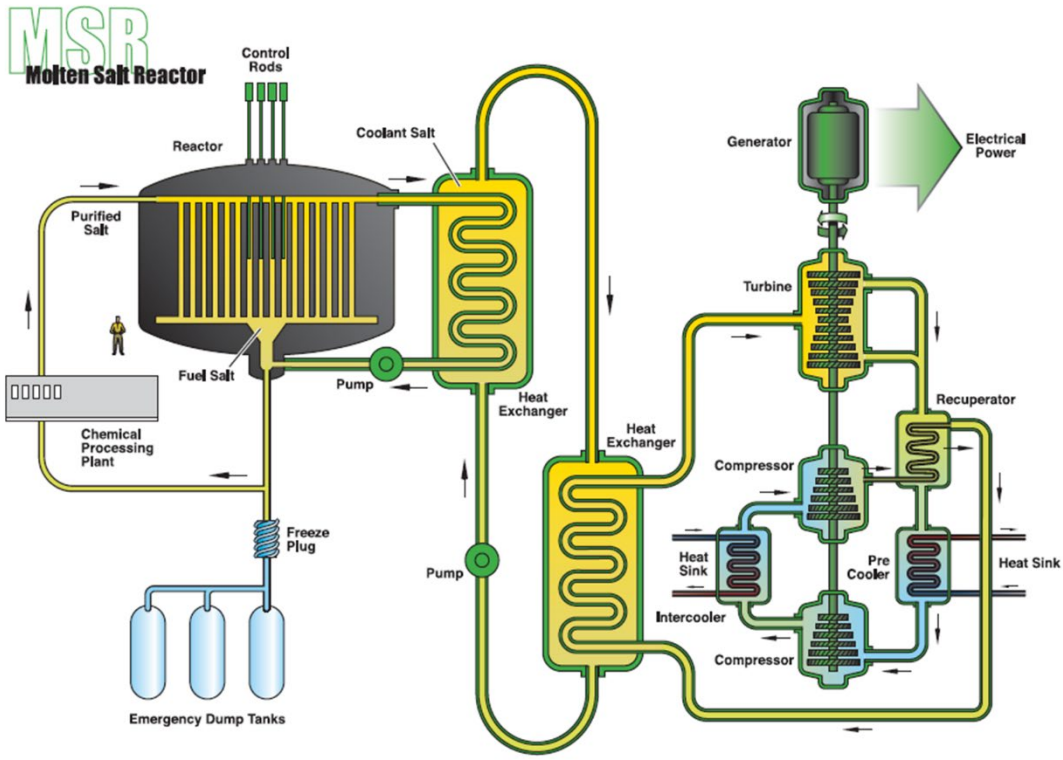

Figure 1-1: Schematic of a molten salt reactor system [3].

1.1 Aircraft Reactor Experiment

Though the MSR is identified as a Generation IV nuclear system, the basic concept of the MSR was actually developed and demonstrated in the early 1950s as part of the Aircraft Reactor Experiment (ARE) at Oak Ridge National Laboratory (ORNL) [7]. The goal of the experiment was to demonstrate the operation of a small nuclear reactor system that could be incorporated into long range aircraft systems [7, 8]. Successful operation of the ARE was achieved in 1954 when after reaching criticality, the reactor operated for 221 hours. The ARE demonstrated for the first time that a reactor using a fluoride-based liquid fuel mixture of NaF-ZrF_4-UF_4 was possible.

During the course of the experiment, the operators were able to demonstrate stable operation and satisfactory instrument performance including the performance of salt pumps [7]. Several promising aspects of the MSR concept were also demonstrated during this experiment. The removal of neutron poisoning gaseous fission products such as xenon was achieved by the pumping action of the liquid fuel. Additionally, the negative reactor feedback coefficient of the fuel was shown. As the fuel heats up, the salt expands naturally removing fissile uranium from the core which prevents the reactor from being able to "run-away" [5, 7]. However, after the ARE program concluded and the feasibility of the MSR concept was demonstrated, a nuclear powered aircraft was never built.

1.2 Molten Salt Reactor Experiment

After the relative success of the ARE, ORNL took the MSR concept and began considering it for civilian power generation, and so began a series of experiments known as the Molten Salt Reactor Experiments (MSRE) [9]. Led by MacPherson's group, ORNL started working on what they had considered to be the best design approach to achieving a commercial scale MSR concept that could generate commercial power, and in 1959 a US Atomic Energy Commission task force determined that the MSR concept had a high "probability of achieving technical feasibility" [9, 10].

Ultimately, it was decided that the MSRE would require a different design than that of the ARE as the focus for commercial power had different necessities. For the design of the MSRE, a single fluid concept was adopted with a salt mixture of LiF-BeF_2-ZrF_4-UF_4. For neutron moderation, BeO used in the ARE was replaced with uncladded graphite [11]. By 1965 the MSRE was completed and researchers worked to reach criticality for the first time. A photograph of the completed MSRE is shown in Figure 1-2.

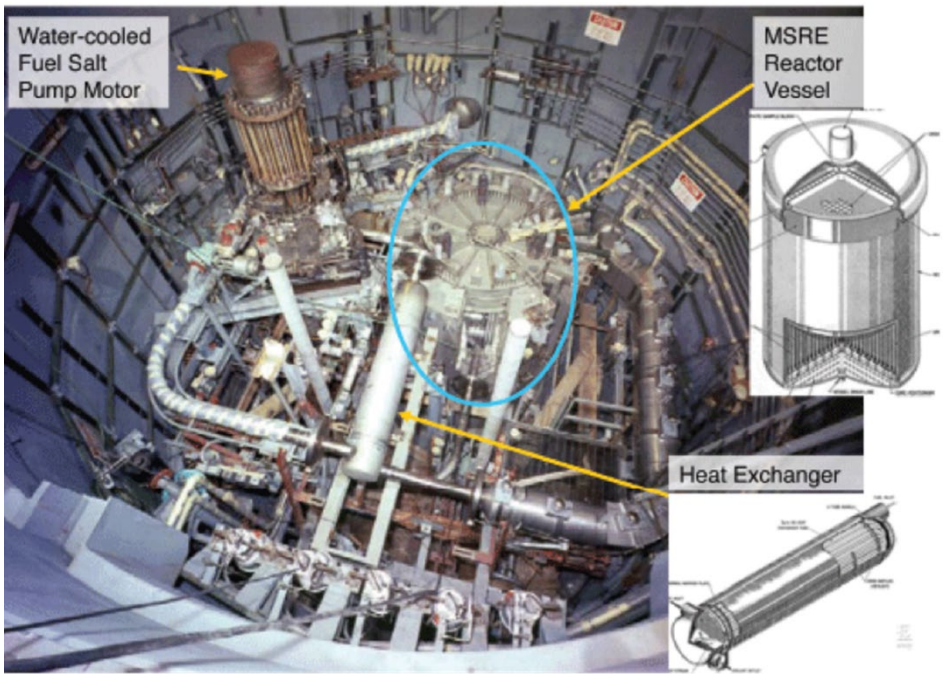

Figure 1-2: Photograph of the completed MSRE [12].

The MSRE was an 8 MW_t reactor, but since the reactor was only experimental the heat was sent into the atmosphere instead of a power generation cycle. First criticality was reached in 1965 and by 1968 the MSRE completed its first phase of experiments [9]. During its operation, the MSRE did not come without its own difficulties which are well described by Haubenreich, P. and J. R. Engel [13]. But, the MSRE successfully completed several phases of testing including the world's first nuclear operation using fuel enriched with ^{233}U [13]. Additionally, the MSRE operated for a short time with PuF_3 containing fuel salt showing the successful operation of a plutonium fueled MSR. By 1969, the MSRE was permanently shut down so that funding could be directed to other research efforts and development programs [14].

During the MSRE and continuing after its shutdown, much of the R&D efforts went into salt chemistry, component and materials design, and design of a new molten salt breeder reactor concept (MSBR). The materials design became a major topic for consideration, because although the MSR operated without any major corrosion issues, corrosion studies revealed that molten salt coolants have a tendency to aggressively attack metallic structural alloys. Unfortunately, by the

late 1970s the MSR concept lost much of its funding due to advancements in light water reactor technologies and liquid metal fast breeder reactor concepts [5].

It wasn't until relatively recently, that the MSR concept began gaining significant interest again, as mentioned previously it was identified as one of the most promising reactor concepts to help reduce greenhouse gas emissions from the burning of fossil fuels [3, 4]. Additionally, the inherent safety benefits of the MSR design have made it an attractive concept given recent events in the geopolitical climate [5, 15]. So, with the increased interest and questions remaining from the now decades old research of the MSRE program it's critical for current MSR researchers, designers, and regulators to enhance the understanding on potential issues facing MSR development. Specifically, an understanding of materials corrosion and interaction mechanisms in molten halide salt fluid is warranted.

1.3 Corrosion Challenge in Molten Salt Fluids

In most fluid environments, the corrosion of a metallic alloy is typically characterized by the oxidation of the elements that make up a given alloy. This oxidation is a result of some anodic (oxidizing) corrosion reaction that in most environments leaves behind an oxide layer on the alloy. In some alloys, these oxides may be brittle eventually flaking off leading to the degradation of the alloy, but in many circumstances, alloys are specifically chosen for their use because they form a dense stable oxide layer that helps to passivate an alloy from further degradation [16]. High temperature alloys such as stainless steel and nickel-based alloys for example, are commonly alloyed with chromium because in oxygen rich atmospheres chromium oxide (Cr_2O_3) scales are stable and provide a low diffusivity layer on top of the alloy [17]. An example of chromium oxide formation on a Fe-28Cr alloy is shown in Figure 1-3.

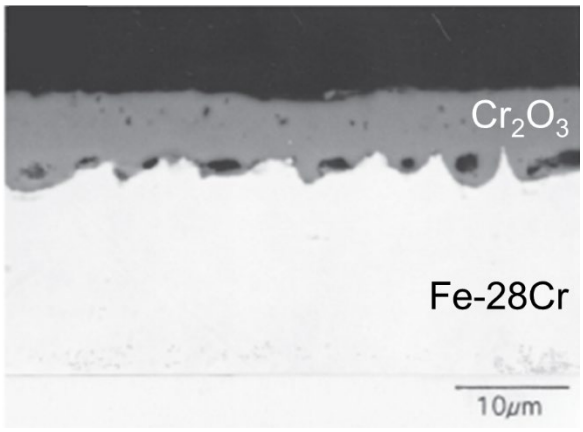

Figure 1-3: Cr_2O_3 scale grown on Fe-28Cr at a temperature of 1000 °C [17].

Unfortunately, in molten halide salt mediums, especially those based on molten fluorides, these protective oxides are dissolved by a fluxing action leaving the base alloy exposed to the molten salt [18]. Without a protective layer, the corrosion of the alloy surface exposed to the salt is essentially controlled by thermodynamic and kinetic driving forces for alloying element dissolution. To help visualize the susceptibility of an alloying element to dissolve in salt, it's helpful to consider the Gibbs free energies of formation for metal fluoride compounds presented in Figure 1-4. These values are calculated based on the generic reaction with fluorine gas shown in RXN 1-1.

$$xM + \frac{y}{2}F_2 \rightarrow M_xF_y \qquad \text{RXN 1-1}$$

The most stable fluoride compounds are the alkali (Li, Na, etc.) and alkali earth (Be, Ca, etc.) metal fluorides; because of their stability, these are typically used as the base fluorides for a salt mixture. Typical transition metal alloying elements are shown in solid lines. Their fluoride stability ranks in the order of Mn > Cr > Fe > Ni > W > Mo, meaning that thermodynamically Mn and Cr are the two elements most prone to attack in a molten fluoride salt melt. Because Mn is typically only used in minor concentrations (< 2 wt%), Cr ends up being the primary alloying element that is of concern in most high-temperature alloys [18].

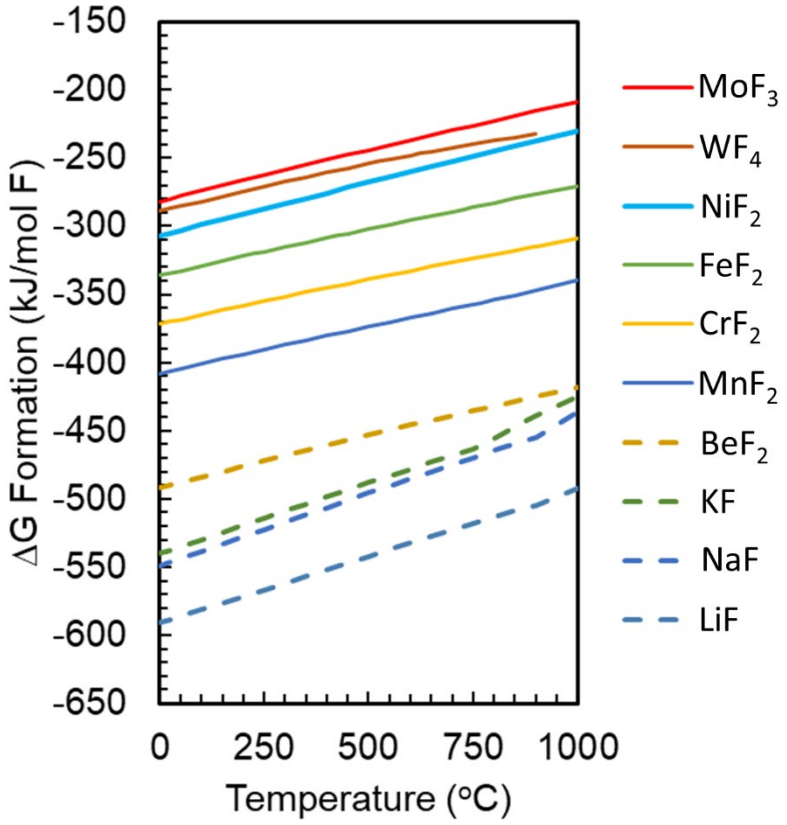

Figure 1-4: Gibbs free energies of formation for several metal fluorides. Data was generated with HSC Chemistry V7.00 [19].

The ability of the salt to remove any alloying element from a material is restricted by the salts fluorinating potential. This is often referred to as the salt redox potential which is essentially a measurement of the salts ability to donate electrons to an alloy by remove alloying elements [20]. The redox potential is defined by the Nernst Equation as

$$E = E^o - \frac{RT}{nF}\ln(Q) \qquad \text{RXN 1-2}$$

Where E^o is the standard potential, R is the gas constant, T is temperature, n is the number of electrons transferred in a reaction, F is Faraday's constant, and Q is the reaction quotient. From the free energies plot in Figure 1-4, it can be seen that alkali and alkali-earth metal fluorides that typically make up a fluoride salt mixture are extremely stable with respect to the transition metal fluorides. This would mean in a theoretically pure salt, the redox potential of the fluoride salt

mixture would be reducing with respect to reactions with the transition metals that make up a high-temperature alloy, and high-temperature alloys would be unaffected by the salt melt.

However, 100% pure salts both on a laboratory scale and a commercial scale are impossible to produce. Salt mixtures are inevitably exposed to oxygen, moisture, and other impurities during their preparation. All of these impurities act to move the salt redox potential to an oxidizing state with respect to the reactions with transition metals; therefore alloy corrosion is practically impossible to avoid. Additional details on how salt purity affects corrosion and how higher purity salt mixtures can be achieved are covered in Sections 2.1 and 4.1, respectively.

To increase the complexity of the corrosion challenge, once corrosion products have entered the salt melt, they too can alter the way that materials in the salt melt interact with one another. This is a phenomenon that has been previously referred to as activity gradient driven corrosion [21-23]. Details on activity gradient driven corrosion mechanisms are covered in Section 2.3. All of these challenges ultimately mean that understanding how a material behaves and interacts with the molten salt melt is critical for determining what alloys perform the best in realistic salt conditions and what factors change the performance of the tested alloy in a prototypical salt exposure experiment.

1.4 Prototypical Salt Exposure Experiment

During the ARE and MSRE programs, a large effort was put towards evaluating the corrosion performance of possible high-temperature alloys using thermal convection test loops. An example of just one row of thermal convection test loops along with the design schematic is shown in Figure 1-5 [24]. In these thermal convection loops, half of the loop section (i.e. the hot leg and bottom crosser) are heated to a specified temperature while the top crosser and cold leg are not actively

heated. This creates a density gradient in the salt due to the temperature differences which in turn causes the salt to naturally circulate (NC) through the loop without the use of a pump [24, 25]. Using these loops the ARE and MSRE programs tested many alloys collecting invaluable corrosion data for modern researchers to build on and eventually attempt to replicate.

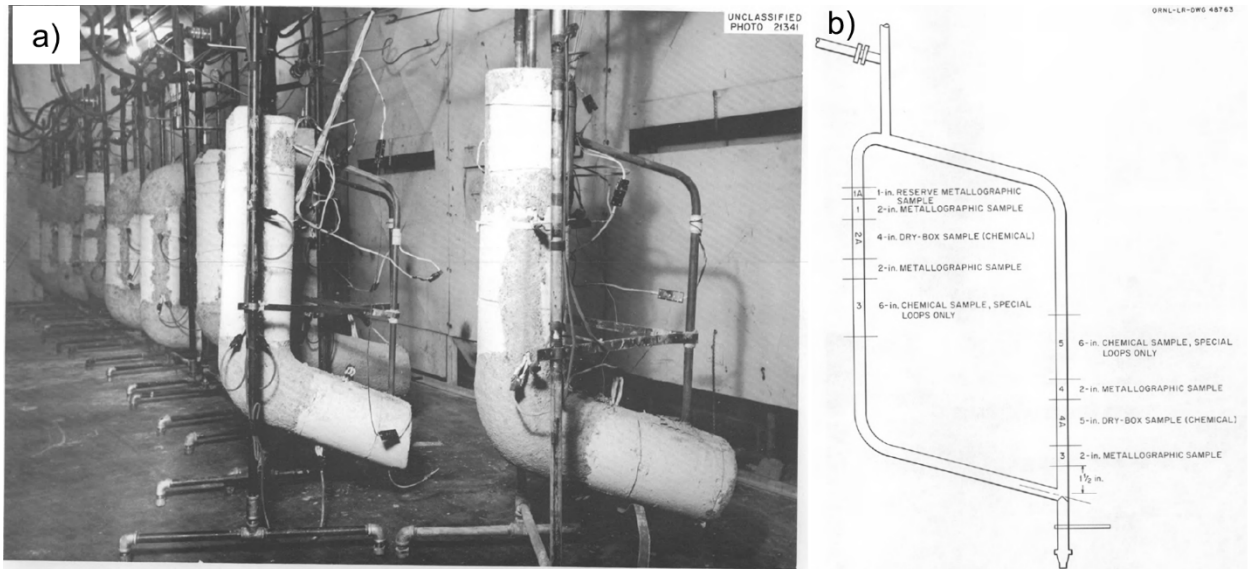

Figure 1-5: Example of thermal convection test loops. a) Photograph of a row of test loops. b) Schematic of the test loop design

To run these NC loops, each loop had to be constructed out of the alloy of interest. For modern day research universities and small groups this approach of building, operating, and evaluating hundreds of NC loops is a significant challenge. Additionally, the development of modern MSR concepts has introduced the need to test materials that are impractical to build NC loops out of. Therefore, the prototypical approach to testing alloy and material compatiblity in molten salts today has primarily transitioned into performing static isothermal salt exposure tests. Typically, these tests are conducted using either a sealed capsule [22, 26-29] or an open crucible with an inert cover gas [30-33]. In either of these testing conditions, samples of metal alloys or other materials are submerged in a salt that is not actively flowing at a given test temperature for a pre-determined amount of time.

The design of these tests can vary greatly, but some of the advantages of these tests is that they are simpler to perform than NC loops and they allow for the testing of materials that can't be used to construct NC loops. However, it's the variation of the test designs that ultimately draw into question many of the results that come out of these static isothermal salt-exposure tests. Raiman, S. and S. Lee [34] recent published an aggregation of the corrosion data from several researchers and found that there exists a complete scattering of the corrosion data even when researchers are studying the same test alloy, in the same salt media, at the same test temperature, and same test time. An example of the scattered data is shown in Figure 1-6. Raiman, S. and S. Lee went on to suggest that many parameters in a static isothermal salt exposure test have effects on the results that came out of the tests providing some of the inspiration for the work performed in this dissertation. In Chapter 2, the effects studied as part of this dissertation will be discussed in detail and Chapters 3-5 will describe the experimental designs and results that show how each of the studied effects affect the outcomes of salt-exposure tests in a LiF-NaF-KF (46.5-11.5-42 mol%) salt mixture known as FLiNaK.

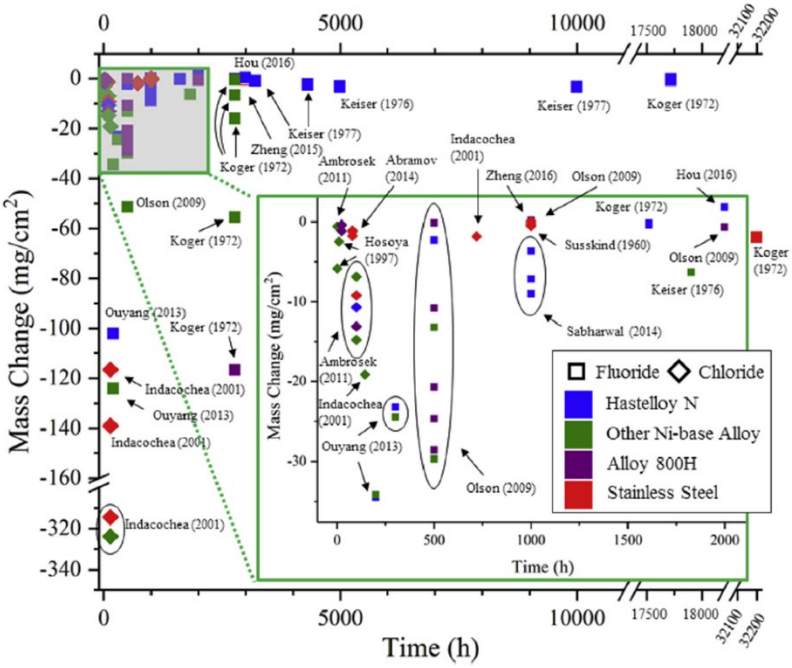

Figure 1-6: Aggregated mass change data for corrosion experiments on alloys in fluoride and chloride based salts showing a vast scattering in the data [34].

Chapter 2

Corrosion Aspects

In the prototypical corrosion experiment that has become popular for testing alloys and materials in molten salt environments described in Section 1.4, it has become apparent that the design considerations of a static isothermal salt exposure cell have important effects on the overall outcomes of one's corrosion experiments. Ideally, to reduce the influence of the cell design parameters on the outcome of the experiment there would be a standard that researchers or corrosion engineers could reference when building molten salt corrosion experiments, such as an ASTM standard. However, because the testing of materials in molten salts is a relatively new topic with a rather narrow field of interested parties, there is currently no standard for researchers to reference. This leaves researchers with only previous manuscripts to loosely follow. In some circumstances, this provides groups the freedom to change the molten salt testing environment as they see fit to get what they believe will be the best design for studying what they need, but this situation is also what has created some the issues investigated in this dissertation.

Currently, only one known manuscript has attempted to do a thorough investigation on what parameters appear to affect the results of a molten halide salt corrosion experiment. As mentioned earlier, Raiman, S. et al.'s [34] aggregation of the corrosion data from multiple molten halide salt corrosion experiments showed that there is a large scattering of the corrosion data even when the same salt, test temperature, and alloy are being studied. This scattering of the corrosion data, of course puts both reactor designers and regulators in a difficult position when it comes to determine the best alloys and materials for use in molten salt environments. Raiman, S. et al.'s aggregation

of the data lead them to conclude that the most influential parameter in the design of a molten salt experiment was the purity of the molten salt being used. However, due to the many testing parameters that can be adjusted in a static isothermal molten salt exposure test, not all of the parameters were covered in detail. The following sections in this chapter attempt to outline a few of the corrosion environment parameters that exist in a static isothermal salt exposure test cell and how those parameters would affect the outcome of a corrosion experiment in FLiNaK salt.

2.1 Salt Purity

The importance of the purity of the fluoride salt on the corrosion performance of an alloy was not necessarily realized recently, in fact, during the MSRE program it was well understood that for an MSR to operate efficiently without significant degradation the salt used in the reactor had to be of extremely high quality. The Reactor Chemistry Division even had a general specification that their fluoride mixtures were supposed to meet in order to be considered high enough quality [35]. This specification is provided in Table 2-1. The original specification only provided impurity concentrations in terms of wt % so the final column of wt-ppm was added for readability. Note that some of these allowable impurities were restricted based on neutron poisoning considerations which isn't a problem for non-fissile experiments, but several of the impurities also act as oxidizers to possible structural alloys [11].

Table 2-1: General Chemical Specifications for MSRE Fluoride Mixtures [35].

Impurity	Allowable Concentration (wt%) (1ppm = 0.0001 wt %)	Concentration converted to wt-ppm
Water	0.1	1000
Cu	0.005	50
Fe	0.01	100
Ni	0.0025	25
S	0.025	250
Cr	0.0025	25
Al	0.015	150
Si	0.01	100
B	0.0005	5
Na	0.05	500
Ca	0.01	100
Mg	0.01	100
K	0.01	100
Li (natural)	0.005	50
Zr (natural)	0.025	250
Cd	0.001	10
Rare earths (total)	0.001	10

In order to produce high purity salts, the MSRE program developed a purification method for fluoride salt mixtures based on the sparging of hydrogen and gaseous hydrogen fluoride (HF) to remove oxidizing impurities in the fluoride mixtures. In this section, only the importance of removing the oxidizing impurities is discussed, but additional details on salt purification are provided in Chapter 4. As described in Section 1.3, the corrosion of a structural alloy in a molten salt electrolyte is driven by the thermodynamic driving force and kinetics of the formation of metal fluoride compounds because protective oxide layers are not stable [18]. Thus, it is useful to consider the Gibbs free energies of formation for metal fluorides. A plot of the fluoride formation

energies was shown in Figure 1-4. It can be observed that the formation of the alkali and alkali earth metal fluorides (Me) which are typically used as the base fluorides in fluoride salt mixtures have very low (more negative) free energies of formation. Meaning that the Me-fluorides are more stable than the transition metal alloying element fluorides. This suggests that if one were able to achieve perfect salt purity, the redox potential of the salt would be reducing because the Me-fluoride salt constituents would not be corrosive towards structural alloys. However, perfect purity in a processed salt is impossible to achieve and what becomes critically important is the level of impurities which ultimately determines the salts redox potential.

Impurity-driven corrosion is of concern because many of the impurities like, moisture, oxides, and other metallic fluorides are bound to get incorporated with the fluoride salt either during salt production or reactor operation and each of these impurities act as oxidizers that accelerate the attack on metal alloys [18]. Moisture is one of the most aggressive impurities that can accelerate the corrosion of alloys in fluoride salts because of hydrolysis reactions with fluoride salts leading to the generation of HF through the following reactions [36]:

$$MeF + H_2O \rightarrow MeOH + HF \quad \text{RXN 2-1}$$

$$2MeF + H_2O \rightarrow Me_2O + 2HF \quad \text{RXN 2-2}$$

Where Me is one of the base alkali or alkali earth metals such as (Li, Na, K, Be, etc.). The HF that is generated through these hydrolysis reactions is then very corrosive (i.e. makes the redox potential more oxidizing) to many metals or metal oxides that are then present in the molten salt system such that the following oxidizing reactions of the metal are possible:

$$xM + yHF \rightarrow M_xF_y + \frac{y}{2}H_2 \quad \text{RXN 2-3}$$

$$MO + xHF \rightarrow MF_x + \frac{x}{2}H_2O \quad \text{RXN 2-4}$$

Where M is any of the possible alloying elements (Mo, Ni, Fe, Cr, etc.) in a metal alloy. Whether produced by the reactions with HF or introduced into the salt during processing, these metal fluorides are also oxidizers towards other alloying elements that form more stable fluorides. Again, considering the free energies of metal fluoride formation, Figure 1-4, out of common alloying elements, Cr forms one of the most stable fluorides. Meaning that if the reaction with HF produces iron or nickel fluoride compounds, those compounds can lead to the further oxidation of Cr through the following fluorine exchange reactions:

$$NiF_2 + Cr \rightarrow CrF_2 + Ni \qquad \text{RXN 2-5}$$

$$FeF_2 + Cr \rightarrow CrF_2 + Fe \qquad \text{RXN 2-6}$$

Finally, a very important impurity that can be found in the raw constituents (LiF, NaF, etc.) that make fluoride salt mixtures is sulfur in the form of sulfates [20, 37, 38]. The actual reaction mechanisms that the sulfur impurities go through that lead to accelerated corrosion are not fully understood, but it is believed that the sulfates can partially thermally decompose into sulfur trioxide and sulfur dioxide compounds at the elevated temperatures where fluoride salts are used [20]. Then the sulfate ions, sulfur trioxide, and sulfur dioxide can either oxidize metals in the fluoride salts forming an oxide layer or form soluble metal sulfides. Because oxides are unstable in fluoride salts, any formed oxide due to the reactions with sulfur species is fluxed away from the alloy. Thus overall, sulfur has led to the accelerated corrosion of the structural alloys by being present in the salt melt. Several researchers have confirmed that elevated concentrations of sulfates in fluoride salts increase the corrosion rates of Fe-based and Ni-based alloys [37-39]. Therefore, the purity of the fluoride salt melt is extremely important for how a metal alloy is expected to perform.

2.2 Volume of Salt and Exposed Surface Area

Intimately linked to the effect of salt purity on corrosion is the effect of the volume of salt to exposed surface area ratio, simply referred to as the Vol/SA ratio throughout this dissertation. In the prototypical static isothermal corrosion experiment, the quantity of salt and therefore the volume of salt is rather straightforward to determine. Williams, D. et al. [40] for example provides salt density information on several fluoride salt mixtures that can be used to determine the volume of salt used in an experiment at a given test temperature as long as one records the mass of salt added to an experiment.

On the other hand, determining the surface area of material in a given experiment is not necessarily as straightforward. Much of that determination depends on how one plans to setup the experiment. The prototypical molten salt exposure test generally has two pieces that contribute surface area that is exposed to the molten salt. The first piece is the sample material under study and the second piece is the container material used to contain the molten salt melt. With the lack of an accepted standard approach, many groups take different considerations when choosing what container material to pair with their sample material (this is also one of the largest sources of dissimilar material interactions covered in Section 2.3). One approach that is often taken is to match the container material to the sample material [30, 41]. While this approach is somewhat easily feasible when commercially available alloys like stainless steel are being investigated, often materials that are being studied in molten salt are not available in all form factors making the construction of a salt container impractical. So, the second approach often used is to find a container material that is believed to be “inert” to the molten salt melt and the corrosion products of the sample material being studied [42-46].

Each of these approaches to the salt container material brings its own challenges in terms of their effects on the Vol/SA ratio. In the first approach by matching the container material to the sample material, the exposed surface area to the molten salt is dramatically increased and the salt container surface area becomes the biggest contributor to the decreased Vol/SA ratio. Consider the simplest form of a salt container, a cylindrical container. The volume of salt and exposed surface area then become highly dependent on the containers dimensions. Ignoring the contribution of sample surface area, the equation for the Vol/SA ratio is:

$$\frac{Volume\ of\ Salt}{Exposed\ Surface\ Area} = \frac{\pi r^2 * h}{\pi r^2 + 2\pi * r * h} \qquad \text{Equation 2-1}$$

Where r and h are the radius and the height of the salt container, respectively. This equation simplifies to:

$$\frac{Volume\ of\ Salt}{Exposed\ Surface\ Area} = \frac{r * h}{r + 2h} \qquad \text{Equation 2-2}$$

If one restricts the radius of the container to a specific sized bore hole or pipe size, then the Vol/SA ratio only approaches 2 as the height goes to infinity. Obviously, a salt container can't have an infinite height, so realistically, the largest Vol/SA ratio one might achieve is just above 1.5 cm^3/cm^2. Similarly if the height is restricted, then the Vol/SA ratio approaches h as r goes to infinity. An infinite r is impractical, which essentially means the container once again becomes extraordinarily large in order to achieve a Vol/SA ratio much larger than 1.5 cm^3/cm^2. So, by using a container that matches the sample material, there is a lot of surface area that is being exposed to the salt that isn't the sample of interest. All of this surface area interacts with the salt and therefore consumes impurities through corrosion reactions potentially limiting the corrosion that is observed by the sample coupon.

In the second approach of choosing an "inert" material for the salt container, one expects that only the surface area of the sample is now relevant and the surface area of the container can be ignored. With this situation, the Vol/SA ratio can now be easily adjusted by changing the volume of salt or the size of the sample material. The primary challenge with this approach is that few materials are truly "inert" to interactions with molten salt and potential alloy corrosion products. This challenge is covered in more detail in Section 2.3 and Chapter 5. Briefly, "inert" materials like nickel and molybdenum have both been shown to interact with corrosion products from tested alloys [31, 47], and even graphite has been shown by several researchers to form carbides with corrosion products coming from tested alloys [27, 46, 48, 49]. Of all the "inert" materials that could be found in the literature, only pyrolytic boron nitride has been shown to be inert to molten fluoride salts and corrosion products coming from tested alloys making it an ideal choice for studying the effects of the Vol/SA ratio as well as many other effects [46, 50].

The importance of not only knowing the amount (i.e. volume) of salt in a salt exposure experiment, but the exposed surface area primarily comes down to the concentration of impurities and corrosion product solubility limits in the salt. Impurities in the salt are typically reported in terms of wt-ppm or µg of impurity per g of salt. As discussed in Section 2.1, impurities in the salt greatly contribute to how corrosive a salt is by changing the salts redox potential. For example, consider a fluoride based salt that has a density of 2.02 g/cm^3 that contains 300 ppm of FeF_2 and a 1 cm^2 stainless steel test material tested at a Vol/SA ratio of 1 cm^3/cm^2 and 10 cm^3/cm^2. The tests then contain either 1 cm^3 or 10 cm^3 of salt. Using the density that means the tests have either 2.02 g or 20.2 g of salt which corresponds to either 6e-4 g or 6e-3 g of total FeF_2 in the salt. Because of the stability of chromium as a fluoride, the FeF_2 impurities would be expected to undergo RXN 2-6 with the Cr in the stainless steel test material. RXN 2-6 would then proceed until the amount of

FeF_2 consumed has lowered the redox potential below that of the stainless steel. So in the salt volume with more FeF_2, more total FeF_2 has to be consumed in the test meaning more Cr is lost. Therefore, it can clearly be seen that the stainless steel in the larger Vol/SA ratio test would experience a greater degree of Cr loss. So, the Vol/SA ratio has a large impact on the amount of corrosion that is expected.

A major component missing to this is the reaction kinetics. Unfortunately, this is one of the largest missing components in the molten salt literature. Currently, little is known about the reaction kinetics of the corrosion reactions. But the simply analysis above demonstrates, that adjusting the Vol/SA ratio has a clear impact on the overall magnitude of corrosion. The main goal then for designing a test would be to have a large enough Vol/SA ratio that the expected corrosion reactions don't consume enough impurities to lower the redox potential, because if the corrosion stops at an unknown time then one cannot accurately determine a corrosion rate for the alloy being tested. In Chapter 3, the use of a new corrosion performance metric to qualitatively judge tested materials will be discussed in order to account for the unknown reaction kinetics.

2.3 Dissimilar Material Interactions in Salt

2.3.1 Manifestation of Dissimilar Material Interactions

As introduced previously, in the prototypical static isothermal salt-exposure test, one potential source of dissimilar materials interactions is the interactions between the sample material being studied and the salt container being used for the test. In order to avoid this interaction between the sample material and salt container, one method is to use the same materials for both the sample and the salt container. However, as covered in Section 2.2 this creates a major challenge in achieving a high Vol/SA ratio in the test. Another challenge with this method is that not all of the

materials that need to be studied in a molten salt environment are easily manufactured into salt containers.

So to get over these challenges, often one has to use a material that is somewhat simple to manufacture a salt container out of while testing samples. In this approach it is desired to find a salt container material that is not only manufacturable, but also reasonably expected to be "inert" to the molten salt and resistant to interactions with the sample material. For choosing an "inert" material, once again consideration is typically given to the Gibbs free energy of formation for the "inert" materials main element. So, referencing the free energies in Figure 1-4, the most common materials chosen for an "inert" salt container are nickel [42, 51], molybdenum [44], and graphite [43, 52]. Unfortunately, while the container materials maybe reasonably expected to be "inert" to the molten salt, it's difficult to call these materials truly "inert" with regard to interactions with the sample material. In this approach dissimilar materials are potentially being put into electrical contact with each other in a corrosive electrolyte, which are the three conditions needed for the creation of a galvanic couple [16]. Additionally, even if the materials are kept electrically isolated from each other, several researchers have demonstrated that dissimilar materials in a molten salt environment can also interact with each other through activity gradients [21, 31, 46, 47]. Therefore understanding the effects of a galvanic couple and activity gradients between dissimilar materials in molten salt media is critically important for understanding results on salt exposure tests where sample materials are tested in the presence of a dissimilar material.

2.3.2 Galvanic Coupling

For a galvanic couple to occur three things are required, (i) dissimilar materials are present, (ii) those materials are present in a corrosive conducting media, and (iii) the materials are in electrical contact. In any media, materials have a specific corrosion potential E_{corr}. When materials with

differing E_{corr} are put into electrical contact with one another, a flow of electrons occurs from the material with a more negative E_{corr} towards the material with a more positive E_{corr}. In this sense, the material with a more negative E_{corr} acts as an anode and is preferentially corroded with respect to the more positive E_{corr} material, the cathode [16, 53]. The general tendency for materials to form a galvanic couple can be determined by looking at a galvanic series. But, any changes in the media's composition or temperature can result in a change in a materials position on the series, therefore these series are really only qualitative in nature [16].

In a galvanic couple, the exchange of electrons (i.e. current) between the anode and cathode materials is driven by oxidation and reduction reactions. A general schematic of a galvanic couple is shown in Figure 2-1. Consider an active metal as the anode material, the oxidation reaction, RXN 2-7, of the metal is the reaction occurring that liberates electrons from the anode.

$$M \rightarrow M^{m+} + me^{-} \qquad \text{RXN 2-7}$$

Where m is the number of electrons that are released due to the oxidation of the metal M. Accompanying the oxidation reaction at the anode is the reduction reaction that takes place at the more noble material (i.e. the cathode). The exact reduction reaction that takes place is difficult to predict and typically depends on the electrolyte. In molten fluoride based salt electrolytes such as FLiNaK it has been hypothesized that the reduction reactions could be the reduction of metal ions that are multivalent [54, 55], hydrogen ion reduction [49], HF reduction [28, 49], or possibly sulfate reduction [28]. Insinuating that these types of impurities likely need to be present in the FLiNaK in order for a reduction reaction to occur.

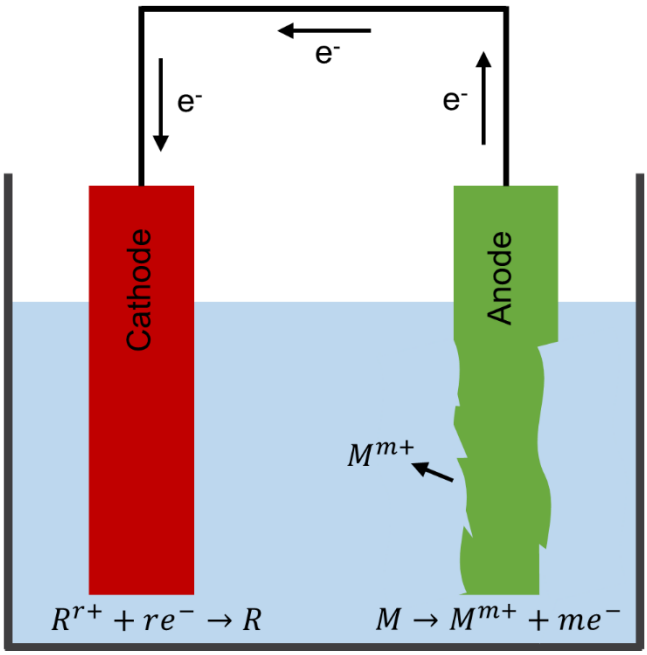

Figure 2-1: Generic schematic of a galvanic couple in an electrolyte. When an electrical connection is made between the cathode and the anode, the anode will be preferentially attacked by the electrolyte.

Predicting and measuring the behavior of a galvanic couple can be performed in several ways. Polarization tests for example take uncoupled materials and sweeps them through a potential range that covers both a cathodic and anodic region of that material, as shown in Figure 2-2a. If individual polarization curves of different materials are collected and overlaid on the same graph then the behavior of those two materials coupled together can be predicted by mixed potential theory.

If the two materials are coupled together, electrons will flow from the anode to the cathode polarizing the materials such that the couple causes the two materials to behave just as if an external source was causing the polarization. The coupled materials are then polarized until they reach the same potential, E_{couple}. So that excess charges don't accumulate, as required by mixed potential theory, the rates of oxidation at the anode and the rates of reduction at the cathode have to be equal to each other such that a steady state current is reached. This is the coupled galvanic current, I_{couple}, for the two materials [16]. So, individual polarization measurements of the

materials can be used to predict the galvanic current if the two materials are coupled together by determining the crossing point of the active materials anodic curve and the noble materials cathodic curve, as shown in Figure 2-2b.

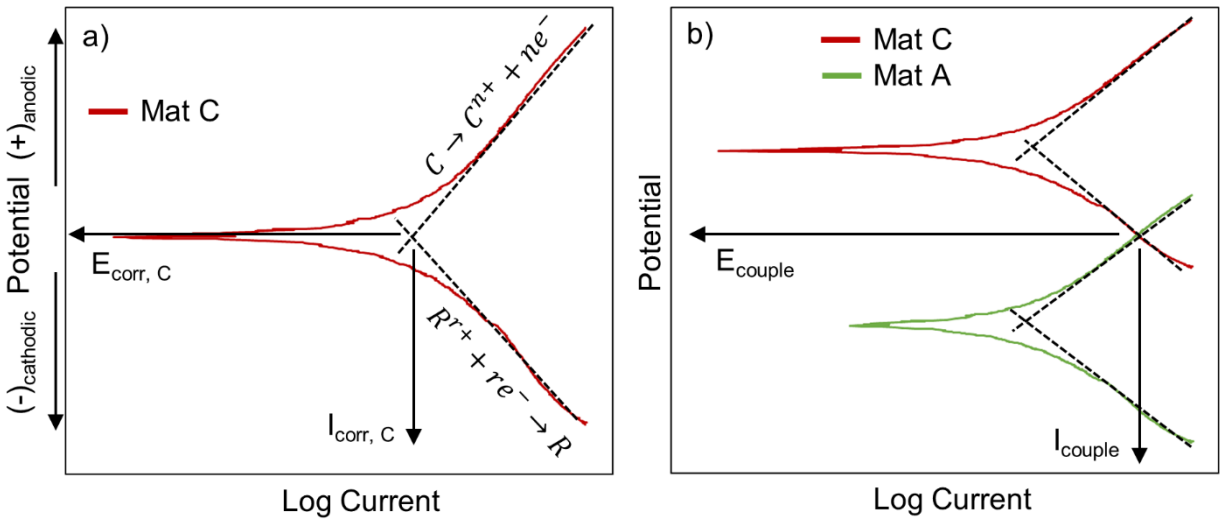

Figure 2-2: Example of polarization measurements for estimating galvanic couple behavior. a) individual polarization measurement. b) overlaid polarization measurements showing crossing point of the cathodic curve of material C and the anodic curve of material A.

The polarization and therefore the coupled current of the dissimilar materials can also be measured more directly using a zero resistance ammeter (ZRA) technique on a potentiostat. In a ZRA measurement, the cathode and anode material behave as though they are connected to each other through a zero resistance wire. The potentiostat does not apply a voltage or current and only measures the free-flowing current between the anode and cathode [56]. A benefit to measuring the coupled current with a ZRA technique is that the current can continuously be monitored during a test. This technique has been applied to dissimilar material coupled current measurements in many electrolytes [57-59] including FLiNaK salt [49, 54]. Qiu, J. et al for example measured the coupled current between 316L stainless steel (316LSST) and graphite using the ZRA technique and found that in this couple 316LSST always behaved as the anode material while graphite behaved as a cathode; therefore demonstrating that the graphite coupled to 316LSST should increase the corrosion rate of the 316LSST [49].

In terms what effect galvanic corrosion may have on the results coming from a prototypical salt exposure test, the challenge really comes from the situation of using dissimilar materials for the salt container and sample material. For example, if the salt container is expected to behave as a cathode (i.e. trying to use an “inert” container) and the sample material is likely to behave as an anode, then the corrosion rate of the sample material measured in the prototypical test would potentially not accurately reflect the sample materials true performance because of the galvanic couple. Because of this, often when an “inert” container is being used as the salt container in a salt exposure test, the galvanic couple between the container and the sample material is eliminated by suspending the samples from an electrically insulating ceramic strip. It is then thought that by removing the electrical couple, interactions between the dissimilar materials should be eliminated. However, many researchers have clearly demonstrated that the elimination of the electrical contact doesn’t stop dissimilar materials from interacting with one another in molten salts.

2.3.3 Activity Gradient Driven Mass Transportation

Activity gradient mass transport between dissimilar materials in a molten salt environment effectively refers to how quickly the activity of a transporting element in a second material reaches the same activity level that it had in the original material it is transporting from as the concentration of that element increases in the second material, although for brevity it is referred to simply as activity gradient mass transport [47]. It was hypothesized and later shown that this mechanism does not require electrical contact between the dissimilar materials and, rather than being enabled by a galvanic connection, is enabled by a disproportion reaction of potential corrosion products in the molten salt media [21, 31, 46, 47]. A general schematic of the mass transport process is shown in Figure 2-3.

As described in Section 1.3 and shown in the Gibbs free energy diagram, Figure 1-4, the corrosion of materials in a fluoride medium typically follows the trend of fluoride stability [18]. Several metallic elements such as Mo, Cr, Fe, etc. can form metallic fluorides with different oxidation states of the metal ion [60-62]. Because of this, the corrosion of materials containing such elements can result in corrosion reactions that produce metallic fluorides of multiple oxidation states. For simplicity, Figure 2-3 shows corrosion products with metal ions in the 2+ and 3+ oxidation state. As described in Section 2.1 these corrosion products can be produced through reactions with a number of different impurities in the salt media. For simplicity, RXN 2-8 and RXN 2-9 are generalized by using $F_{2_{(g)}}$ as the impurity where the subscript *g* means gaseous.

$$M_{(material\ 1)} + F_{2_{(g)}} \rightleftharpoons MF_{2_{(d)}} \qquad \text{RXN 2-8}$$

$$M_{(material\ 1)} + \frac{3}{2}F_{2_{(g)}} \rightleftharpoons MF_{3_{(d)}} \qquad \text{RXN 2-9}$$

In RXN 2-8 and RXN 2-9 the subscript *d* and g indicates a dissolved or gaseous species, respectively, while *M* represents a metal susceptible to the corrosion reaction. These generalized corrosion reactions therefore put corrosion products with different metal ion oxidation states into the fluoride salt. With both metal ion oxidation states existing in the salt, there must also be a disproportionation reaction (RXN 2-10) that occurs somewhere in the salt.

$$3MF_{2_{(d)}} \rightleftharpoons 2MF_{3_{(d)}} + M_{(s\ or\ d)} \qquad \text{RXN 2-10}$$

Here the subscript *s* indicates a solid metal species.

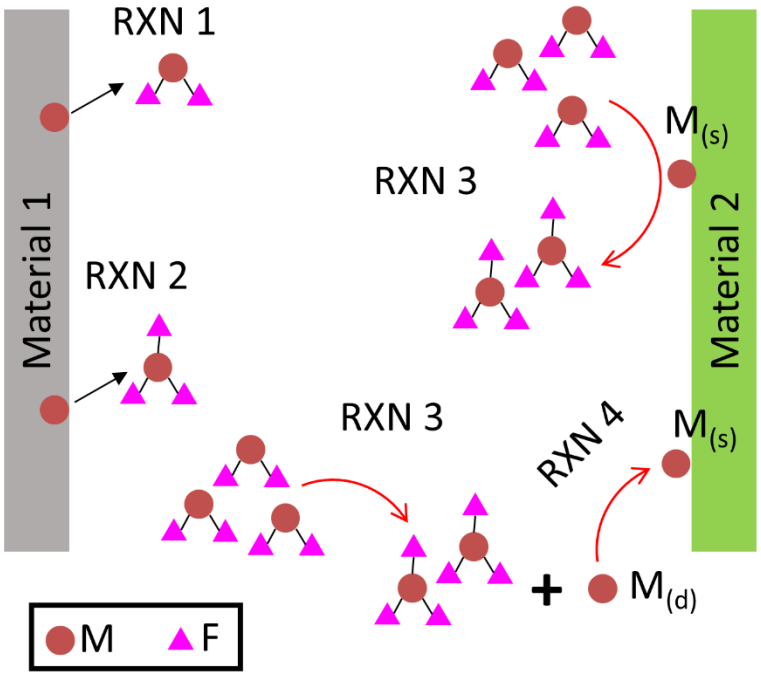

Figure 2-3: Schematic of the activity gradient driven mass transport process.

From RXN 2-10, it is hypothesized that *M* could form in either a solid or a dissolved species. Ozeryanaya [21] and Olson et al. [46] speculated that the disproportionation reaction would occur at the surface of another material in the salt such that an absorbed atom, M_s, is formed on the material. Then, based on the chemical potential of the absorbed atom at the surface, it could potentially go on to form a solid solution, compound, or an intermetallic with the material if a favorable formation energy exists. As mentioned previously, in the case of Olson et al.'s experiments, they found that the corrosion of Incoloy-800H and Hastelloy-X in graphite containers resulted in the transport of Cr (as well as Fe in the case of Incoloy-800H) which then formed a carbide compound with the graphite. While the disproportionation reaction could take place at the surface of a material, it is also highly likely that it would occur within the salt media itself resulting in the formation of dissolved metal species M_d.

Williams et al. [40] reported that certain mixtures of fluoride based salts, like FLiNaK, tend to be fluorobasic meaning that the salt is likely completely dissociated. Because of this, metal species such as Cr and Fe are likely to be present in oxidation states of 2+ and 3+ in salt. Further evidence

of Cr disproportionation in FLiNaK was shown by Wang et al. [62] and Peng et al. [60] while Ai et al. [63] demonstrated the disproportionation of Fe in FLiNaK. Since the disproportionation reaction of certain metal species is possible within the salt itself, the creation of dissolved metal, M_d, is highly probable. Any dissolved metal within the salt medium is then able to transport to the surface of other material submerged in the salt via diffusion along a chemical potential gradient. Once again, if a favorable formation energy for solid solution, intermetallic, or compound formation of the dissolved metal exists it may undergo an absorption reaction (RXN 2-11).

$$M_d \rightarrow M_s \qquad \text{RXN 2-11}$$

This series of reactions and specifically the disproportionation of the potential corrosion products coming from one material, provides a pathway for elemental transport in the salt media without the need for electron transfer between two materials (i.e. galvanic contact). The transport is primarily driven by the fact that there exists an activity gradient of elements in one material to a specific concentration of those elements that could exist in a second material. Unique to this mechanism is that it has the potential to cause significant elemental transport even in the case of elements that have low solubility in the salt. This is analogous to the well-known chemically driven transport mechanism of elements like Ni or C in liquid Na metal where the primary mode of alloy degradation is elemental metal solubility in liquid Na [64, 65].

Chapter 3

Effect of the Volume of Salt to Surface Area Ratio

In the prototypical static isothermal corrosion experiment for alloy and material testing in molten salts, the size of not only the sample but also the size of the container determines the overall volume of salt to surface area ratio of the testing environment. If the salt container material and the sample material are the same, then achieving a large Vol/SA ratio is practically impossible due to the limitations of testing systems. If a truly "inert" material is used for the salt container, however, adjusting the Vol/SA ratio can be done by changing the quantity of salt in the test or by changing the size of the sample material. In either case, performing these experiments requires specialized equipment to keep the salt under a satisfactory environment such that it doesn't absorb moisture and oxygen impurities as well as to control the temperatures of the salt exposure tests.

3.1 Experimental Design

3.1.1 Glovebox and Furnace Design for Static Isothermal Salt Exposure Testing

Due to the tendency of the molten fluoride salts to absorb oxygen as well as their hygroscopicity, the design of the glovebox and furnace system for salt exposure testing is critical to ensure that the corrosion testing is not being influenced by uncontrolled uptake of moisture or oxygen. For this reason, all of the experiments described in this dissertation utilized the same glovebox and overall furnace design, but the glovebox and furnace system will only be described in the following section. Details on the changes to corrosion test crucibles are described in the appropriate experimental chapters and sections.

The glovebox used for this dissertation work was an LC-180 glovebox system, LC Technologies Solutions, Salisbury, MA. The glovebox is full stainless steel construction and equipped with a gas purification system. While connected to ultra-high-purity grade argon, the gas purification system is capable of maintaining an argon atmosphere where oxygen and moisture levels do not exceed 3 ppm and 1 ppm, respectively. Additionally, the glovebox has multiple KF40 style flanges located at the back wall that allow power and thermocouple probes to be located inside the glovebox. A photograph of the glovebox system is shown in Figure 3-1

Figure 3-1: LC-180 glovebox system used for handling salt and performing salt exposure tests.

The furnace used for salt exposure tests is incorporated into the LC-180 glovebox itself. Coming off of the bottom of the glovebox floor are two 6.875 inch outside diameter wells that are 24 inches deep. The wells are connected to the glovebox via a flange that is sealed with a silicone O-ring. This flange allows the wells to be sealed from the inside of the glovebox such that the wells can be removed if desired or if one wishes to change the gas phase environment during a salt-exposure

test without affecting the primary glovebox atmosphere. Otherwise, the wells can remain connected to the glovebox such that the inert atmosphere in the glovebox is shared with the atmosphere in the well. To keep the silicone O-ring from melting during the high temperature testing of a typical isothermal salt-exposure test, the flange has a built in water cooling jacket that can be connected to a once through or recirculating water system. Additionally, to ensure the main glovebox environment doesn't become excessively heated, the glovebox has a cooling radiator that is also connected to the same water supply as the flange water jacket. Thermocouple probes throughout the glovebox monitor the temperature of the primary glovebox environment as well as the temperature of the well connection flange to ensure the safety of the silicone O-ring. The inlet and outlet temperatures of the cooling water are also monitored with thermocouple probes.

To provide heat to the well, two 1800 W Watlow® semi-cylindrical clam shell style ceramic fiber heaters are attached to the outside diameter of the well. The heaters have a 12 inch heated zone and 3 inch tall vestibules keep the heating elements from coming into contact with the stainless steel well. A thermocouple probe is positioned near the heater elements to monitor the temperature at the heater walls. Additionally, a thermocouple probe is positioned inside the well to monitor the test temperature as close to the salt exposure test as possible. To provide adequate insulation for the heaters, two layers of 10 mm thick Pyrogel® HPS insulation are wrapped around the Watlow heaters. Two layers of the insulation were also added to cover the top and bottom of the heaters to ensure as little heat would escape as possible. A photograph of a completed heated assembly is shown in Figure 3-2.

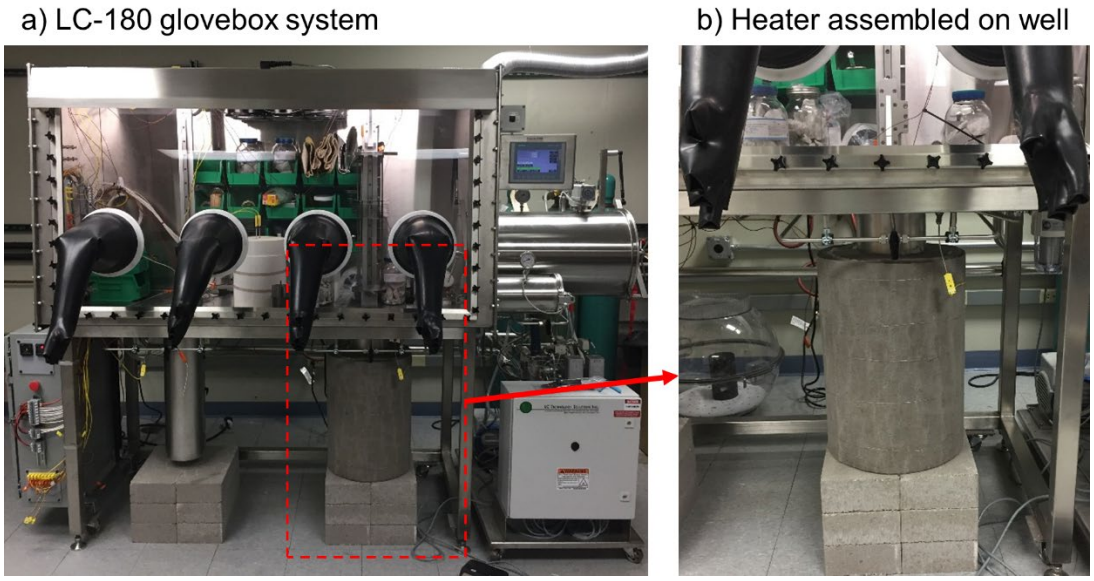

Figure 3-2: LC-180 Glovebox system with one completed furnace well assembly. a) Overview of system with one furnace completed (right) and one furnace uncovered (left). b) Completed furnace well.

All of the heaters and temperatures around the glovebox and well are controlled and monitored via a custom LabVIEW program that is connected to a cRIO data acquisition and control module. The LabVIEW program allows the user to set the temperature of any heater connected to the glovebox as well as data log the temperature information coming from all of the thermocouple probes. Several safety checks are programmed into the LabVIEW control to ensure the silicone O-ring connecting the well to the glovebox remains below a safe temperature.

For lifting salt exposure tests in and out of the furnace well, a custom lifting assembly was also constructed. The main lifting mechanism is a pneumatic cantilever lift designed by LC Technology Solutions and installed above the well. Attached to the pneumatic lift is the lid of the well which allows for the attaching of a lifting plate. The lifting plate was designed and built in-house. A photograph of the lifting plate is shown in Figure 3-3. Three 5/16 inch 316SST threaded lifting rods are used to connect the bottom lifting plate to the well lid. Details on the mechanical design basis using creep rupture data from the American Iron and Steel Institute [66] are provided in Appendix A. Also connected to the lifting rods are a stack of planar thermal heat shields. Details

on the thermal design basis of the heat shields are also provided in Appendix B. The design of the shields followed an approach published by Argonne National Laboratory specifically for heat shield design on gloveboxes [67]. The heat shields help to ensure an even temperature distribution in the heated zone of the well, as well as to drastically reduce the temperature in the well on the opposite side of the heat shields once again ensuring the safety of the silicone O-ring. The thermocouple probe monitoring the salt-exposure test temperature passes through a small hole in the heat shields and another thermocouple probe is positioned on the top most heat shield to monitor the temperature drop across the heat shields. Operating experience of the well has shown that while the furnace is operating at 700 ºC, the top heat shield temperature stays below 150 ºC and the temperature directly near the silicone O-ring did not exceed 80 ºC which is well within the service temperature range of silicone (-115 ºC to 232 ºC [68]).

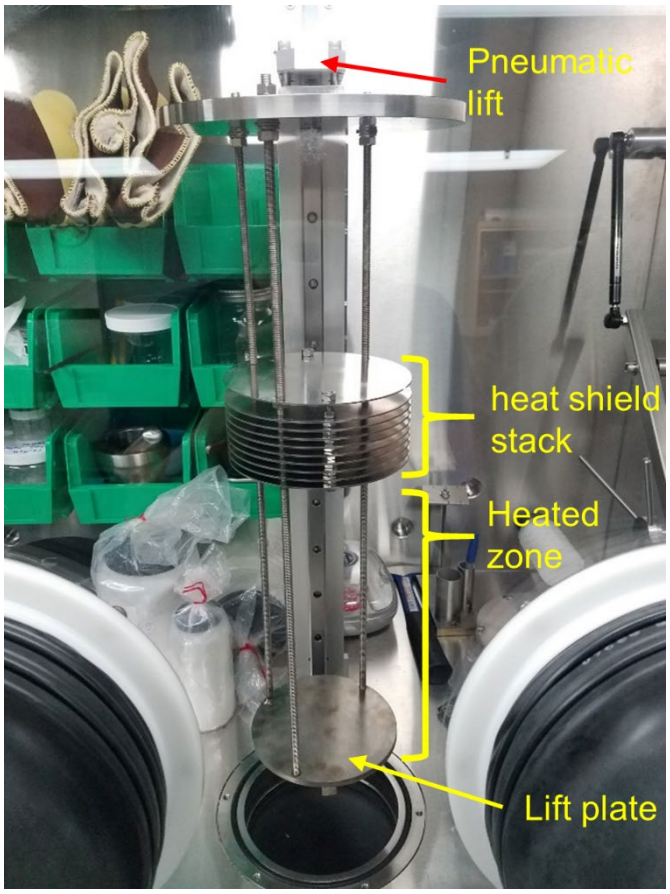

Figure 3-3: Lifting assembly for raising and lowing salt exposure test in and out of the glovebox furnace well.

For a salt exposure experiment, a salt catch cup is positioned on top of the bottom lifting plate in order to catch any salt that may leak out of a crucible in the event of a crucible failure. The diameter of the catch cup and design of the positioning plate varied depending on the restraints of the salt exposure experiment, but all catch cups followed the same basic design. A cylindrical cup made out of stainless steel was positioned in the center of the lifting plate. A crucible positioning plate was then added to the top of the cup. This plate helped ensure the crucibles stayed up right during the duration of the salt exposure experiment.

Design of and the material used to make the salt exposure crucibles varied depending on the salt exposure experiment being performed. Details on the salt exposure crucibles used in each experiment are provided in the appropriate chapters of this dissertation.

3.1.2 Materials and Methods Used for Vol/SA Ratio Experiments

The salt used in many of the experiments in this dissertation was a eutectic mixture of FLiNaK (46.5% LiF, 11.5% NaF, and 42% KF, in mol%). The FLiNaK salt was procured from Materion Corporation, Milwaukee, WI. Materion prepared 10 kg of the FLiNaK mixture using LiF, NaF, and KF powders that were at least 99.9 % pure. The powders were mixed and melted inside a graphite crucible. Upon cooling, the mixed FLiNaK salt ingot was removed from the graphite crucible. Any visible graphite stuck to the salt ingot was then brushed off and the ingot was broken down into pieces less than 3 inches in size, but not into a fine powder as to limit the salt's surface area for moisture and oxygen uptake. The salt was packaged and sealed in 5 individual glass containers under argon and shipped to the University of Wisconsin-Madison. Upon delivery, the salt containers were transferred into the ultra-high purity argon glovebox described in Section 3.1.1 where any open handling of the salt was performed. A photograph of four of the as-received

FLiNaK containers is shown in Figure 3-4. A sample of FLiNaK from one of the jars was taken and sent to the Wisconsin State Laboratory of Hygiene (WSLH) for trace impurity analysis using inductively coupled plasma mass spectroscopy (ICP-MS) to ensure the as-received salt was of acceptable quality. A table with the results of the top 10 highest impurity elements is presented in Table 3-1. Overall, the quality of the salt was determined to be good, given that all of the metallic impurity elements were below 100 ppm with only S having elevated concentrations. Noteworthy, the S concentration is the largest impurity element, but the concentration is not greatly above the limit set by the guidelines for MSRE salt shown in Table 2-1 even though it has not been purified with the complicated chemical purification of H_2/HF sparging.

Figure 3-4: Photograph of four of the five as-received containers of Materion FLiNaK after being transferred into an ultra-high purity argon glovebox.

Table 3-1: Top 10 impurity elements as determined by ICP-MS found in the as-received Materion FLiNaK.

Element	S	Rb	Ca	P	Fe	B	Al	Ni	La	Cr
Concentration (μg/g)	362 ± 41	48 ±2.5	25 ±3.8	20 ±2	15 ±0.8	9.0 ±0.6	5.8 ±0.5	5.0 ±0.3	4.3 ±0.5	3.9 ±0.2

Samples for the Vol/SA Ratio experiments were made from stainless steel 316H (316HSST). A ½ inch thick plate of 316HSST was procured from Sandmeyer Steel Company, Philadelphia, PA. Table 3-2 shows the certified composition of the 316HSST plate provided by Sandmeyer Steel Company. To create samples from the plate, a bar approximately 0.625 x 11.5 inches was water jet cut from the plate. The bar was then sent to Wire Works Engineering, LTD., Madison, WI to have 0.06 inch diameter holes electrode drilled through the top and bottom of the bar down the entire 11.5 inch length of the bar. Then the entire length of the 0.5 x 0.625 x 11.5 inch bar was sectioned into several 0.06 inch thick coupons using wire electrical discharge machining (EDM) such that the final coupons had approximate dimensions of 0.5 x 0.625 x 0.06 inches.

Table 3-2: Chemical certification for 316HSST provided by Sandmeyer Steel Company

Element	Fe	Cr	Ni	Mo	Mn	C	Si	Co	Cu
Composition (mass %)	Bal.	16.61	10.26	2.006	1.536	0.041	0.329	0.152	0.392

Before FLiNaK exposure, 316HSST samples were ground on all faces and edges up to a P4000 grit using SiC abrasive paper. After grinding the samples were ultrasonically cleaned using a mixture of deionized water and acetone. Each sample then had its initial dimensions recorded using digital calipers and micrometer. Initial sample masses were also recorded using a Satorius electronic balance with a 0.002 mg accuracy. With initial dimensions and masses recorded, sample strings of three 316HSST samples were prepared using stainless steel 316L (316LSST) wire. The sample strings were all hung from a 316LSST cap. A photograph showing the pre-salt exposure sample strings from part 1 of the experiments are shown in Figure 3-5. Once the sample strings

were attached to their respective caps, they were transferred into the argon glovebox for FLiNaK exposure.

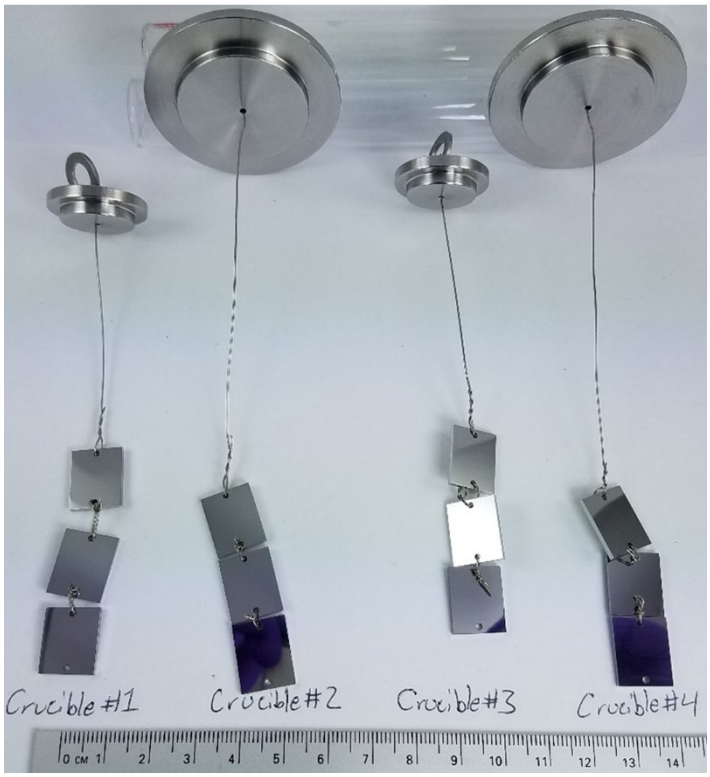

Figure 3-5: Prepared 316HSST samples strings for FLiNaK exposure tests. Crucibles 1 and 3 tested at Vol/SA ratio of 1.67 cm^3/cm^2. Crucibles 2 and 4 tested at Vol/SA ratio of 5 cm^3/cm^2.

Based on its performance in previous experiments with FLiNaK [46, 50] and the fact that it would not contribute to the exposed metal surface area, pyrolytic boron nitride (PyBN) was used as the salt containment crucibles. In total four PyBN crucibles in two different sizes (two of each size) were procured from Stanford Advanced Materials, Lake Forest, CA so that two different volumes of salt could be used to adjust the Vol/SA ratio in the corrosion experiments without changing the dimensions of the alloy sample material. In two PyBN crucibles (crucibles 1 and 3, see Figure 3-5), approximately 50 g of FLiNaK was crushed and added, while approximately 150 g of FLiNaK was added to the other two PyBN capsules (crucibles 2 and 4, see Figure 3-5). The volume of FLiNaK in each PyBN crucible at the test temperature of 700 ºC was then calculated using the FLiNaK density correlation shown in Equation 3-1, where T is the temperature in Celsius as

reported by Williams et al. [40]. With the size of the samples known, and the volume of salt calculated, the Vol/SA ratio was then determined for the two PyBN crucible sizes to be 1.67 cm^3/cm^2 (crucibles 1 and 3) and 5 cm^3/cm^2 (crucibles 2 and 4).

$$\rho(T) = 2.530 - 0.00073 * T \ [\frac{g}{cm^3}] \quad \text{Equation 3-1}$$

To prepare the salt for the loading of the 316HSST sample strings. Each PyBN crucible was positioned in a salt catch cup which was then placed on the lifting plate of the furnace assembly described in Section 3.1.1. The PyBN crucibles with loaded FLiNaK before heating are shown in Figure 3-6a. The PyBN crucibles were lowered into the furnace well and heated to 200 ºC to allow the salt to prebake. Then the furnace temperature was increased to the test temperature of 700 ºC. Once the furnace was at 700 ºC the temperature was held for a few hours to ensure the salt temperature had time to homogenize at 700 ºC before introducing the 316HSST samples. The crucibles were then lifted out of the furnace while at 700 ºC (Figure 3-6b) and the 316HSST samples were introduced to the FLiNaK salt by positioning each sample string on top of its respective crucible (Figure 3-6c). The positioning of all sample strings took less than 90 seconds, ensuring the salt never had enough time to cool dramatically below 700 ºC. The crucibles were then lowered back into the furnace (Figure 3-6d) and the samples were continuously exposed to FLiNaK at 700 ºC for either 100, 250, 500, or 1000 hrs.

At the conclusion of each test duration, all the crucibles were lifted out of the furnace well and the caps for the sample strings of that test duration were lifted off the PyBN crucibles to remove the 316HSST samples from the FLiNaK salt. The sample strings were then allowed to cool in the ultra-high purity argon environment. Additionally, the post exposure FLiNaK salt was collected by lifting the PyBN crucibles out of the salt catch cup and dumping the molten FLiNaK into stainless steel 304 (304SST) cups. The FLiNaK dumped in the 304SST cups froze in less than 5

minutes providing some confidence that the 304SST cup did not introduce further corrosion products into the FLiNaK salt sample. After the samples were removed, and the FLiNaK salt was collected, the remaining PyBN crucibles were lowered back into the furnace well to continue the FLiNaK exposure test. If the final duration samples were being collected, the furnace was shutoff and allowed to cool.

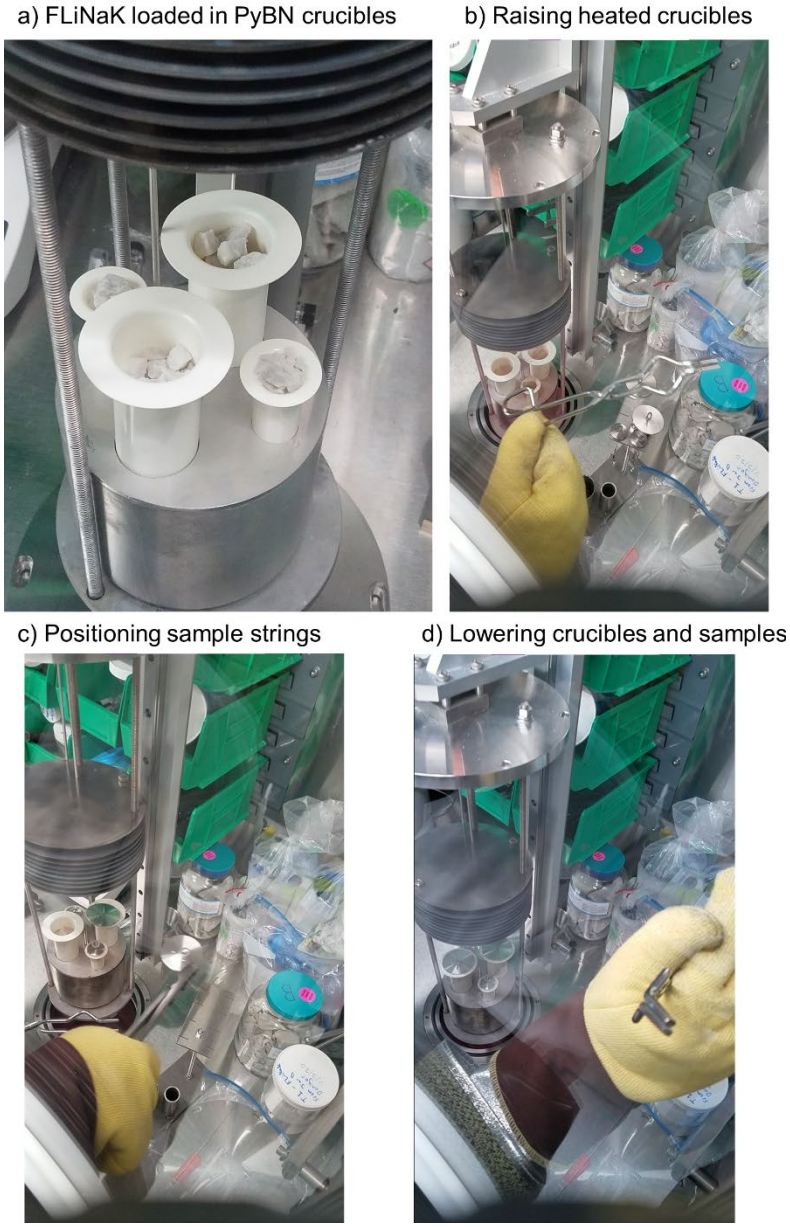

Figure 3-6: Various stages of loading 316HSST sample strings into glovebox furnace well. a) PyBN crucibles loaded with as-received Materion salt ready for heating. b) Raising PyBN crucibles out of furnace at 700 °C for sample loading. c) Positioning 316HSST sample strings onto PyBN crucibles. d) Lowering PyBN crucibles back into glovebox furnace well marking hour zero of FLiNaK exposure test.

After the 316HSST sample strings were cooled, they were removed from the glovebox for cleaning to remove any residual FLiNaK still stuck to the sample surfaces. The cleaning method used was similar to the one described by Olson for removing residual FLiNaK from post-salt exposure samples [22]. 316HSST samples were sonicated in a 1M solution of $Al(NO_3)_3$ for three ten minute sessions. Between sessions, the solution was replaced. Finally, the samples were sonicated in DI water for multiple sessions until the mass changes between sonication sessions no longer changed. The samples then went through a final sonication in isopropyl alcohol and were allowed to dry. Once dry, the post-FLiNaK exposure sample masses were recorded on the same Satorius electronic balance the initial masses were recorded on.

Notice that four test durations were performed: 100, 250, 500, and 1000 hrs, but only two PyBN crucibles per Vol/SA ratio were available for each initial furnace loading. To get all four time intervals, the Vol/SA ratio experiments were conducted in two parts. In part one, 316HSST samples at Vol/SA ratios of 1.67 cm^3/cm^2 and 5 cm^3/cm^2 were exposed to FLiNaK salt at 700 ^oC for 500 and 1000 hrs. After part one, the PyBN crucibles were removed from the glovebox and the inside of each crucible was cleaned using 1M $Al(NO_3)_3$ solution. Solution was poured into each crucible and the crucibles were sonicated for multiple sessions. Then the crucibles were sonicated with DI water in multiple sessions. Between each 1M $Al(NO_3)_3$ and DI water sonication, the inside of the PyBN crucibles were lightly brushed with a soft bristle brush. The crucibles then went through a final sonication with acetone, ethanol, and finally isopropyl alcohol. Example photographs of PyBN crucibles before and after cleaning are shown in Figure 3-7 After cleaning, the inside diameters of the PyBN crucibles looked nearly as they did when they were new (unfortunately photographs of the brand new crucibles were not collected, photograph in Figure 3-6a is the best example photograph of new crucibles) providing some confidence that the cleaning

procedures worked and the PyBN crucibles are reusable if cared for properly. Note that the outside diameters and crucible lip where the cap rests on the PyBN crucibles were not cleaned thoroughly as they do not come into contact with the salt. Thus the outside of the crucibles and lip do have some discoloration even after cleaning, but is not of concern.

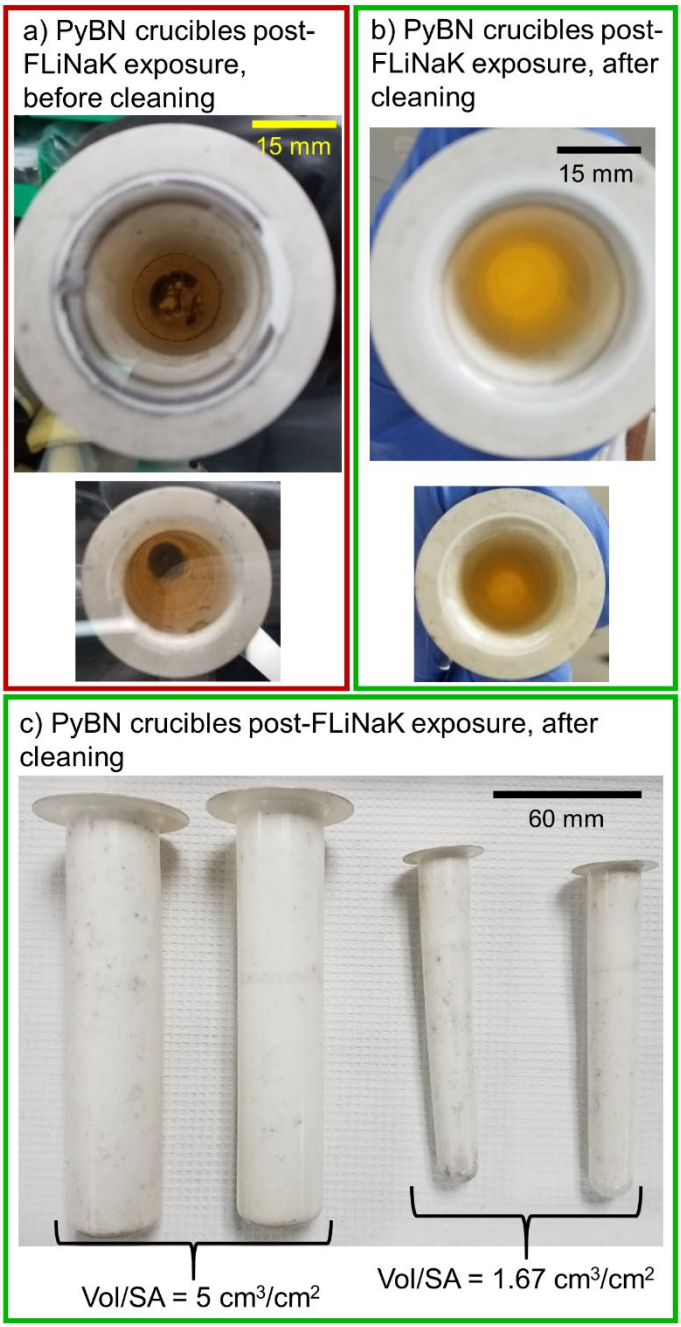

Figure 3-7: PyBN crucibles before and after cleaning post-FLiNaK exposure for part one of Vol/SA ratio tests. a) PyBN crucibles for Vol/SA = 5 (top) and Vol/SA = 1.67 (bottom) before cleaning. b) same PyBN crucibles after cleaning. c) All four PyBN crucibles after part one of tests after cleaning and ready for part two.

With the cleaned PyBN crucibles, FLiNaK loading and 316HSST sample string preparation were repeated. Part two of the Vol/SA ratio experiments was then performed for 100 and 250 hrs. All sample preparation and cleaning steps were repeated for both parts of the experiments.

3.1.3 Post-FLiNaK Exposure Sample Analysis

Using the initial and post-FLiNaK exposure sample masses, the mass change per unit area could be calculated using the following equation:

$$Mass\ Change = \frac{M_f - M_o}{Sample\ Surface\ Area} \quad \text{Equation 3-2}$$

Where M_o and M_f are the initial and post-FLiNaK exposure sample masses, respectively. Using Equation 3-2, a negative value of mass change does indicate mass loss while a positive value indicates mass gain. In the sample surface area calculation, the area of all faces and edges were included as well as the area lost due to the sample hanging holes being drilled and the area gained due to the circumference of the drilled holes.

Reference x-ray diffraction (XRD) and post-FLiNaK exposure XRD patterns were collected using the top sample from each sample chain. The XRD patterns were collected on a Bruker D8 Discovery using CuK-α x-rays (wavelength = 1.5406 Å [69]), and a Vantec 500 area detector with a 14 cm diameter active area. During the collection a 2 mm diameter collimator was used and the sample stage was oscillated in the x and y directions in order to collected diffractions from as many grains as possible.

To look at the depth of the corrosion attack on the 316HSST samples, two methods were used. For determining an averaged corrosion depth based on the depletion of Cr, glow discharge optical emission spectroscopy (GDOES) was performed on the top sample from each sample chain. GDOES sputters away and analyzes a 4 mm diameter area giving an averaged depletion depth. In

order to investigate the samples for more localized attack such as pitting or grain boundary corrosion, the bottom sample from each sample chain was prepared for cross-sectional analysis using the scanning electron microscope (SEM) equipped with an energy dispersive x-ray spectrometer (EDS).

For GDOES analysis, all of the analyzed samples were run on a Horiba GD Profiler 2 using a pressure of 720 Pa and a power of 40 W for the plasma generation. Positioning of the 316HSST sample coupons on the GDOES stage proved to be difficult because of the size of the samples. The sample has to be carefully positioned such that the O-ring that creates a seal for the GDOES analysis is positioned between the two sample hanging holes in the 316HSST samples. To ensure that the samples were positioned properly, the samples were repositioned until the seal was able to produce a base vacuum of <350 Pa before running the 70 second flushing sequence. Photographs of positioning a 316HSST sample are shown in Figure 3-8. The calibration method used for the analysis of the 316HSST samples was specifically developed for the analysis of stainless steel alloys. Details on the GDOES calibration can be found in the following reference [70].

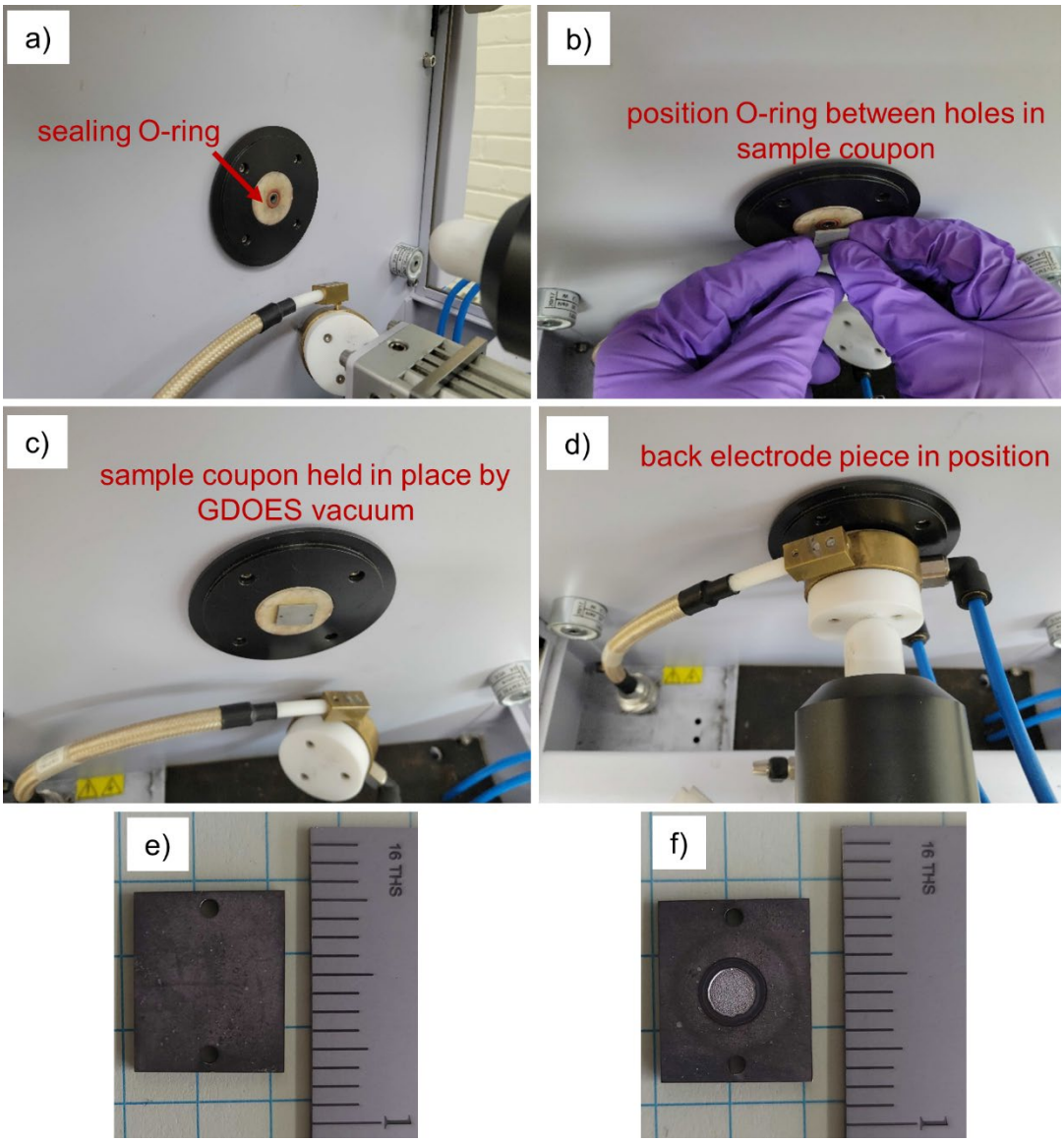

Figure 3-8: Positioning 316HSST sample coupons on GDOES analyzer. a) Overview of the sample holding area. b) Positioning 316HSST sample coupon on sealing O-ring. c) Sample coupon properly positioned with base vacuum reaching <350 Pa. c) Rear electrode in position, GDOES ready for sample run. e) 316HSST sample surface before GDOES analysis. f) 316HSST sample surface after GDOES analysis showing 4mm diameter analysis area. Scale in e) and f) is inches.

All SEM/EDS was performed on a Zeiss LEO 1530 equipped with a ThermoFisher Scientific UltraDry EDS and Pathfinder software. To prepare the samples for cross-sectional analysis, all of the 316HSST samples were first sputter coated using a Leica EM ACE 600 sputter coater on both sides of the samples with approximately 10 nm of Au in order to ensure the surfaces were electronically conductive. Following the sputter coating the samples were then electroplated with

Cu using a 1M copper sulfate solution. The Cu electroplating voltage was adjusted until the current was between 0.1-0.2 A, and each sample was plated for approximately 10 min. A photograph of the electroplating system and 316HSST sample before and after Cu coating are provided in Figure 3-9. Note that the purpose of the Cu electroplated coating is to help with edge retention of the 316HSST samples during the metallographic polishing steps. Additionally, the Cu coating provides a sharp indication of the sample surface during SEM/EDS analysis. This procedure for coating the samples with 1M copper sulfate solution provides a good enough coating for the purposes of cross-sectional examination, but should not be used if a high quality copper coating is desired for other purposes such as corrosion protection.

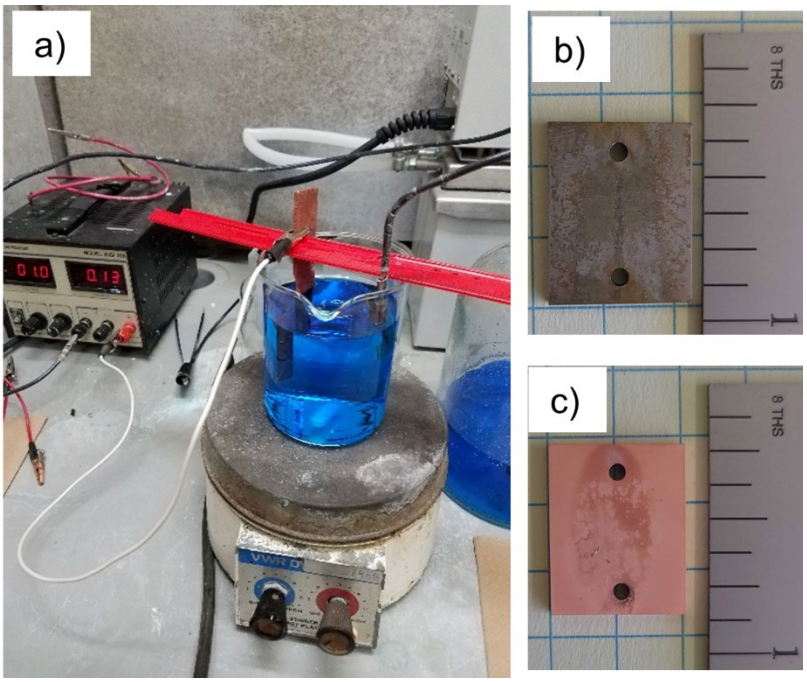

Figure 3-9: Post-FLiNaK Cu coating preparation for cross-sectional sample analysis. a) 1M copper sulfate copper electroplating setup. b) 316HSST sample before Cu electroplating. c) 316HSST sample after Cu electroplating ready for mounting and metallographic preparation. Scale in b) and c) is inches.

3.2 Results and Discussion

For testing the effect of the Vol/SA Ratio, one of the first crucial parts of the test was making sure that the crucible material could truly be considered “inert” to both the molten salt environment and

to interactions with the potential Cr and Fe containing corrosion products of the 316HSST coupons. From its previous use in literature PyBN was hypothesized to be the best choice. Olson et al.'s [46] work appeared to show PyBN being the best choice if a non-interacting crucible was needed. Additionally, Doniger [50] showed that PyBN crucibles used to test several different alloy compositions had no evidence of corrosion product interaction using SEM/EDS analysis. Finally, after using a standard method for washing residual FLiNaK off of sample material, the PyBN crucibles used in this dissertation once again showed no interaction with corrosion products through visual inspection. Therefore it is believed that PyBN is a valid crucible material when a non-interacting material is needed for salt containment such is the case in this dissertation.

Perhaps the most important piece to consider is the mass change post-FLiNaK exposure for the 316HSST samples. The mass change per surface area calculated for the 100, 250, 500, and 1000 hour samples tested in a Vol/SA ratio of 1.67 cm^3/cm^2 and 5 cm^3/cm^2 are shown in Figure 3-10. Several observations from these mass changes can be observed that clearly demonstrate that the Vol/SA ratio has a strong effect on the corrosion of the 316HSST samples. It was originally thought that the mass losses in both ratios should be similar at shorter time scales, but would diverge at longer time scales as the impurities in the salt volume are consumed by the corrosion reactions and therefore shifting the salts redox potential. Both salt volumes should contain identical concentrations of impurities initially meaning the initial salt redox potentials are the same, but the overall mols of impurities in each volume would be different. At the shorter test times, 100 and 250 hrs, it was believed that the mols of impurities should be enough to keep the salt redox potential in a state of oxidation continuously causing corrosion in both salt volumes. However, it can be seen that in as little as 100 hrs, the effects of the different overall mols of impurities in the salt volume already cause differences in the mass loss of the 316HSST samples. Meaning that

enough impurities in the salt are already consumed such that the salt redox potential is shifting towards a less oxidizing potential.

Overall, the 316HSST samples tested in a Vol/SA ratio of 5 cm^3/cm^2 clearly show a much higher mass loss, almost 2x higher at 1000hrs, than any of the 316HSST samples tested at a Vol/SA ratio of 1.67 cm^3/cm^2. Additionally, after only 500 hours of FLiNaK exposure in the Vol/SA ratio of 1.67 cm^3/cm^2 the mass loss of the 316H samples begins to plateau.

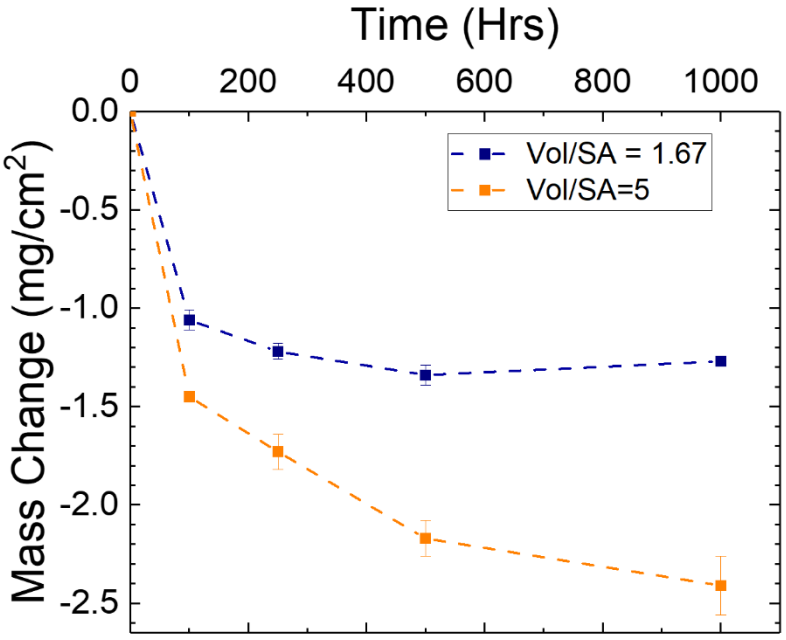

Figure 3-10: Mass change for 316HSST samples exposed to FLiNaK salt for 100, 250, 500, and 1000 hrs at Vol/SA ratios of 1.67 cm^3/cm^2 and 5 cm^3/cm^2.

An important thing to consider is that the plateau in the mass loss during the FLiNaK exposure could potentially create challenges if one were to attempt to calculate a corrosion penetration rate (CPR). In most cases it's easiest to design around a CPR and not a mass loss, so the penetration rate is normally calculated using Equation 3-3:

$$CPR = \frac{KW}{\rho A t} \qquad \text{Equation 3-3}$$

Where W is the mass loss after salt exposure time t; ρ and A are the density and the exposed surface area of the sample, respectively, and K is a constant that corrects for units [71]. However,

drastically different CPRs can be calculated depending on the time, mass loss, and Vol/SA ratio one uses from the results in Figure 3-10. To clearly illustrate the problem, the average CPR for each sample string was calculated for all FLiNaK exposure times at both Vol/SA ratios assuming a density of 8.00 g/cm^3 for 316HSST. The results are presented in Table 3-3. The calculated CPR completely depends on the Vol/SA ratio and the FLiNaK exposure time, which makes calculating an accurate CPR that can be used in design or regulation difficult to determine. It's clear just from the mass change data that the Vol/SA ratio plays an important role in the overall corrosion results coming from the prototypical static isothermal corrosion test. Furthermore, small Vol/SA ratios are likely not appropriate for long term static isothermal salt exposure tests as the mass loss appears to quickly plateau as the impurities in the salt are consumed. Therefore if one wishes to perform static isothermal corrosion test for extended periods of time, the test design will likely require a Vol/SA ratio in excess of 5 cm^3/cm^2. The most ideal situation could be to determine what a realistic Vol/SA ratio is expected to be in an actual MSR design, and use that ratio in the static isothermal tests.

Table 3-3: Average Corrosion Penetration Rate (CPR) in mm/yr for each 316HSST sample string at all FLiNaK exposure times and at both Vol/SA ratios.

FLiNaK Exposure Time (hours)	Vol/SA Ratio	
	1.67 cm^3/cm^2	5 cm^3/cm^2
100	0.12 ± 0.006	0.16 ± 0.001
250	0.053 ± 0.002	0.076 ± 0.004
500	0.029 ± 0.001	0.047 ± 0.002
1000	0.014 ± 0.0001	0.026 ± 0.002

To characterize the corrosion behavior of the 316HSST samples further, the samples were investigated using XRD to observe any potential changes in the phases present in the samples due to the FLiNaK exposure at 700 ºC. XRD spectrums from samples exposed to the FLiNaK salt at

100, 250, 500, and 1000 hrs at ratios of both 1.67 cm^3/cm^2 and 5 cm^3/cm^2 are shown in Figure 3-11 along with a reference 316HSST XRD spectrum. Stainless steel 316H is an austenitic stainless steel, but as can be observed in the reference pattern, there is evidence of some residual ferrite in the as-received material. The presence of the ferrite phase is not necessarily that surprising as this is often observed during the casting of many 300 series stainless steels. The formation of the ferrite phase depends on the rate of cooling during the original cast, actual composition of the steel, and the solidification method [72, 73]. All of which is to say that the as-received 316HSST is as reasonably expected.

During the FLiNaK exposure, the 316HSST samples are not only undergoing corrosion by the FLiNaK salt, but are also essentially undergoing a long heat treatment at the FLiNaK exposure test temperature of 700 ºC. So, not only could it be expected to see phase changes due to the corrosion by the FLiNaK salt, but also as a result of the heat treatment. As expected, after all of the FLiNaK exposure times, the 316HSST samples retain their primary austenite phase and the residual ferrite phase. Additionally little change in the peak positions is observed. In the 316HSST reference sample as well as the samples exposed to FLiNaK at 700 ºC for 100 and 250 hours, the only ferrite peaks that are observable are the (110) and (211) peaks. After exposure at 700 ºC for 500 and 1000 hours, however, the (200) ferrite peak also becomes noticeable. This may suggest that the overall ferrite phase fraction has increased during the FLiNaK exposure. Nelson-Riley analysis (Equation 3-4) was performed on both the austenite and ferrite peaks to see if any significant changes in the lattice parameters occurred. Results from the analysis showed that at all exposure times, the lattice parameter of the austenite phase remained 3.60 Å and the ferrite phase lattice parameter went from 2.89 Å in the as-received 316HSST material to 2.87 Å after all exposure times. However, only 2-3 peaks of the BCC ferrite phase could be used for analysis so the accuracy is likely reduced. In

both cases the lattice parameter for both the austenite and ferrite phases match reported literature values [74].

$$Nelson - Riley = \frac{cos^2\theta}{sin\theta} + \frac{cos^2\theta}{\theta} \quad \text{Equation 3-4}$$

Besides the ferrite phase, no other secondary phases are observed in the XRD spectrums for the as-received 316HSST or the 316HSST samples exposed to 700 ºC for 100 and 250 hours. However, at both Vol/SA ratios, after 500 and 1000 hours at 700 ºC, minor peaks in the low two theta range can start to be observed around 40, 42 and 48 degrees two theta. In the temperature range of 500 ºC to 800 ºC (note that the FLiNaK exposure temperature is 700 ºC), 300 series stainless steels are known to undergo microstructural changes as a result of sensitization [75-77]. In typical oxygenating environments this sensitization can prove to be deleterious to 316HSST in terms of corrosion because it causes local changes in the chromium concentration near the grain boundaries due to the formation of chromium rich carbides at the grain boundaries. The peaks in the XRD spectrums potentially match those of the $M_{23}C_6$ type, but with some peak shifting likely due to the carbides being off stoichiometry of the particular $M_{23}C_6$ available in the matching database.

Although the formation of the grain boundary carbides in 316HSST are typically found to be deleterious in oxygenating environments, previous work on 300 series stainless steels in fluoride salts has suggested that the grain boundary carbides could be beneficial for salt corrosion. Zheng et al. [78] for example hypothesized that the formation of chromium carbides could potentially help stabilize Cr preventing dissolution in a LiF-BeF_2 salt mixture known as FLiBe. Recent work by Doniger [50] also hypothesized that pre-sensitizing 316LSST and 316HSST before corrosion in FLiNaK salt helps to minimize the outward diffusion of Cr because of the grain boundary carbides providing obstacles for Cr diffusion.

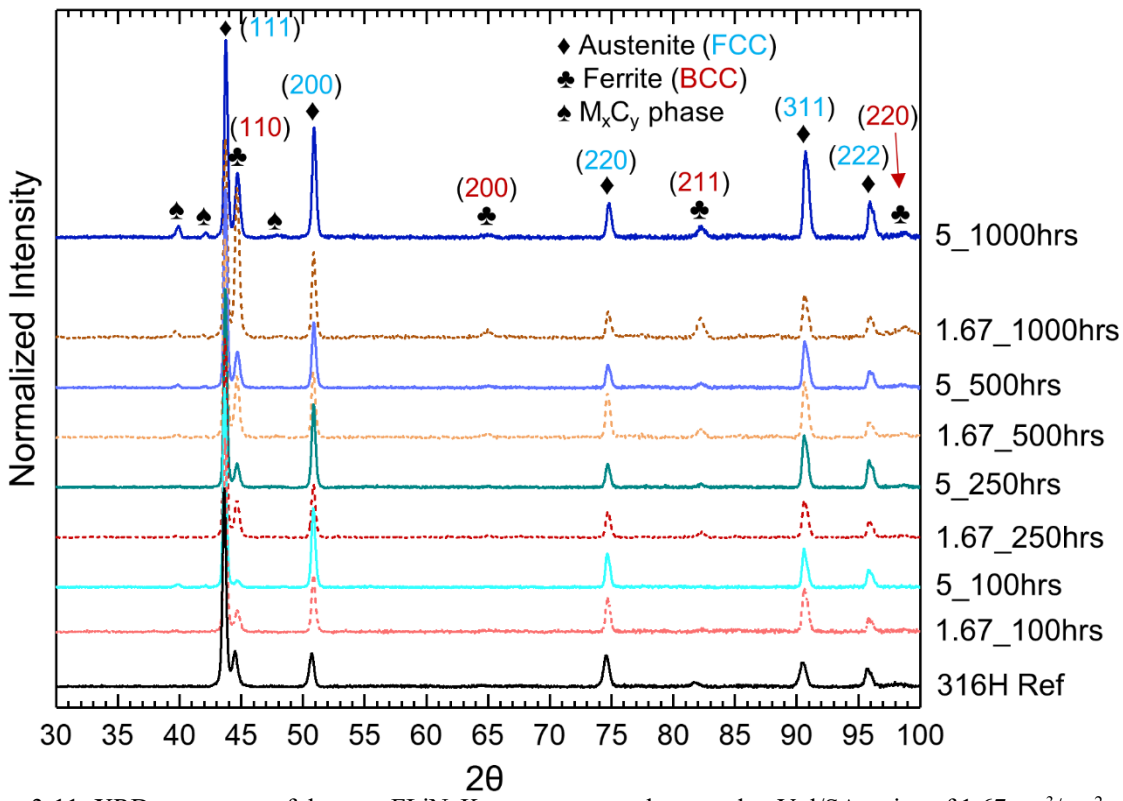

Figure 3-11: XRD spectrums of the post FLiNaK exposure samples tested at Vol/SA ratios of 1.67 cm^3/cm^2 and 5 cm^3/cm^2 for either 100, 250, 500, or 1000 hrs.

As mentioned in Section 3.1.3, GDOES was performed on select samples in order to get an averaged measurement of the Cr depletion depth. The samples analyzed with GDOES include the 316HSST samples tested in Vol/SA ratio of 1.67 cm^3/cm^2 for 500 and 1000 hrs since those two samples showed similar mass losses even though they were exposed to FLiNaK for different time scales. Additionally, 316HSST samples tested at the Vol/SA ratio of 5 cm^3/cm^2 for 100 and 1000 hours were investigated as those sample sets showed a large increase in the mass loss with increased FLiNaK exposure. The results of the Cr depletion depth analysis for the samples investigated with GDOES are presented in Table 3-4 and the concentration profiles of the analyzed samples are provided in Figure 3-12. The process of determining the Cr depletion depth from GDOES analysis is provided in Appendix C.

Generally, one would expect the Cr depletion to increase as the mass loss of the 316HSST samples increases. For the most part this trend is true as seen in Table 3-4. The 316HSST samples tested at

a Vol/SA ratio of 5 cm^3/cm^2 for 1000 hrs showed the highest mass loss which is reflected in also showing the deepest amount of Cr depletion. However, the Cr depletion may not be quite as high as one would expect. With a mass loss that is approximately 1.7x higher than the 100 hour 316HSST sample, the Cr depletion depth only increases by approximately 1.2x. Additionally, as seen in the 316HSST samples tested at a Vol/SA ratio of 1.67 cm^3/cm^2 for 500 hrs, the mass loss in these samples is slightly lower than the mass loss in the 316HSST samples tested at a Vol/SA ratio of 5 cm^3/cm^2 for 100 hrs and yet the Cr depletion is approximately identical. The likely explanation for this is that the attack on the 316HSST samples is not uniform attack, but a localized attack in the form of either pitting or intergranular attack. Therefore while GDOES provides a good averaged analysis, investigation of the 316HSST cross-sections for localized attack may reveal a more detailed picture of the corrosion attack.

Table 3-4: Cr depletion depths of 316HSST samples tested at both Vol/SA ratios and varying FLiNaK exposures times. The mass change results for the sample sets are also provided for direct comparison of the Cr depletion depths.

Vol/SA Ratio and Time	1.67 cm^3/cm^2 500 hrs	1.67 cm^3/cm^2 1000 hrs	5 cm^3/cm^2 100 hours	5 cm^3/cm^2 1000 hours
Mass change (mg/cm^2)	-1.34 ± 0.05	-1.27 ± 0.01	-1.44 ± 0.01	-2.41 ± 0.15
Cr Depletion Depth (μm)	2.9	2.7	2.7	3.5

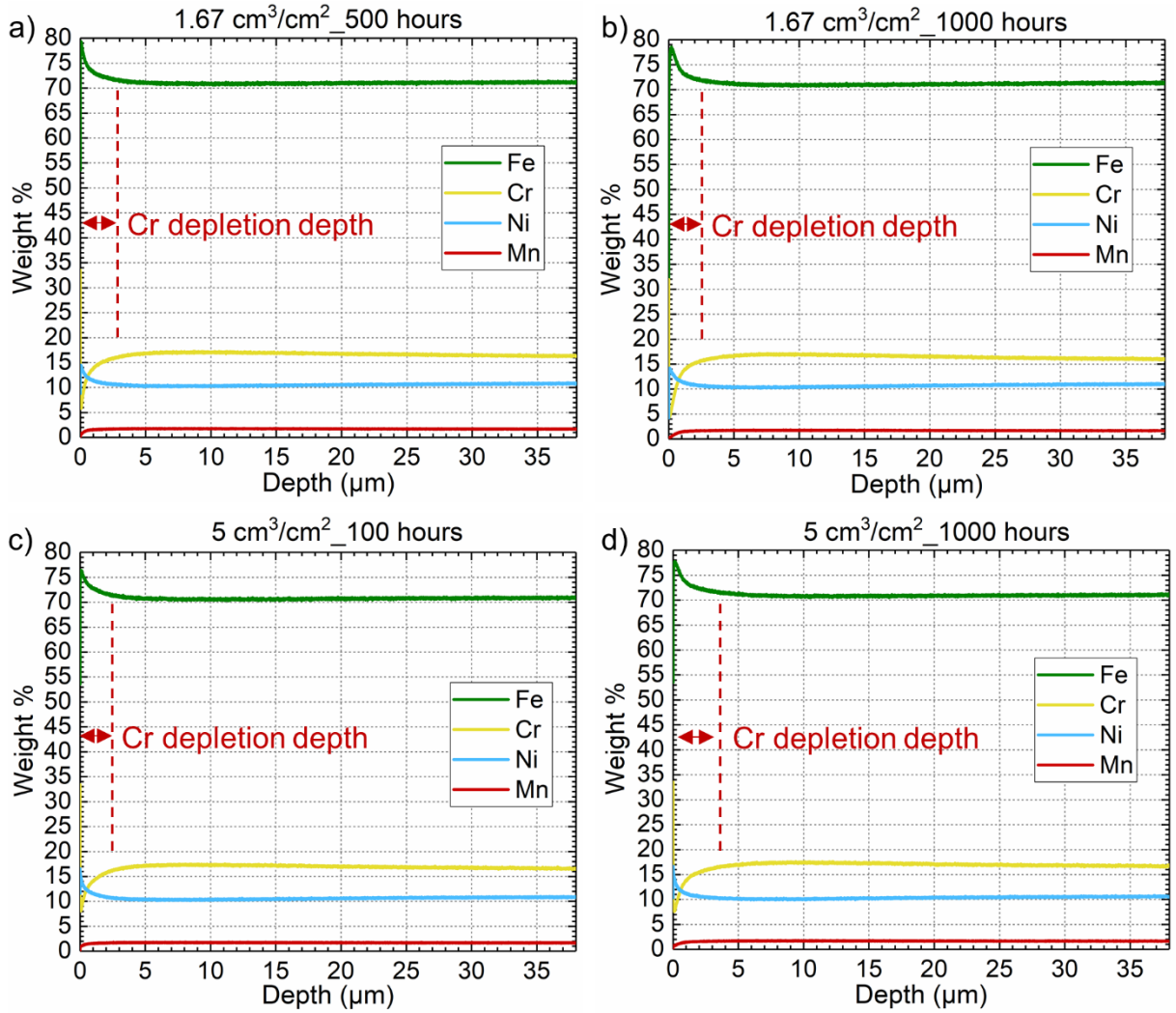

Figure 3-12: GDOES analysis on Vol/SA ratio 316HSST samples. a) and b) 316HSST samples tested at a Vol/SA ratio of 1.67 cm^3/cm^2 exposed to FLiNaK salt for 500 and 1000 hours, respectively. c) and d) 316HSST samples tested at a Vol/SA ratio of 5 cm^3/cm^2 exposed to FLiNaK salt for 100 and 1000 hours, respectively.

Because the 316HSST samples tested at a Vol/SA ratio of 1.67 cm^3/cm^2 for 500 and 1000 hrs showed a plateau in the mass loss, the cross-sections of 316HSST samples from these tests were investigated with the SEM/EDS to see if there were any differences in the corrosion on a more localized scale. The results of the SEM/EDS analysis on the 316HSST samples tested at Vol/SA ratio of 1.67 cm^3/cm^2 for 500 and 1000 hours are shown in Figure 3-13. The 316HSST samples exposed to FLiNaK in a Vol/SA ratio of 1.67 cm^3/cm^2 clearly show that the corrosion attack by the FLiNaK salt can be rather localized and the deepest regions of attack are primarily along the grain boundaries. The line scan collected on the 500 hr 316HSST sample was performed

perpendicular to the corrosion surface, and shows that directly from the surface the Cr depletion depth is rather minimal as observed in the averaged GDOES data. However, the depth of attack along the grain boundaries for both exposure times extends to a greater depth and is similar at approximately 19 μm and 23 μm for the 500 hr and 1000 hr sample, respectively. This appears to agree well with the similar mass losses from both sample sets.

Additionally, from the cross-sectional SEM/EDS analysis, the grain boundary microstructure changes due to the thermal treatment at 700 ºC can be seen. As observed in the XRD patterns shown in Figure 3-11, 500 hrs exposure at 700 ºC is when the carbide peaks begin being observed. The 316HSST sample exposed to FLiNaK at a Vol/SA ratio of 1.67 cm^3/cm^2 for 500 hrs, Figure 3-13a, shows faint grain boundary Cr enrichment which likely corresponds to carbide peaks that begin to appear in the XRD spectrum. Just as the carbide XRD peaks after 1000 hrs exposure become more prominent, so does the Cr enrichment in the 316HSST sample exposed to FLiNaK at a Vol/SA ratio of 1.67 cm^3/cm^2 for 1000 hrs, Figure 3-13b. In the Cr mapping for this sample, the Cr enrichment at the grain boundaries is much easier to observe. Intragranular Cr enrichment also appears to be observed in this sample. This result was also observed by Stoter for 316SST exposed to temperatures of 650 ºC for >28,000 hrs [74], and it is still believed that this Cr enrichment corresponds to the $M_{23}C_6$ type carbide phase.

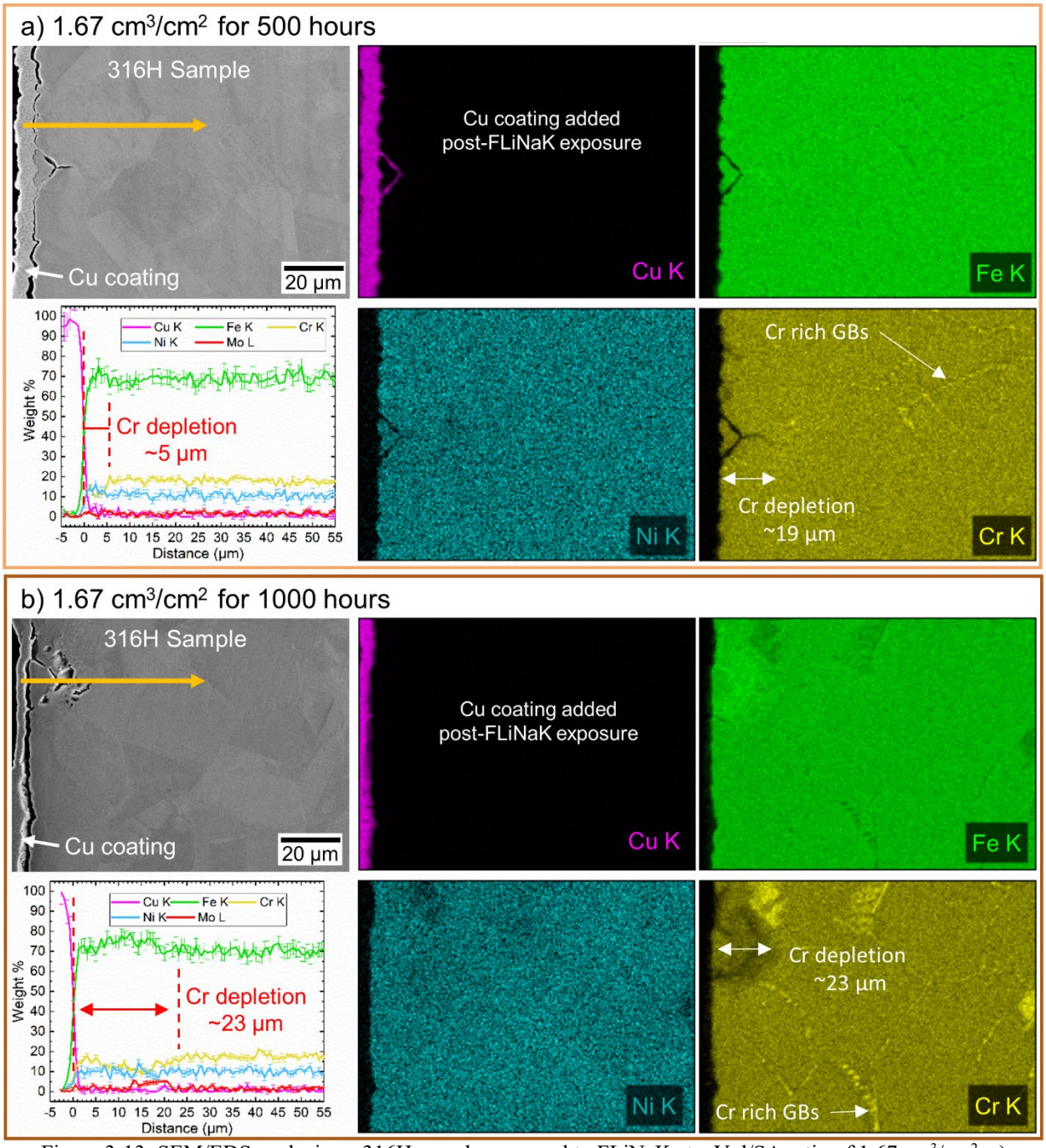

Figure 3-13: SEM/EDS analysis on 316H samples exposed to FLiNaK at a Vol/SA ratio of 1.67 cm^3/cm^2. a) FLiNaK exposure time of 500 hrs. b) FLiNaK exposure time of 1000 hrs.

Differing from the 316HSST samples exposed to FLiNaK at a Vol/SA ratio of 1.67 cm^3/cm^2, the 316HSST samples exposed to FLiNaK at a Vol/SA ratio of 5 cm^3/cm^2 continued to lose mass all the way to 1000 hours. So, investigating how the corrosion by FLiNaK proceeds from the shortest exposure time of 100 hrs to the longest exposure time of 1000 hrs was considered important to

characterize with SEM/EDS as well. The results of the SEM/EDS analysis for the 316HSST samples exposed to FLiNaK at a Vol/SA ratio of 5 cm^3/cm^2 for 100 hrs and 1000 hrs are presented in Figure 3-14. In both of the 316HSST samples exposed to FLiNaK at a Vol/SA ratio of 5 cm^3/cm^2 it can be observed that the depth of attack, especially along the grain boundaries, is deeper than the 316HSST samples exposed to FLiNaK at a Vol/SA ratio of 1.67 cm^3/cm^2, which corresponds well with the increased mass losses at a Vol/SA ratio of 5 cm^3/cm^2. Even the 100 hrs exposure sample shows a Cr depletion depth at least 2x deeper than the 1000 hrs 316HSST sample at 1.67 cm^3/cm^2.

In both cases of the 316HSST samples at 5 cm^3/cm^2, the Cr depletion profile appears to match the observable grain boundary void formation. In both samples, an EDS line scan was performed perpendicular to the corrosion surface, and it can be observed when the scan crosses a grain boundary, that there is a noticeable drop in the Cr concentration. Furthermore, when the line scan goes through a bulk grain it can be observed that the Cr concentration in the grain is approximately equal to the nominal concentration of Cr in the as-received 316HSST material, composition provided in Table 3-2. Suggesting then that the corrosion attack primarily occurs along the grain boundary and the actual grains are not greatly affected.

Something of noticeable difference between the 316HSST sample after 100 hrs versus 1000 hrs is the Cr enriched grain boundary behavior. As noted in the XRD spectrums in Figure 3-11, the 316HSST samples exposed to 700 ºC for only 100 hrs do not show the presence of the carbide phase while those samples exposed to 700 ºC for 1000 hrs clearly show the carbide peaks. This behavior is nicely reflected in the Cr EDS maps. The 316HSST sample after 100 hrs exposure at 700 ºC shows little evidence of any Cr enrichment. The 316HSST sample after 1000 hrs exposure to 700 ºC, however, clearly shows a great deal of Cr enrichment along the grain boundaries.

Suggesting that the Cr enrichment at the grain boundaries is due to the thermal exposure (i.e. sensitization) rather than due to a corrosion induced microstructural change. Of note, is that the Cr enriched grain boundaries appear to always be just in front of the corrosion induced Cr depletion. This may suggest one of two possibilities. Either the formation of the grain boundary carbides indeed helps slow the Cr diffusion towards the alloy/salt interface as suggested by previous studies [50, 78], or the grain boundary carbides are areas of preferential attack by the molten which has also been suggested in the molten salt literature [32, 79].

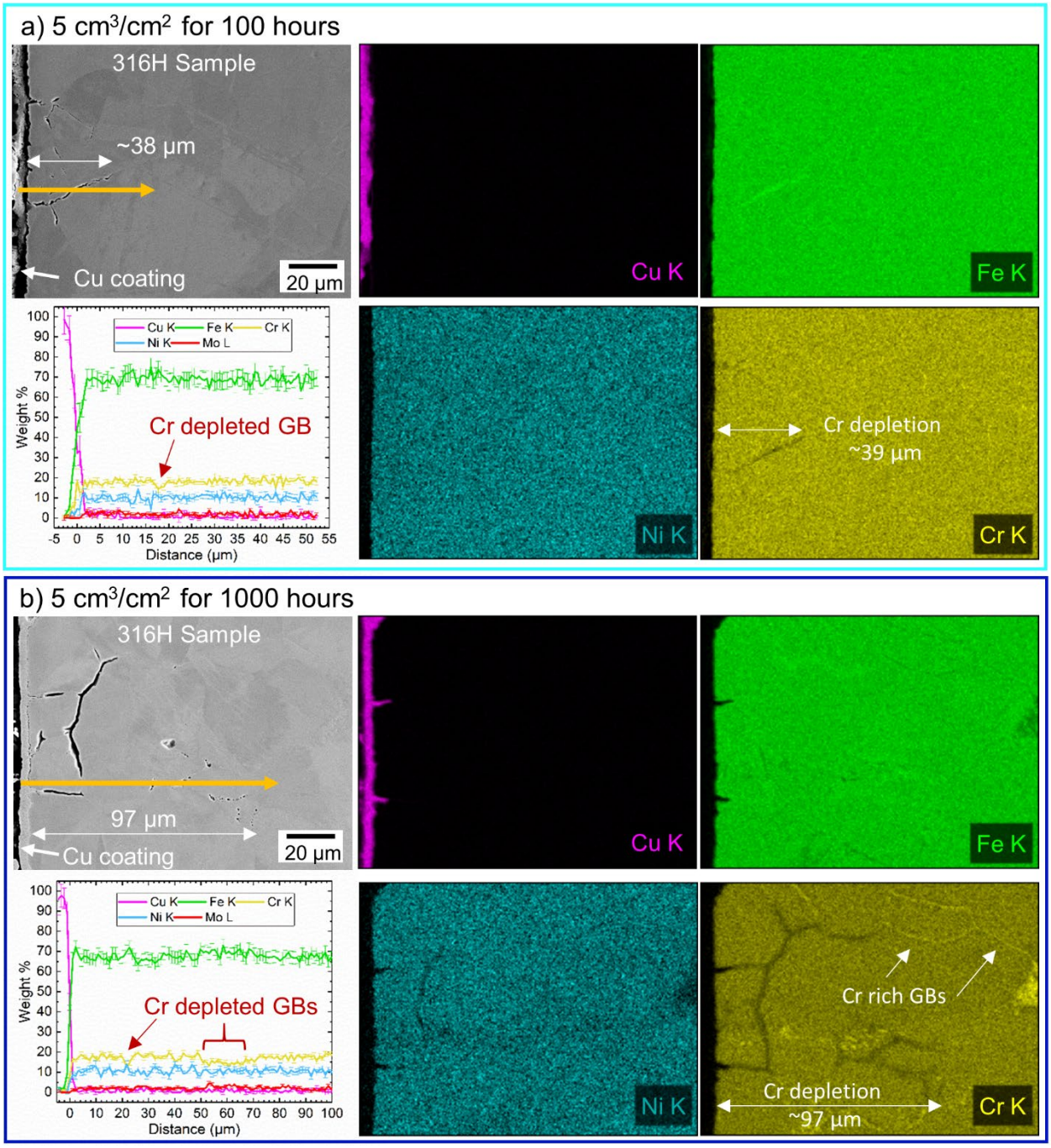

Figure 3-14: SEM/EDS analysis on 316HSST samples exposed to FLiNaK at a Vol/SA ratio of 5 cm^3/cm^2. a) FLiNaK exposure time of 100 hrs. b) FLiNaK exposure of 1000 hrs.

3.3 Conclusions from Vol/SA Ratio Effects

While the effects of the Vol/SA ratio on the overall performance of 316HSST in FLiNaK could clearly be seen in the mass loss results in Figure 3-10, the further investigation of the 316HSST

samples only demonstrates that the Vol/SA ratio has a significant effect in the prototypical static isothermal salt exposure test. The effect of the Vol/SA ratio is intimately connected to several parameters of the static isothermal exposure test including the exposure time and the salt purity. At short salt exposure times the Vol/SA ratio appears to have a slightly smaller effect as the salt likely contains enough impurities to keep the redox potential in a corrosive state to continue the corrosion of an alloy. However, as seen in this work, in as little as 100 hrs the corrosion of an alloy in a small Vol/SA ratio test starts to severely slow down as the impurities in salt melt are consumed. The Vol/SA ratio of 1.67 cm^3/cm^2 appears to be mostly acceptable for corrosion tests up to approximately 500 hrs, but if one desires to test the long term performance of an alloy in a static isothermal salt exposure test, a Vol/SA ratio in excess of 5 cm^3/cm^2 is likely required. Again, this result could greatly depend on the quality of the salt being used. This work used commercially available salt that appears to have acceptable quality, but if one were to further purify the salt such that practically zero impurities exist in the salt melt making the initial redox potential of the salt less oxidizing, the alloy corrosion could plateau at an even lower salt exposure time.

A potential new way of evaluating and comparing the performance of alloys in a salt melt could be by determining the corrosion plateau time for a given salt, temperature, and Vol/SA ratio. Consider the Vol/SA ratio of 1.67 cm^3/cm^2. The 316HSST in this work appeared to have a corrosion plateau time of approximately 500 hrs at 700 ºC in Materion's commercially available FLiNaK mixture. From previous work, 316HSST is regarded to have acceptable performance in fluoride salt mixtures such as FLiNaK [50, 80], but other alloys have been shown to have better performance [50, 81]. If one designs a FLiNaK exposure experiment for these better performing alloys, it's likely that their corrosion reactions would be slower meaning that the impurities in the salt melt will be consumed at a slower rate. Therefore, the corrosion plateau time for an alloy that

has a better performance than 316HSST should be greater than 500 hrs. Again, this is likely to greatly depend on the salt quality, so if one were to design such an experiment, all of the salt should come from the same salt ingot such that the initial salt redox potential is the same for all tests.

Chapter 4

The Effect of Salt Purity

As previously mentioned in Section 2.1, the importance of salt purity on the corrosiveness of molten fluoride salts was something that was recognized during the MSRE program. Unfortunately, the method for purifying fluoride based salt that was developed during the MSRE program involves the use of both gaseous H_2 and gaseous anhydrous HF. These gases individually are complex to handle, but handling the two together creates even more challenges. Not every research group looking at materials behavior in fluoride based salts has the necessary safety equipment, departments, and personnel to handle fluoride salt purification. So, having a good understanding of the differences between a commercially available fluoride salt mixture like the FLiNaK salt mixture prepared by Materion Corporation described in Section 3.1.2 and a purified mixture of FLiNaK is a crucial parameter for evaluating alloy performance in a static isothermal salt exposure test.

4.1 FLiNaK Salt Purification

The FLiNaK salt used for purification comes from the same FLiNaK jars that were produced by Materion Corporation described in Section 3.1.2. As mentioned in Section 3.1.2, this commercially available mixture of FLiNaK was already determined to be of somewhat good quality based on the ICP-MS analysis shown in Table 3-1. However, the concentration of the sulfur impurities was shown to be greater than 360 ppm in one ICP-MS check, which exceeds the salt chemical specification for MSRE quality salt shown in Table 2-1. So, at a very minimum the sulfur

concentrations ideally could be corrected to bring the salt quality to even higher standards. Additionally, ICP-MS provided no information on dissolved oxygen, dissolved moisture, or oxide impurities. All of these impurities are known to increase the corrosiveness (i.e. redox potential) of molten salt [82], and it would not be without some speculation that a commercially produced FLiNaK salt likely contains these types of impurities.

As already mentioned previously, to remove impurities from fluoride based salts, the best method that was developed during the MSRE program was to sparge the fluoride salt melt with a gas mixture of anhydrous hydrogen fluoride (AHF) and hydrogen (H_2). In the earlier stages the sparging of AHF and H_2 took place in a stepwise fashion were AHF was first sparged for a given amount of time to remove certain impurities in the salt melt such as oxides and sulfur through the following generalized reactions [35]:

$$O^{2-} + 2HF \rightleftharpoons 2F^- + H_2O \qquad \text{RXN 4-1}$$

$$2HF + S^{2-} \rightleftharpoons H_2S + 2F^- \qquad \text{RXN 4-2}$$

Where the oxides and sulfur convert to gaseous products that are bubbled out of the melt through the agitation caused by the sparging. As mentioned in Section 2.1 sulfur is believed to be mostly present in the form of sulfates initially, so it's believed that these sulfates must first either react to reduce or thermally decompose to dissolved sulfur before being removed by AHF [35]. Other impurities such as metal oxides or hydroxides are also removed by the AHF sparge through the reversed reactions of RXN 2-1 and RXN 2-2 [83].

The disadvantage of using a sparge of pure AHF is that HF is also a very corrosive gas to the purification vessel itself, as shown in RXN 2-3. If they weren't already present in the salt melt as impurities, this reaction results in the introduction of metal fluorides into the salt melt which can also increase the redox potential of the salt. Therefore the sparging of AHF was always followed

up by the sparging of pure H_2. The sparge of H_2 lead to RXN 2-3 being reversed such that metal fluorides were reduced to dissolved metals and the HF produced by the reaction left the melt as a gaseous product. Purification of a salt melt was then performed by alternating sparging of AHF and H_2 with an H_2 reduction always being the final step. Any reduced metal clusters formed as part of the final H_2 reduction could then be filtered out of the salt using a micron pore filter. Eventually, the sparging process was adjusted such that a mixture of AHF and H_2 was continuously used instead of alternating steps. The reasoning for this is demonstrated by considering a reaction with a vessel made of nickel. The nickel vessel itself is attacked by the HF through the following reaction:

$$Ni + 2HF \rightleftharpoons NiF_2 + H_2 \qquad \text{RXN 4-3}$$

This reaction has an associated equilibrium constant defined as

$$K_{eq} = \frac{p_{H_2} * a_{NiF_2}}{p_{HF}^2} \qquad \text{Equation 4-1}$$

Where p is the partial pressure and a is the activity, which for nickel fluoride is defined as

$$a_{NiF_2} = \gamma_{NiF_2} x_{NiF_2} \qquad \text{Equation 4-2}$$

In his work on solubility of metal fluorides in fluoride salt melts Blood then defined an equilibrium constant, K_N, as [84]:

$$\frac{1}{K_N} = \frac{K_{eq}}{\gamma_{NiF_2}} = \frac{p_{H_2} * x_{NiF_2}}{p_{HF}^2} \qquad \text{Equation 4-3}$$

Blood then reported values of K_N for Cr, Fe, and Ni. For this example, the value of K_N for Ni at 600 °C is reported as 1.73e4 [84]. So, at 600 °C Equation 4-3 becomes:

$$5.78e-5 = \frac{p_{H_2}}{p_{HF}^2} x_{NiF_2} \qquad \text{Equation 4-4}$$

From Equation 4-4 it can be seen that as the ratio of p_{H_2}/p_{HF}^2 decreases (i.e. more HF than H_2) then the concentration of the nickel fluoride increases. To meet the MSRE specifications on salt

quality shown in Table 3-2 (less than 25 ppm of Ni), it was then determined that if a nickel vessel was used for purification then the H_2 to HF ratio should remain between 5:1 and 10:1 to effectively remove impurities while limiting the corrosion of the nickel vessel [35, 83, 84].

Other purification methods have been attempted to reduce the need for handling a highly toxic gas mixture like AHF, however, the chemistries of other fluorinating agents almost always result back to HF or F_2 gas, which is an even stronger oxidant than HF. For example nitrogen trifluoride was used for purification, but above 400 ºC it decomposes into fluorine and if that mixture is combined with a pure hydrogen stream, then HF is produced and the purification chemistry is back to a H_2:HF mixture [85]. So, for producing purified FLiNaK for this dissertation, the commercially procured FLiNaK from Materion was purified using the H_2:HF sparging purification method.

4.2 Experimental Design and Methods

The University of Wisconsin-Madison has a successful history of developing fluoride purification systems for salt batches on the scale of 10s of kgs as well as smaller systems [20, 83]. For producing purified FLiNaK on the scale necessary for this dissertation as well as smaller fluoride salt experiments, a purification system was constructed that could accommodate laboratory scale batches on the order of a few kgs, though the system could also handle larger batches depending on the design of the salt containment vessel.

4.2.1 Purification Vessel

As described in section 3.1.1, one of the features on the LC-180 gloveboxes is the flange on the bottom of the glovebox that connects the furnace wells. Using these flanges the wells can be disconnected and other equipment can be attached to the glovebox if needed. Therefore, the purification vessel design for FLiNaK purification was designed with the intention of being able

to connect it to the glovebox for salt loading and unloading to ensure the FLiNaK never has to be exposed to air or moisture.

The purification vessel consists of the outer containment unit that connects to the glovebox and heaters, the nickel salt crucible, and the lid that seals the salt vessel when it is disconnected from the glovebox. The nickel crucible was manufactured by Stanford Advanced Materials. It is constructed out of 1/16” thick nickel sheet material that was rolled into a 3” diameter x 17” tall cylinder and welded using gas tungsten arc welding. A 3” diameter nickel circle was then welded on the bottom of the cylinder to complete the crucible. A small semicircular alignment plate was then tack welded onto the top of the crucible for aligning the gas sparging tube.

The main vessel was designed in-house and then constructed by Cortest, Inc., Willoughby, OH. A series of photographs of the main vessel are shown in Figure 4-1. The vessel is constructed out of 316LSST and consists of a lower vessel where the salt crucible is loaded and sealed while connected to the glovebox and an upper portion that allows the vessel to connect to the glovebox. As seen in Figure 4-1a, the lower portion is 4” in diameter and 18” tall. This portion of the vessel is heated using two externally mounted 1250 watt Watlow® semi-cylindrical clam shell style ceramic fiber heaters. A thermocouple probe is inserted through the heaters and is positioned near the heater elements to control the temperature of the vessel. The heaters are insulated with two layers of 10 mm thick Pyrogel® HPS insulation to prevent as much heat loss as possible. When the vessel is connected to the glovebox, the custom LabView program discussed in Section 3.1.1 is used to control the heaters. When connected to the salt purification system a similar custom LabView program is used.

As seen in the top view images, Figure 4-1b and c, the glovebox connection ring uses the same bolt pattern as the wells designed by LC Technologies such that the purification vessel can easily

be connected to the well connection ring. Just like the furnace wells, the silicon O-ring on the glovebox flange is what creates an air tight seal when the purification vessel is attached. The lower vessel sealing flange is a custom flange used to seal the lower portion of the purification vessel once it has been loaded with the salt containing nickel crucible. This flange is sealed with a high-temperature graphite gasket. As seen in Figure 4-1c, the lid that seals the bottom portion of the purification vessel contains several standard tube sized ports that allow feedthroughs or gas supply/effluent to be connected with the use of Swagelok compression fittings. Two of the ports are 3/8” diameter tubes that are used for a connection to an Ar purge when the vessel is connected to the FLiNaK purification system described in Section 4.2.2. The other 3/8” diameter port is used for the effluent gas during FLiNaK purification. Handling of the effluent gas is described in Section 4.2.3. A 1/4” diameter port is used for the insertion of a non-salt wetted thermocouple probe that monitors the inside temperature of the vessel. The final 1/2" diameter port is used for the insertion of a 1/4” diameter nickel sparging tube. This tube is inserted into the salt containing nickel crucible and is used to bubble the H_2:HF gas mixture through the FLiNaK salt in its liquid state.

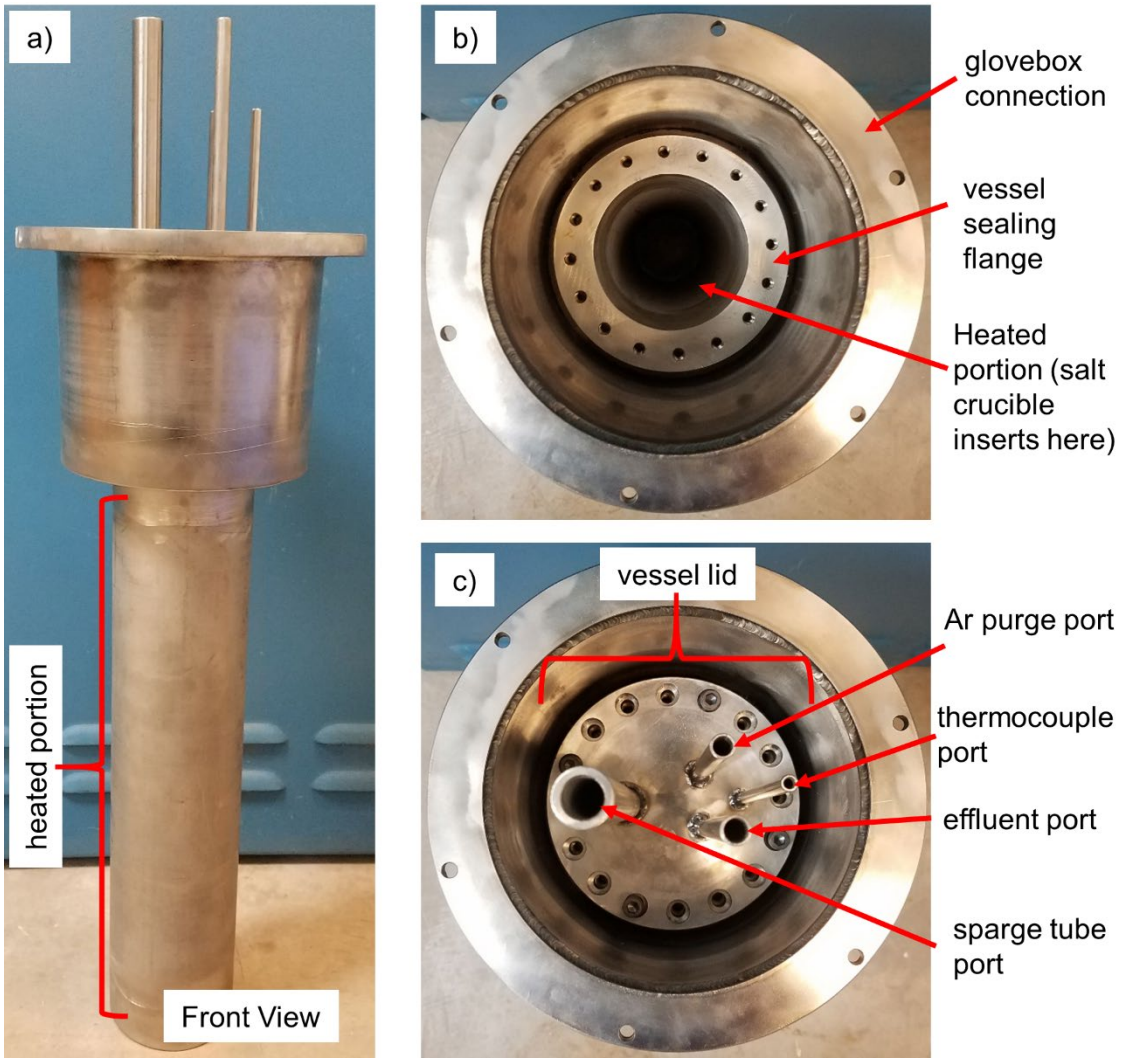

Figure 4-1: Purification reaction vessel that connects to the glovebox. a) front view. b) top view without the vessel lid. c) top view with vessel lid

To install the purification vessel on the glovebox, both the weight of the vessel and the extra height from the four ports required additional components to be fabricated. To accommodate the added height of the four ports, instead of using the flat plate provided by LC Technologies to seal the inside of the glovebox connection ring, a "top hat" style sealing assembly was design and constructed in-house. Photographs of the "top hat" sealing assembly allowing the four vessel ports to enter the glovebox are shown in Figure 4-2. Note that in Figure 4-2a the original furnace well is removed and the ultra-high purity Ar atmosphere in the glovebox is unaffected. In Figure 4-2b, the purification vessel has been attached to the glovebox and the "top hat" has been removed so

that the vessel ports are inside the glovebox. Once again the glovebox atmosphere is unaffected. To accommodate the weight of the completed purification vessel, a vessel cage was constructed out of 80/20 T-slot aluminum and a chain driven lifting mechanism was constructed to help lift the vessel up to the glovebox connection ring.

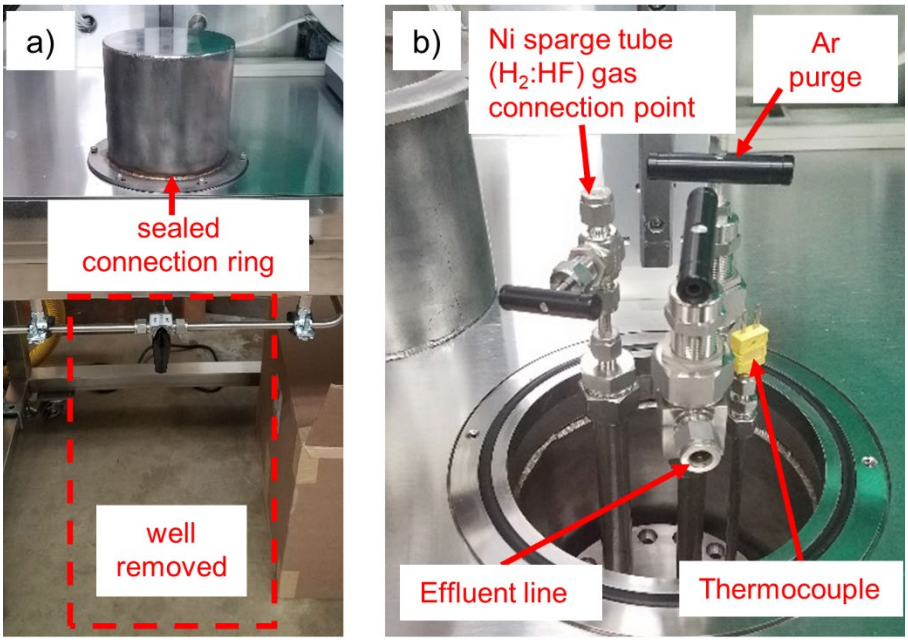

Figure 4-2: Photographs of the "top hat" sealing assembly allowing the ports on the purification vessel to pass into the glovebox. a) glovebox connection ring sealed with "top hat". b) purification vessel ports inside the glovebox.

4.2.2 Gas Delivery and Containment

The handling of H_2 and AHF gases each come with their own safety considerations. Anhydrous HF is an extremely corrosive and toxic gaseous product that must be handled with extreme care. The threshold limit of exposure is only 3 ppm while 30 ppm is considered immediately dangerous [86, 87]. Hydrogen on the other hand is highly flammable and can become explosive in concentrations in excess of 4% in air [88]. Therefore both of these gases must be handled with extreme caution and in a safe work area. Thus the H_2 and AHF gas delivery systems are contained within a large walk-in fume hood that is capable of maintaining negative pressure. The walk-in fume hood has been discussed in detail previously in reference [20]. Briefly, the walk-in fume hood is constructed of an aluminum 80-20 and carbon steel frame with aluminum and plastic wall

panels. The negative pressure inside the room is accomplished by a grated air inlet and a large fan capable of moving 1625 cubic feet of air per minute connected to the room's ductwork. All of the air is pulled through a HEPA filter before being exhausted out of the building.

The walk-in fume hood provides some safety in ensuring that the concentrations of H_2 and AHF cannot reach dangerous levels, but as another factor of safety both the H_2 and AHF gas bottles and much of the delivery equipment are further contained in their own individual gas bottle cabinets. A photograph of the gas bottle cabinets is shown in Figure 4-3.

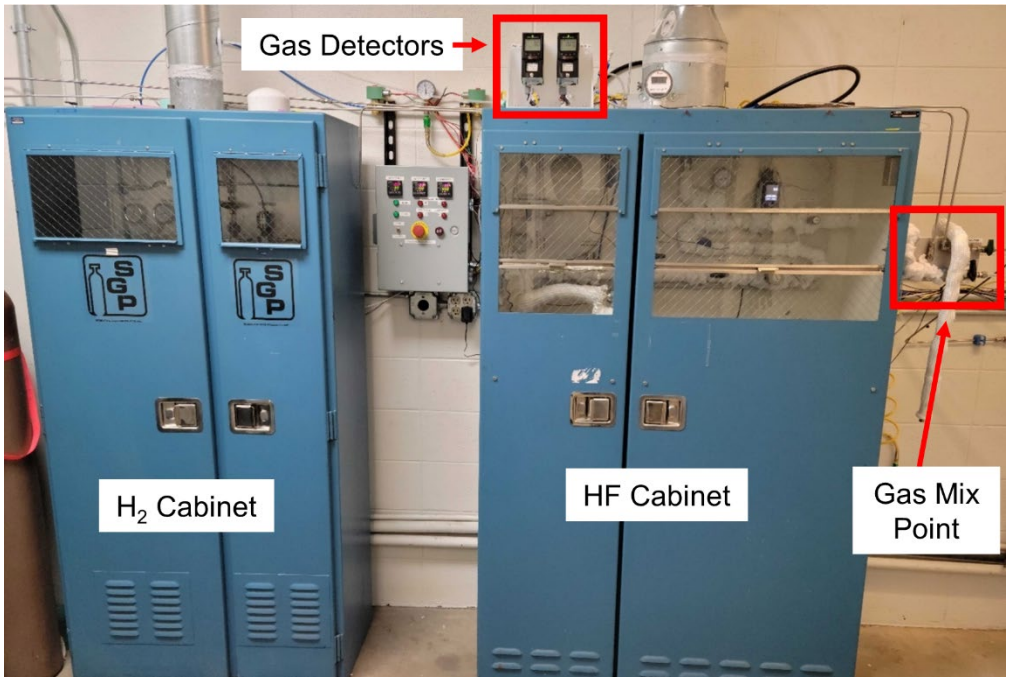

Figure 4-3: H_2 and AHF gas cabinets overview

To develop the piping and instrument diagrams (P&ID) for both the H_2 and AHF delivery, a professional engineer from Erie Shore Engineering, Inc. was consulted and assisted in the development of the P&IDs. The gas delivery systems for both H_2 and AHF were then constructed in-house and are shown in Figure 4-4. Each system primarily uses 316LSST tubing and Swagelok compression fittings if moisture is not expected to be in the gas stream. Each gas cabinet contains a pneumatic normally closed valve that is controlled remotely by a custom LabView program. These valves are positioned close to each gas bottle and are used as the primary shutoff valves if

the gas flows need to be shut off quickly. Both cabinets also contain a pressure regulator to precisely control the pressure of the gases before they go into the mass flow monitors. In hindsight, the regulator on the AHF gas lines may be redundant as the AHF gas bottle is low pressure to begin with. The pressure just before each mass flow monitor is monitored remotely by pressure transducers connected to the custom LabView program. Mass flow monitors with a 4-20 mA output are used to monitor the flow rate of each gas remotely. Additionally, the mass flow monitors have a visible readout on them for local monitoring. The mass flow monitors are Teledyne Hastings monitors with maximum flow ranges of 200 mL/min and 2 L/min for the AHF and H_2 gas systems, respectively. The flowrate of each gas is controlled by observing the flowrate on the monitors and adjusting needle valves ahead of the monitors. Again, in hindsight, mass flow controllers though more expensive would have likely been a more ideal option so that the flow rates of each gas could be controlled remotely instead of locally. After the mass flow monitors, each of the gases exits their respective gas cabinet and are mixed directly at a tee junction labeled in Figure 4-3 before entering the purification vessel. For safety, the concentration of H_2 and HF in each gas cabinet is monitored by individual gas detectors as seen in Figure 4-3. Though not pictured, the concentration of H_2 and HF in the walk-in fume hood is also monitored by gas detectors positioned directly above the purification vessel.

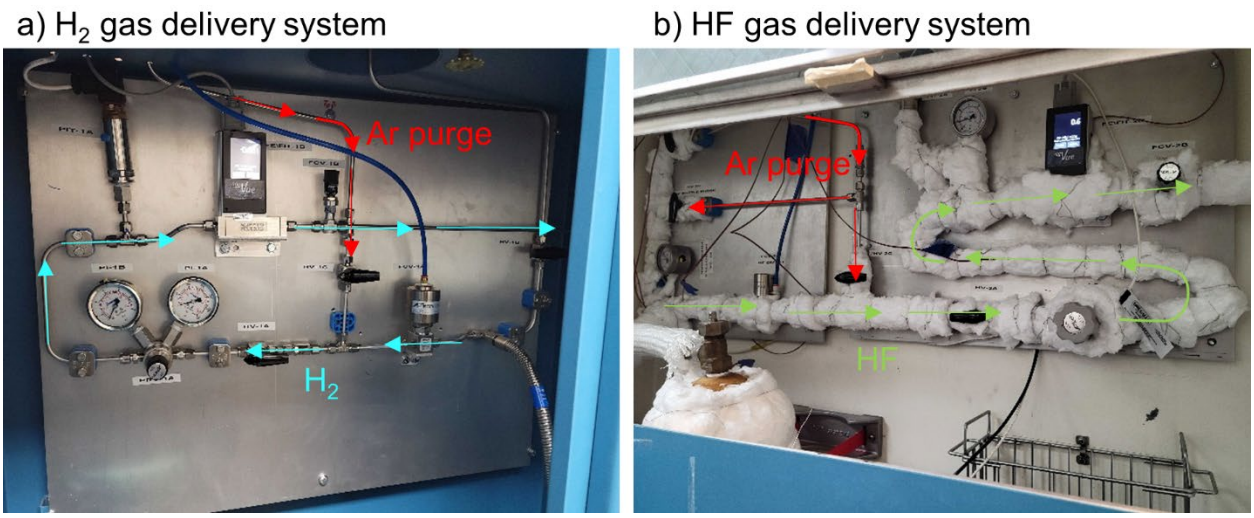

Figure 4-4: Overview of both the H_2 and HF gas delivery systems. a) H_2 gas lines. b) HF gas lines.

As mentioned earlier, the need for a gas regulator in the AHF gas lines may be redundant because the AHF gas lines are low pressure as a result of HF's rather high boiling point. Anhydrous HF boils at 20 ºC, so at most laboratory temperatures the AHF bottle actually has to be heated in order to get a decent delivery pressure for AHF. As observed in Figure 4-4b, the AHF gas bottle and any lines that are expected to contain AHF are wrapped in Kaowool ceramic fiber insulation. Underneath the insulation, the AHF bottle is heated using a flexible bottle heating pad while the gas lines are heated using flexible rope heaters in two separate heating zones. All of the heaters are controlled remotely with a custom LabView program.

4.2.3 Effluent Stream Scrubbers

During the purification process unreacted HF is bound make it through the salt sparge. Additionally, as purification goes on, less HF should react as the impurities requiring it are consumed. Therefore, the effluent stream coming out of the purification vessel must be safely scrubbed to ensure HF is not being released. HF is highly soluble in water so bubbling the effluent through water allows all of the unreacted HF to be captured. Thus a scrubber system consisting of three high density polyethylene (HDPE) water baths is used to scrub the effluent stream of any

unreacted HF. The three HDPE containers are also contained within a large HDPE container in case one of the baths were to leak. A photograph of the effluent scrubber system is shown in Figure 4-5. All of the connection to the scrubber baths are made with Swagelok stainless steel bulkhead compression fittings through the lids of the HDPE containers. The bulkhead threads are sealed with Teflon gaskets.

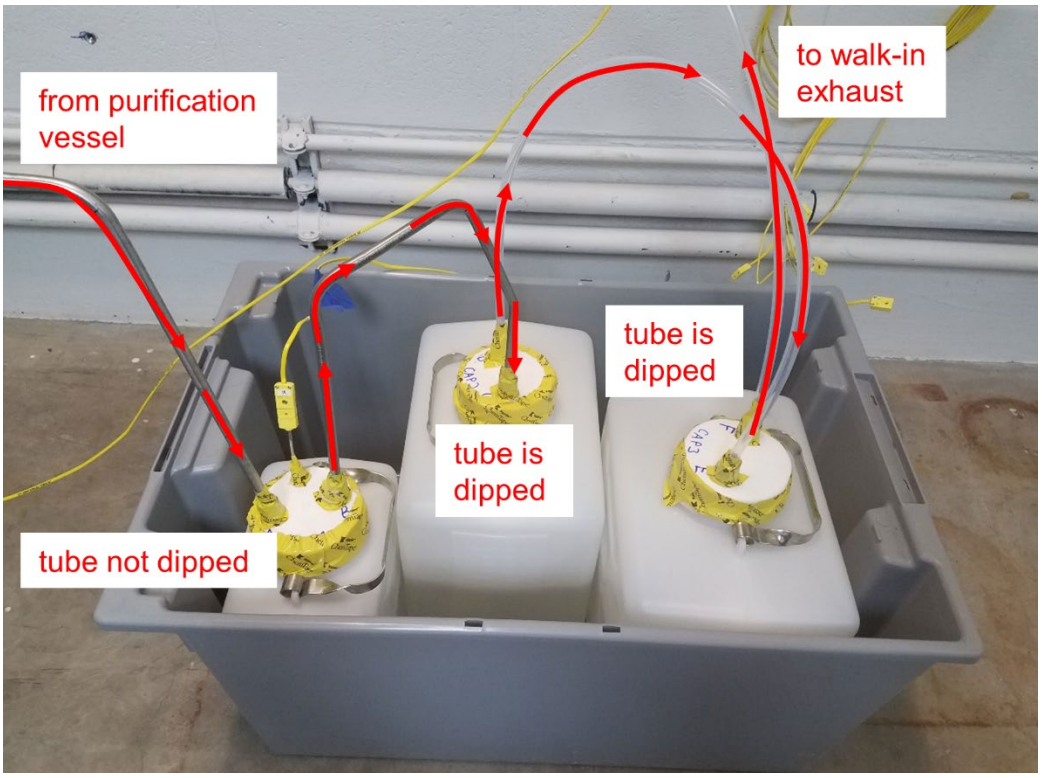

Figure 4-5: Water bath effluent scrubbers used to capture unreacted HF.

As some of the purification reactions are also expected to produce gaseous water, it's reasonable to assume then that the effluent coming out of the purification vessel could condense after leaving the heated zone to produce hydrofluoric acid (note this is HF dissolved in water, not anhydrous HF). Hydrofluoric acid can attack stainless steel, so the metallic tubing leaving the purification vessel to the first water bath is made of Monel. This first water bath is a 9 L HDPE carboy filled approximately with 4 L of water. In this bath, the Monel tube does not dip into the water. The effluent simply enters the bath and some of HF in the effluent dissolves into the water. The Monel

tube is not dipped into water in the 9 L bath so that if over pressure occurs in this bath, water cannot be pushed back up the effluent line into the purification vessel.

Connecting the 9 L carboy to the second carboy is another Monel tube. The second carboy is a 20 L carboy filled halfway with water. In this carboy the Monel tube is dipped into the water so that the effluent has to bubble through the water. This helps ensure any HF in the effluent has to go through water and is captured. For added assurance, a third 20 L carboy filled halfway with water is also used. The second carboy is connected to the third carboy with flexible fluorinated ethylene propylene (FEP). Once again, the FEP tubing is dipped into the water to force the effluent to bubble through the water. After the third carboy the effluent is connected to the walk-in fume hood's exhaust.

Neutralizing the effluent scrubbers is performed after purification is completed. Previous experience has shown that on-line neutralization is difficult and can actually lead to the formation of an insoluble film on the surface of the water that creates excess pressure in the carboys [20]. Phenol Red pH indicator is added to the water baths, however, to observe when the pH in each carboy begins to become acidic. In acid conditions Phenol Red will begin to turn orange and eventually yellow if the pH goes below 6.

Note that the Monel tubing was used to connect the purification vessel to the first carboy and to connect the first carboy to the second carboy because the temperature of the effluent was of concern. However, during one purification the temperature of these tubes was monitored and it was found that they did not exceed 50 ^{o}C. In the future, at least the Monel tubing connecting the first carboy to the second carboy can likely be replaced with another section of FEP or other HF compatible plastic so that the connection is simpler to make.

4.2.4 Salt Transferring and Filtration

After the H_2:HF sparging process, the purification vessel is once again connected to the glovebox so that the now purified salt can be retrieved from the vessel. Because of the design of the vessel, if a non-wetted crucible material or a tapered crucible is used, the salt could potentially be removed from the crucible in a solid ingot. However, even though the nickel crucible is relatively inert to FLiNaK it is still expected to be wetted by FLiNaK salt. Additionally, as mentioned in 3.1.2 the Materion produced FLiNaK mixture was originally melted in graphite crucibles so there is likely graphite particles suspended in the salt in its molten state. Furthermore, the H_2 reduction step is expected to produce metallic products from the reverse of RXN 2-3. These metallic products could form metal clusters that are also suspended in the salt when it is in the molten state. The potential existence of the graphite particles and metal clusters then leads to the need to filter the salt. Therefore, to remove the purified FliNaK from the purification vessel the salt is pumped out of the crucible and forced through a filter before collecting it in a different container.

Once the purification vessel has been reconnected to the glovebox, salt transferring and filtration is accomplished by disconnecting the needle valve from the Ni sparging tube and using the Swagelok compression fittings to attach an in-line filter connected to a heated transferring arm. The uninsulated transfer arm with filter is shown in Figure 4-6. The transfer arm is constructed from 1/4" nickel tubing. It is heated by a rope heater whose temperature is controlled by the glovebox's custom LabView controller. Two thermocouple probes are attached to the transfer arm; one of the thermocouple probes is used to control the heater, while the second is used to monitor the temperature of the transfer arm near the transfer arm exit. The filter is a standard stainless steel 316 Swagelok in-line welded filter with a 15 μm pore size. Because the salt moves through the filter rather quickly it is not believed that the filter introduces a significant quantity of impurities.

Another thermocouple probe is attached to the filter body to monitor the temperature at the filter ensuring that the filter temperature is high enough to prevent salt freezing in the filter.

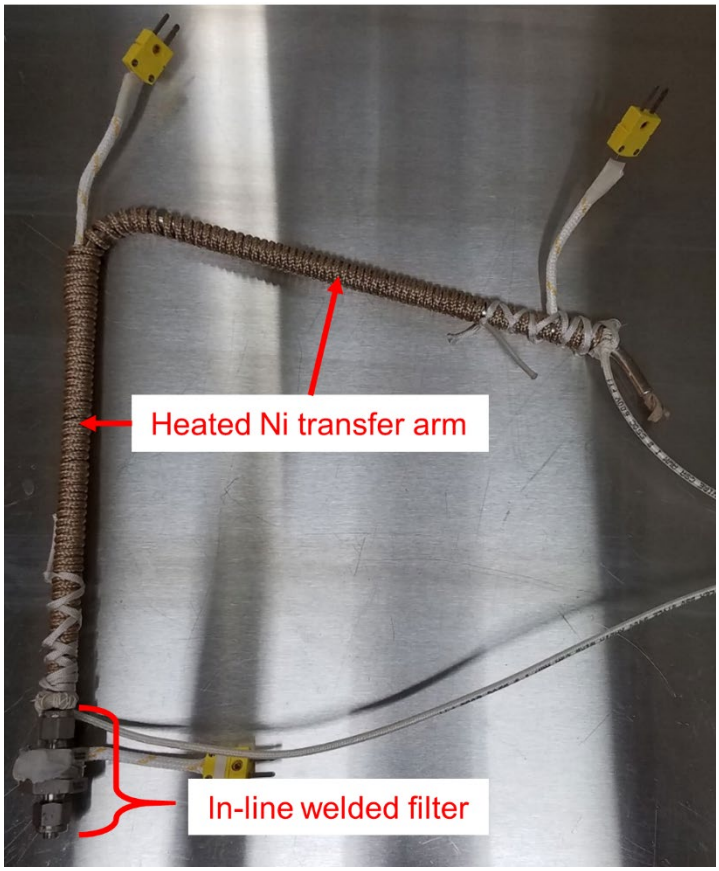

Figure 4-6: Heated nickel transfer arm with in-line filter attached for transferring and filtering purified FLiNaK out of the purification vessel.

To transfer the salt out of the purification vessel, pressure must be applied to the lower portion of the vessel in order to "push" the salt up through the sparging tube, through the filter, and out of the transferring arm. This is accomplished by utilizing the valves connected to the Ar purge and effluent ports as shown in Figure 4-7. The heated transfer arm with filter are connected to the nickel sparging tube. Connected to the effluent valve is a short section of tubing with a pressure gauge for monitoring the pressure inside the vessel during transfer. Connected to the Ar purge valve is a 3-way ball valve that allows ultra-high purity Ar to pressurize the vessel. This Ar line is fed into the glovebox via one of the feedthroughs installed by LC Technology Solutions. The 3-

way ball valve also allows the purification vessel to be depressurized during the salt transfer if needed.

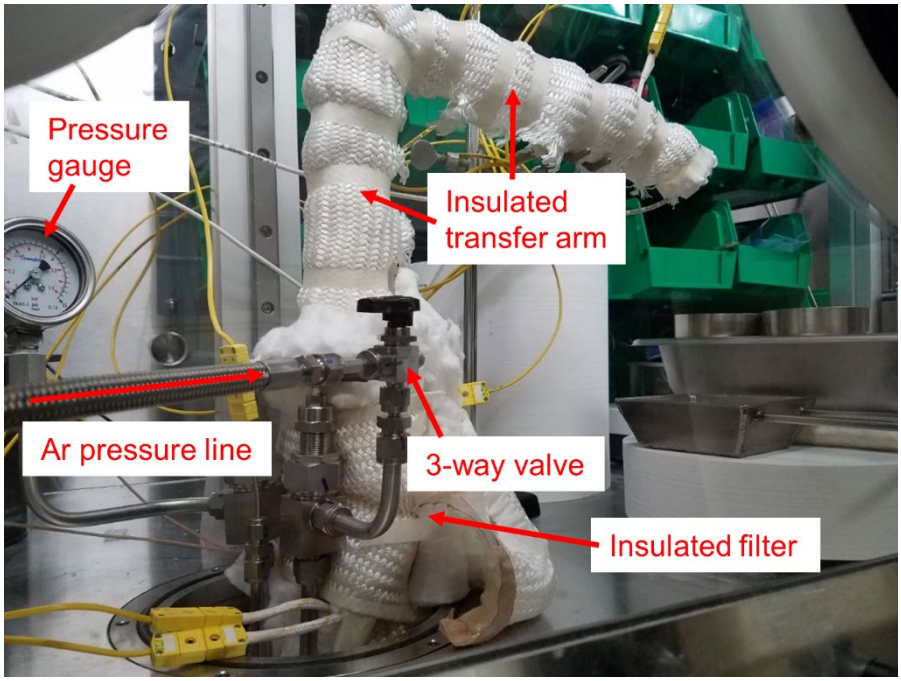

Figure 4-7: Purification vessel pressurization setup for transferring and filtering purified FLiNaK out of the purification vessel.

4.2.5 Producing Purified FLiNaK from Commercially Sourced Materion FLiNaK

The same commercially sourced FLiNaK mixture from Materion Corporation described in Section 3.1.2 was used for the production of H_2:HF purified FLiNaK. As mentioned in Section 3.1.2, 10 kgs of FLiNaK was originally procured. The FLiNaK came in large pieces sealed in 5 containers with approximately 2 kg of FLiNaK per container. For purification, the salt in one of these containers was crushed into smaller pieces so that the nickel purification crucible could be loaded with the FLiNaK pieces. As shown in Figure 4-8a and b, the nickel sparging tube was first placed into the nickel crucible centered around the alignment plate on the nickel crucible. Then the crushed FLiNaK pieces were loaded into the crucible. Approximately 2 kgs of the commercial FLiNaK was loaded into the crucible. Then as shown in Figure 4-8c, the nickel crucible was placed into the lower portion of the purification vessel while it was attached to the glovebox. Following

this, the purification vessel lid was positioned onto the lower vessel using a graphite gasket to seal the lower vessel. The lid was tightened using a torque bar so that the bolts on the lid were properly tightened. Then Swagelok compression fittings were connected to the 1/2" port that the nickel sparge tube passes through. Finally, the sparging needle valve was tightened onto the nickel sparge tube before disconnecting the purification vessel from the glovebox.

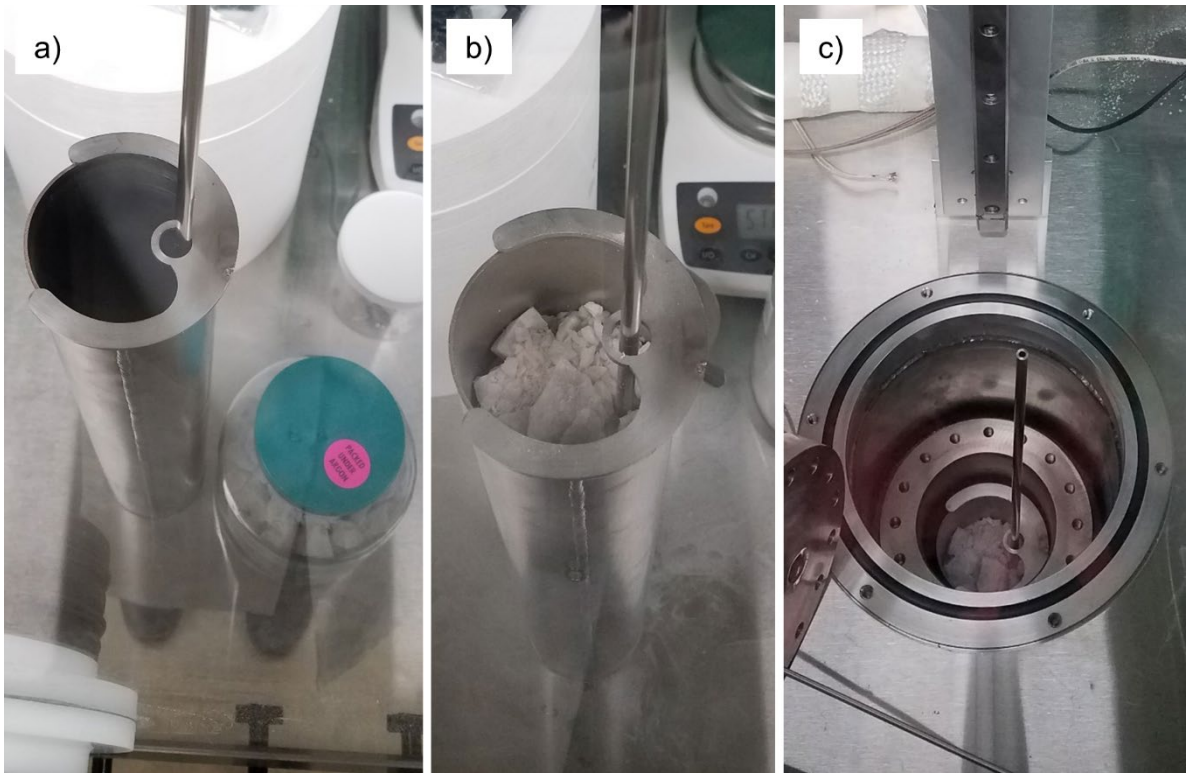

Figure 4-8: Loading commercial FLiNaK into purification vessel. a) positioning of the nickel sparging tube inside the nickel crucible. b) nickel crucible loaded with commercial FLiNaK. c) FLiNaK and nickel crucible loaded into purification vessel.

After disconnecting the purification vessel from the glovebox, the purification vessel was moved into the walk-in fume hood and connected to the H_2:HF gas delivery systems, the Ar purge line, and the effluent scrubber baths. Photographs of the connected vessel are shown in Figure 4-9. All of the heater and thermocouple connections were made so that the vessel could begin heating. Before heating the vessel, the effluent valve and Ar purge valve were opened so that the

purification vessel was actively being purged with Ar gas as the vessel was heated. This is done so that the purification vessel does not pressurize as it is heated.

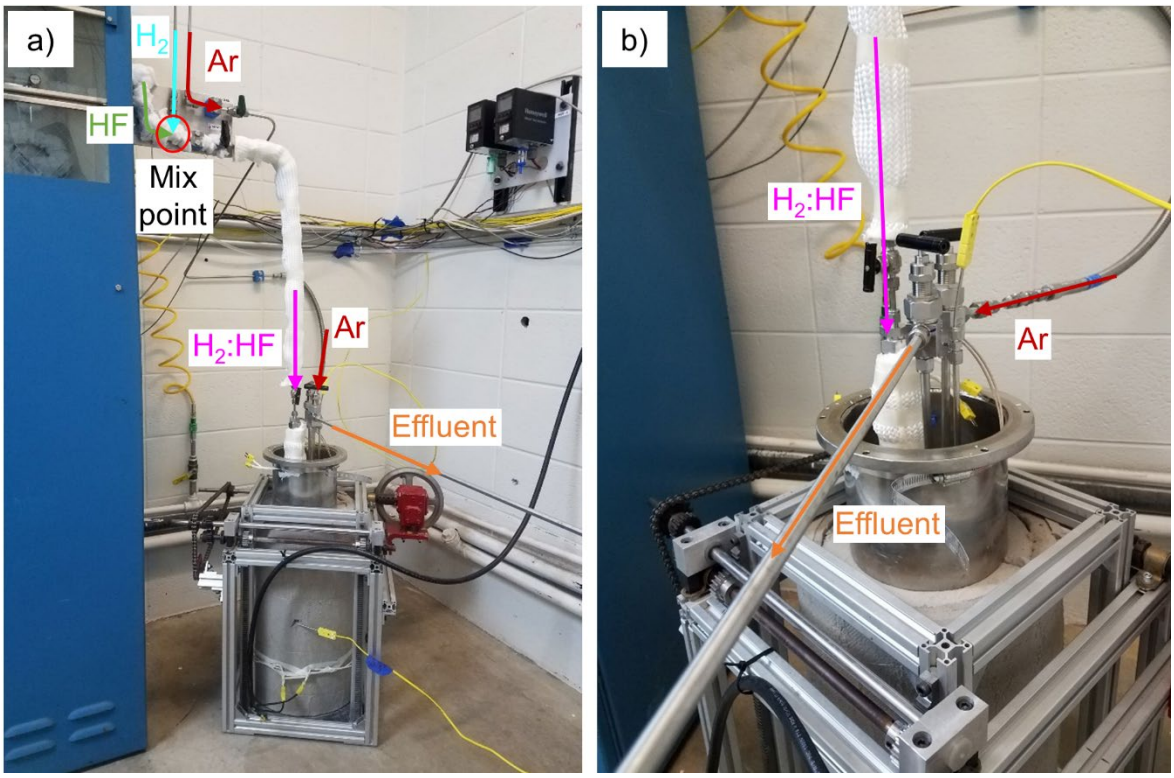

Figure 4-9: Purification vessel connected to the H_2:HF gas delivery system. a) Overview of the purification vessel. b) close up of the valve connections

The purification vessel was first heated just above 200 ºC to do an initial bakeout of the vessel and salt for 2 hrs. Then the vessel was heated to approximately 600 ºC for purification. Once the heater thermocouple probe reached 600 ºC the vessel and salt temperature were allowed to equilibrate for 8 hrs under the flow of the Ar purge before sparging began. The Ar purge was shutoff and the H_2 gas flow was started at a rate of approximately 410 ml/min. Then the AHF gas flow was started at a flowrate of approximately 41 ml/min such that the ratio of H_2:HF was 10:1. The mixture of H_2 and AHF was sparged through the molten FLiNaK for 4 hrs at a temperature of 600 ºC. After 4hrs the AHF gas flow was stopped so that the H_2 reduction step could begin. The H_2 flowrate was then increased to 450 ml/min and the H_2 reduction step was allowed to go for an additional 2 hrs. Once the H_2 reduction step was completed, the flow of H_2 was turned off and the Ar purge was turned

back on to purge out the gas space within the reaction vessel. The heaters to the purification vessel were then turned off and the Ar purge was allowed to continue as the vessel cooled to room temperature.

When the purification vessel had cooled, all of the valves to the vessel were closed and capped off when the lines were disconnected. The purification vessel was moved back to the glovebox and reconnected to the glovebox flange so that salt transfer and filtering could take place. Once reconnected to the glovebox, the needle valve on the sparging tube was removed and the insulated transfer arm with the stainless steel in-line filter was connected to the sparging tube. Additional insulation was added around the filter to ensure that it could heat up to a sufficient temperature. The Ar pressuring line and pressure gauge were also attached. To transfer, the salt purification vessel was heated to 650 ºC to ensure the salt would not freeze during the transfer process. The transfer arm was heated above the melting point of FLiNaK, 454 ºC, to a temperature just above 500 ºC so that the likelihood of the FLiNaK freezing during the transfer was reduced. Once the vessel and transfer arm were at temperature, the Ar pressuring line was used to introduce approximately 3-4 psig of pressure into the vessel. This pressure was sufficient to push the FLiNaK through the transfer arm and filter. A photograph of the flowing FLiNaK salt is shown in Figure 4-10a. The FLiNaK was poured into three separate nickel containers and allowed to freeze inside the glovebox. Photographs of the freezing process are shown in Figure 4-10b and c. The salt starts to freeze at the bottom of the containers and additional salt crystals can be seen nucleating at the walls of the nickel containers. In total three ingots of salt were collected with a combined mass totaling just over 1.95 kg, showing that almost all of the original 2kgs of FLiNaK were collected.

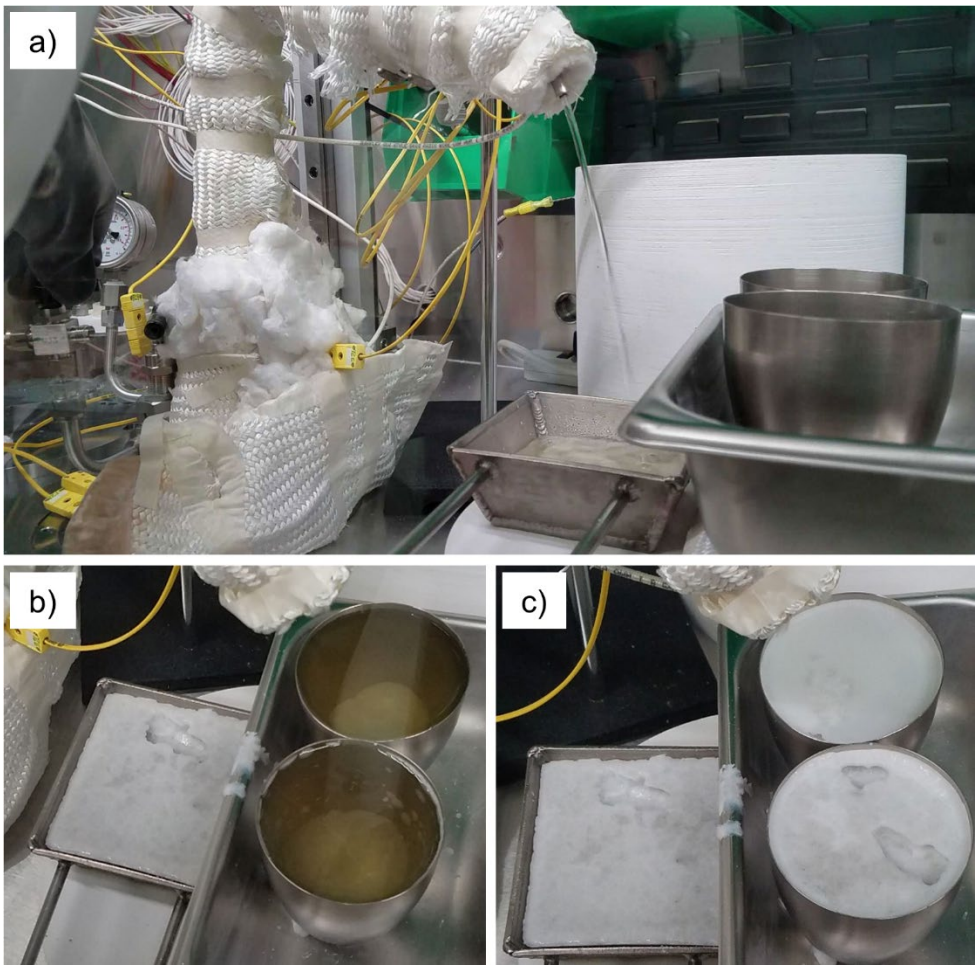

Figure 4-10: Photographs captured during the FLiNaK transfer and filtering process. a) FLiNaK pouring out of the transfer arm into a nickel tray. b) FLiNaK ingots during the freezing process. c) Frozen FLiNaK ingots.

During the transfer process the liquid FLiNaK was extremely clear and flowed very easily similar to how a laminar flow of water appears. Once solidified the FLiNaK ingots were noticeable whiter in appearance as compared to the original commercially procured pieces of FLiNaK. A photograph comparing the appearance of the as-received FLiNaK to the as-purified FLiNaK is shown in Figure 4-11. Generally speaking, a whiter color of salt indicates higher purity. As seen in Figure 4-11, the as-received commercially procured FLiNaK has a slight gray hue to it, likely indicating the presence of suspended graphite from the original melting process in graphite crucibles. To truly characterize the purity of the salt before and after purification, a salt sample of the as-received FLiNaK from the jar used for purification as well as samples from all three purified FLiNaK ingots

were collected and analyzed with ICP-MS. Those results are shown in Table 4-1. FLiNaK from this purification process was used for investigating the effects of salt purity on the corrosion of 316HSST.

Figure 4-11: Commercially procured FLiNaK before (left) and after (right) purification and filtration [50].

4.2.6 Methods for Investigating the Effect of Salt Purity

Samples of 316HSST for the salt purity experiment came from the same 1/2" thick plate of 316HSST that the samples for the Vol/SA ratio experiments used covered in Section 3.1.2. For this 316HSST exposed to purified FLiNaK test, the same exposure cell configuration as that used in the 1.67 cm^3/cm^2 Vol/SA ratio test was used. Similar to the Vol/SA ratio experiments, before exposure to purified FLiNaK, the 316HSST samples were ground on all faces and edges up to a P4000 grit finish using SiC abrasive paper. The samples were then ultrasonically cleaned in acetone followed by IPA before having their initial dimensions and masses recorded. One sample string consisting of three 316HSST samples was prepared using 316LSST wire connected to a 316LSST cap. A photograph of the prepared 316HSST sample string is shown in Figure 4-12a.

One of the same PyBN crucibles used in the 1.67 cm^3/cm^2 Vol/SA ratio tests was used after it was thoroughly cleaned using the cleaning procedure described in 3.1.2. A photograph of the inside diameter of the cleaned PyBN crucible is shown in Figure 4-12b. As was the case during the first

cleaning of the PyBN crucibles, after cleaning, the inside of the PyBN crucible appears almost as it did when it was new.

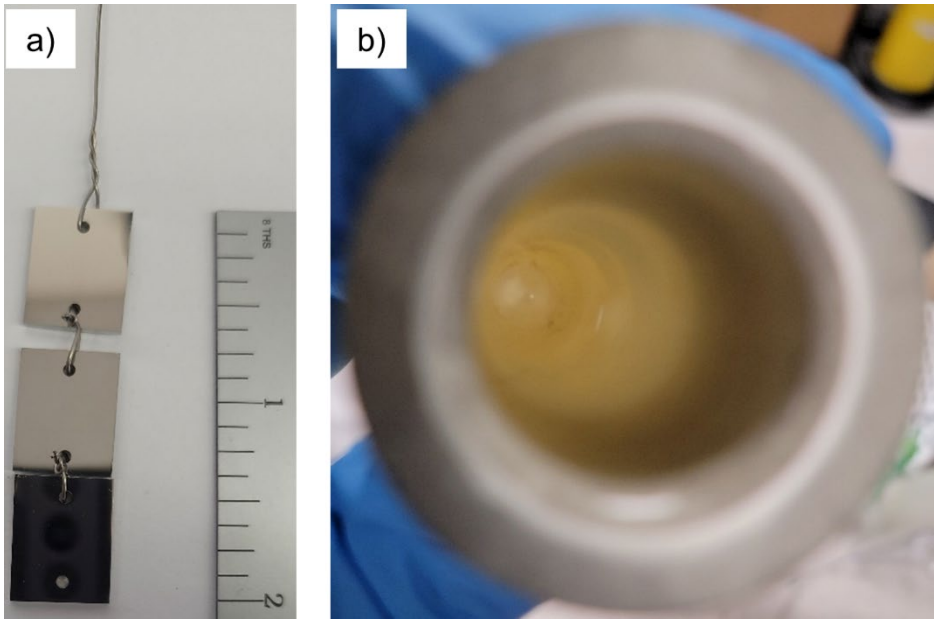

Figure 4-12: a) prepared 316HSST sample string for the purified FLiNaK exposure test. b) cleaned PyBN crucible.

All of the salt handling and salt exposure was performed in the same glovebox described in Section 3.1.1. To achieve the same Vol/SA ratio for the 316HSST samples in this test, approximately 50 g of the purified FLiNaK was crushed and loaded into the cleaned PyBN crucible before placing the crucible in a salt catch pan and lowering it into the glovebox furnace well. The furnace well was heated to 250 ºC and held for 12 hrs for a bake out. Then the furnace was heated to 500 ºC and held for 2 hrs to allow the purified FLiNaK to melt in the PyBN crucible. Finally, the furnace was heated to 700 ºC and held for 2 hrs to allow the salt temperature to homogenize before introducing the 316HSST samples. As in the Vol/SA ratio experiments, the crucible was lifted out of the furnace well while at temperature, and the 316HSST samples were introduced to the purified FLiNaK by positioning the crucible cap onto the crucible with the samples hanging down in the salt. Once the samples were positioned in the PyBN crucible, the crucible was then

lowered back into the furnace. The 316HSST samples were then continuously exposed to the purified FLiNaK salt for 500 hrs at a Vol/SA ratio of 1.67 cm^3/cm^2.

After 500 hrs, the crucible was lifted out of the furnace while it was still at 700 ºC and the 316HSST samples were removed from the salt by lifting the PyBN crucible cap off of the crucible. The 316HSST sample string was then allowed to cool in the Ar glovebox atmosphere. Once the samples were cooled they were removed from the glovebox so that residual FLiNaK stuck to the samples could be washed off. To wash the residual FLiNaK off of the samples the 316HSST sample string was initially sonicated in warm DI water for two 15 min sessions where the DI water was replaced between sessions. Then the samples were sonicated in warm DI water for multiple 10 min sessions where the mass of the bottom sample was recorded between sessions until the mass did not change between sonications. The samples then went through a final sonication in IPA and allowed to dry before having their post exposure masses recorded.

The post-exposure sample characterization for the 316HSST samples exposed to Purified FLiNaK for 500 hrs at a Vol/SA ratio of 1.67 cm^3/cm^2 followed the same sample analysis as the Vol/SA ratio samples described in Section 3.1.3.

4.3 Results and Discussion

As seen in Figure 4-11, the visual appearance of the purified FLiNaK is much improved as compared to the piece of commercially as-received FLiNaK. Generally, it is thought that the whiter a piece of salt is the higher the purity, because the presence of impurities is what seems to affect the color of the salt [83, 89]. ICP-MS provides a more quantitative measurement of the level of metallic impurities, although it cannot determine the concentration of some important impurities like carbon, dissolved oxygen, and moisture. The results of two ICP-MS checks on the

commercially procured as-received FLiNaK and samples from the three purified FLiNaK ingots is provided in Table 4-1. Note that Commercial FLiNaK 1 and Commercial FLiNaK 2 come from the same 10 kgs of FLiNaK procured from Materion Corporation but are taken from separate 2 kg jars. Commercial FLiNaK 1 comes from the same salt sample described in Section 3.1.2 while Commercial FLiNaK 2 comes from a salt sample taken from the 2 kgs of FLiNaK used for purification.

Overall the purification by H_2:HF sparging appears to have helped reduced the concentration of certain impurities while potentially introducing additional Ni impurities, likely as a result of the HF attack on the nickel crucible. In hindsight, the H_2 reduction step likely could have been performed at a higher temperature than 600 ^{o}C and for a longer duration to help remove this Ni. Otherwise, other impurities known to be oxidants such as S and P are reduced by the purification process and although ICP-MS cannot determine concentrations of dissolved oxygen it is reasonably believed that it should be significantly reduced by the H_2:HF sparging. Perhaps a better indication of the improved purity of the salt is the performance of the 316HSST samples exposed to the purified FLiNaK.

Table 4-1: Concentration of impurity elements found in the as-received commercial FLiNaK and purified FLiNaK ingots as determined via ICP-MS. Concentrations are provide in units of µg/g (wt-ppm)

Element	S	P	Fe	B	Al	Ni	Cr	Mn	Mo
Commercial FLiNaK 1	362 ±41	20 ±2	15 ±0.8	9.0 ±0.6	5.8 ±0.5	5.0 ±0.3	3.9 ±0.2	0.5 ±0.05	1.1 ±0.1
Commercial FLiNaK 2	55 ±2.8	10 ±0.6	78 ±5	1.9 ±0.5	8.7 ±0.5	4 ±0.3	2.8 ±0.1	0.7 ±0.1	0.8 ±0.1
Purified FLiNaK 1	47 ±4.4	7 ±0.5	39 ±2	5.9 ±0.6	25 ±2	84 ±3	3.7 ±0.2	0.7 ±0.04	0.1 ±0.01
Purified FLiNaK 2	36 ±5.2	6.6 ±0.6	30 ±3	4 ±0.5	36 ±2	81 ±4	3.7 ±0.2	0.7 ±0.1	0.1 ±0.01
Purified FLiNaK 3	40 ±5.8	8.9 ± 1	41 ±2	4.8 ±0.8	11 ±2	83 ±4	5.8 ±0.4	1.1 ±0.1	0.1 ±0.01

As was done in the Vol/SA ratio tests, the mass change per surface area was calculated for the 316HSST samples exposed to the purified FLiNaK at a Vol/SA ratio of 1.67 cm^3/cm^2. The results are plotted in Figure 4-13 along with the mass change results from the 316HSST samples exposed to the as-received FLiNaK from the Vol/SA ratio test at 1.67 cm^3/cm^2 for a direct comparison of the results. Immediately observable from the mass change data in Figure 4-13 is that the 316HSST samples exposed to the purified FLiNaK at a Vol/SA ratio of 1.67 cm^3/cm^2 for 500 hrs at 700 ºC lost nearly half as much mass as the 316HSST samples exposed to the as-received FLiNaK. With all of the parameters for the two tests being nearly identical except for the use of purified FLiNaK, it's clear that the purification of FLiNaK must have been successful in removing a significant quantity of the impurities that drove the corrosion of the 316HSST samples exposed to the as-received FLiNaK.

Also hypothesized from these results is the likely effect of the consumption of all the impurities available in the purified FLiNaK (i.e. purification also puts the intial salt redox potential in a less oxidizing condition). As noted in Section 3.2, the plateau in the mass loss of the 316HSST samples exposed to the as-received FLiNaK after 500 hrs is hypothesized to be a result of the consumption

of impurities which increase the redox potential, and without another driving force for corrosion being present the corrosion of the 316HSST essentially stopped once the redox potential wasn't oxidizing enough towards 316HSST. Therefore it was speculated that at a Vol/SA ratio of 1.67 cm^3/cm^2, corrosion tests beyond 500 hrs may lead to erroneous results for an alloy moderately susceptible to corrosion, such as 316HSST. However, with the results of the 316HSST in purified FLiNaK, it could potentially also mean that the choice of Vol/SA ratio and time are directly tied to the salt purity. With the purified salt, the mass loss observed in Figure 4-13 is likely the plateaued mass loss for 316HSST in these purified FLiNaK conditions. So, it's speculated here that the corrosion plateau time for the same alloy can also be an indication of the quality of the salt if all other test parameters are held constant.

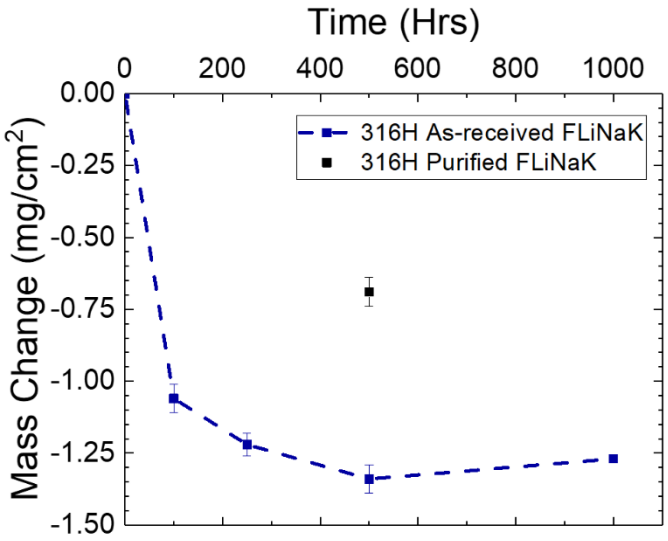

Figure 4-13: Mass loss results for the 316HSST samples exposed to as-received and purified FLiNaK at a Vol/SA ratio of 1.67 cm^3/cm^2 at 700 ºC.

Any changes in the phases in the 316HSST samples exposed to purified FLiNaK for 500 hrs were investigated using XRD. The results are plotted in Figure 4-14 along with the reference 316HSST sample and the 316HSST sample from the Vol/SA ratio test exposed to as-received FLiNaK also at Vol/SA ratio of 1.67 cm^3/cm^2 for 500 hrs at 700 ºC. As was the case with all of the 316HSST samples in the Vol/SA ratio tests described in Section 3.2, the 316HSST sample exposed to

purified FLiNaK retains its primary austenite phase with the retained ferrite phase also being present. Additionally, there is little shifting in the peak positions. Nelson-Riley analysis on both the austenite and ferrite phases once again shows that the lattice parameter of both phases is 3.60 Å and 2.87 Å, respectively after the purified FLiNaK exposure at 700 ºC for 500 hrs. This is the same result found for all of the 316HSST samples from the Vol/SA ratio tests. Finally, just like the Vol/SA ratio tests the 316HSST sample exposed to purified FLiNaK at 700 ºC for 500 hrs shows signs of sensitization as evident by the slight appearance of the M_xC_y peaks below the austenite (111) peaks. As a reminder the exposure to FLiNaK whether purified or not is also a heat treatment for the 316HSST samples so the appearance of the carbide phase is not believed to be a corrosion effect but rather an effect of the heat treatment.

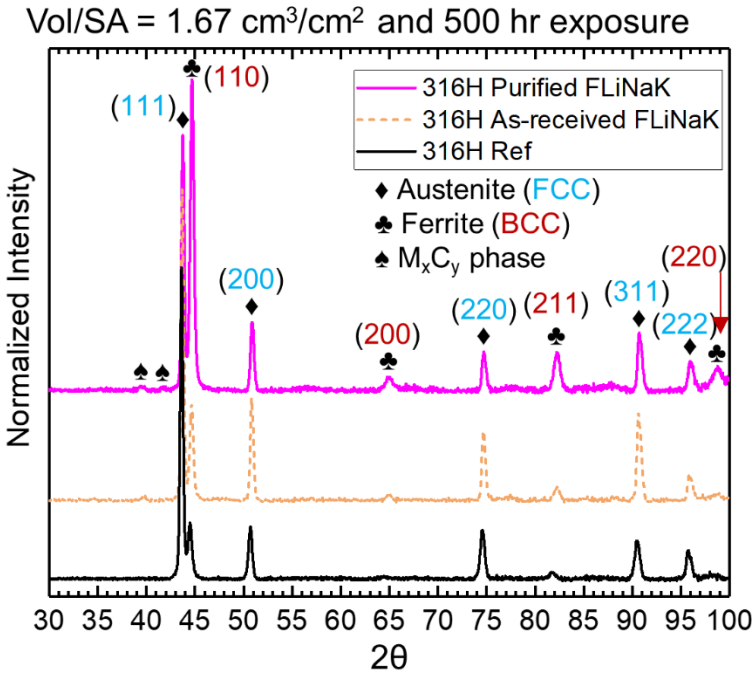

Figure 4-14: XRD spectrum for the post purified FLiNaK 316HSST sample plotted along with the 500 hr as-received FLiNaK 316HSST sample tested at a Vol/SA ratio of 1.67 cm^3/cm^2 at 700 ºC and the reference 316HSST sample.

To look at the depth of attack on the 316HSST samples exposed to the purified FLiNaK, the top sample from the sample chain was used for GDOES analysis while the middle sample was used for cross-sectional SEM/EDS analysis. The GDOES plot is not provided here as it shows almost

identical behavior as the plots shown in Figure 3-12; but, the averaged Cr depletion depth determined by GDOES analysis showed a Cr depletion depth on the order of 4 μm. For comparison the 316HSST sample from the Vol/SA ratio tests showed an averaged Cr depletion depth of only 2.9 μm even though this sample experience approximately twice the amount of mass loss as the 316HSST sample exposed to purified FLiNaK.

As with the previous Vol/SA ratio 316HSST samples, the 316HSST sample exposed to purified FLiNaK also showed clear evidence of highly localized corrosion attack that isn't capture by the averaged GDOES analysis. One of the areas in the cross-section of the 316HSST sample exposed to purified FLiNaK analyzed with SEM/EDS is shown in Figure 4-15. Just as in the as-received FLiNaK, the line scan on the 316HSST sample exposed to purified FLiNaK shows that the localized corrosion attack primary occurs along the grain boundaries in the form of Cr depletion. A drop in the Cr concentration as the line scan crosses one of the grain boundaries is clearly observed while little Cr depletion within the salt facing grains is observable. From the SEM image and Cr EDS mapping, it can also be seen that the depth of the Cr depletion does not extend much past the depth of the grain boundary void formation. Additionally, in front of the Cr depletion along the grain boundaries, it can also be observed that the grain boundaries are again enriched in Cr. As was the case in the Vol/SA ratio tests, this enrichment likely corresponds to the chromium carbide phase that forms as a result of sensitization.

The localized Cr depletion depth as measured from the Cr EDS mapping is approximately 23 μm. This depth is similar to the 19 μm depth measured on the 316HSST exposed to as-received FLiNaK at a Vol/SA ratio of 1.67 cm^3/cm^2 for 500 hrs that had approximately twice the mass loss. Understanding why these two samples show similar depletion depths is complicated, but it's hypothesized here that this occurs because of surface recession. Doniger [50] recently showed that

316HSST samples that are corroded in as-received salt can show greater than 1 µm of surface recession. So, if this is occurring in the Vol/SA ratio 316HSST sample, then the majority of the mass loss from that sample is coming from the surface recession and not the Cr depletion along the grain boundaries.

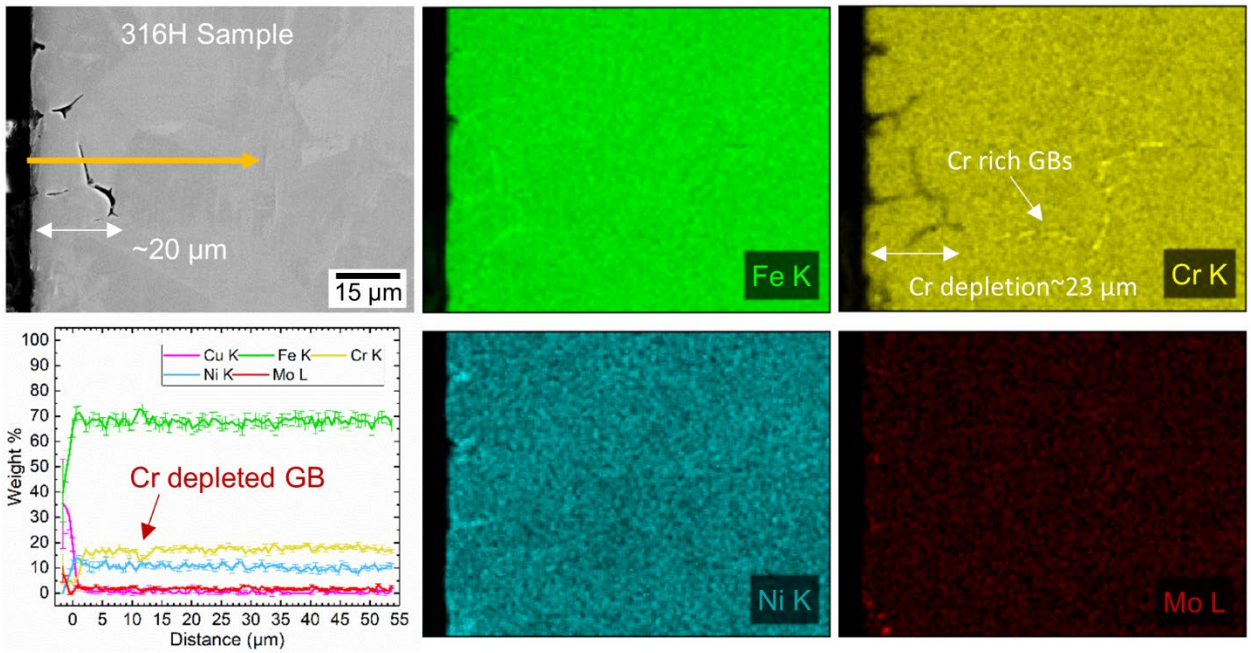

Figure 4-15: SEM/EDS analysis on 316HSST sample exposed to purified FLiNaK at a Vol/SA ratio of 1.67 cm^3/cm^2 for 500 hrs at 700 °C.

4.4 Conclusions from Salt Purity Effects

Using the results from the exposure of 316HSST samples to purified FLiNaK at a Vol/SA ratio of 1.67 cm^3/cm^2 for 500 hrs at 700 °C and comparing them directly to the 316HSST samples from the Vol/SA ratio experiments in Chapter 3, it can be observed that the purity of salt also plays an important role on the outcomes from a static isothermal corrosion test. It was observed that the 316HSST samples exposed to commercial FLiNaK at a Vol/SA ratio of 1.67 cm^3/cm^2 had a plateau in the mass loss data indicating that the corrosion of the 316HSST essentially stopped after approximately 500 hrs. Furthermore, it was speculated that this plateau was primarily a result of

the impurities in the commercial FLiNaK being consumed such that the salt redox potential became less oxidizing after 500 hrs. In this chapter it was demonstrated that by sparging a gaseous mixture of H_2 and HF through the commercially procured FLiNaK, the quality of the FLiNaK can be improved as a result of impurity removal and therefore improved redox potential. Due to this impurity removal, the overall quantity of impurities in the same volume of salt used in Chapter 3 is dramatically reduced. Therefore the 316HSST samples exposed to purified FLiNaK at a Vol/SA ratio of 1.67 cm^3/cm^2 for 500 hrs have an improved corrosion resistance as evident by the mass loss being cut in half. Nothing has changed about the 316HSST samples and so the improvement in their corrosion performance must be directly tied to the salt purity. Therefore, just as the Vol/SA ratio plays a significant role in the outcome of a static isothermal corrosion test, so does the salt purity.

Chapter 5

Dissimilar Material Interactions in Fluoride Salt

5.1 Predicting Activity Gradient Interactions with Computational Tools

As discussed previously in Section 2.3.3, the interactions of materials in salts as a result of activity gradients is hypothesized to occur because specific elements in one material have a relatively high activity, and can reach a lower activity level by migrating to a second material. Further, the mechanism that enables this elemental transports is hypothesized to occur in several steps; those being (i) corrosion reactions that put corrosion products in the salt in multiple oxidation states for a given element (i.e. RXN 2-8 and RXN 2-9), (ii) a disproportion reaction of the corrosion products leaving either solid or dissolved metal species in the salt medium (i.e. RXN 2-10), and (iii) absorption reactions at a material in the salt medium leading to the uptake of dissolved metal species (i.e. RXN 2-11). The mechanism requires no electrical contact meaning electrons are not transported from one material to another through a galvanic connection as a result of oxidation and reduction reactions. This mechanism therefore, presents a unique situation for predicting material interactions that may not be predicted through tradition galvanic measurements or mixed potential theory. So, a primary questions that comes out of this mechanism is whether or not the material interactions can be predicted using computational tools?

The approach taken here, was to predict material interactions by using computational tools to calculate the possible presence of activity gradients between materials potentially submerged in the same salt medium. For this approach, that meant it was necessary to choose materials that would represent material 1 and material 2, as shown in Figure 2-3. Additionally, to simply the

anticipated transport behavior, it was desired to have a reasonable expectation that the elements undergoing transport would primarily come only from material 1 while material 2 would be expected to be inert to the salt medium and provide the avenue for the activity gradient for elements originating from material 1. Finally, all of these assumptions had to be reasonable expected in the salt medium we wanted to work with, FLiNaK. As discussed in previous sections, two elements that are susceptible to dissolution in FLiNaK that have also been shown to exist in multiple oxidation states are Fe and Cr [60, 62, 63, 90]. Because of the large amount of interest in using 316SST in nuclear fluoride salt systems due to it's existing ASME Section III Division 5 code certification, 316SST presented itself as an obvious choice for material 1 in our FLiNaK system as it is an Fe-based alloy with high concentrations of Cr.

Now with material 1 chosen as 316SST, the choice of material 2 will dictate how large of an elemental activity gradient is provided for potential Fe and Cr transportation. Again, as an additional requirement for material 2 it was desired for it be reasonably expected to be more corrosion resistant than 316SST to help lower the chance of introducing other corrosion products that could participate in transportation. To identify possible materials for material 2, HSC Chemistry 7 [19] software was used to calculate the Gibbs free energies of formation for fluoride compounds for all of the elements available in the PanHEA [91] and PanNickel [92] thermodynamics databases. The results of the Gibbs free energy calculations as a function of temperature are shown in Figure 5-1.

Since 316SST was already chosen as material 1, only elements with higher (less negative) free energies of fluoride formation than Fe (solid lines) were considered. With that requirement, the elements left for possible second materials were Sn, Co, Ni, W, Mo, Cu, C, Ag, Pt, and Au. Of these elements, Sn based materials were not considered for material 2 due to the low melting

temperature of Sn (232 ºC) [93]. For the initial computational work on predicting activity gradient mass transportation, C was also excluded. Mass transport involving C will be discussed in Section 5.4. With this initial screening, only Co, Ni, W, Mo, Cu, Ag, Pt, and Au were identified for further consideration of material 2.

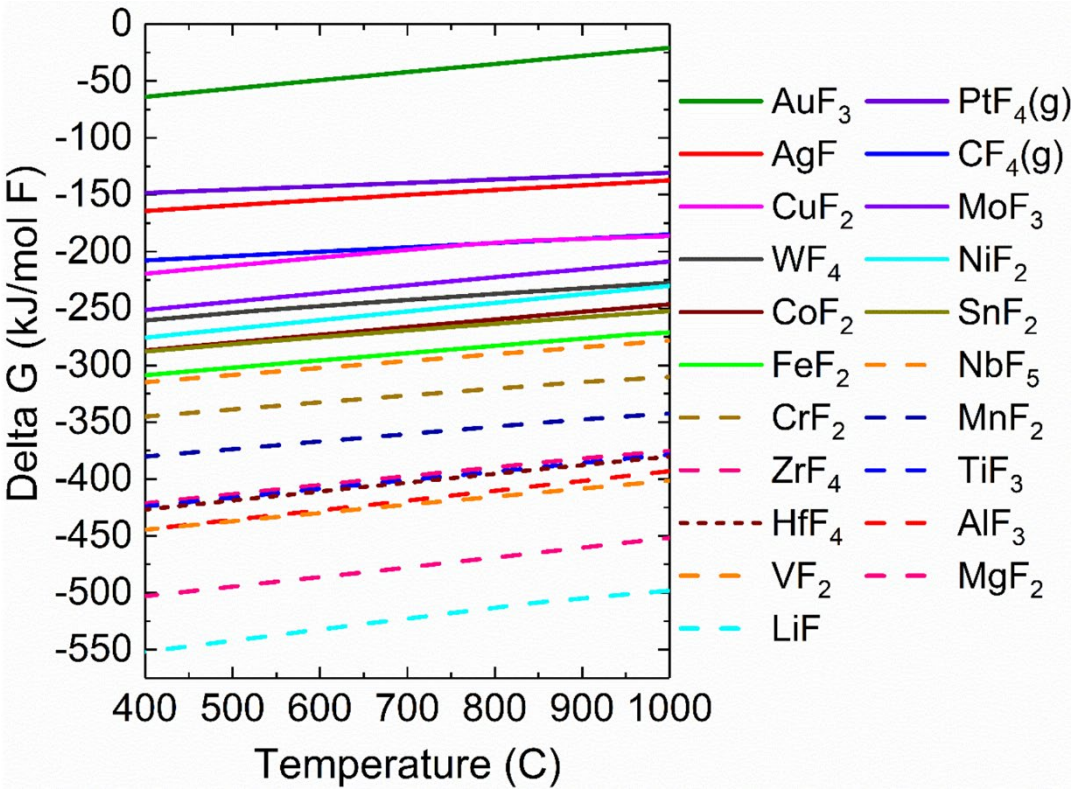

Figure 5-1: Gibbs free energies of fluoride formation for all elements available in the PanHEA and PanNickel thermodynamics databases.

With a set of possible materials for material 2 identified the next step in the approach to predict activity gradient mass transport was to compute the possible presence of activity gradients between the 316SST and the materials identified as material 2. Pandat software [94] was used to calculate the activities of elements in both 316SST and all the possible materials identified as material 2. To perform these calculations, every element must be assigned a reference phase. The reference phases assigned to each element are presented in Table 5-1. First, the activities of the primary alloying elements in 316SST were computed as a function of temperature; the results are presented in Figure 5-2. The activities of the alloying elements mostly follow their weight fraction trend in

316SST. Being that 316SST is an Fe-based alloy, Fe has the highest concentration in 316SST and the highest activity level followed in concentration and activity by Cr. Note that the activity trend for Mo and Ni are opposite of their trend of concentration in 316SST, as Ni has a higher concentration than Mo. This switch in activity trend is a result of Ni having a high solubility in the FCC austenite phase resulting in a low activity level, whereas Mo, which is referenced to its BCC phase, exists in an FCC phase as well as several intermetallic phases in 316SST [76]. As mentioned previously, 316SST was chosen as material 1 because it contains both Fe and Cr which were believed to be the primary elements susceptible to corrosion and transport. For this reason, the activity values of Cr and Fe are of primary concern in determining how large of an activity gradient exists in the presences of material 2. Furthermore, a typical temperature used for static corrosion experiments in salt environments is 700 ºC [50, 95, 96], so the activity levels of Fe and Cr at 700 ºC were recorded as threshold values for evaluating activity gradients, and are equal to 0.72 and 0.55, respectively.

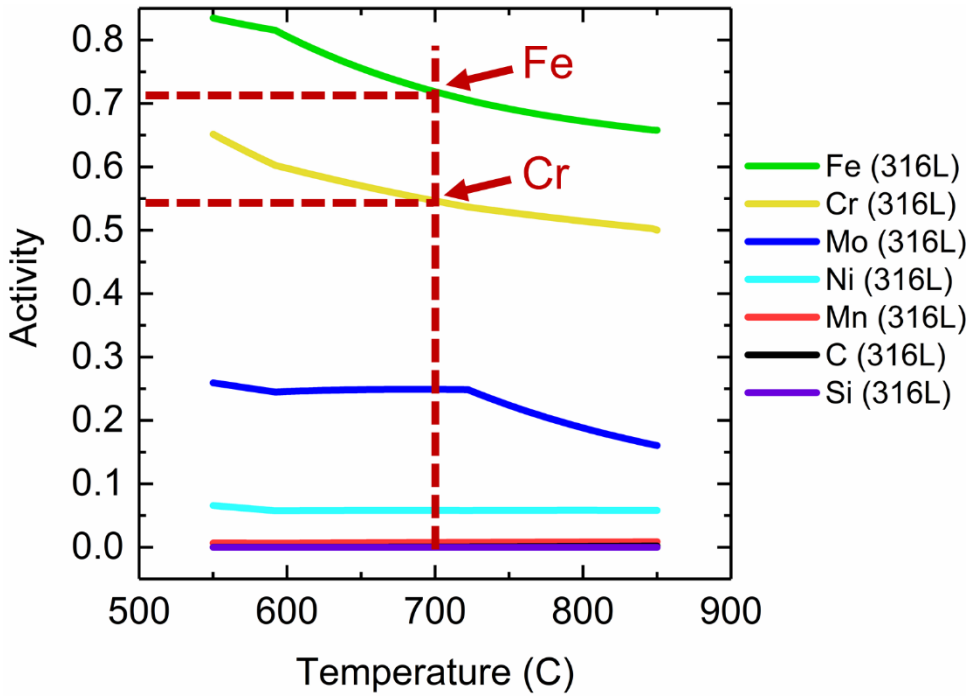

Figure 5-2: Activities of the primary alloying elements in 316LSST as a function of temperature. Computed by Pandat software and the PanHEA Database.

Table 5-1: Reference phases assigned to each element in Pandat software for activity calculations.

Element	Reference Phase
C	Graphite
Cr	BCC
Fe	BCC
Mn	CBCC_A12
Mo	BCC
Ni	FCC
Si	Diamond
Cu	FCC
Zr	HCP
Ti	HCP

As previously discussed in Section 2.3.3, the existence of an activity gradient for mass transport effectively means that an element originating from material 1 can transport to material 2 and exist in material 2 in a non-negligible concentration before that element has the same activity level in material 2 as it had in material 1. So, to determine how large of an activity gradient exists for Fe and Cr in each of the possible materials identified as material 2, the activity of Fe and Cr as a function of increasing concentration were then computed in Co, Ni-201, W, TZM, Cu, Ag, Pt, and Au. Note that Ni-201 was used instead of pure Ni because it is the commercially available form of pure nickel and TZM was used instead of pure Mo as it is a 99.4% pure Mo alloy and is garnering significant interest for use in high-temperature molten salt systems [26, 97].

An example of the activities of Fe and Cr as a function of increasing concentration in Ni-201 are provided in Figure 5-3. The left most data point in each calculation correspond to the nominal composition of Ni-201. As either the concentration of Fe or Cr increases, the concentration of all the other elements in Ni-201 decrease uniformly. Shown in both Figure 5-3a and Figure 5-3b is a dotted line corresponding to the activity levels of Fe and Cr in 316LSST. As the concentration of Fe or Cr increases in Ni-201, their activity levels also increase. The concentration of Fe or Cr at which point the activity of Fe or Cr is equal to that of 316LSST (i.e. where the activity gradient becomes zero) was now treated as the threshold concentration of Fe and Cr in Ni-201. It can be

observed that initially, a large activity gradient does exist for both Fe and Cr migration as Fe and Cr have the potential to reach considerably high concentration in Ni-201 (65 wt% and 25 wt%, respectively) before the activity gradient becomes zero. These concentrations were then treated as threshold concentrations for the degree of the activity gradient. This suggest strongly that both Fe and Cr could undergo significant mass transport if Ni-201 is present in the same FLiNaK medium as 316LSST.

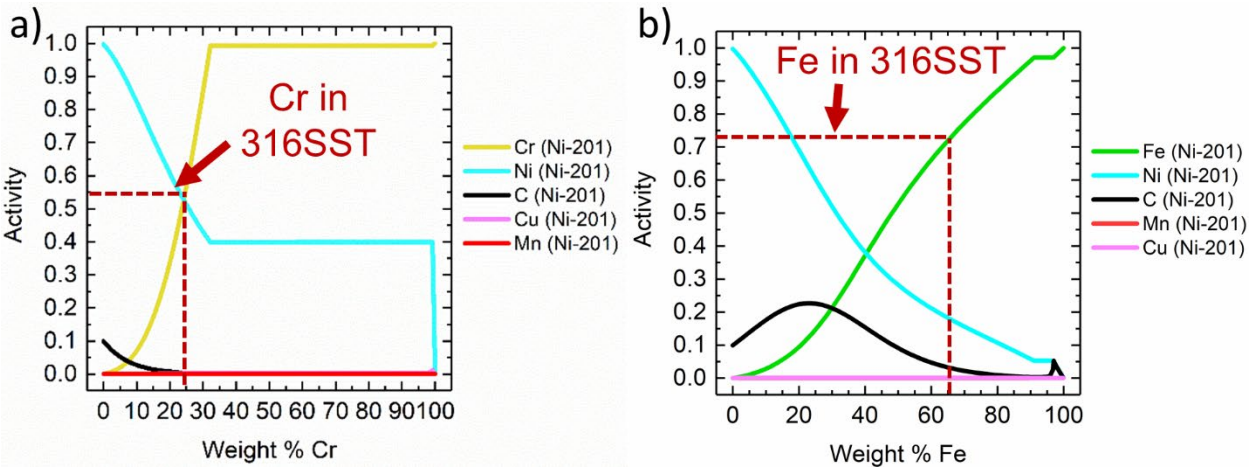

Figure 5-3: Activity of Cr and Fe as functions of increasing weight % in Ni-201. a) Cr, b) Fe.

This same approach for activity modeling of Fe and Cr in all of the possible materials identified as material 2 was performed, and the additional plots can be found in Appendix D. Threshold concentrations of Fe and Cr in Co, Ni-201, W, TZM, Cu, Ag, Pt, and Au are all plotted in Figure 5-4. From these plots of threshold concentration, it can be observed that three different trends for the activity gradient of Fe and Cr exist. First, a large activity gradient for both Fe and Cr is observed if either Ni-201, Co, or Pt are used as material 2. Meaning that significant transport of Fe and Cr would be expected. Second, a large gradient for Fe and a small gradient for Cr exists if either TZM or W are used as material 2. Meaning that Fe transport would be expected, but Cr transport would be much smaller. Lastly, no significant activity gradient exists for either Fe or Cr if Au, Cu, or Ag are present as material 2. Meaning no significant transport of Fe or Cr is expected.

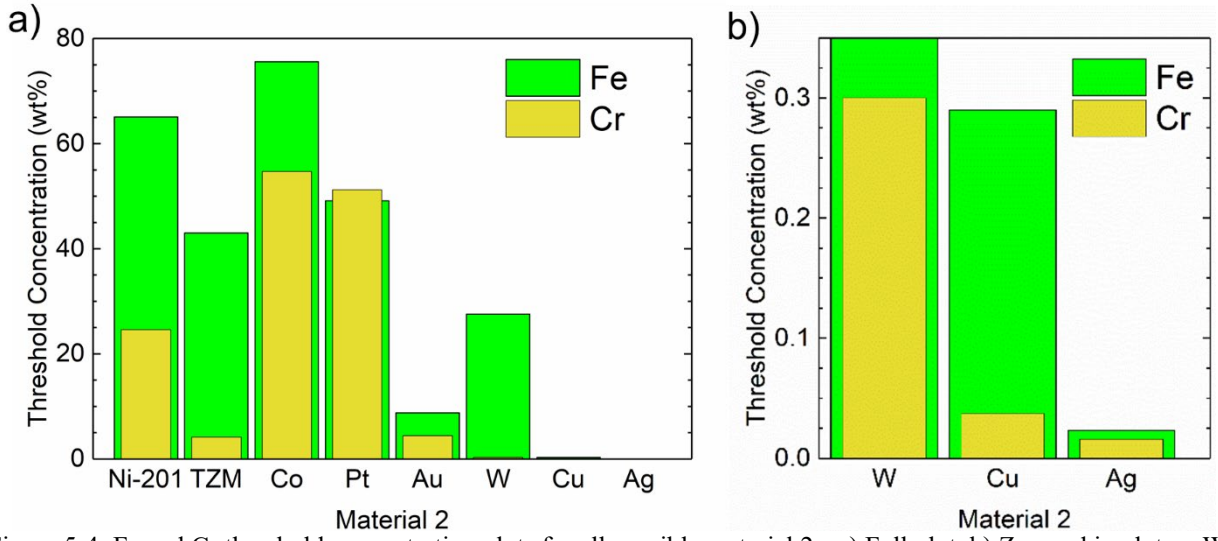

Figure 5-4: Fe and Cr threshold concentration plots for all possible material 2s. a) Full plot. b) Zoomed in plot on W, Cu, and Ag.

5.2 Verification of Computational Predictions

In order to verify the computational predictions presented in Section 5.1, a set of FLiNaK exposure experiments were conducted. Recall from the results presented in Figure 5-4a and b, that the threshold concentrations presented three different trends in the activity gradient behavior for Fe and Cr. In the first case, there is a high activity gradient for both Fe and Cr transport from 316SST if Ni-201, Co, or Pt was present in the FLiNaK salt medium. For this case it was determined that Ni-201 would be used to verify this scenario as commercially pure nickel is receiving interest for use in molten salt applications as a corrosion resistant cladding material, so it's possible that a real reactor condition 316SST/Ni-201 couple could be realized [26, 29, 96, 98, 99]. The second activity gradient scenario showed a high activity gradient for Fe and low gradient for Cr if either TZM or W are used as material 2. TZM was chosen to test this scenario. Similar to Ni-201, TZM materials and coatings have gained a significant interest for use in salt environments [26, 97]. The final activity gradient scenario shown in Figure 5-4 is no significant activity gradient for either Fe or Cr if Cu, Ag, or Au are used as material 2. For this final scenario, Cu was chosen for testing. Simply

from an engineering standpoint, it would be far more likely for Cu to be used in an industrial application than Ag or Au based on cost. Additionally, while the work is limited, Cu has been demonstrated to have good performance as a cladding material for 316SST in FLiNaK [96].

5.2.1 FLiNaK Exposure Testing: Methods

The FLiNaK salt used in the following salt exposures is the same as-received commercial FLiNaK described in Section 3.1.2. Corrosion crucibles for the FLiNaK exposure tests were prepared from 316SST tubing that was 127 mm in length with a 25.4 mm outer diameter and 2.1 mm wall thickness. One end of tubing was sealed by machining a 316SST plug from 25.4 mm diameter round stock which was welded in place using gas tungsten arc welding (GTAW) by the Edison Welding Institute, Columbus, OH. The tubes were backfilled with Ar during the GTAW process to limit oxide formation during GTAW. Welded crucibles were then polished on the inside and outside diameters using abrasive pads to begin removing any trace oxides from the GTAW process. Lastly, the crucibles were sonicated in a mixture of Oakite 33 and deionized water overnight to further remove any residual oxides. A final cleaning with deionized water was performed to rinse out any remaining Oakite 33 and the crucibles were allowed to dry.

The composition of the Ni-201, TZM, and copper alloy C110 are provided in Table 5-2. Ni-201 round bar stock was procured from Corrosion Materials, Houston, TX. Samples with dimensions 19 mm x 9.9 mm x 1.7 mm were then sectioned from the bar stock and two 1.6 mm diameter holes were drilled at the top and bottom of each sample for suspending the samples in FLiNaK salt. TZM sample material was procured from H.C. Stark, Cleveland, OH. The samples were made via arc casting before being cut into 17.8 mm x 10.2 mm x 2 mm samples with two 1.7 mm holes. A 19 mm x 9.5 mm rectangular bar of copper alloy C110 (referred to simply as copper henceworth) was procured from a commercial vendor, and 1.8 mm thick samples were sectioned off using a high-

speed saw. All of the samples were ground to a P4000 grit finish on all faces and edges using SiC abrasive paper followed by a final cleaning in a 50:50 volume mixture of deionized water and acetone. Lastly, the initial masses and dimensions of all samples were recorded before suspending the samples.

Table 5-2: Nominal composition of the Ni-201, TZM, and copper alloy C110 used to make FLiNaK exposure test samples.

Sample Material	Ni	Fe	Cr	Cu	Mo	Zr	Ti	C
Ni-201	99.74	0.007	-	0.011	-	-	0.002	0.016
TZM	-	-	-	-	99.2 min	0.08 max	0.50 max	0.04 max
C110	99.99	-	-	-	-	-	-	-

Units are mass %

Several sets of samples were prepared for salt exposure tests. Two sets of two TZM samples while two sets of three Ni-201 and copper samples were prepared. TZM samples were suspended with pure Mo wire, Ni-201 samples were suspended with pure Ni wire, and copper samples were suspended using copper wire. One set of each sample material was suspended from a 316SST cap so that the samples and the 316SST corrosion crucibles were electrically in contact with each other (i.e. galvanically coupled) while the second set of each sample material was suspended from a boron nitride (BN) cap to electrically isolate the samples from the 316SST corrosion crucible. Photographs of the pre-salt exposure samples as well as a schematic of the corrosion crucible system and sample placement are shown in Figure 5-5. The purpose of testing the sample sets in both direct electrical contact (DC) and electrical isolation was to look at the possible influence the galvanic couple would have between the samples and the 316SST crucible.

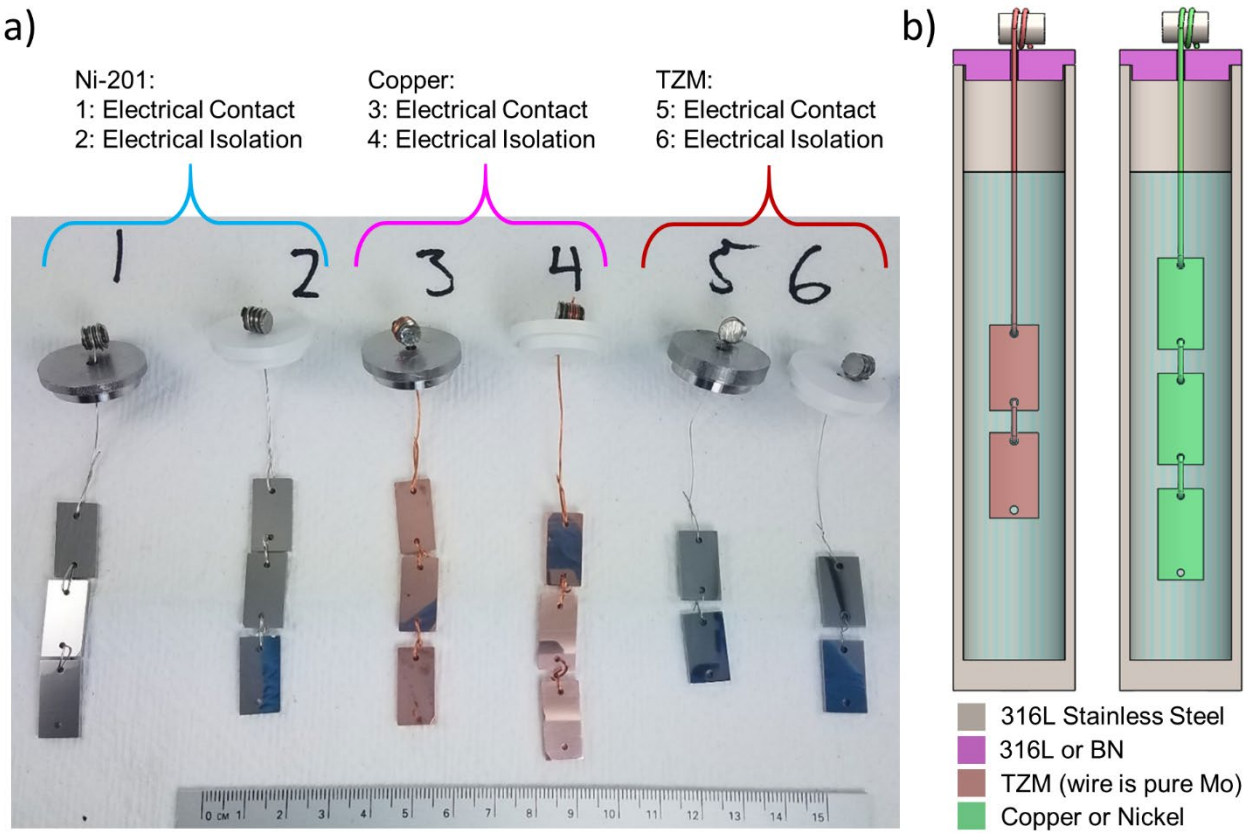

Figure 5-5: Samples pre-FLiNaK exposure and schematic of the corrosion crucible with sample placement. a) Ni-201, copper, and TZM samples suspended from either a 316SST cap for electrical contact with 316SST crucible or suspended from a BN cap for electrical isolation from the 316SST crucible. b) Schematic of the corrosion crucible showing sample placement within the crucible during the FLiNaK salt exposure. Units on scale are in cm.

All of the salt preparation for the FLiNaK exposure test was performed inside the same ultra-high purity argon environment glovebox described in Section 3.1.1. Each of the 316SST corrosion crucibles were filled with approximately 70g of FLiNaK salt. The salt volume was then calculated assuming the FLiNaK density correlation shown in Equation 3-1. Using this correlation and the surface area of the N i-201, copper, and TZM samples, the ratio of FLiNaK volume to the exposed sample surface area was 2.5 cm^3/cm^2 for the Ni-201 and copper sample sets while the TZM samples had a ratio of 3.3 cm^3/cm^2. Additionally, the volume to exposed 316SST crucible surface area was 0.5 cm^3/cm^2.

With the salt loaded in each crucible, the crucibles were placed inside of the glovebox furnace well heated to the test temperature of 700 ºC to allow the salt to melt inside the crucibles. Once the

furnace temperature had reached 700 ºC, the salt temperature was allowed to equilibrate for 6 hrs. After 6 hrs, the corrosion crucibles were lifted out of the furnace while still at temperature, and all samples were quickly introduced to their respective corrosion crucibless by securing the lids to the top of the corrosion crucibles. All corrosion crucibles with samples now submerged in FLiNaK were then lowered back into the furnace. The FLiNaK exposure tests were then conducted at 700 ºC for a duration of 500 hrs.

After 500 hrs, the corrosion crucibles were once again lifted out of the furnace while at 700 ºC. The samples were removed from the FLiNaK salt by lifting the caps off of each corrosion crucible. All samples were then allowed to cool in the argon glovebox atmosphere. Post-corrosion salt samples from all corrosion crucibles were collected by pouring the FLiNaK salt out of each corrosion crucible while near 700 ºC into 304 stainless steel cups. The salt solidified in less than 5 min ensuring that no significant additional corrosion products from the cups were introduced into the post-salt exposure salt samples. In preparation of post-salt exposure analysis, all of the samples were then removed from the glovebox after cooling to room temperature and any residual FLiNaK on the samples was removed by sonicating in a 1 molar $Al(NO_3)_3$ solution followed by ultrasonic cleaning in deionized water and ethanol.

5.2.2 Post-FLiNaK Exposure Sample Analysis

Much of the post-FLiNaK exposure analysis was the same as that described in Section 3.1.3. All of the cleaned post-FLiNaK sample masses were first measured using an electronic balance with a 0.002mg accuracy so that the mass change per area could be calculated with Equation 3-2. The uppermost sample from each crucible was used for XRD. Planar SEM/EDS analysis was also performed on the uppermost sample from each crucible. The bottommost sample from each crucible was mounted and polished in cross-section for SEM/EDS analysis for possible Fe and Cr

transport. For the cross-sectional analysis, the Ni-201 and TZM samples underwent the procedure for electroplated Cu coating described in Section 3.1.3. The two copper samples were not coated before being mounted in cross-section because a Cu coating would interfere with the Cu signal coming from the sample.

X-ray photoelectron spectroscopy (XPS) was performed on the uppermost TZM sample from the two TZM samples sets, while the middle samples from the two copper sample sets were used. XPS measurements were done using a ThermoFisher Scientific K-Alpha XPS equipped with a monochromatic AlK-α x-ray source (wavelength = 8.338 Å [69]) that has a spot size of approximately 400 x 600 μm^2. XPS analysis consisted of a survey scan from 0 to 1100 eV, then a scan over the Cu2p peak range of 925 to 965 eV, Ni2p range of 844 to 884 eV, Fe2p range of 700 to 740 eV, Mn2p range of 633 to 660 eV, Cr2p range of 570 to 595 eV, O1s range of 525 to 545eV, Mo3d range of 222 to 242 eV, and Zr3d range of 174–194 eV. The XPS binding energy scales for the surface scan were corrected by setting the 1 s orbital energy of adventitious carbon to 284.6 eV often used for carbon on metal surfaces [100]. XPSPeak 4.1 software was used for fitting the XPS data [101].

GDOES was performed on the two middles samples from the two Ni-201 sample sets. To generate the plasma for the Ni-201 samples a pressure of 550 Pa and a power of 40 W was used. The system required a new calibration using the sputtering rate correction to accurately run the Ni-201 samples. Calibration was performed with five Ni-based alloys of known compositions. Calibration samples covered concentration ranges of 60-100 wt% Ni, 0-25 wt% Cr, and 0-5 wt% Fe. Certified low and high alloy steels were used to build a calibration curve for the quantification of carbon concentration between 0-2 wt% and to extend the concentration range for accurate Ni and Fe

quantification. Additional information on GDOES calibration for steels and Ni-based alloys can be found in [70].

Post-salt exposure FLiNaK samples that were collected were sent to the WSLH for analysis using ICP-MS. In order to digest the FLiNaK salt for ICP-MS analysis, two acid mixtures are used. Both digestions are aided by a Teflon bomb digestion and use a mixture of nitric and hydrochloric acids. One mixture includes the addition of hydrofluoric acid to aid in the recovery of certain elements. All digestions used approximately 100 mg of FLiNaK.

5.2.3 Result and Discussions from FLiNaK Exposure Testing

ICP-MS was used to observe any changes in the elemental concentrations in the FLiNaK salt both before the salt exposure test and after. The results of the ICP-MS analysis are presented in Table 5-3. The as-received FLiNaK shows low concentrations of all metal impurities. After the 500 hr FLiNaK exposure at 700 ºC, a few changes in the metal impurity concentrations can be noted. As expected from the corrosion of the 316SST crucible, the concentrations of both Cr and Mn increase in the post-salt exposure FLiNaK samples. Both of the these elements have large negative free energies of formation for their respective fluoride compounds, as shown in Figure 5-1, and are known to be elements most susceptible to dissolution in 316SST [84, 95]. Zr and Ti, minor alloying elements in TZM with compositions <0.5 wt%, also have large negative free energies of formation for their respective fluoride compounds [52], but their concentrations in the post-salt exposure FLiNaK samples do not change significantly. The concentration of Fe and Ni in every post-salt exposure FLiNaK sample decreases except in the Ni-201 BN insulated sample. Due to this sample being the only one to show this behavior, this result is mainly contributed to sampling statistics. As mentioned in Section 5.2.2 when sub-sampling the FLiNaK for ICP-MS only 100mg of the total 70g is collected, and the post-salt exposure FLiNaK is likely not to freeze into a homogenous

puck making sub-sampling difficult. Finally, Mo and Cu either remain unchanged or decrease in the post-salt exposure FLiNaK samples.

Table 5-3: ICP-MS results for the as-received FLiNaK and post-salt exposure FLiNaK samples

Sample	Fe	Cr	Ni	Mn	Cu	Mo	Ti	Zr
As-received FLiNaK	15 ± 0.8[a]	3.9 ± 0.2[a]	5.0 ± 0.3[a]	0.5 ± 0.05[a]	0.2 ± 0.02[a]	1.1 ± 0.1[a]	1.2 ± 0.3[b]	1.0 ± 0.08[b]
Ni-201 electrical contact	4 ± 0.3[a]	306 ± 45[a]	0.5 ± 0.08[a]	29 ± 1.6[a]	0.3 ± 0.02[b]	0.04 ± 0.01[a]	3.1 ± 0.4[a]	0.8 ± 0.1[a]
Ni-201 BN insulated	18 ± 0.8[a]	307 ± 32[a]	11 ± 1[a]	24 ± 1.1[b]	0.2 ± 0.01[a]	0.9 ± 0.1[a]	2.6 ± 0.2[a]	0.8 ± 0.08[b]
TZM electrical contact	3.5 ± 0.2[a]	317 ± 33[b]	0.2 ± 0.04[a]	22 ± 0.9[b]	0.09 ± 0.02[a]	0.08 ± 0.02[a]	0.7 ± 0.1[a]	0.6 ± 0.06[b]
TZM BN insulated	2.6 ± 0.2[a]	331 ± 49[a]	0.2 ± 0.04b	25 ± 1.4[a]	0.1 ± 0.01[b]	0.08 ± 0.02[a]	1.3 ± 0.1[a]	0.7 ± 0.1[a]
Copper electrical contact	4.1 ± 0.2[a]	257 ± 27[b]	0.3 ± 0.04[a]	19 ± 0.8[a]	0.4 ± 0.03[a]	0.1 ± 0.02[a]	0.9 ± 0.08[a]	1.5 ± 0.1[a]
Copper BN insulated	10.6 ± 0.5[a]	269 ± 28[b]	0.2 ± 0.03[a]	21 ± 0.9[b]	1.3 ± 0.07[a]	0.06 ± 0.01[a]	12 ± 0.7[b]	0.7 ± 0.07[b]

Units are µg/g (wt ppm)

[a]Result comes from digestion without HF acid

[b]Result comes from digestion with HF acid

As a first assessment of mass transport, all post-salt exposure sample masses were recorded. The change in sample mass per unit area was then calculated and the results are shown in Figure 5-6. Note, that because the sample materials chosen for material 2 in this FLiNaK exposure test are expected to be more corrosion resistant than the 316SST corrosion crucible used as material 1, a sign of mass transport of either Fe or Cr from the 316SST crucible to the samples would be mass gain (i.e. positive values of mass change). As seen in Figure 5-6 both of the Ni-201 and TZM sample sets gained mass after the FLiNaK exposure, indicating Fe or Cr has transported to these samples. Both copper sample sets show no change in their masses after FLiNaK exposure. A single

sample from each copper sample set showed some possible change in mass and these are plotted separately; their masses are also not included in the average calculation or standard deviation.

Several important first observations about mass transport can be noted from the mass change results. First, it can be seen that the mass gain in the electrical contact and the BN insulated sample configurations for the Ni-201 (1.12 ± 0.04 mg/cm^2 and 1.26 ± 0.06 mg/cm^2, respectively), copper (-0.005 ± 0.005 mg/cm^2 and -0.01 ± 0.002 mg/cm^2, respectively), and TZM (0.15 ± 0.002 mg/cm^2 and 0.15 ± 0.001 mg/cm^2, respectively) sample sets are the same. This result is the first indication that galvanic contact between material 1 and material 2 does not influence the mass transport behavior. Secondly, the mass change data also gives a first indication that the predictions from the activity gradient calculations are accurate. The activity gradient calculations predicted a large gradient for Fe and Cr in the case of Ni-201, suggesting a high degree of mass transport. TZM was predicted to only have a moderate gradient for only Fe, suggesting mass transport would occur, but to a lesser degree than Ni-201. Finally, copper was predicted to be both corrosion resistant to FLiNaK based on the formation energy of copper fluoride, see Figure 5-1, and provide no activity gradient for either Fe or Cr, suggesting that these coupons should show little corrosion attack and no mass transport.

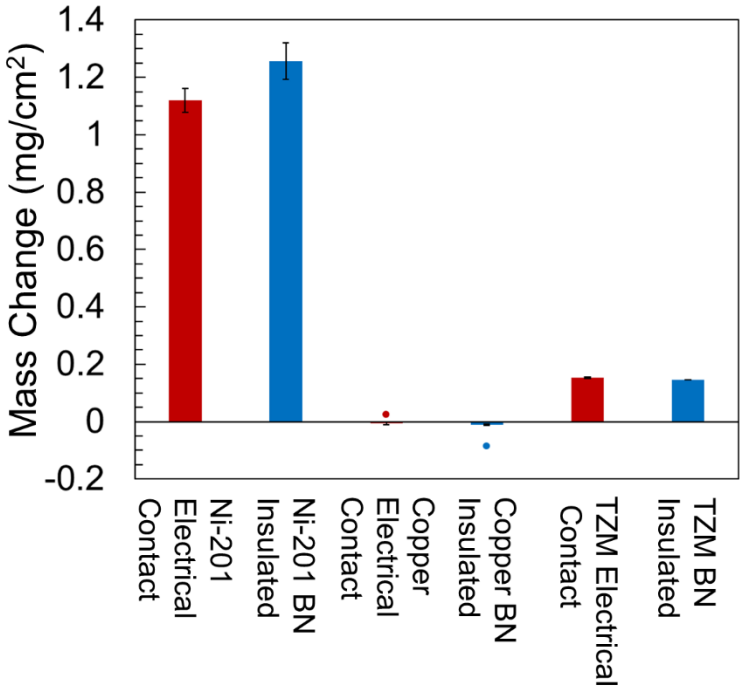

Figure 5-6: Post-salt exposure mass change results for the Ni-201, copper, and TZM sample sets. Error bars are standard deviations between samples in the same set.

To look for any signs of different phase formations or changes in the surface region after FLiNaK exposure, XRD analysis was used and is presented in Figure 5-7. In Figure 5-7a, possible minor peaks in the low 2θ values appear to correspond to a Cr_7C_3 (PDF #00-036-1482) phase. As shown in the material specification table (Table 5-2), Ni-201 does not contain Cr originally, so for there to be carbide formation, Cr would have to transport from the 316SST crucible. Additionally, as mentioned in Section 5.2.1 the Materion FLiNaK was prepared in graphite crucibles. ICP-MS is not able to determine carbon concentration, but it's within reason to believe the salt would contain an elevated concentration of carbon and therefore could be the carbon source for carbide formation. Also seen in Figure 5-7a, there appears to be two ordered FCC phases now in the near surface region of both Ni-201 samples. At low 2θ values (see Figure 5-7b for zoomed in window), the (111) and (200) peaks show a shift towards lower 2θ values as compared to the reference Ni-201 sample. Additionally, the (220), (311) and (222) peaks show a separation into two separate peaks labeled Ni FCC and Ni-Fe-Cr FCC. The Nelson-Riley function [102] was used to calculate the

lattice parameter of both apparent FCC phases present. From the Ni FCC peaks, the lattice parameter calculated for both the electrical contact and BN insulated samples was 3.52 Å which is only slightly below the lattice parameter for the Ni reference sample of 3.53 Å. The shift in the (111) and (200) peaks to lower 2θ values as well as the separation of the (220), (311), and (222) peaks is likely a result of the original Ni lattice expanding due to Fe and Cr migration and diffusion into both Ni-201 samples. The Nelson-Riley analysis on the Ni-Fe-Cr peaks shows that the lattice parameter of this phase is 3.54 Å and 3.55 Å for the BN insulated and electrical contact sample, respectively. Further discussion on why the XRD spectrums show both the Ni-Fe-Cr and Ni FCC peaks are presented along with the SEM/EDS analysis below.

The XRD analysis on the TZM samples in Figure 5-7c shows that the original Mo BCC peaks are still present as well as several new phases. Nelson-Riley analysis on the Mo BCC peaks from the reference TZM sample as well as from both the electrical contact sample and the BN insulated sample shows the Mo BCC phase has a lattice parameter of 3.15 Å before and after the FLiNaK exposure. The new peaks in the electrical contact and BN insulated TZM samples are consistent with each other. Again, indicating the galvanic contact has little significance on mass transport and phase formation. Several of the new peaks in the XRD spectrums were matched to a M_6C phase (PDF #01-083-3017) with a stoichiometry of Fe_3Mo_3C. At least two of the new peaks did not match the M_6C peaks from the database and are marked as not identified in Figure 5-7c. According to the binary phase diagram of Fe and Mo, two possible intermetallic compounds between Fe and Mo are possible at the salt exposure temperature of 700 ^oC [103]. The database used for peak matching only contained information on the μ-phase (Fe_3Mo: PDF #00-031-0641). This stoichiometry of the μ-phase did match one of the unidentified peaks. In addition, α-Mo_2C (PDF #00-035-0787) appeared to match both of the unidentified peaks.

Figure 5-7d shows the XRD spectrums of the copper samples as well as the copper reference sample, and shows no changes in the phases in the near surface region post-salt exposure. The Nelson-Riley analysis also shows that the pre and post-salt exposure lattice parameters do not change as the Cu FCC phase maintains a lattice parameter of 3.62 Å. However, after being exposed to the salt exposure temperature of 700 ^{o}C for 500 hrs, the electrical contact and BN insulated samples show a clear sign of grain growth. This is evident by the preferential diffraction and suppression (see for instance the (200) relative to the (111) peak intensities) of characteristic FCC peaks. A 2mm diameter collimator was used during the XRD scan without sample rotation, which may explain why a more random distribution of diffracted grains is not observed.

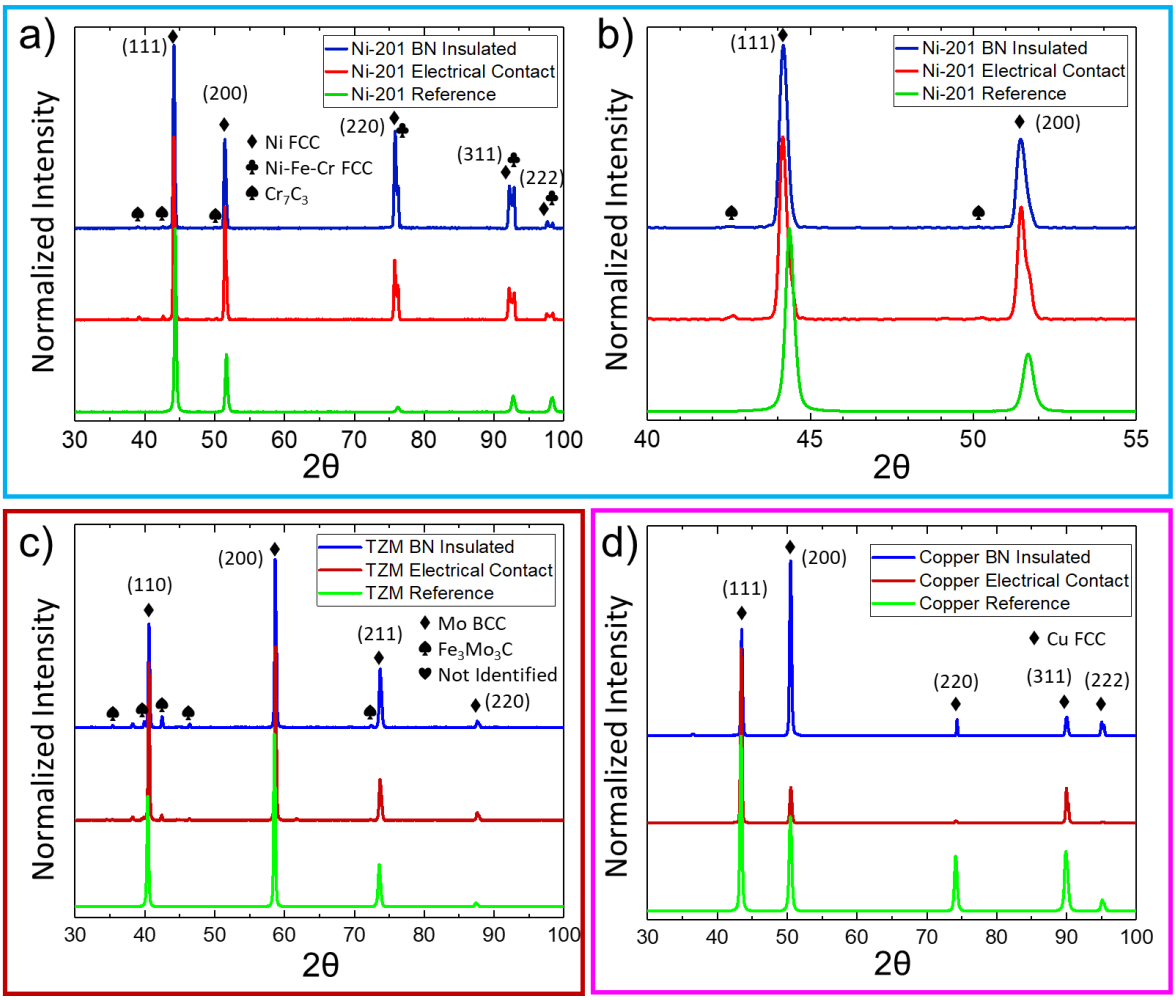

Figure 5-7: XRD patterns from all sample sets with their respective reference samples. a) Ni-201 full XRD spectrum. b) Ni-201 zoom in on (111) and (200) FCC peaks. c) TZM full spectrum. d) Copper full spectrum.

SEM/EDS analysis was performed on all samples including both planar and cross-sectional analysis. The SEM/EDS results for the Ni-201 samples in electrical contact with and BN insulated from the 316SST crucible are presented in Figure 5-8. Figure 5-8a and c shows that both of the post-salt exposure Ni-201 sample sets are covered in a "web" structure that is rich in Cr and deficient in Ni. The pre-salt exposure Ni-201 does not contain Cr so this Cr rich structure must form from Cr mass transport from the 316SST corrosion crucible. Furthermore, it is suspected that this Cr-rich "web" is the chromium carbide that is seen in the XRD patterns in Figure 5-7.

Similarly to the planar analyses, the cross-section of the Ni-201 sample in electrical contact with and the sample BN insulated from the 316SST crucible shown in Figure 5-8b and c, respectively, show the Fe and Cr mass transport behavior is almost identical regardless of the electrical configuration. In both samples it can be seen that the near surface region is now rich in both Fe and Cr and both samples show a similar Cr-rich film directly on the sample surfaces. The Cr-rich film likely corresponds to the "web" structure seen in the planar analysis. Additionally, both Fe and Cr have diffused into both Ni-201 samples. Fe especially, appears to have transported from 316SST and diffused into the Ni-201 to a rather significant degree with the diffusion depth reaching approximately 16 μm and 19 μm in the electrical contact and BN insulated samples, respectively. The surface concentrations of Fe in both samples is also rather large, reaching 12 wt% in the electrical contact sample and 14 wt% in the BN insulated sample.

Clearly observed in the cross-section analysis of both samples is that the near surface region of both Ni-201 samples has essentially become a ternary mixture of Ni-Fe-Cr grading down to the original commercially pure Ni concentration of Ni-201 at greater depths. This result would explain the peak separation observed in the XRD patterns in Figure 5-7a. The Ni-Fe-Cr mixture in the surface region would introduce strain in the FCC lattice resulting in the slightly lower 2θ shifted

(220), (311), and (222) peaks. At low 2θs the CuK-α x-rays have lower penetration depth into the sample so only the shifted (111) and (200) peaks are observed, but at higher 2θ values the CuK-α x-rays have a higher penetration depth that reaches both the Ni-Fe-Cr ternary FCC and Ni FCC regions making both peaks appear in the XRD spectrum.

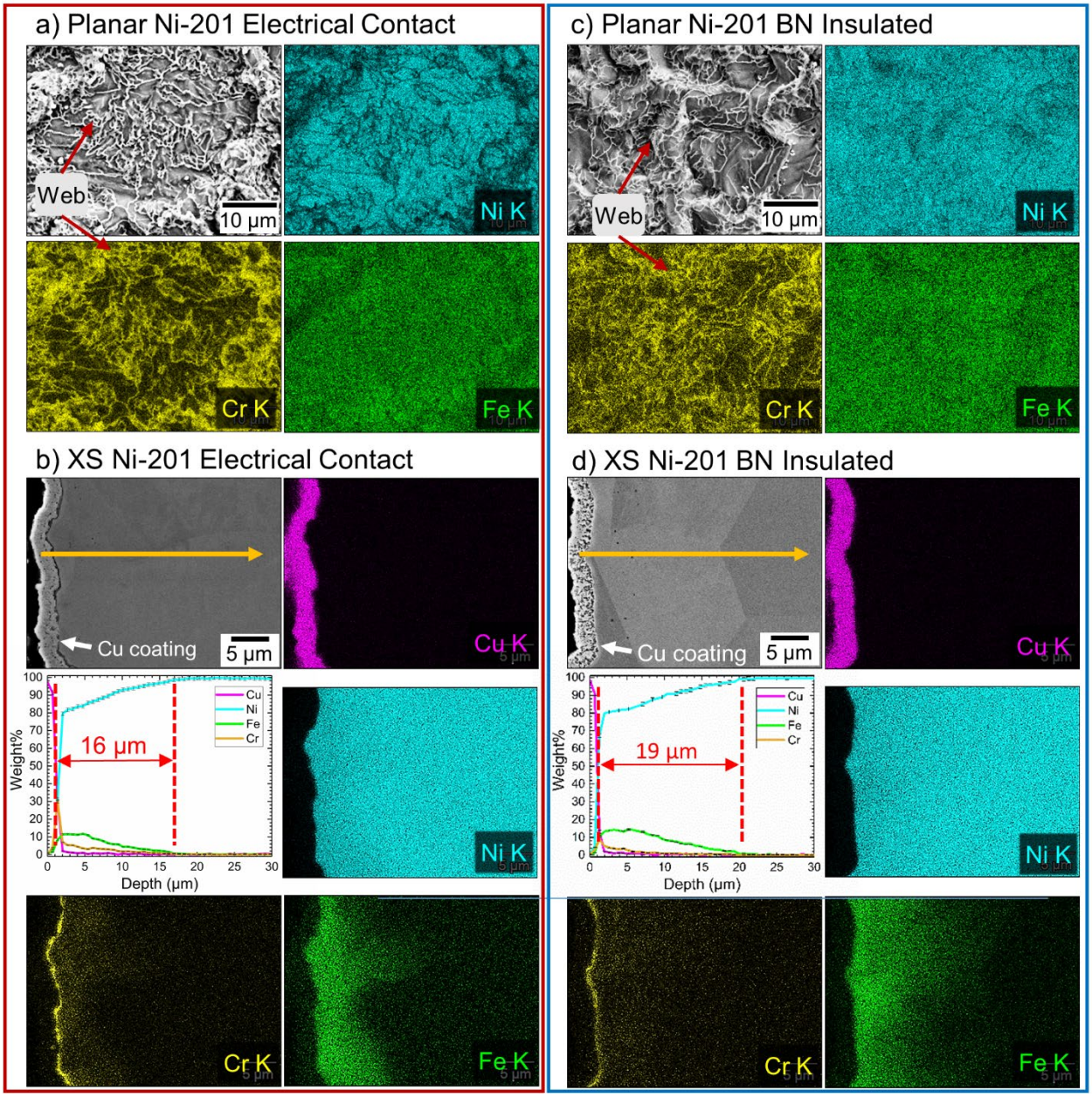

Figure 5-8: SEM/EDS analysis of Ni-201 samples. a and c) Planar analysis on the electrical contact and BN insulated samples, respectively. b and d) cross-sectional (XS) analysis on the electrical contact and BN insulated samples, respectively. Note that the Cu coating in the cross-section samples was added post-salt exposure for edge retention during metallographic preparation.

SEM/EDS results for the TZM sample in electrical contact with and BN insulated from the 316SST crubiles are presented in Figure 5-9. Additionally, point EDS analysis was performed on the planar samples and is presented in Table 5-4; the point locations correspond to the yellow markers in the planar SEM images in Figure 5-9a and c. From the planar analysis in both the electrical contact and BN insulated TZM samples, it can be observed that post-salt exposure the samples are now decorated with a thin film of nanometer-sized precipitates as well as "bare" regions were the precipitates have not covered. These precipitates are believed to be the carbide phase that appears in the XRD measurements shown in Figure 5-7b. Due to the size of the precipitates and the interaction volume of a 20kV electron beam with the TZM samples, true quantitative measurements of composition in the precipitate region and "bare" region are not possible. However, qualitatively the concentration of elements in the regions with a high-density of precipitates (points 1, 2, 5, and 6 in Table 5-4) appear to have elevated concentrations of both Mo and Zr while the "bare" regions have elevated concentrations of both Fe and Cr.

The cross-section of both the electrical contact and BN insulated TZM samples shown in Figure 5-9b and d, shows that no matter the electrical configuration, the mass transport behavior is essentially the same. As predicted by the activity calculations, the transport of Fe is much more substantial than the transport of Cr. In the secondary electron image of both cross-sections, a thin layer with a faint change in contrast can be seen between the Cu coating and the bulk TZM samples. The EDS mapping and line scans show that in both the electrical contact and BN insulated samples, that this thin layer is primarily enriched in Fe with only a faint signal of Cr. From the line scans, it can be observed that the Fe and Cr only exists in the thin layer, and further diffusion into the TZM samples is not observed. Again, the thin layer likely corresponds to the carbide phase and possible intermetallic phase seen in the XRD spectrums in Figure 5-7b. Because of the lack of

diffusion of Fe and Cr into the TZM sample, this carbide/intermetallic layer may act as an effective diffusion barrier for both Fe and Cr.

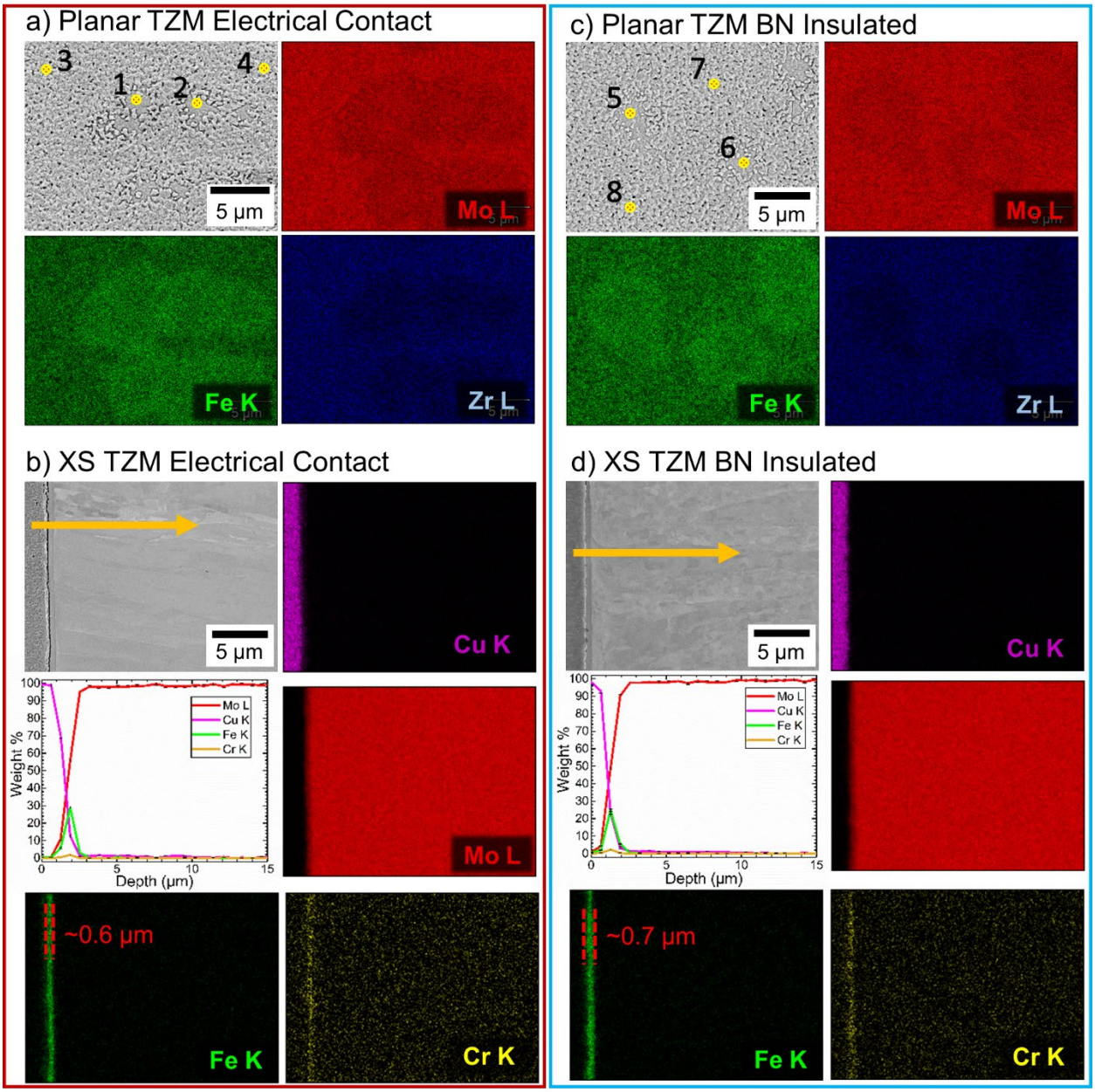

Figure 5-9: SEM/EDS analysis of TZM samples. a and c) Planar analysis on the electrical contact and BN insulated samples, respectively. b and d) XS analysis on the electrical contact and BN insulated samples, respectively. Note that the Cu coating in the XS samples was added post-salt exposure for edge retention during metallographic preparation.

Table 5-4: EDS point analysis performed on the planar TZM samples. Point correspond to those labeled in Figure 5-9a and c.

Point	Cr K	Fe K	Ni K	Zr L	Mo L
TZM Electrical Contact					
1	4.45 ±0.21	42.33 ±0.46	0.20 ±0.16	1.11 ±0.09	51.46 ±0.31
2	4.16 ±0.21	42.05 ±0.46	0.26 ±0.16	1.11 ±0.09	51.97 ±0.31
3	3.73 ±0.23	38.90 ±0.49	0.00 ±0.00	1.65 ±0.22	55.19 ±0.40
4	3.60 ±0.13	37.54 ±0.49	0.11 ±0.18	1.59 ±0.23	56.73 ±0.41
TZM BN Insulated					
5	3.51 ±0.22	38.23 ±0.48	0.34 ±0.17	1.36 ±0.10	56.09 ±0.34
6	3.91 ±0.22	38.55 ±0.47	0.10 ±0.17	1.33 ±0.10	55.54 ±0.34
7	3.83 ±0.23	36.87 ±0.49	0.00 ±0.14	2.31 ±0.23	56.67 ±0.41
8	3.24 ±0.24	35.93 ±0.50	0.24 ±0.18	2.24 ±0.24	58.11 ±0.42

Reported units are in atomic %

The SEM/EDS analysis on both of the electrical contact and BN insulated copper samples presented in Figure 5-10 showed little to no evidence of significant mass transportation of either Fe or Cr from the 316SST crucibles, which corresponds well with the little to no mass change seen in Figure 5-6. Planar SEM/EDS analysis on the copper samples showed similar results for both samples. In both samples, it can be seen that the post-salt exposure surfaces are now decorated with large globular-shaped particles. These large globules are only present in small patches throughout the surfaces and appear to be enriched in both Fe and Cr. However, the particles also do not appear to be fully embedded in the copper sample suggesting that they may have come to be present during the salt cooling process at the termination of the FLiNaK exposure. Further evidence of this is seen in the potassium map, where a rich potassium particle can be observed. This particle clearly exists on the copper surface and comes from the salt that was not washed off during the post-salt exposure cleaning process.

Cross-sectional analysis on both of the copper samples was performed, but showed only pure Cu in the cross-section, so the data was not presented here. The cross-section data can be found in Appendix E. To look at elements with lower concentrations than what can be reliably determined with EDS, XPS analysis was utilized. Figure 5-10c shows the XPS spectra collected on the post-salt exposure samples as well as a reference copper sample that was not exposed to FLiNaK salt. The surface signal is primarily dominated by Cu and shows some signs of Cu oxidation after salt exposure and sample cleaning in 1M $Al(NO_3)_3$. Scans over the *Mn2p* and *Fe2p* binding energy ranges show that the relative intensities in the peaks do not change post-salt exposure suggesting that the concentrations of both elements have not changed, meaning no transport of Mn or Fe has occurred between the 316SST crucibles and copper samples. Additionally, the scan over the *Cr2p* binding energy range also shows that no transport of Cr has occurred. The peak observed at the binding energy of 570 eV is characteristic of the *CuLMM* peak and comes from the copper sample [104, 105]. Once again, regardless of the electrical configuration of the copper samples with respect to the 316SST crucible, the SEM/EDS and XPS analysis shows that very limited to no mass transport of Fe or Cr has occurred for the copper samples post-salt exposure. All of which was predicted by the activity calculations in Section 5.1.

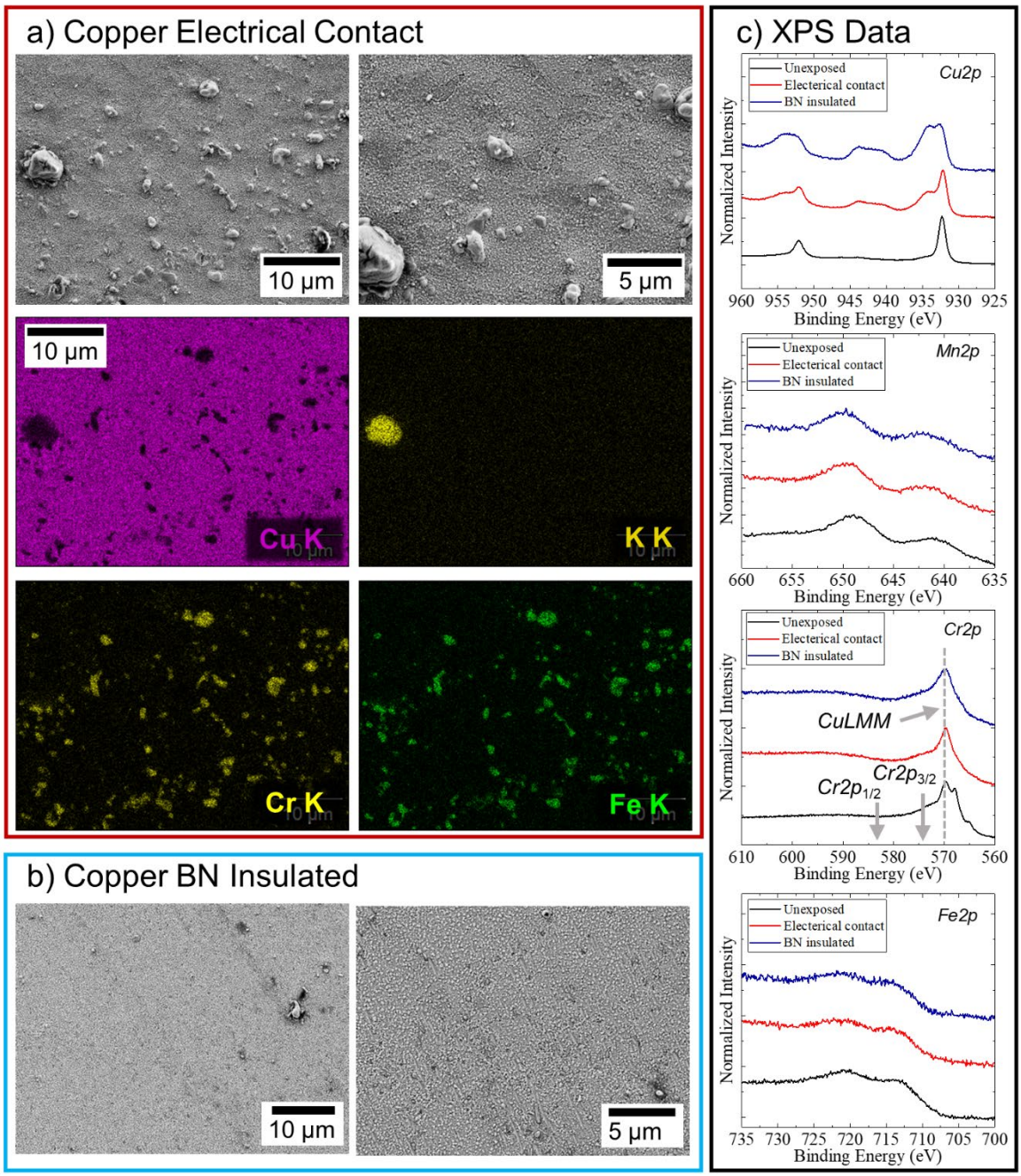

Figure 5-10: SEM/EDS and XPS analysis of the copper samples. a) Planar SEM images with EDS maps corresponding to the top left SEM image for the copper sample in electrical contact with the 316SST crucible. b) Planar SEM images of the BN insulated sample. c) XPS binding energy plots from both copper samples plotted with reference data collected on a copper sample that was not exposed to FLiNaK at 700 °C for 500 hrs.

The results presented here clearly demonstrate that the mass transport behavior of Fe and Cr from the 316SST corrosion crucible do not depend on the electrical configuration of the corrosion system. In all cases, the electrical contact samples showed identical transport behavior to the BN insulated samples. Furthermore, the results on the Ni-201, TZM, and copper samples validate the

activity gradient calculations presented in Section 5.1 and show the calculations accurately predicted the mass transportation behavior of the Fe and Cr. Ni-201 was chosen as a sample material, because activity gradient calculations predicted that there would be a high degree of mass transport of both Fe and Cr. This transport was clearly shown to have occurred in the SEM/EDS analysis shown in Figure 5-8. TZM samples were chosen so that only Fe was targeted for transport. The activity calculations showed that TZM presented a large activity gradient for Fe and no significant gradient for Cr. Once again, Figure 5-9 clearly demonstrates that Fe was selectively transported from 316SST while Cr transport was drastically reduced. Finally, from the activity calculations, copper was predicted to present no significant gradient for either Fe or Cr, and the mass change data along with the SEM and XPS data in Figure 5-10 shows that no Fe or Cr was transported.

5.3 Effect of Activity Gradient Transport on the Corroding Alloy

The validation experiments for the activity gradient mass transport predictions presented in Section 5.2 clearly demonstrated that the mass transport behavior of Fe and Cr could be accurately predicted through activity calculations and that the transport behavior is not affected by the electrical configuration. However, the experiments only showed how the mass transport of Fe and Cr would affect the material that Fe and Cr is transporting too. For example, the near surface region of Ni-201 clearly becomes a ternary mixture of Ni-Fe-Cr due to transport, TZM develops a thin surface film rich in Fe that could act as a diffusion barrier, while copper shows no interaction with Fe and Cr. The validation experiments did not show how the stainless steel material is affected by the presence of the activity gradients or the electrical configuration of the dissimilar material couple. The experiment presented in this section intends to take the information on Fe and Cr

transport behavior and determine what effect the activity gradient as well as the electrical configuration has on the corrosion of the stainless steel material.

From the validation experiment in Section 5.2, the two most dramatic activity gradient scenarios (i.e. dissimilar material couples) were created when Ni-201 or copper was present in the same FLiNaK salt with stainless steel. The Ni-201 created a large activity gradient for the mass transport of both Fe and Cr, while the copper presented no gradient for either Fe or Cr. To see how this affects the stainless steel material, the corrosion crucible setup in Figure 5-5b needs to be reversed. Additionally, electrochemical measurements were introduced to investigate the effect of the direct contact and BN insulated configurations.

5.3.1 Methods

The salt used in the following experiments is the same salt as described in Section 3.1.2. All of the electrochemical measurements were performed at 700 ^{o}C inside of a Thermolyne bench top muffle furnace located inside of an ultra-high purity argon atmosphere glovebox. A schematic of the muffle furnace is shown in Figure 5-11a [106]. The top of the muffle furnace has three penetrations through it that allow electrodes to be passed into the furnace. The temperature is controlled by the furnace's own PID controller. A glassy carbon crucible was used during all measurements to contain the FLiNaK salt. All connections to the electrodes are done using alligator clips carefully positioned so that the electrodes do not touch one another as shown in Figure 5-11b.

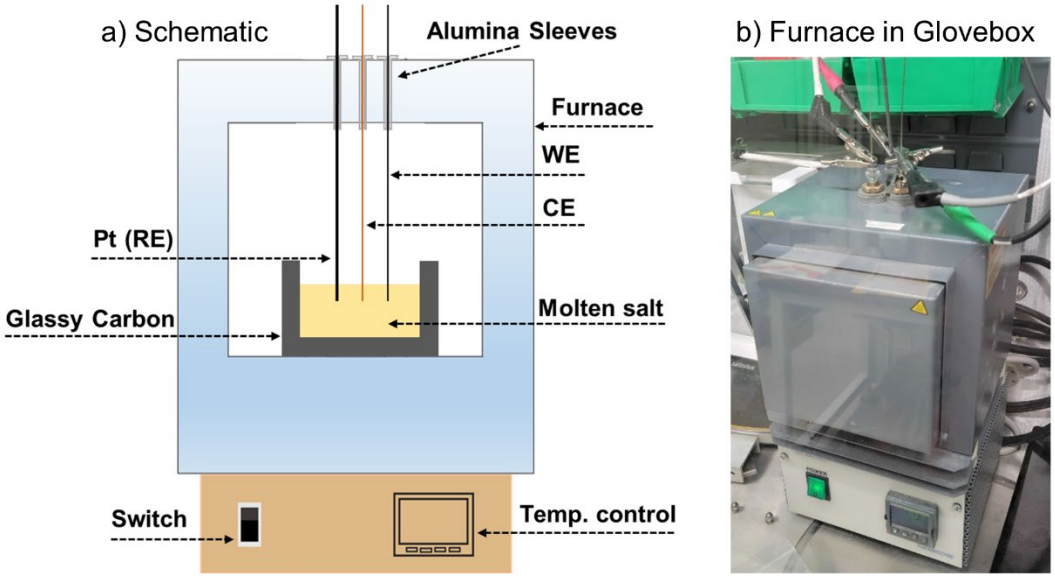

Figure 5-11: Electrochemical furnace for potentiodynamic polarization and ZRA measurements. a) Schematic of the furnace. b) Photograph of the furnace inside the argon atmosphere glovebox.

Electrochemical measurements required several material forms to construct electrodes suitable for both potentiodynamic polarization (polarization) and zero-resistance ammeter (ZRA) measurements. A schematic of the electrode setup for the polarization measurements is shown in Figure 5-12a. For polarization measurements, 3.2 mm diameter stainless steel 304 (304SST), commercially pure Cu, and pure Ni rod electrode materials were procured. In the polarization measurements, the 304SST, Cu and Ni electrodes acted as the working electrodes (WE) while a 3.2 mm diameter graphite rod served as the counter electrode (CE). A 1 mm diameter pure Pt wire was used as a quasi-reference electrode (RE). To keep all of the electrodes isolated from the furnace, electrodes were sheathed in alumina single bore tubes.

ZRA measurements were performed using the electrode configuration shown in Figure 5-12b. Electrodes were made out of 1 mm diameter pure copper, pure nickel, and 304SST wires. Based on the free energy of formation for copper, nickel, iron, and chromium fluoride compounds shown in Figure 5-1 and previous research [54, 96], it was hypothesized that the copper or nickel electrode would act as the cathode as both Cu and Ni are resistant to corrosion in fluoride salts while 304SST

would act as the anode during the ZRA measurements. To increase the surface area of the copper and nickel cathodes, the wires were bent around a #10 sheet metal screw to create a uniform coil. The 304SST was used as a straight wire. This coiled electrode setup provided either a copper or nickel cathode surface area that was approximately six times greater than the 304SST anode surface area. The copper or nickel coil electrode and the 304SST electrode were sheathed in a double bore alumina sleeve to electrically isolate them from the one another and the furnace. Once again, 1 mm diameter Pt wire was used as a quasi-reference electrode, but it is not shown in Figure 5-12b.

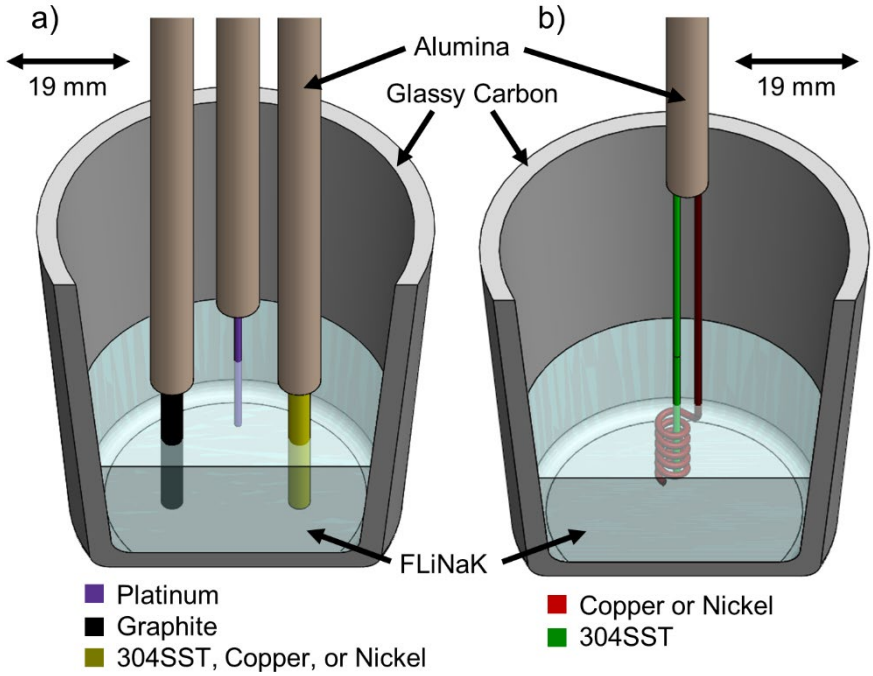

Figure 5-12: Schematics of the electrochemical electrode configurations. a) Electrode configuration for polarization measurements where the CE is graphite, the RE is Pt, and the CE is either 304SST, copper, or nickel. b) Electrode configuration for ZRA measurements where the 304SST wire is connected to the WE, the copper or nickel coil is connected to ground, and not pictured, the Pt wire is connected to RE.

The polarization and ZRA measurements were performed using a Princeton Applied Research VersaSTAT 3F potentiostat. For the polarization experiments, the open circuit potential (OCP) versus the Pt quasi-reference was measured for 500 seconds before the polarization to determine the appropriate polarization window. The polarization window was then set to approximately -300

mV to +200 mV of the measured OCP at a scan rate of 5 mV/s. ZRA measurements were performed by using the Pt quasi-reference electrode and connecting the 304SST electrode to the WE and the copper or nickel coil to the ground electrode. With the VersaSTAT 3F this creates a direct connection between the 304SST and either the copper or nickel coil through a "0" resistance wire so that any measured current is the coupled galvanic current between the two materials. The ZRA was then set to record for one hour.

In addition to the electrochemical measurements, FLiNaK exposure tests were also performed. In these salt exposure tests, the material setup from the validation experiments was reversed. Coupon samples of 304SST were prepared from 1.5 mm thick sheet using wire EDM by Xact Wire EDM Corporation, Waukesha, WI. The coupons were wire EDM'd to dimensions of 19 mm x 9.5 mm and the nominal composition of the 304SST sheet used to make samples is provided in Table 5-5. To prepare the sample coupons for salt exposure tests, the coupons were ground on all faces and edges using P4000 grit SiC paper followed by a final cleaning in isopropyl alcohol.

Two copper and nickel salt crucibles were prepared using copper alloy C101 (copper) and nickel 200/201 (nickel). Material specification on the copper and nickel are provided in Table 5-5. The capsules were machined from 25.4 mm diameter solid round bar stock. Multiple 152.4 mm long pieces were cut from the copper and nickel bar stock and 21 mm diameter holes were bored out of the bar stock to a depth of 146 mm using conventional machining techniques. All machining was performed by the University of Wisconsin-Madison Physics Instrument Shop. After machining, the crucibles were cleaned by lightly polishing them with a SiC Scotch-Brite pad on the outside and inside diameters. Following the polish, each crucible was sonicated in acetone followed by ethanol.

Table 5-5: Nominal composition of the 304SST sheet used to make samples and the copper and nickel bar stock used to make salt crucibles.

Material	Weight %						
	Fe	Cr	Ni	Cu	Mn	Mo	C
304 Stainless Steel	Balance	18.18	7.93	--	1.58	0.31	0.05
Nickel 200/201	0.24	--	Balance	0.008	0.084	--	0.01
Copper C101	--	--	--	>99.99	--	--	

Similar to the activity gradient mass transport validation experiments, two 304SST sample configuration were tested in each crucible material and each sample string contained three 304SST samples. One 304SST sample string in a copper crucible and one 304SST sample string in a nickel crucible used a stainless steel cap so that the 304SST samples and either the copper or nickel crucible were in electrical contact with each other while the other sample string used a BN cap to keep the 304SST samples electrically isolated from the copper or nickel crucible. Again, the purpose of the two sample configurations was to investigate the effect that a galvanic couple may have on the corrosion behavior of the 304SST samples. If 304SST truly acts an anode material when it is electrically connected to copper or nickel, there should be a measureable difference in the corrosion behavior between the electrical contact and BN isolated sample strings. A photograph of the sample strings, corrosion crucibles, and a schematic of the corrosion crucible with sample placement are provided in Figure 5-13.

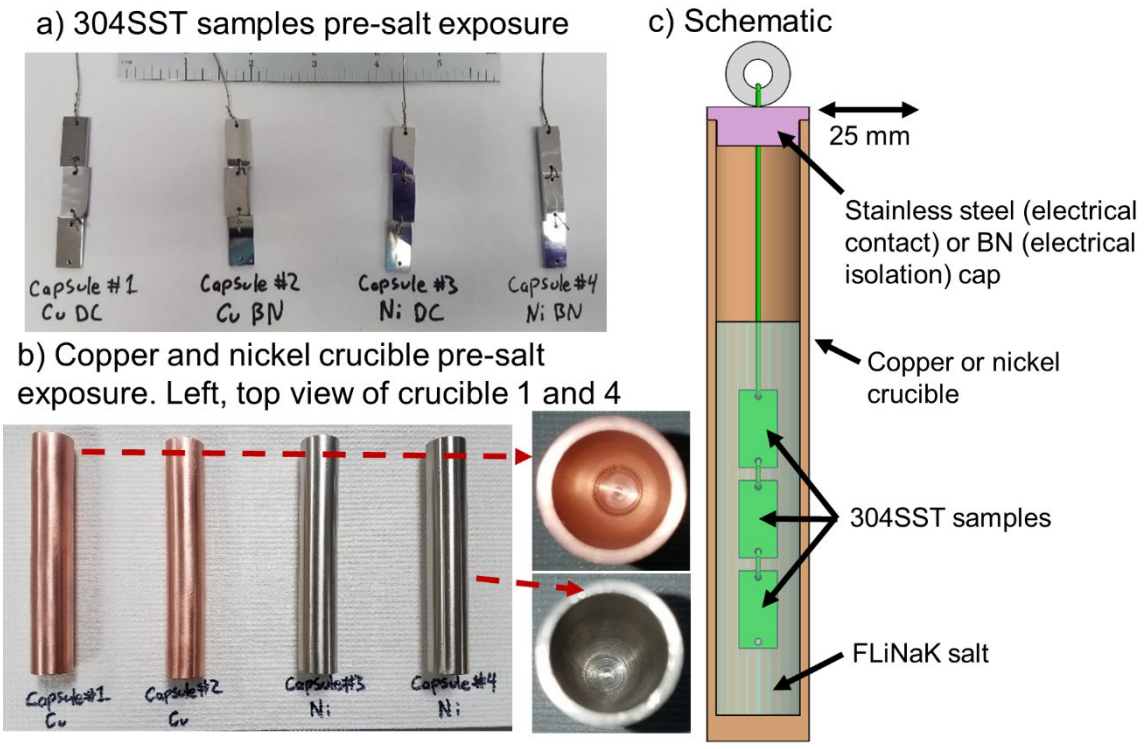

Figure 5-13: Salt exposure samples and crucibles pre-salt exposure. a) 304SST samples after P4000 preparation and cleaning. b) Copper and nickel crucibles after polish and cleaning. c) Schematic of FLiNaK exposure setup showing sample placement within crucible.

For each salt exposure test, each corrosion crucible was loaded with approximately 68.5 grams of FLiNaK salt. This quantity of salt, along with the size of the 304SST samples, and the density correlation shown in Equation 3-1 [40] gives a volume of salt to surface area ratio equal to 0.5 cm^3/cm^2 and 2.5 cm^3/cm^2 for the crucibles and the 304SST samples, respectively. The same furnace well connected to the glovebox described in Section 3.1.1 was used. All four salt capsules with solid FLiNaK were loaded into the furnace well. The crucibles were first pre-baked at 200 ºC for 8 hrs and then heated to salt exposure test temperature of 700 ºC to melt the salt. The furnace well temperature was then held at 700 ºC for 4 hrs in order to let the salt melt and to assure the salt temperature has homogenized at 700 ºC. To introduce the samples to the FLiNaK salt, the crucibles were raised out of the furnace well while still at temperature. The crucible caps with samples attached were then fitted to their respective salt crucibles. The crucibles were then lowered back into the furnace. The cap fitting and lowering of the crucibles took less than 90 seconds ensure the

salt temperature remained near 700 ºC. Once the crucibles were lowered back in the furnace, the salt exposure tests were performed for 500 hrs.

After the 500 hrs salt exposure, the crucibles were raised out of the furnace well again and the samples were removed by lifting the crucible caps off of each crucible. The samples were then allowed to cool in the argon atmosphere. Post-salt exposure FLiNaK samples were collected by pouring the FLiNaK out of each corrosion crucible into 304SST cups. The FLiNaK solidified in less than 5 minutes ensuring no additional corrosion products from the cups were introduced into the salt. Once cooled to room temperature, all post-salt exposure 304SST samples were removed from the glovebox and cleaned by ultrasonicating in 1M $Al(NO_3)_3$ followed by ultrasonicating in DI water with a final sonication in isopropyl alcohol. The post-salt exposure sample masses were then recorded using an electronic balance with 0.002 mg accuracy.

Post-salt exposure characterization followed similar steps as those described in Section 3.1.3. Post-salt exposure FLiNaK samples were sent to WSLH for ICP-MS analysis. The middle sample from each sample chain was used for cross-section analysis using the SEM/EDS. The 304SST samples from the nickel capsule in electrical contact and BN insulated were electroplated with Cu in a Cu-sulphate bath prior to mounting in cross-section for edge retention during metallographic preparation. As to not interfere with detecting potential Cu mass transport, the 304SST sample from the copper capsule in electrical contact and BN insulated configurations were not Cu electroplated before mounting in cross-section.

In addition to sample analysis, samples from all four salt crucibles were also prepared by sectioning the two copper and two nickel crucibles using a SiC abrasive cutting blade in two steps to expose the inner diameter that was exposed to the FLiNaK salt. Each sectioned crucible piece was imaged

and analyzed using the SEM/EDS to investigate mass transport between the 304SST samples and copper or nickel salt crucibles.

5.3.2 Electrochemical Measurement Results and Discussions

Electrochemical measurements were performed in part to predict the behavior of the galvanic connection between the 304SST samples and the copper or nickel crucibles used in the FLiNaK exposure tests. From the polarization measurements shown in Figure 5-14a, it can be observed that the OCP of nickel, copper, and 304SST are -175, -280, and -445mV vs. Pt, respectively. This ordering of the OCPs indicates that in a galvanic coupled system (i.e. electrical contact), 304SST is going to serve to as the anode material while nickel or copper would behave as cathodes. Thus, in the FLiNaK exposure tests it would be expected to see the 304SST samples in electrical contact with either a copper or nickel crucibles to have a noticeable difference in corrosion behavior compared to the samples that are BN insulated from the copper or nickel salt crucibles.

Additionally, based on the mixed potential theory as described in Section 2.3.2 the polarizations provide a first estimation of the coupled potential (E_{couple}) and coupled current (I_{couple}) for the 304SST nickel and 304SST copper couples. The crossing point of the 304SST anodic curve and the copper or nickel cathodic curve is the location were the rates of oxidation and reduction in a couple would be equivalent (i.e. the location of E_{couple} and I_{couple}). At the crossing point of the anodic curve and cathodic curve, the I_{couple} for the 304SST nickel couple is approximately 150 $\mu A/cm^2$ while the I_{couple} for a 304SST copper couple is approximately 260 $\mu A/cm^2$. In addition to 304SST acting as the anode, these values for I_{couple} also provide a prediction on which couple would have a larger impact on the 304SST samples.

The magnitude of the I_{couple} provides a prediction on the rate of oxidation (corrosion) that could occur at the 304SST material if coupled to either nickel or copper. Since the I_{couple} for the 304SST

copper couple is larger in magnitude that would suggest that if 304SST were coupled to copper, then one would expect a larger effect on the corrosion behavior of the 304SST than if it was coupled to nickel.

ZRA measurements shown in Figure 5-14b were performed to get a more direct measurement of the coupled current between a 304SST nickel and 304SST copper couple. Since the two materials are connected to each other through a "0" resistance wire, any measured current is therefore a measurement of the coupled current. In Figure 5-14b, it can be observed that both couples initially showed a large positive current, possibly indicating that 304SST is in fact the anode and either nickel or copper is acting as a cathode, but more likely this large initial current is more representative of built up charge being discharged at the initiation of the measurment. This large positive current quickly decays towards 0 $\mu A/cm^2$ in less than 45 seconds in both measurements. The inset graph in Figure 5-14b shows the measured current over the final 15 minutes of the measurement. In both couples the current simply oscillates between a positive and negative current while never reaching a maximum or minimum value over ± 200 nA/cm^2. This result suggests that despite the coupled predictions from the polarization measurements, the ZRA measurements show that there exists no galvanic current in either the 304SST nickel or 304SST copper couples.

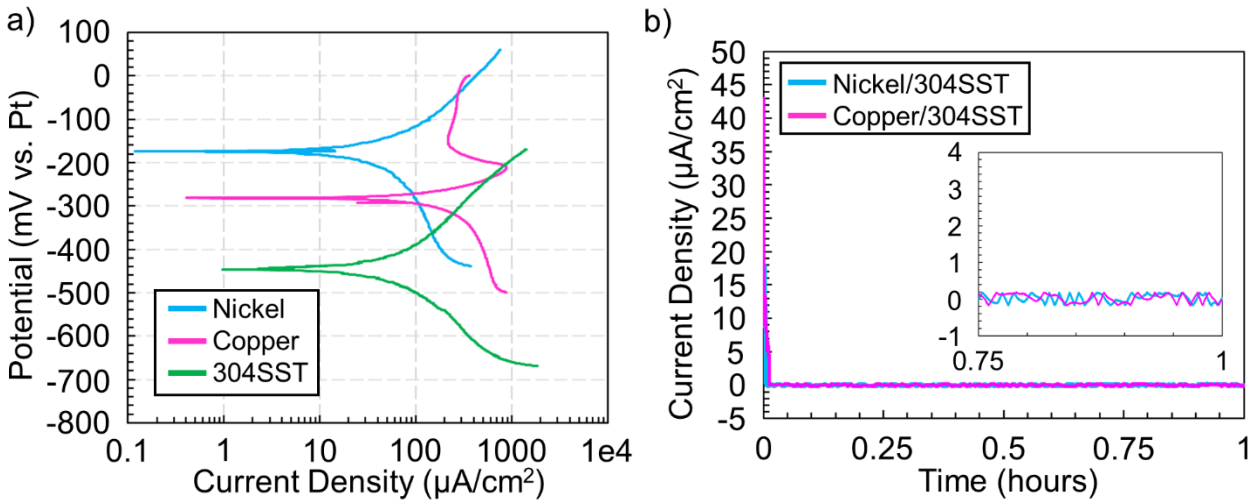

Figure 5-14: Electrochemical measurement results. a) individual polarization measurements of 304SST, copper, and nickel. b) ZRA measurements between coupled nickel and 304SST and coupled copper and 304SST.

As a result, the ZRA measurements indicate something similar to what was found out in the activity gradient mass transport validation salt exposures. The electrical connection between dissimilar metals in a FLiNaK environment may have little effect on the interaction behavior of the metals and therefore little effect on the corrosion of the corroding material. Understanding why the ZRA measurements performed here do not show a galvanic current is complex. Other studies have been able to measure a galvanic current between graphite and stainless steel in a FLiNaK environment [49].

As a check on the potentiostat setup, ZRA measurements have been performed at room temperature in a saturated KCl environment. The measurements were performed on an exact electrode copy of the 304SST copper coil and are presented in Appendix F. Those measurements showed that a mostly stable current measurement is possible using the ZRA setup on the VersaSTAT 3F so the 0 $\mu A/cm^2$ measurement is unlikely a result of the potentiostat setup and therefore a real result for the couples in FLiNaK.

In order for there to be a galvanic current between dissimilar materials there has to be an oxidation reaction at the anode that releases electrons to the electrode. These electrons move along a

conductive path and cause a reduction reaction at the cathode. This electron movement (i.e. current) is what the ZRA measures. In the FLiNaK environment, the oxidation reactions are the corrosion reactions of 304SST (i.e. chromium being oxidized to chromium fluoride), but it's unclear what the reduction reaction would be in a high quality salt. Qiu, J. et al. [49] performed their experiments in a gas phase environment that contained moisture and speculated that the moisture impurity produced HF. Therefore the galvanic current was limited by either HF or H^+ reaching the cathode. In the high-purity argon glovebox, there is no measureable moisture in the atmosphere and the salt is good quality. A likely explanation for 0 $\mu A/cm^2$ current is that the FLiNaK environment does not contain enough impurities to drive a significant reduction reaction at the cathode.

In terms of what these results imply in a dissimilar material couple in the glovebox system used in this work, is that the electrical contact has little effect on the couple, as already predicted by the results in Section 5.2.3. However, if the predictions from the polarization measurements are taken into account two effects in the salt exposure tests are to be expected. (i) In a 304SST nickel or 304SST copper couple, 304SST will serve as an anode material meaning electrical contact will result in an increased corrosion rate for the 304SST material as compared to the 304SST that is BN insulated from the nickel or copper. (ii) The coupled current for the 304SST copper couple is predicted to be higher than the 304SST nickel couple so 304SST samples coupled to copper should experience a higher corrosion rate than 304SST samples coupled to nickel. If these results are not observed in the FLiNaK exposure tests, the ZRA measurements are likely accurate. Additionally, if the 304SST samples coupled to nickel show a greater corrosion effect then the 304SST samples coupled to copper, then that has to be a result of non-galvanic dissimilar material interactions like

activity gradient mass transport because nickel provides an activity gradient for Fe and Cr while copper does not.

5.3.3 FLiNaK Exposure Results and Discussions

All of the post-FLiNaK exposure 304SST samples showed a mass loss indicating that 304SST underwent corrosion in both the copper and nickel capsules and in both electrical configurations. The mass change from all three samples in each set was averaged and is shown in Figure 5-15. Additionally, it can be observed that no matter the electrical configuration of the sample sets, the 304SST samples that were exposed to FLiNaK salt in a nickel capsule experienced a dramatic increase in the mass loss as compared to the 304SST samples in copper capsules. In the nickel capsules the average mass loss for the 304SST sample sets was -6.5 ± 1.8 mg/cm^2 and -5.7 ± 0.9 mg/cm^2 for the electrical contact and BN insulated sample sets, respectively. In copper capsules the average mass loss of the 304SST samples sets was only -1.6 ± 0.1 mg/cm^2 and -1.9 ± 0.1 mg/cm^2 for the electrical contact and BN insulated sample sets, respectively. Similarly to the previous test validating the activity gradient mass transport, it can be observed that the electrical configuration appears to have no effect on the mass loss experienced by the 304SST samples.

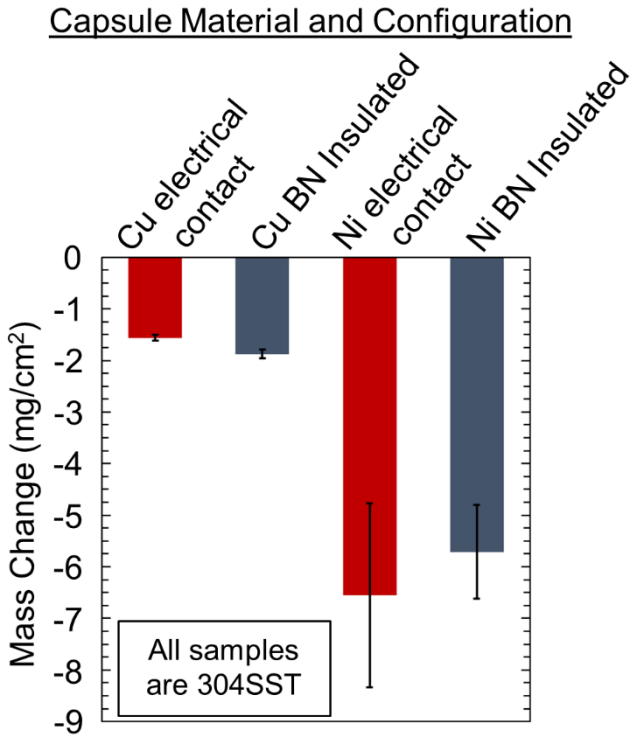

Figure 5-15: Mass change results for 304SST samples after FLiNaK exposure at 700 °C for 500 hrs.

To evaluate the extent of the corrosion layer in the 304SST samples, all of the middle samples from each capsule were analyzed in cross section. The results for the 304SST samples in electrical contact with and BN insulated from the copper capsules are presented in Figure 5-16. In both electrical configurations, it can be observed that the corrosion layer in the 304SST samples is rather mild. The Cr depletion depth in each configuration is also similar with 11 µm and 12 µm of Cr depletion in the electrical contact and BN insulated samples, respectively. In this same region, it can also be observed that the Fe concentration is elevated. This is not believed to be due to actual enrichment, rather because the surface of the alloy is now depleted in Cr, Fe appears artificially enriched.

The nature of the Cr depletion is also of note in both of the 304SST samples. Perhaps best observed in the BN insulated sample, Figure 5-16b, but also seen in the electrical contact sample, the Cr depletion primarily appears to be occurring along the grain boundaries of the 304SST. Alternatively, the depletion within the actual grains appears to be rather minimal. This behavior of

Cr depletion is somewhat expected, as Cr has a much higher diffusion coefficient along grain boundaries as compared to in bulk [107]. All of the cross sectional analysis on the 304SST samples exposed to FLiNaK in copper capsules corresponds well with the low mass loss observed in Figure 5-15.

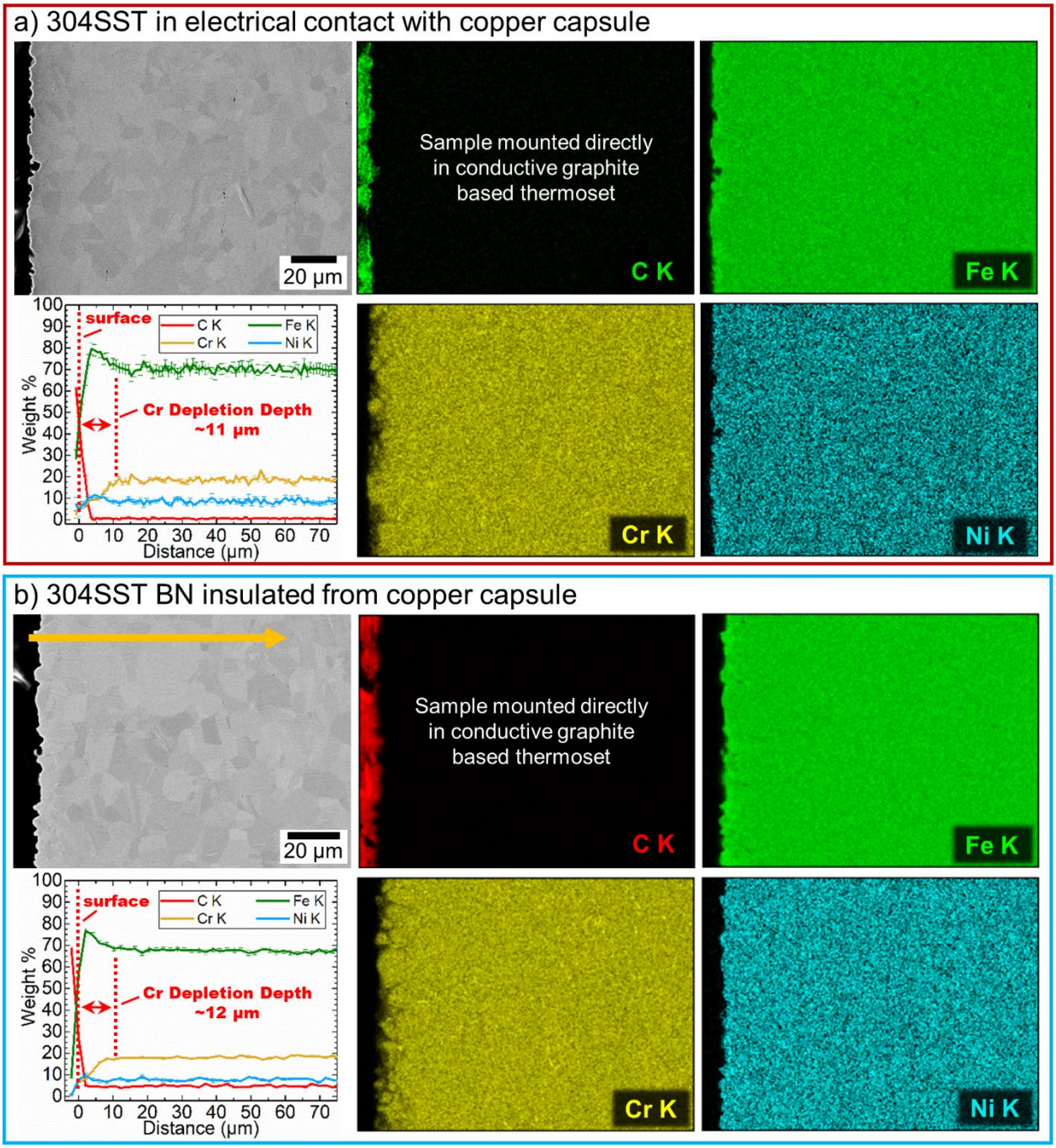

Figure 5-16: Cross-section SEM/EDS analysis on the 304SST samples tested in copper capsules. a) 304SST sample in electrical contact with copper capsule. b) 304SST sample BN insulated from the copper capsule.

As compared to the 304SST samples tested in copper capsules the results for the 304SST samples in nickel capsules in Figure 5-17 show a much more dramatic corrosion layer. In both the electrical contact and BN insulated 304SST samples in nickel capsules, the corrosion layer is filled with deep subsurface voids. The deepest voids observed in the electrical contact sample reached a depth

of approximately 71 μm. The SEM/EDS analysis on the BN insulated sample in Figure 5-17b was not performed at the site of the deepest voids which in the BN insulated sample reached approximately 43 μm. While the deeper void formation in the electrical contact sample may correspond well with the higher average mass loss for the electrical contact samples shown in Figure 5-15, it's believed that the true difference in depth is likely more a result of the SEM being a localized analysis technique. It's likely that there is a region in the BN insulated sample that has a similar void depth to the electrical contact sample.

In terms of the Cr depletion in both of the samples tested in nickel capsules, it can be observed that the depletion behavior almost matches that of the void formation and the Cr depletion also mostly occurs along the grain boundaries. To see clear evidence of this, the line scan shown in Figure 5-17a, performed on the electrical contact sample, was done adjacent to the deepest void formation. It can be observed that when the line scan goes over a bulk grain, the Cr concentration in the grain is near the nominal composition of 304SST. However, as the scan goes over the grain boundary or void, there is a large drop in the Cr concentration. This same observation can be seen in the BN insulated sample shown in Figure 5-17b.

Measuring the maximum Cr depletion depth in both the nickel capsule 304SST samples is complicated by the unknown effect of surface recession in these samples. As seen in Figure 5-17a, the line scan performed on the electrical contact 304SST sample was started in a recessed surface region. So, if the Cr depletion depth was determined from the line scan, one would assume the Cr depletion depth to be approximately 65 μm. However, in the Cr elemental map, the apparent surface of the sample can be corrected for. That's not to say that this surface is the original sample surface, because it's not possible to determine that. From the apparent sample surface, the Cr depletion depth is approximately 75 μm. This depth only extends a short distance past the deepest

void formation, again showing that the Cr depletion behavior is following that of the void formation. A similar observation can be made from the BN insulated sample in Figure 5-17b.

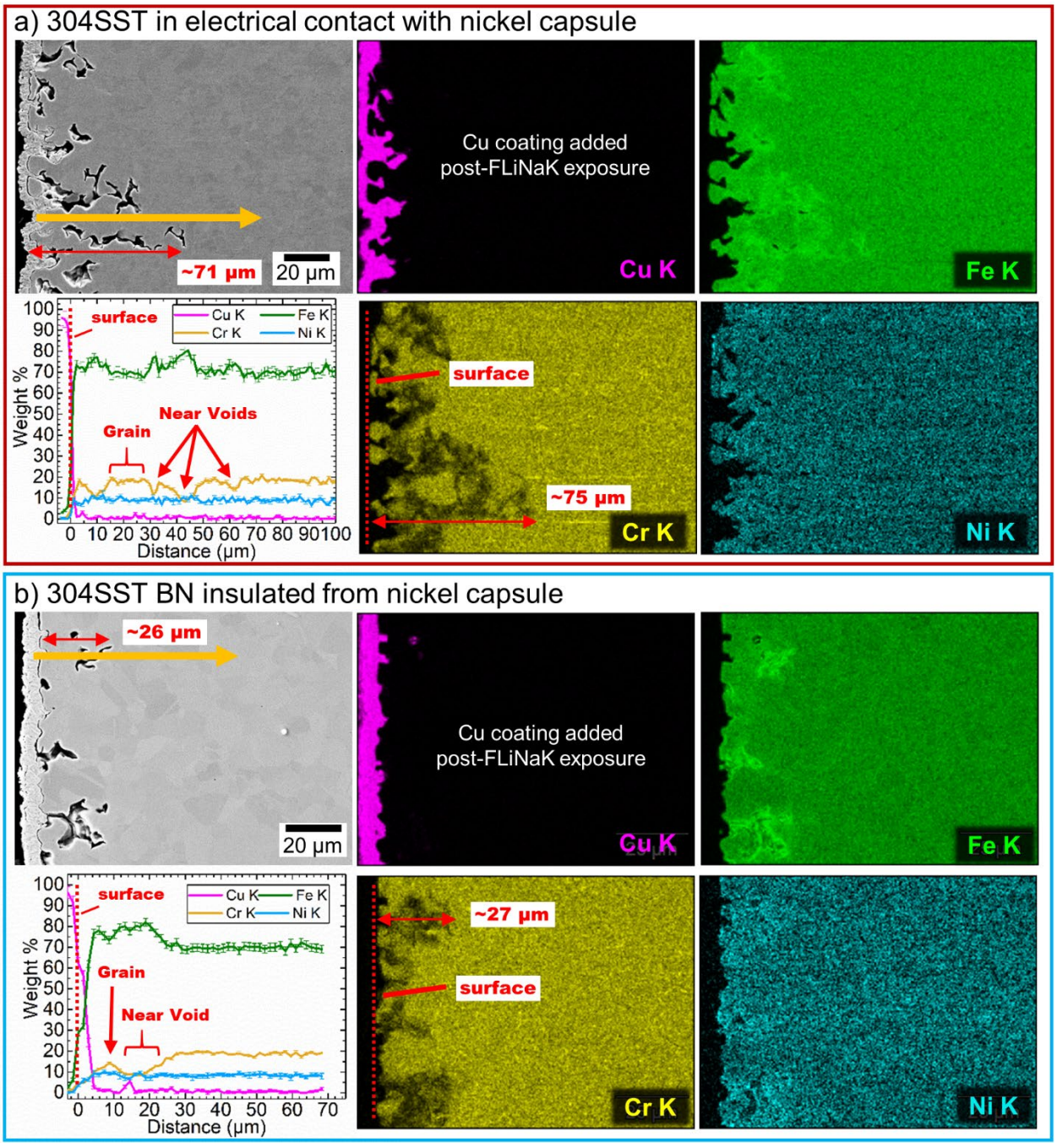

Figure 5-17: Cross-section SEM/EDS analysis on the 304SST samples tested in nickel capsules. a) 304SST sample in electrical contact with nickel capsule. b) 304SST sample BN insulated from the nickel capsule.

From the mass change and SEM/EDS data, it can clearly be observed that the 304SST samples tested in nickel crucibles experience a much greater degree of corrosion than the 304SST samples

tested in copper crucibles. Additionally, it can be observed, that between the electrical contact and BN insulated configurations, there is little difference in the corrosion of the 304SST samples. From the predictions made based on the polarization experiments in Figure 5-14, this behavior is opposite of what would have been predicted if conventional galvanic corrosion mechanisms were taking place between the dissimilar metals. Likely what is actually causing the large difference between the 304SST samples tested in nickel and copper crucibles is better explained by the activity gradient mass transport mechanism described in Section 2.3 and validated in experiments described in Section 5.2.

To understand how the activity gradient mass transport mechanism explains the behavior of the 304SST sample in nickel and copper crucibles, post-salt exposure FLiNaK samples were analyzed with ICP-MS. Additionally, SEM/EDS analysis of the post-salt exposure copper and nickel crucibles was performed. The results from the ICP-MS analysis performed by the WSLH as well as photographs of the post-salt exposure FLiNaK samples are presented in Figure 5-18. First, looking at the photographs of the post-salt exposure FLiNaK samples it can be observed that the salt from both of the copper capsules is much darker in appearance than the FLiNaK from the nickel capsules. Typically, the color of the salt is a first indication of a how many impurities are in the salt. Perfectly white almost translucent salt more often has lower impurities than darker grey salt [83]. The ICP-MS data somewhat confirms that the appearance of the salt samples does indicate increase impurity concentration in the FLiNaK salt collected from the copper capsules.

Post-salt exposure, all of the salt samples show a dramatic increase in the concentration of Cr. However, the concentration Cr in the copper capsule FLiNaK samples is approximately 2x greater than the concentration in the nickel capsules. This result appears counterintuitive at first, but from Section 5.2 it was demonstrated that the Cr has an activity gradient for mass transport if Ni (i.e. a

nickel crucible) is present in the system. Meaning that if Ni is in the system Cr could leave the FLiNaK solution in favor of forming an alloy or compound with Ni and would therefore likely be present in the salt in a reduced concentration.

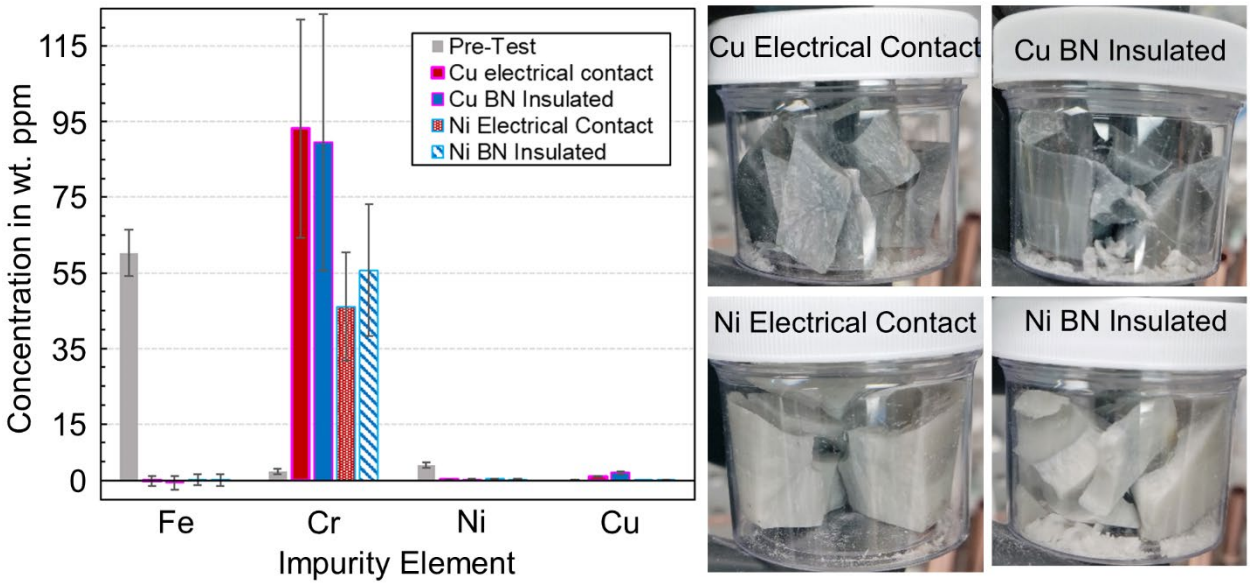

Figure 5-18: Results of the ICP-MS analysis (left) and photographs of the post-salt exposure FLiNaK samples collected from all copper and nickel capsules (right).

For the analysis on the copper and nickel crucibles, the sectioned piece described in Section 5.3.1 was analyzed using SEM/EDS. The average composition of the capsule surface was determined using EDS and is presented in Table 5-6. From the nominal composition of the nickel and copper used to make the crucibles shown in Table 5-2, the original crucible materials are greater than either 99% pure nickel or copper. After FLiNaK exposure, it can be observed that the composition of the nickel capsules has dramatically changed. As nickel presents a large activity gradient for both Fe and Cr mass transport, the concentration of both Fe and Cr in the nickel capsules has increased post-FLiNaK exposure. What this indicates is that the nickel capsule is taking in Fe and Cr corrosion products coming from the 304SST samples therefore increasing the corrosion of the 304SST when in a nickel capsule. Copper on the other hand presents no significant activity gradient for either Fe or Cr transport and therefore doesn't interact with the corrosion products.

This means that as the corrosion product concentration increases in the salt, the corrosion reactions will start to slow down because the reaction may be approaching equilibrium. Hence a copper capsule behaves more like the pyrolytic boron nitride crucibles in the sense that it doesn't interfere with corrosion products and may be a good material choice if a non-interacting container is needed for testing Fe-based alloys.

Table 5-6: Average surface composition of the post-FLiNaK exposure nickel and copper crucibles.

Material	Weight % Determined by EDS Analysis			
	Fe	Cr	Ni	Cu
Ni Crucible DC	5.18 ± 0.02	4.12 ± 0.01	90.70 ± 0.12	N/A*
Ni Crucible BN	2.47 ± 0.02	3.87 ± 0.01	93.66 ± 0.12	N/A*
Cu Crucible DC	0.47 ± 0.01	0.64 ± 0.01	0.20 ± 0.01	98.68 ± 0.15
Cu Crucible BN	0.13 ± 0.01	0.05 ± 0.00	0.07 ± 0.01	99.75 ± 0.15

*element not including in quantification. Not present in either sample or crucible material in their as-received state

Of note is the lack of Fe in the post-FLiNaK ICP-MS data. It can be observed that the nickel capsules clearly up took Fe corrosion products because the surface concentration of the nickel crucible now contains a non-negligible concentration of Fe, however, the ICP-MS data shows that the Fe concentration in salt actually decreased post-salt exposure. This can be explained by the relative rates of the mass transport process. As 304SST is an Fe-based alloy, the rate of Fe transport won't be rate limited by Fe diffusion in 304SST. Fe is always present at the 304SST surface. Once in the salt, Fe mass transport could depend on iron fluorides diffusion through FLiNaK. However, using electrochemical techniques like cyclic voltammetry and chronoampometry, several researchers have shown that the diffusion of metal halides through halide salts are orders of magnitude faster than diffusion of metal atoms through an FCC metal lattice [61, 62, 108-111]. Specifically for Fe, Peng et al. determined the diffusion coefficient for iron in FLiNaK to be on the order of 10^{-6} cm^2/s [61] versus less than 10^{-12} cm^2/s in an FCC lattice [110]. So diffusion

through the salt is also not a rate limiting step for Fe transport. That leaves the absorption and diffusion of Fe at the nickel capsule as the rate limiting step. This would make sense as the concentration of Fe at the very surface clearly increases over time.

Overall, the results from these experiments clearly demonstrate that the presence of an activity gradient for mass transport can drastically alter the corrosion of the corroding material, in this case 304SST. Once again, the effect of the activity gradient has been demonstrated to not be dependent on the electrical configuration of the dissimilar materials. Furthermore, the effect of the activity gradient has also been demonstrated to be more significant than the effect of galvanic connection. This is critical because a reactor system may be engineered in such a way to eliminate galvanic couples, but that won't prevent the more important interaction mechanism of the activity gradients when it comes to dissimilar metals.

5.4 Activity Gradient Transport and Graphite

In the previous sections of Chapter 5, it has clearly been demonstrated that the material interactions through activity gradients in molten FLiNaK, and more generally in halide salts, can have profound effects on how dissimilar materials interact with each other. Furthermore, the interaction through activity gradients does not appear to depend on electrical contact. Up to this point, the dissimilar material computations, experiments, and discussions have primarily focused on dissimilar metals. However, often prototypical corrosion experiments as well as a fluoride salt based reactor system have an additional dissimilar material that is either often used or will be present in the system. That material is graphite. Fluoride salt based nuclear reactor systems are going to operate in a thermal neutron spectrum meaning the neutrons created from fission need to be slowed down via a moderator. To moderate neutrons, the material of choice is graphite. Additionally, some fluoride

salt based reactor concepts such as the Fluoride-salt-cooled High Temperature Reactor (FHR) are planning to use graphite based solid fuels known as TRISO particles. This fuel choice introduces a large surface area of graphite to the reactor system, so understanding how and finding ways to potentially eliminate activity gradient driven mass transport interactions between metals and graphite is of critical importance.

As shown in the Ellingham diagrams for carbide formation of transition metals in Figure 5-19, the primary challenge with graphite is that most transition metals, and especially those that are often used in metallic alloys (i.e. Cr, Fe, Mo, Al, etc.), have a driving force for carbide formation. Meaning that there is going to be a driving force present for pushing the disproportionation reaction (RXN 2-10) forward or for the uptake of any dissolved metal species (RXN 2-11). In summary, an activity gradient for elements to transport is always present if graphite is present in the same salt medium as a metallic alloy. Additionally, since activity gradient mass transport doesn't require electrical contact, even electrical isolation won't prevent graphite interaction and potential accelerated degradation of the metallic structure.

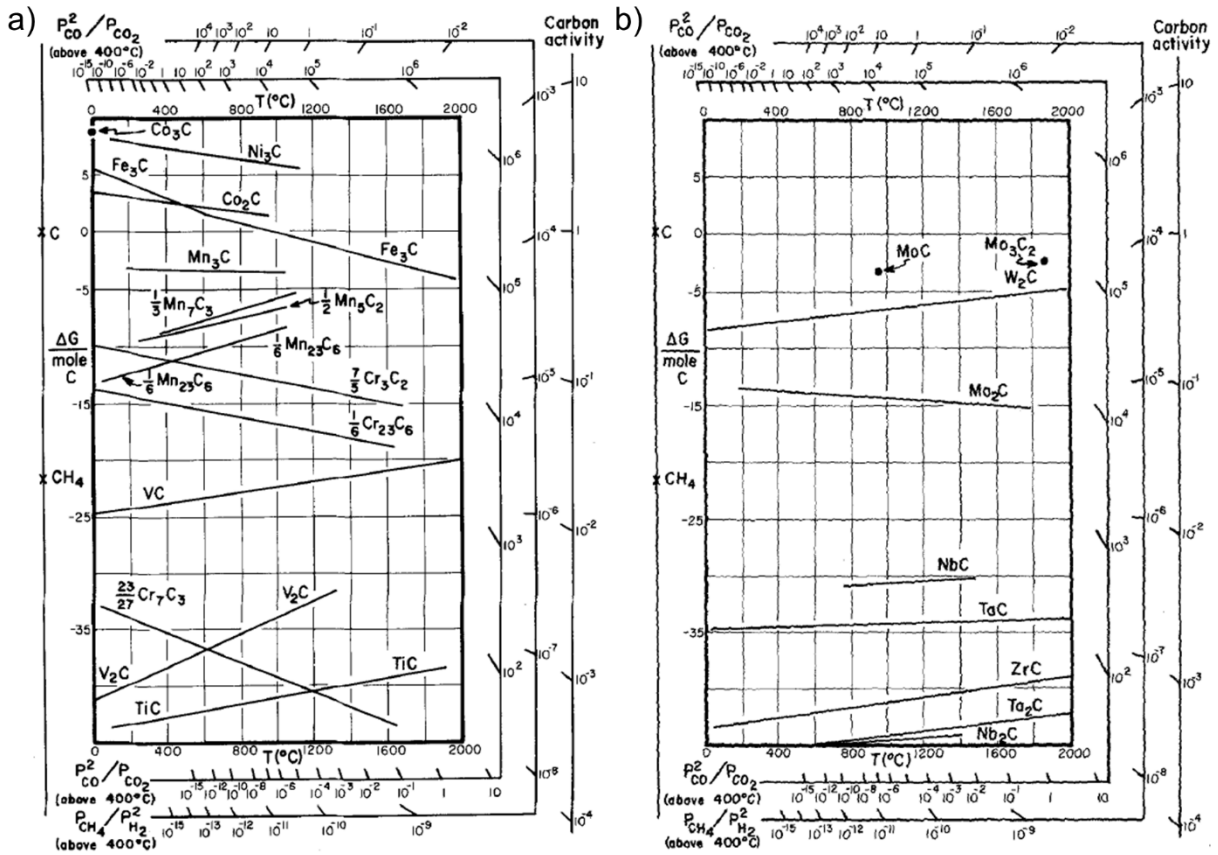

Figure 5-19: Ellingham diagrams for transition metal carbides. a) First transition metal series. b) Second and third transition metal series. Gibbs energies are reported in calories and normalized to 1 mole of carbon [112].

Many studies have showed that the presence of graphite does lead to interaction with Fe and Cr containing corrosion products ultimately resulting in the accelerated degradation of the metallic samples that were in the same salt medium. A collage of the interactions from literature are shown in Figure 5-20. Sellers et al. [48] found visible films had plated out onto their graphite material after being in the same salt medium as 316LSST samples. Olson et al. went as far as to performing SEM/EDS analysis on a graphite fixture rod that had a film on it after testing Incoloy-800H in the same salt medium. The film showed that both Fe and Cr had transported to the graphite rod. Ai et al. [27] performed XRD analysis on a film found on their graphite crucibles where alloy GH3535 (Chinese variant of Hastelloy-N) was tested in an electrically isolated configuration and determined the film to be a Cr_7C_3 that must have formed due to graphite interactions with Cr corrosion products from GH3535. Finally, several others have clearly demonstrated that the

presence of graphite leads to accelerated corrosion of the metal alloy being tested in static isothermal corrosion tests [41, 43, 49], with Zheng et al. [80] in particular clearly showing an increase in the mass loss and Cr depletion depth of 316SST when it was tested in graphite salt containers versus being tested in 316SST containers

a) Graphite coupon used in the same test as 316LSST. Before (left) and after (right) test

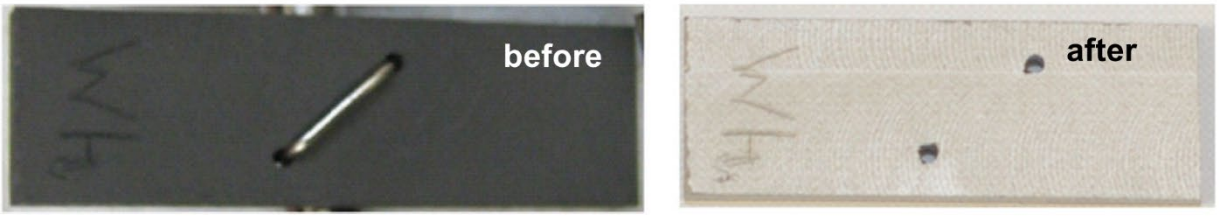

b) Graphite fixture rod used in the same test as Incoloy-800H

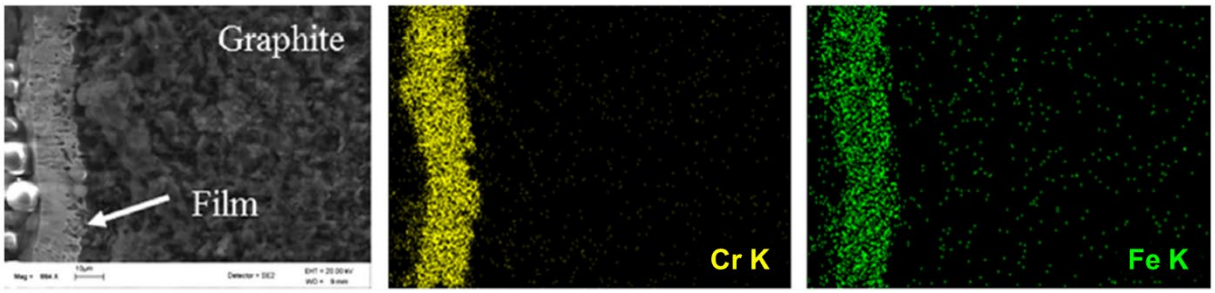

c) Mass loss (left) and Cr depletion (right) data from 316SST tested in graphite versus 316SST salt containers

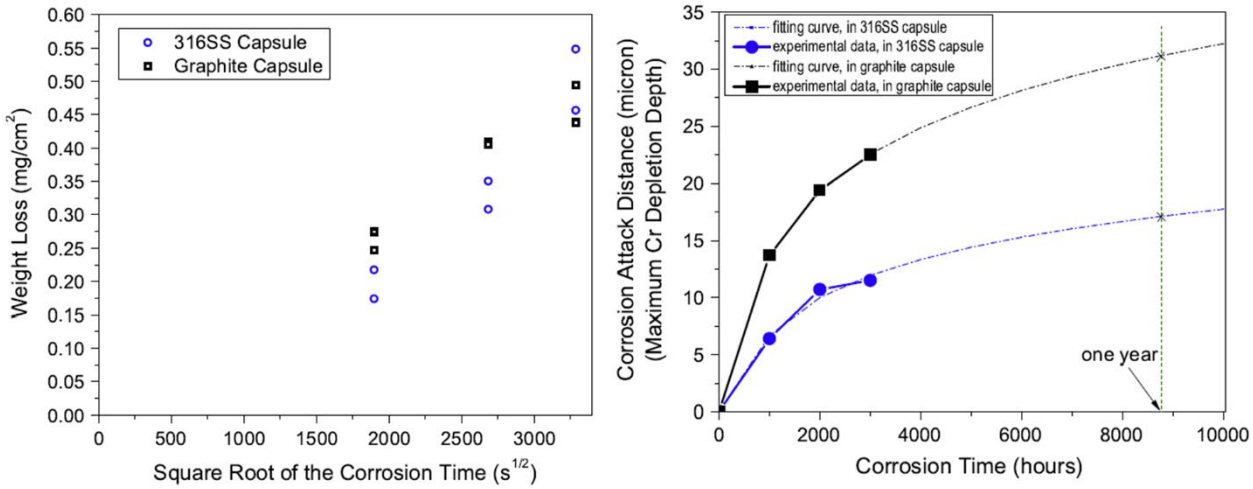

Figure 5-20: Collage of graphite interactions with metallic samples from various literature sources. a) visible carbide film formed on graphite coupon [48]. b) SEM/EDS analysis on a carbide film formed on a graphite fixture rod [46]. c) Increased mass losses and Cr depletions found in 316SST samples tested in graphite containers [80].

Similarly to the results from the verification experiments, the evidence from the literature clearly shows that graphite is not as "inert" to molten fluoride salts or corrosion products as originally believed. In addition to the graphite needed for the moderator, the particular design of the FHR presents another source of graphite in the construction of the TRISO particle fuel as pyrolytic carbon is currently anticipated to make up the outermost layer of the TRISO particle fuel compact [113, 114]. The presence of the graphite in both the reactor system and corrosion tests has an influence on the corrosion of the metal and therefore would ideally be eliminated. One avenue to eliminating graphite interactions with the salt and corrosion products is to prevent it from coming into contact with the salt all together.

As already discussed in Chapter 2 and Chapter 3, PyBN has been shown to perform extremely well in molten fluoride exposure tests not only in this dissertation, but also in previous literature [46, 50]. These results suggest that PyBN could potentially make an excellent fluoride salt facing material that could also prevent graphite-alloy interactions if applied to graphite material as a salt facing coating.

5.4.1 Feasibility of Producing PyBN Coated Graphite Components for Use in Fluoride Salts

One of the primary application areas of the PyBN coating for limiting graphite interactions in a molten salt environment envisioned as part of this work is a new final salt facing layer of the graphite based solid fuels. Graphite based solid fuels are usually based on utilizing the tristructural isotropic (TRISO) particle encased in a larger fuel compact of differing designs [115]. The TRISO particle itself is a several hundred micron diameter multilayer sphere, as shown in Figure 5-21. The sphere center is the fuel kernel whose composition depends on the fuel design that is coated in a porous carbon layer that allows for fission gas build up, which is then covered in one layer of pyrolytic carbon covered by a layer of silicon carbide (SiC) with a final layer of pyrolytic carbon

that helps bond the TRISO particles to the fuel compact. Then to make the final fuel compact, thousands of TRISO particles are coated in an “overcoating” and compacted into the final fuel compact design [115, 116]. The final design of the fuel compact is more often than not proprietary to the reactor designer, but some pre-conceptual designs for TRISO particle fuel applications in FHRs is that the final fuel compact will consist of a low density graphite core surrounded by a TRISO particle embedded graphite matrix that is fully encased in a high density outer graphite coating as shown in Figure 5-21 [117, 118].

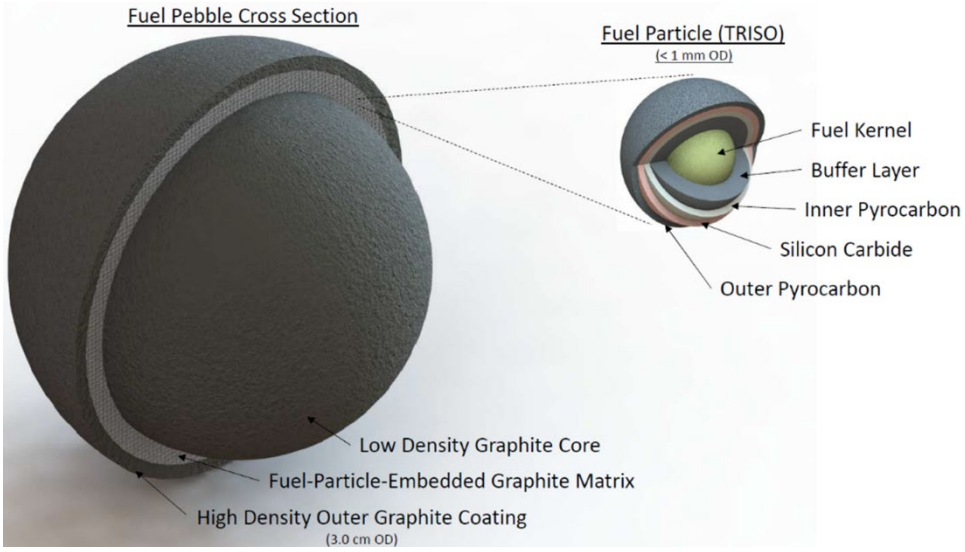

Figure 5-21: Mk1 design for FHR TRISO fuel compact [118].

This pre-conceptual design of the FHR fuel geometry then suggests that the salt facing component of the fuel is graphite, which as discussed previously is available for interaction with metallic corrosion products. The challenge then for adding a PyBN coating to the final fuel form is coating a graphite surface in PyBN. The second application of the PyBN coating envisioned in this work is coating the other graphite based components such as salt facing supporting structures or the graphite moderator. Once again the second application’s challenge comes down to adding a PyBN coating to a graphite surface. Luckily this challenge in all reality is not much of a challenge at all. One of the primary production methods for PyBN is through chemical vapor deposition (CVD).

Using appropriate precursor gases for a boron and nitrogen source PyBN coatings and components are routinely grown on a variety of substrates/molds, with graphite being a common substrate of choice [119]. In fact the PyBN crucibles used as part of this dissertation are grown on graphite molds and one of the main uses of PyBN is for coating graphite heating elements to protect the graphite elements in aggressive environments [120].

Growing PyBN on top of graphite then poses little obstacle in terms of the feasibility of coating graphite materials for use in an FHR application. For the FHR fuel compact it is envisioned that the current high density outer graphite coating is already produced via a CVD method in a fluid bed coater. Therefore, to create a new final coating of PyBN over the graphite, likely all that would be needed is an additional step in the fluid-bed coater that uses the precursor gases for the CVD deposition of PyBN. This would impose only a small addition to the manufacturing process and time needed for the FHR fuel compacts. As for the additional graphite components, the difficulty of applying a PyBN coating greatly depends on the scale of the components but the CVD coating process is perfectly poised for depositing coatings on complex geometries [119]. The primary question remaining is whether or not a PyBN coating will actually reduce the interaction of graphite materials with potential metallic structure corrosion products.

5.4.2 Testing PyBN Coating for Reducing Graphite Interactions

5.4.2.1 Materials and Methods

To see how a PyBN coating on graphite changes the interactions of graphite with potential metallic structure corrosion products from fluoride salt corrosion, a FLiNaK exposure test was developed for testing PyBN coated graphite. The FLiNaK used in these exposure tests came from the commercially procured FLiNaK that was described in Section 3.1.2. PyBN coated pyrolytic graphite (PG) coupons were procured from a commercial vendor. The underlying PG coupons had

dimensions of 25 x 20 x 1.5 mm that were intended to be coated with approximately 200 µm of PyBN. Actual coating thickness measurements will be discussed in the results section. The vendor that produced the PyBN coated PG coupons synthesized the PyBN coating using a CVD process that utilizes BCl_3 and NH_3 as the precursor gases where the overall synthesis reaction is:

$$BCl_3 + NH_3 \rightarrow BN + 3HCl \qquad \text{RXN 5-1}$$

This production method results in a PyBN coating that is greater than 99.99% pure and has virtually no porosity. As a reference the same vendor also provided uncoated PG coupons of the same dimensions as above. Photographs of the as-received PyBN coated and plain PG coupons are shown in Figure 5-22a and Figure 5-22b, respectively. To prepare the coupons for the FLiNaK exposure testing, the as-received coupons were sonicated in isopropyl alcohol for 5 min and then allowed to dry. Following this, the coupons were strung together using 316SST wire twisted in an X pattern. The two samples strung together were then hung from a boron nitride cap with 316LSST wire as seen in Figure 5-22c.

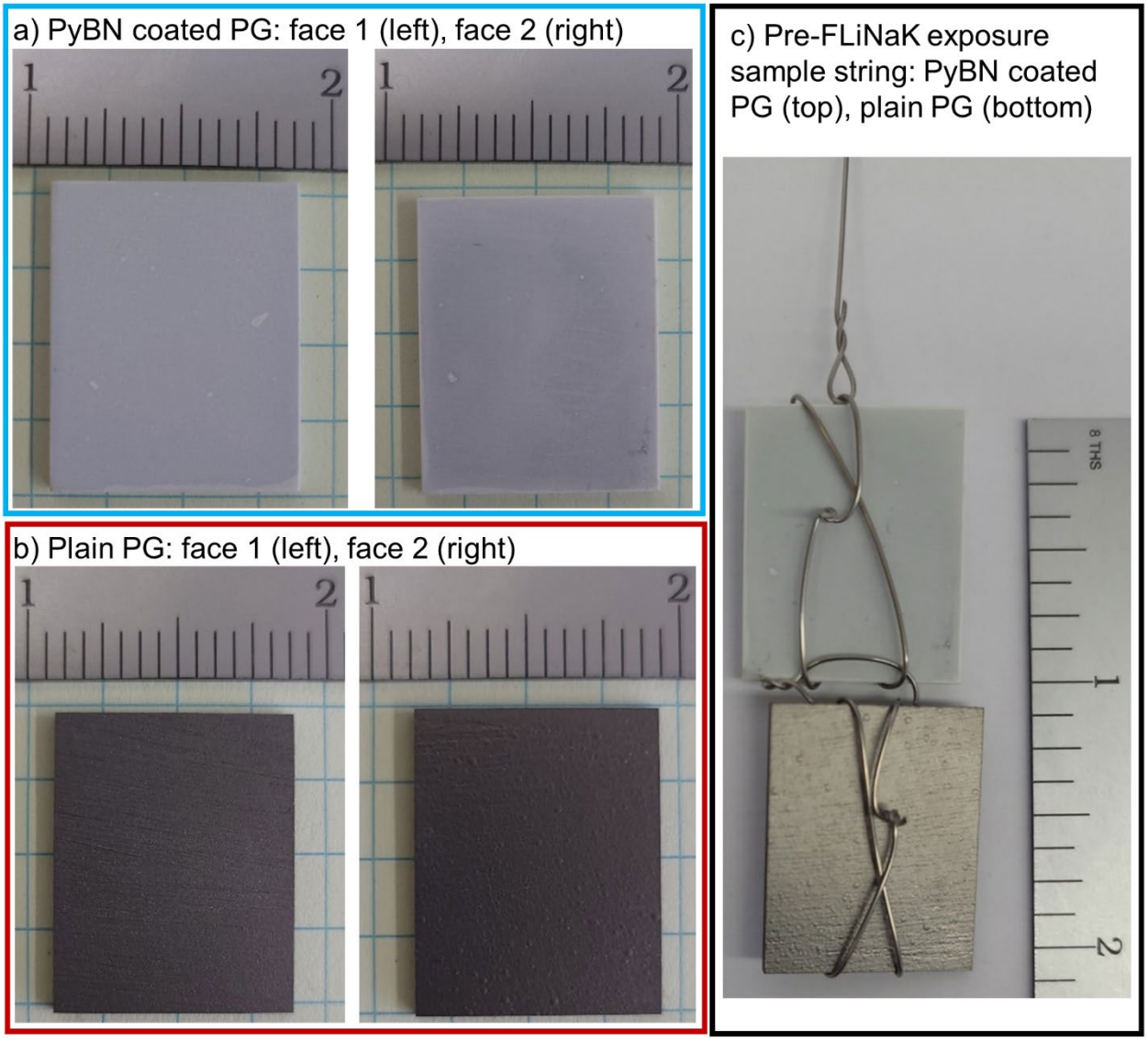

Figure 5-22: As-received PyBN coated PG and plain PG coupons. Units on scale are inches.

To test how these coupons would perform in FLiNaK and how the coupons might interact with corrosion products of potential metallic structural materials, the salt containment crucible for the FLiNaK exposure tests was constructed out of 316SST. This crucible is the same type of 316SST crucible originally described and used in Section 5.2.1. Similar to the activity gradient verification tests in Section 5.2, the FLiNaK exposure is expected to produce Fe and Cr corrosion products through corrosion reaction with the 316SST crucible. Then those corrosion products have the potential to interact with the PyBN coated PG or plain PG if there is a driving force for the

interaction (i.e. activity gradient mass transfer). As observed by previous studies, it's anticipated that Fe and Cr corrosion products will interact with the plain PG coupons by the formation of Fe and Cr containing carbides. On the other hand, as observed in this dissertation the PyBN coating is anticipated to remain not only inert to the FLiNaK salt, but also undergo no interaction with Fe or Cr containing corrosion products from the corrosion of the 316SST crucibles.

All of the salt handling, setup, and FLiNaK exposure was performed in the same glovebox described in Section 3.1.1. The 316SST corrosion crucible was filled with approximately 70 g of the commercial FLiNaK. Using the dimension of the coupons, 316SST crucible, and FLiNaK density correlation in Equation 3-1, the Vol/SA ratios for the 316SST crucible and the PyBN coated PG coupon as well as the plain PG coupon were approximately 0.5 cm^3/cm^2 and 3 cm^3/cm^2, respectively. Once the crucible was filled with commercial FLiNaK, the crucible was lowered into the glovebox furnace for heat up. The furnace was first heated to 250 ºC for 12 hrs for an initial bakeout, then the furnace was heated to 500 ºC for 2 hrs to allow the salt to melt, finally the furnace was heated to 700 ºC and held for 2 hrs to allow the salt temperature to homogenize before introducing the PyBN coated PG and plain PG coupons. After 2 hrs, the crucible was lifted out of the glovebox furnace, the coupon string was positioned on the 316SST crucible, and the crucible was lowered back into the glovebox furnace. The coupons were then continuously exposed to the commercial FLiNaK salt in a 316SST crucible for 500 hrs at a temperature of 700 ºC.

At the conclusion of the 500 hrs exposure, the crucible was lifted out of the furnace, the PyBN coated PG and plain PG coupon were removed from the commercial FLiNaK salt by lifting the boron nitride cap off of the crucible and the coupons were allowed to cool in the glovebox Ar environment. To wash residual FLiNaK off of the coupons, the coupons were washed using the

warm DI wash method discussed in Section 4.2.6 before starting the post-FLiNaK exposure characterization.

5.4.2.2 PyBN coated PG and Plain PG Characterization

One of the as-received PyBN coated PG coupons was used as a reference sample for performing SEM/EDS characterization on a PyBN coated PG coupon without FLiNaK salt exposure. This sample was cut in half using a low speed saw and diamond coated blade before being Cu electroplated and mounted in cross-section to investigate the initial thickness of the PyBN coating using the SEM/EDS. The Cu electroplating was added for edge retention and to provide a distinct marker of the coating surface in EDS. The cross-section of the PyBN coated PG coupon used for SEM/EDS had to be sputter coated in 5 nm of Au to prevent charging in the PyBN layer during SEM/EDS characterization. Additionally both the PyBN coated sample and plain PG sample used in the FLiNaK salt exposure test had their initial XRD spectrums collected using the same system as described in Section 3.1.3 before the FLiNaK exposure tests.

Post-FLiNaK exposure characterization of the PyBN coated PG and plain PG coupons followed some of the same methods described in Section 3.1.3. Visual inspection of the coupons was conducted and photographs were recorded. Mass changes per surface area after FLiNaK salt exposure were calculated to get a first approximation on whether or not interactions with the salt or 316SST corrosion products occurred. XRD spectrums on the post-FLiNaK exposure coupons were collected to observe any changes in phases due to corrosion product interactions. Cross-sectional SEM/EDS analysis was also performed on both coupons to look at any compositional changes as a result of corrosion product interactions. These SEM/EDS samples were also electroplated in Cu before mounting and polishing in cross-section. The polished cross-sections then were coated in 5 nm of Au to help eliminate charging in the SEM.

A transmission electron microscopy (TEM) plasma focused ion-beam (FIB) lift out was also performed on the plain PG sample to investigate changes at the PG salt interface on a smaller scale than can be resolved by SEM. To perform the lift out, an FEI Helios G4 SEM equipped with a plasma FIB and OmniProbe manipulator was used. Images captured during the TEM lift out preparation are shown in Figure 5-23. When a region of interest was found, a thick cap layer of Pt was deposited on top of the region of interest (Figure 5-23a) to protect it during the lift out preparation. Then two large trenches were milled on either side of the region of interest (Figure 5-23b) using the plasm FIB to begin extracting the lift out. The region of interest is then thinned down while still attached to the PG coupon. Once the region of interest was thinned down to a reasonable thickness where the manipulator could still be attached, a partial U cut was made before the manipulator was welded to the lift out using Pt. The U cut was then finished so that the lift out was free from the plain PG coupon. Finally the lift out was welded to a Cu TEM stub so that the final thinning process could be completed. The lift out was then thinned down (Figure 5-23c) until the thickness of the lift out would be transparent to the electron beam in the TEM. The lift out was then removed from the plasma FIB and analyzed using an FEI Titan equipped with an EDS spectrometer.

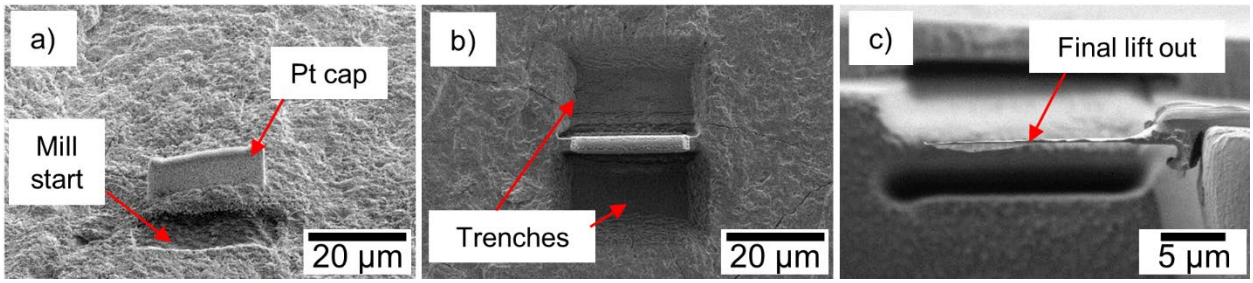

Figure 5-23: Post-FLiNaK exposure plain PG TEM lift out process. a) deposition of the Pt cap layer. b) Trench milling for lift out removal. c) final thinned down lift out sample attached to a Cu TEM stud

5.4.2.3 Results and Discussion

As seen in Figure 5-22a the PyBN coated PG coupons are white in appearance. Due to the thickness of the PyBN coating, it is slightly transparent such that a dull black of the underlying PG substrate

can be observed. Additionally, there appears to be some minor spots that may have coated thicker than the majority of the surface. These spots were not anticipated to be an issue and actually provided a way of identifying each face of the PyBN coated coupon. The plain PG coupons however, did not show significant features on either face. While not necessarily a concern, in fact this would be a good sign for manufacturing, as will be seen later this made identifying each face impossible after the FLiNaK exposure testing.

The cross-sectional SEM/EDS characterization on the PyBN coated PG reference coupon is shown in Figure 5-24. As shown in Figure 5-24a, the reference sample was cut along the width of the sample to perform the SEM/EDS characterization. As shown in Figure 5-24b, the coating thickness varied between the two faces of the coupon by several 10s of μm. The variation in the coating thickness was not expected to have an impact on the overall performance of the coupon in the FLiNaK exposure test. Nor was it expected to change whether or not the PyBN coating helped to eliminate the interactions with the 316SST corrosion products. The coating thickness variation is simply just something to note about the manufacturing of these particular coupons.

The SEM/EDS characterization on the reference PyBN coated PG coupon demonstrated that EDS could qualitatively determine the presence of the PyBN coating. Note the contrast change in the PG substrate and PyBN coating between Figure 5-24b and Figure 5-24c is a result of changing the accelerating voltage of the SEM in order to perform EDS. Additional item to note, is that the nitrogen k-α signal was used to qualitatively determine where the PyBN coating was because the signal from boron's k-α was convoluted in carbon's k-α signal.

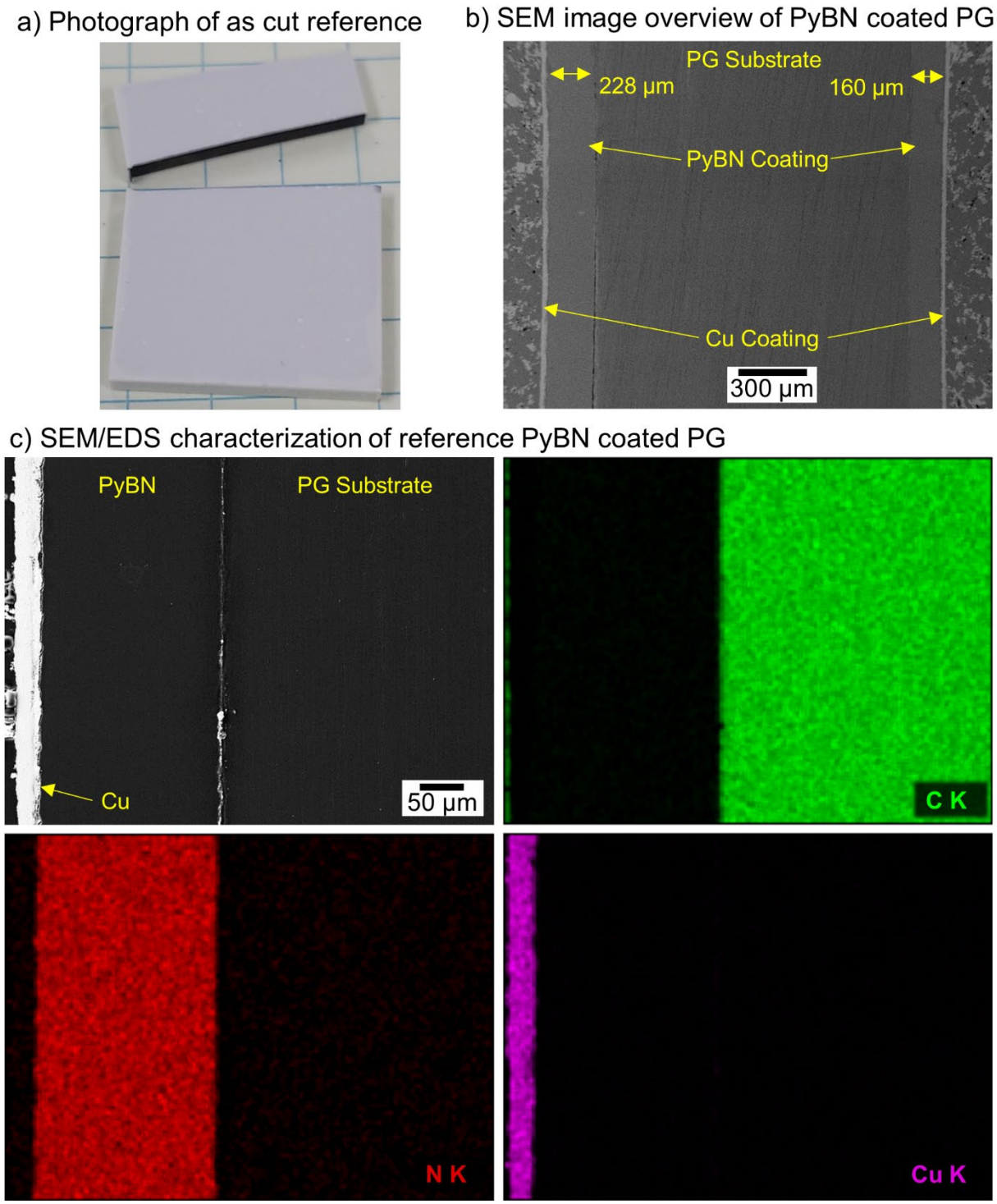

Figure 5-24: SEM/EDS characterization of the as-received reference PyBN coated PG coupon. a) photograph of the as cut reference sample before cross-section mounting. b) zoomed out overview SEM image of PyBN coated PG at 5 kV accelerating voltage. c) zoomed in SEM/EDS characterization at 15 kV accelerating voltage.

Before the FLiNaK exposure testing, XRD spectrums of the as-received PyBN coated PG and plain PG coupon were collected along with their post-FLiNaK exposure spectrums to observed

any changes in phases due to the FLiNaK exposure in a 316SST crucible. Both the as-received and post-FLiNaK exposure XRD spectrums are shown in Figure 5-25. In both of the as-received PyBN coated and plain PG coupon spectrums it is of note that both show that the hexagonal sheets are highly orientated along the c-axis. This is expected as the the pyrolytic production method of both PyBN and PG are done using CVD so it is expected that the materials are essentially grown in 2D hexagonal layers stacked on top of each other. Also of note is that the interplanar spacing between the 2D sheets of boron nitride and graphite determined by the position of the (002) peak, are essentially the same such that the (00*l*) peaks from the PyBN coating and PG substrate are on top of each other. This is observed in literature sources, and the interplanar spacing for both the PyBN coating and PG is observed to be approximately 0.34 nm from the XRD patterns collected in this dissertation [121]. The final thing to note in the as-received PyBN coated PG sample is the appearance of the (100) peak. This peak seems to be the only peak present that could distinctly identify the PyBN coating over the PG substrate. Overall, the XRD spectrums of both as-received materials appears consistent with what is expected suggesting that the manufactured coupons are of relatively good quality in terms of structure.

As for the post-FLiNaK exposure XRD spectrums a number of observations can be made. As seen in Figure 5-25a, after the residual FLiNaK washing procedure, no distinct changes in the PyBN coated PG sample coupon can be observed. All of the (00*l*) peaks as well as the (100) peak are observable with no additional peaks appearing as a result of the FLiNaK exposure in a 316SST crucible. This is a good indication that the PyBN coating has either greatly reduced or eliminated any interactions with the 316SST Fe and Cr containing corrosion products. On the other hand, in Figure 5-25b, it can be observed the plain PG coupon has developed a significant number of additional peaks along with the original (00*l*) peaks as a result of the FLiNaK exposure in a 316SST

crucible. Using peak matching software, the new peaks were matched to a M_7C_3 type carbide phase with a specific stoichiometry of Cr_7C_3 (PDF 00-036-1482). Ai, H. et al. [27] and Sellers, R et al. [48] also identified the carbide phase found on their graphite coupons as Cr_7C_3, but Olson, et al. [46] observed both Fe and Cr in their carbide coating after FLiNaK exposure so it's expected that the carbide phase in Figure 5-25b is likely a M_7C_3 type carbide but with both Cr and Fe. This result clearly demonstrates that the presence of graphite in the system leads to interactions between the graphite and 316SST salt crucible, whereas the PyBN coated PG appears to undergo no interaction with the 316SST crucible.

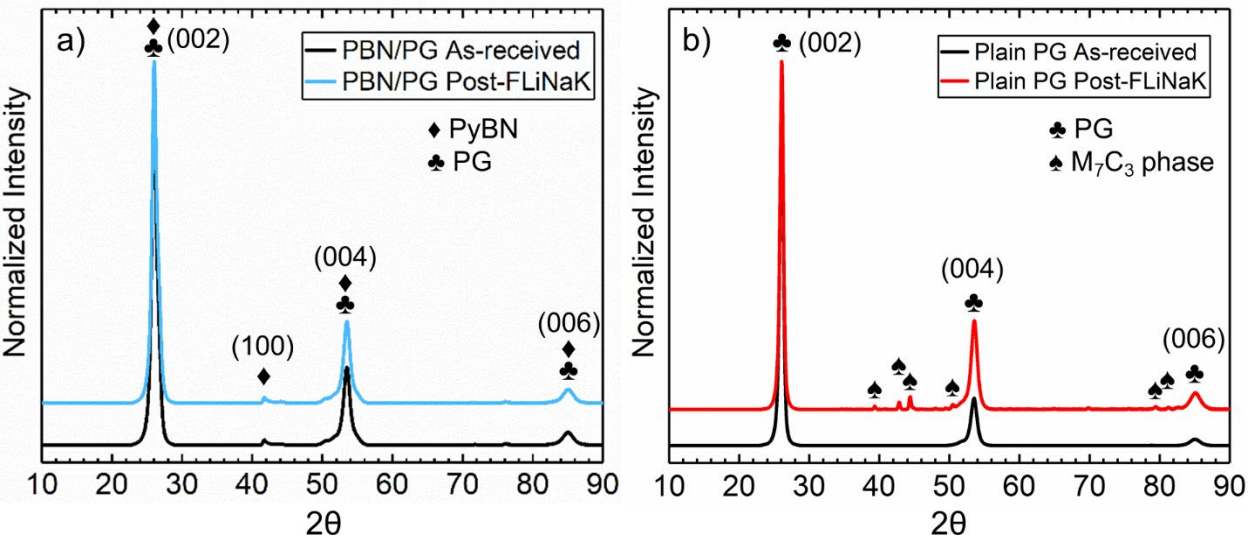

Figure 5-25: XRD spectrums of the a) as-received (black) and post-FLiNaK exposure (blue) PyBN coated PG coupon and b) as-received (black) and post-FLiNaK exposure (red) plain PG coupon.

With the XRD spectrums showing the possible interaction of the plain PG coupon with the 316SST crucible, visual characterization of the post-FLiNaK exposure coupons was also performed. As seen in Figure 5-26a, the PyBN coated PG coupon visually appear to have no change in color as would be expected by a lack of interaction with Fe and Cr corrosion products. However, some damage to the PyBN coating after being exposed to the FLiNaK salt is observed. The damage, however, was not large enough to make determining the original faces impossible. The original spots used to distinguish the two faces of the coupon (marked with red circles) are still observable

after the FLiNaK exposure. The left face of the PyBN coated PG coupon actually appears to have little damage at all. The right face shows a large blister had formed in the PyBN coating. Near the top right of the blister a hole (marked with a red square) in the PyBN coating can be seen, and is believed to be where the blister must have formed. However, it can be observed in Figure 5-27 that the hole does not appear to go through the entire coating. Because of the CVD production method of the PyBN coating, the PyBN coating is essentially individual layers of hexagonal boron nitride grown on top of each other in an AA stacking pattern, so the blister is believed to have formed between the layers, but never breaking entirely though to expose the PG substrate.

As for the plain PG coupon after the FLiNaK exposure test shown in Figure 5-26a, it can be seen that there has been a dramatic change in the visual appearance of the coupon. The coupon has become covered in a visible silvery film similar to the one observed by Sellers et al. shown in Figure 5-20a [48]. The film has made determining the original faces of the plain PG coupon impossible. Additionally, the film appears to be rather flaky. It's possible that some of the film may have flaked off of the coupon during the post-FLiNaK washing process. Following the results from the XRD in Figure 5-25b, it's believed that this film is the M_7C_3 phase formed as a result of the PG's interactions with Fe and Cr corrosion products coming from the corrosion of the 316SST crucible. It's important to note that if this film were to form in a reactor system and indeed showed a tendency to flake off, then it may lead to solid particulate floating in the molten salt system which may contribute to erosion over long periods of time if not filtered out.

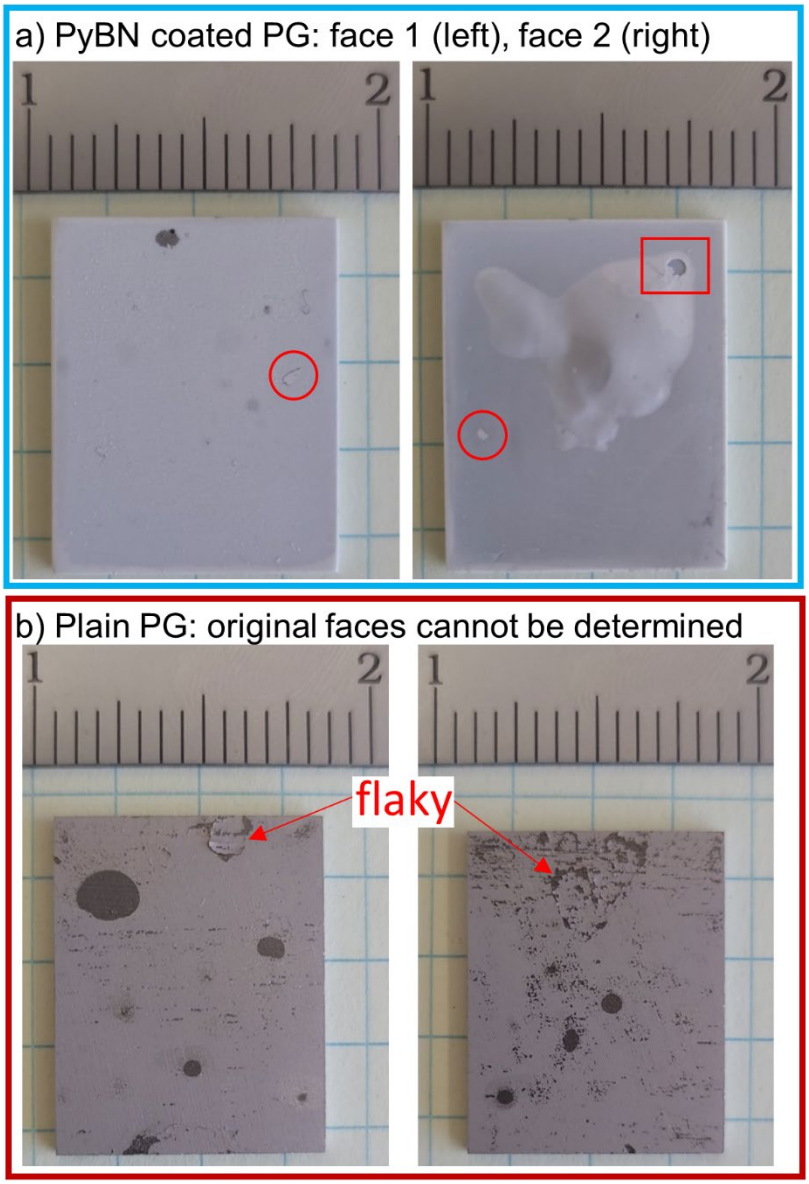

Figure 5-26: Photographs of the cleaned post-FLiNaK exposure coupons. a) PyBN coated PG coupon, original face markers are marked by red circles. b) plain PG coupon. Scale units are inches.

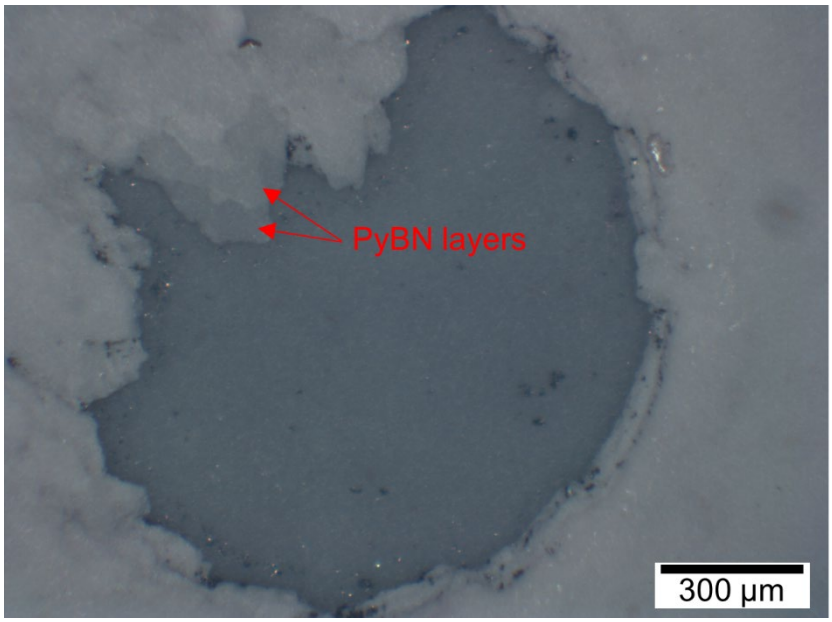

Figure 5-27: Optical image of the hole starting the blister marked in Figure 5-26a. Individual layers of the PyBN coating can be observed, but PyBN coating does not appear to be completely breached.

The mass change results post-FLiNaK exposure provide some indication on how the coupons performed during the salt exposure as well as indicate interaction with corrosion products. As seen in Figure 5-28, the PyBN coated PG coupon does experience a slight mass loss after being exposure to FLiNaK salt in a 316SST crucible after 500 hrs at 700 ºC. However, the mass loss is rather minimal indicating the PyBN coating does perform well and is likely mostly explained by the blistering observed in Figure 5-26a and Figure 5-27. The plain PG coupon showed a somewhat significant amount of mass gain as a result of the FLiNaK exposure in the 316SST corrosion crucible. The PG itself, is not anticipated to be negatively affected by fluoride base salts in terms of being corroded, however as already discuss, the presence of graphite provides a large activity gradient for carbide forming elements. As already observed in the XRD spectrum, Figure 5-25b, and the visual inspection, Figure 5-26b, of the plain PG coupon, it's clear that a new carbide phase exists at the surface of the plain PG coupon. This carbide phase must form as a result of interaction with corrosion products coming from the corrosion of the 316SST crucible, so the mass gain observed in the plain PG coupon is explained by the uptake of the corrosion products as carbide

formation. As noted in the visual inspections, the carbide film does appear to be flaky, and some of the film may have been washed off during the post-FLiNaK washing procedure meaning the mass gain of the plain PG coupon after FLiNaK exposure was likely even higher than what was able to be recorded.

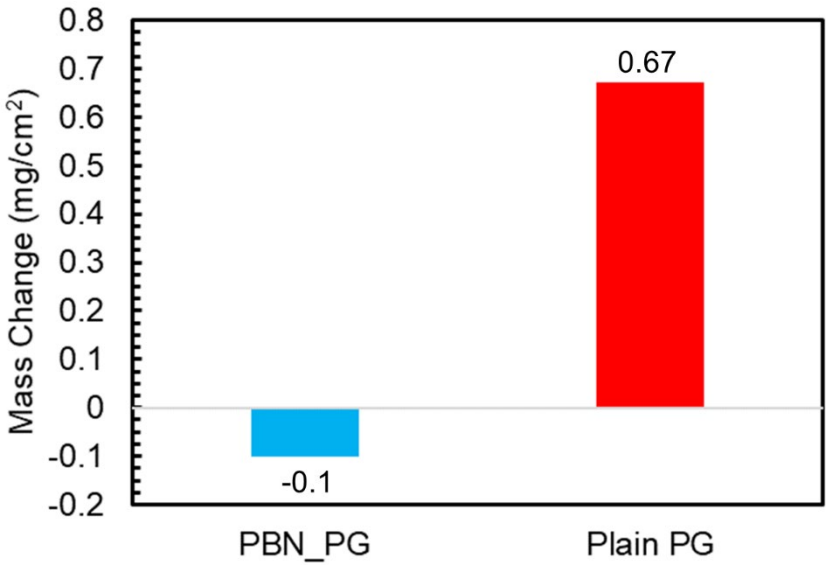

Figure 5-28: Mass change data from the post-FLiNaK PyBN coated PG and plain PG coupons tested in a 316SST salt crucible.

Though the PyBN coated PG coupons showed little to no evidence of interaction to the corrosion products of 316SST, the post-FLiNaK exposure coupon was still sectioned and observed in cross-section for SEM/EDS characterization. As seen in the composite image in Figure 5-29a, the PyBN coating and PG substrate show little change as compared to the reference PyBN coated PG sample. The PyBN coating appears to have largely remained intact. In the zoomed in SEM image in Figure 5-29b, a nm sized gap could potentially be forming about 10 μm into the coating, potentially indicating the start of coating delamination between the PyBN layers. During the EDS collection, the system was not told to exclude any elements and the software was allowed to determine elements present based on the collected spectrum. As seen in Figure 5-29b, only the Cu coating added post-FLiNaK exposure, nitrogen indicating the PyBN layer, and carbon could be identified.

Once again this result shows the PyBN coating was successful in dramatically reducing and potentially completely eliminating graphite interactions.

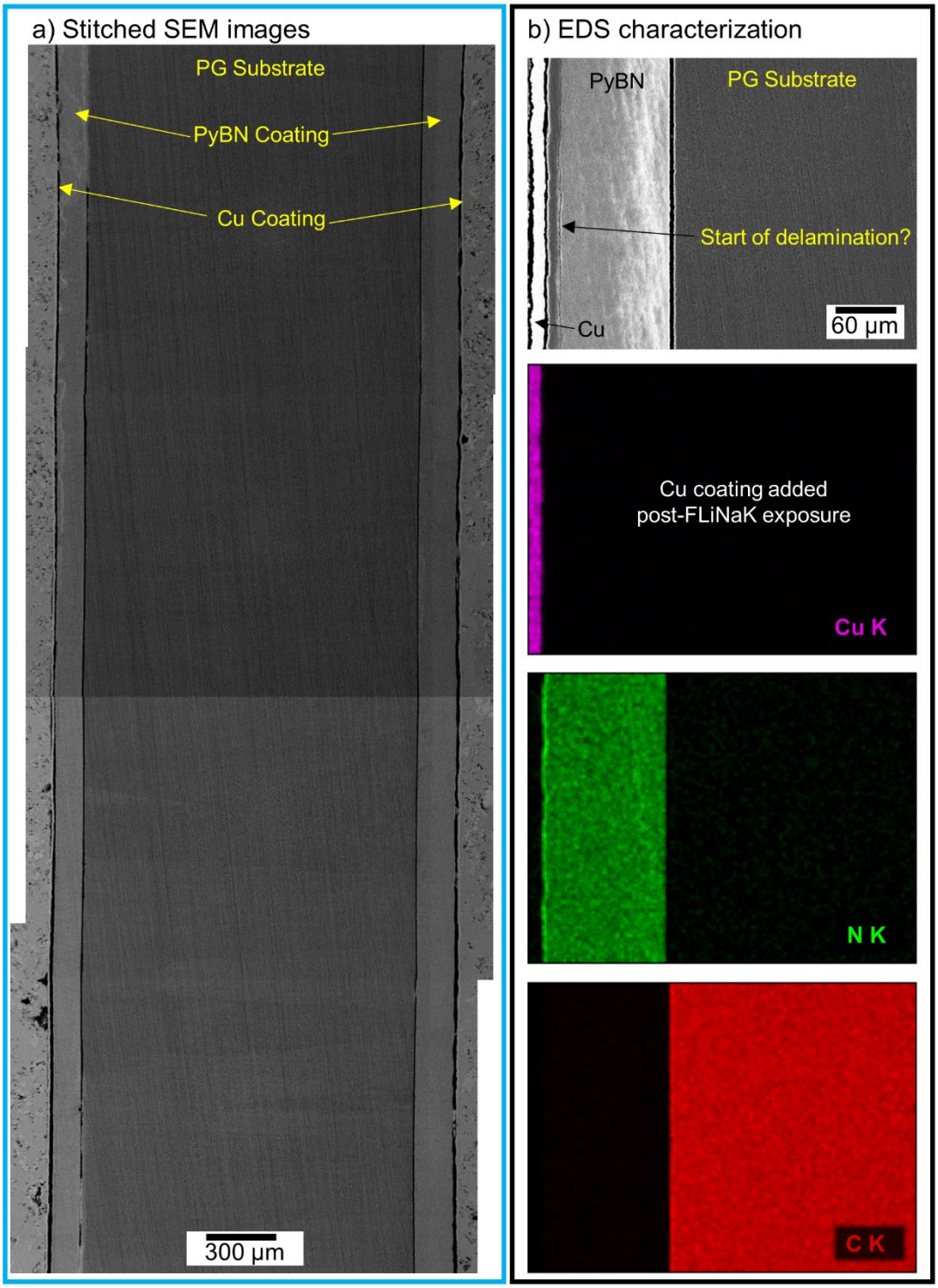

Figure 5-29: SEM/EDS characterization of the post-FLiNaK exposure PyBN coated PG coupon tested in a 316SST crucible. a) composite SEM images along the width of the sample. b) zoomed in region where EDS characterization was performed.

While the PyBN coated PG's cross-section showed little to no interaction with the salt and corrosion products of the 316SST crucible, the plain PG cross-section served to provide more evidence of it's interactions with the Fe can Cr containing corrosion products. The plain PG coupon was electroplated with a Cu layer post-FLiNaK exposure to protect the cross-section during metallographic preparation so as seen in Figure 5-30a, where the Cu coating has good adherence to the PG it can be difficult to see the contrast difference of the M_7C_3 film until a relatively high magnification. But, at high magnification and in the EDS characterization of the salt facing side of the coupon with the graphite layers parallel to the salt, Figure 5-30b, it can be observed that the M_7C_3 film is clearly growing on top of the PG layers. By the EDS maps it's clear that the M_7C_3 film contains concentrations of both Fe and Cr, similar to the film observed by Olson et al. [46], and is approximately 1-2 μm in thickness.

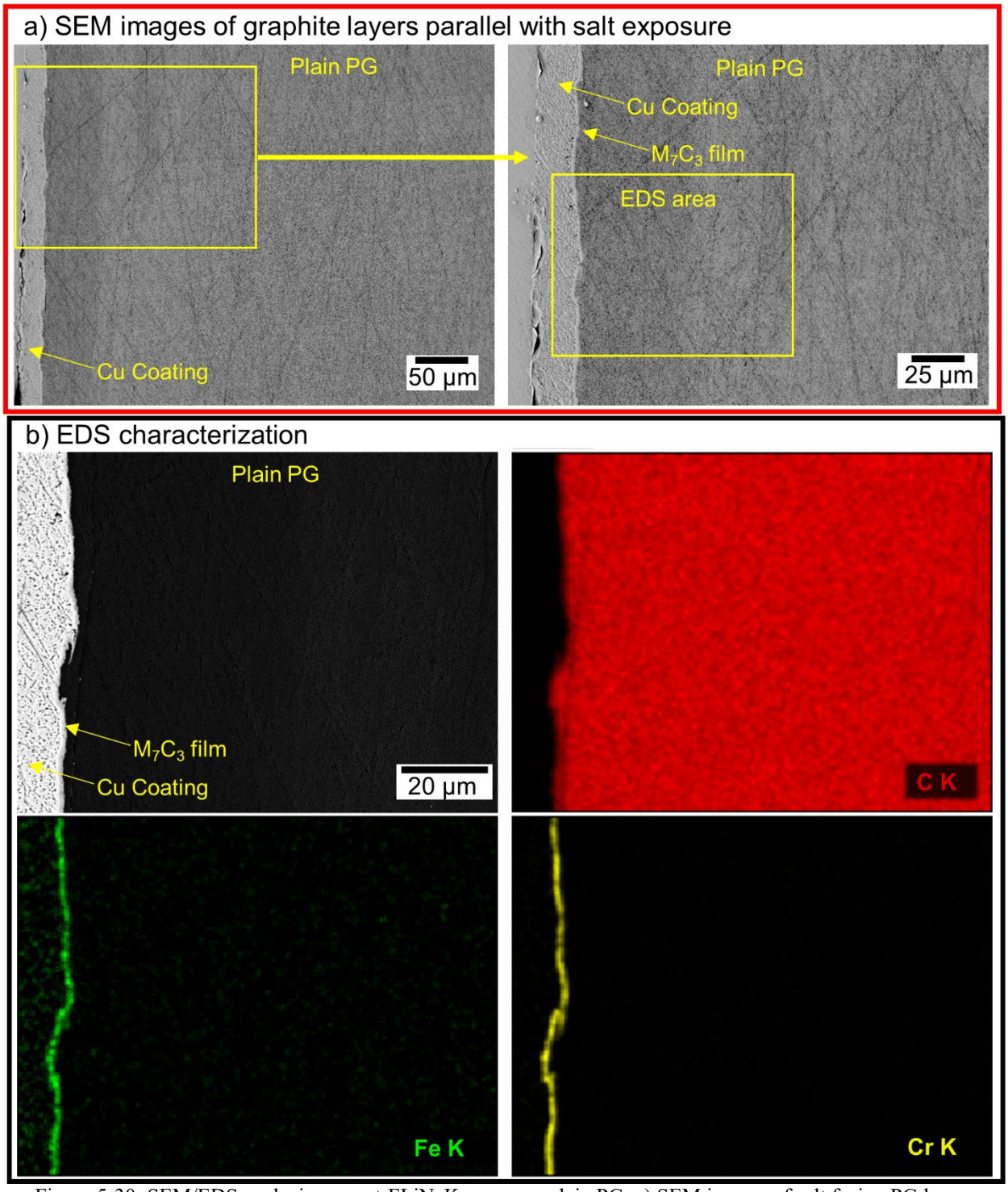

Figure 5-30: SEM/EDS analysis on post-FLiNaK exposure plain PG. a) SEM images of salt facing PG layers parallel to salt. c) EDS characterization. c) SEM images of salt facing edge PG layers perpendicular to salt.

With how the cross-section on the plain PG was prepared, it was also possible to look at the edges of the coupon where the PG layers are perpendicular to the salt facing edge. Along this edge a few

notable differences in the M_7C_3 film can be observed. In Figure 5-31 when the PG layers are perpendicular to the salt the thickness of the M_7C_3 film is slightly larger than the parallel orientation at approximately 2-4 µm. This is assumed to be a result of how either loose carbon in the PG or Fe and Cr diffuse in PG. In the parallel orientation diffusion effectively has to go through hexagonal sheets of carbon which should be slower than diffusion in-between the hexagonal sheets as in the perpendicular orientation. Additionally, in the perpendicular orientation it can be observed that the M_7C_3 film is able to penetrate and grow in-between layers of the PG instead of just on top of the layers. This is observed in both edges of the coupon, but is best observed on the top edge, Figure 5-31b. Again, this is speculated to be because Fe and Cr could more easily diffuse between the hexagonal sheets. It can't be confirmed for certain from this single test, but it's also speculated that because of this penetration, the growth of M_7C_3 film could potentially cause delamination in between the PG layers leading to degradation of the PG overtime.

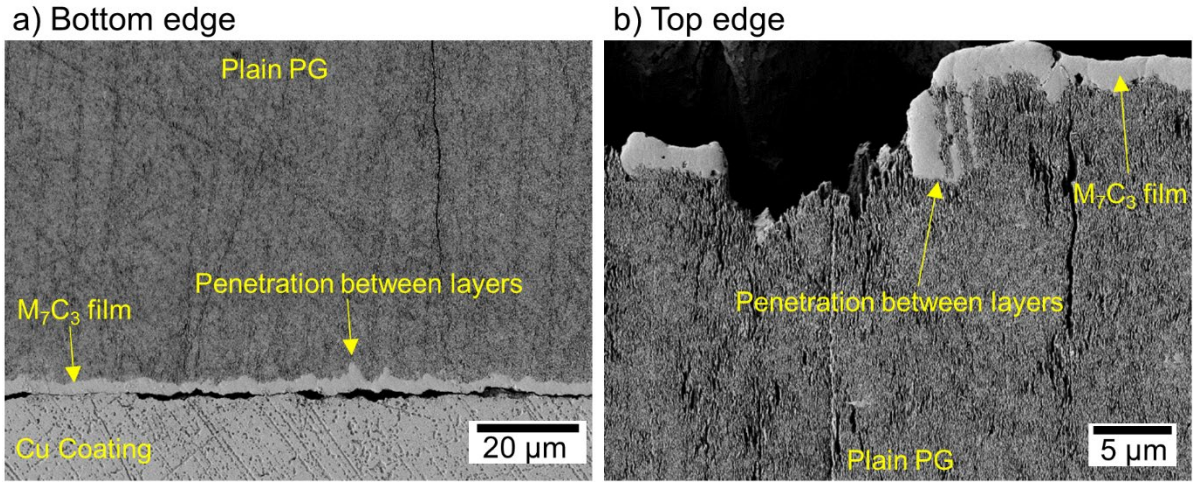

Figure 5-31: Edges of the plain PG coupon where the layers are perpendicular to the salt facing edge of the coupon. a) bottom edge of the coupon. b) top edge of the coupon.

Due to the thickness of the M_7C_3 film, characterization with EDS was really only qualitative as the electron beam interaction volume is on the same order of size as the film thickness. As discussed in Section 5.4.2.2 and shown in Figure 5-23, a thinned down lift out containing the M_7C_3 film was prepared to investigate the film using TEM where the electron beam interaction volume is much

smaller. Shown in Figure 5-32a is the TEM lift out sample that was prepared with FIB. Figure 5-32b and c show the lift out sample imaged in the TEM. As seen in Figure 5-32c the Pt cap protected the M_7C_3 layer on top of the PG during the FIB preparation. The Pt cap layer shows some contrast differences because a thin layer of Pt was deposited with the aid of the electron beam before the remainder of the Pt cap was deposited with the ion beam. Also observed in Figure 5-32b and c are voids within the M_7C_3 layer. It's unclear if these voids formed during the FLiNaK exposure and growth of the M_7C_3 layer or if they formed during the FIB lift out preparation. The primary reason of making this lift out was to get a better quantification of the Fe and Cr inside the M_7C_3 layer. As seen in the line scan analysis, Figure 5-32d, the M_7C_3 layer does primarily consist of Cr, but there is a reasonable concentration of Fe as well. From these ratios it appears the Fe and Cr exist in the M_7C_3 layer in a 1:6 ratio (Fe:Cr) such that the carbide phase stoichiometry is approximately $FeCr_6C_3$.

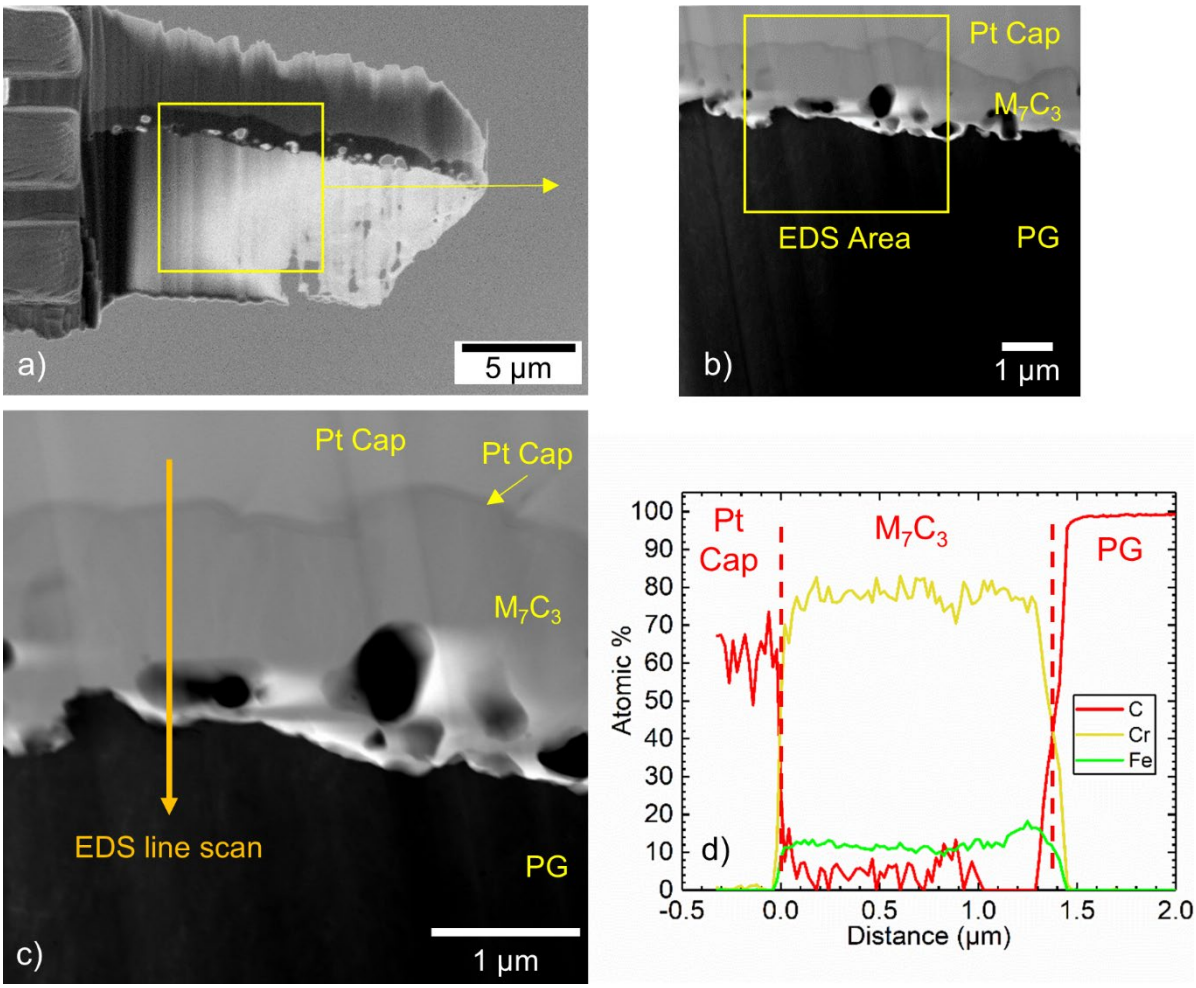

Figure 5-32: TEM/EDS analysis on the plain PG lift out. a) completed thinned down lift out still in SEM FIB. b) Overview of the TEM imaging area. c) Zoomed area where the EDS line scan marked with orange line was performed. c) results of the EDS line scan.

5.5 Conclusions from Activity Gradient Interactions

From all of the investigation and experiments on activity gradient interactions presented in this chapter it's clear that the material interactions in a FLiNaK medium, and more generally a molten salt medium, have significant effects on how dissimilar materials behave when present together. It has been clearly demonstrated that the interactions between dissimilar materials are not dependent on a galvanic connection and therefore cannot be eliminated through electrical isolation. Fortunately, it has also been demonstrated in this chapter that interactions through activity

gradients can be predicted accurately using computational methods to calculate the existence of activity gradients between dissimilar materials, making it possible to predict what dissimilar material couples could result in interaction. Furthermore, when dissimilar materials that show no activity gradient for elemental transport exist in the same molten salt medium their interactions appear to be negligible to non-existent. So, when designing static isothermal salt exposure tests, activity gradients between the materials being tested need to be accounted for because their effects can dramatically change the results of materials being tested. Once again, this result has the effect of producing corrosion results that may not accurately represent how a material performs by itself in a molten salt environment.

Finally, graphite is anticipated to be a very important material for MSR designs, specifically the FHR, likely being present as the moderator, fuel containment material, and possible structure material. Unfortunately, graphite presents a large activity gradient due to the fact that most transition metals used in alloys have a favorable formation energy for carbide formation. This has the potential to present a major challenge for interactions between the graphite based materials and the metallic containment structure of the FHR. These interactions could lead to the accelerated degradation of the metallic structure and formation of debri in the coolant salt as well as potential degradation of the graphite. In this dissertation, the potential novel application of PyBN coatings to graphite have been shown to dramatically reduce graphite interactions with metallic corrosion products. Additionally, the production of these PyBN coatings have the potential to be implemented into production lines of graphite based materials without significant changes being needed to the process.

Chapter 6

Conclusions and Future Work

With ongoing changes to policies and the ever growing need to reduce greenhouse gas emissions, there has been a significant increase in interest in nuclear energy technologies by government agencies, private companies, and research institutions. Specifically, molten salt reactor concepts originally developed almost half a century ago are garnering much of the interest because of their inherent safety advantages over current generation light-water reactor systems. In support of the MSR design and development, many groups are now looking at understanding how current and future alloy systems and materials are going to perform in molten salt coolants. As part of these efforts, a popular test that has been developed is the exposure of interested alloys and materials to salts in static isothermal salt exposure testing environments. A major challenge in these tests is understanding how the different parameters in the test's design in turn affect the results that come out these tests. The primary goal of this dissertation was to explore some of the parameters that can be varied in a static isothermal salt exposure test, and determine what effects the variations have. The parameters studied in this dissertation include the volume of salt to exposure surface area ratio, the purity of the salt medium being used, and the effect that dissimilar materials have on one another.

Salt exposure tests on 316HSST samples conducted at different volume of salt to exposure surface area ratios in this dissertation clearly demonstrate that this ratio can dramatically change how 316HSST performs in the salt medium. In the salt medium, 316HSST is degraded through corrosion reactions that consume impurities in the salt. Therefore in small volumes of salt, the

overall number of impurities available to react with the 316HSST can be limited and therefore as these impurities are consumed the salt redox potential quickly becomes less oxidizing and the degradation of the 316HSST starts to slow down. However, in larger volumes of salt, there exist enough impurities to keep the salt redox potential in an oxidizing condition which in turn continues the degradation of the 316HSST samples for much longer salt exposure times. The primary issue created in this situation is that when determine a corrosion rate, the conversion of mass loss to rate can be completely inaccurate and therefore lead to inaccurate measurements of a materials performance if the degradation stops at an unknown time. A potential new evaluation method for an alloys performance is then to determine the corrosion plateau time for a given alloy in a given salt at a given volume of salt. In this evaluation, high performing materials should consume impurities at a slower rate and therefore plateau at much longer salt exposure times.

Intimately related to the volume of salt to exposed surface area ratio is the salt purity. As mentioned above, the degradation of the 316HSST samples is a result of corrosion reactions with impurities in the salt medium. Therefore, the concentration of impurities in salt at the start of a static isothermal salt exposure test essentially determines the concentration of corrosion products that can result during the salt exposure. In this dissertation, 316HSST samples exposed to as-received commercial FLiNaK and purified FLiNaK at similar volume of salt to surface area ratios and salt exposure conditions clearly showed that purification removes impurities in the as-received FLiNaK and ultimately results in lower degradation of 316HSST. Additionally, it was hypothesized then that the corrosion plateau time could also be an indication of how pure a given salt is. A pure salt with few impurities will plateau at a much faster time as fewer impurities exist in the salt initially.

Finally, perhaps the biggest influence on a static isothermal salt exposure test was shown to be the interaction of dissimilar materials that are present in the same salt medium. Electron transfer through a galvanic couple is often believed to be the root cause of dissimilar material interactions in any medium; however, it has been suggested in molten salt literature and clearly demonstrated in this dissertation that dissimilar materials do not need to be in intimate electrical contact in order to interact with one another in salt mediums. Instead what appears to be the primary driver for dissimilar material interactions is the existence of an activity gradient between elements in one material to that element's activity if it were to exist in another material. These interactions through activity gradients have been demonstrated in this dissertation to be accurately predictable by the use of computational tools. In salt exposure tests involving 316SST salt crucibles and dissimilar metal coupons, the computed activity gradient behavior was accurately reflected in the transport behavior of Fe and Cr containing corrosion products in FLiNaK salt exposure tests. Additionally, exposure tests of 304SST coupons in dissimilar material crucibles clearly demonstrated the enhanced degradation that occurs when an activity gradient for mass transport is present.

Because of its importance to the MSR, specifically the FHR design, a final salt exposure test was conducted with graphite based materials. Graphite is a challenging material when it comes to activity gradient interactions because practically all transition metals used in metal alloys have a favorable formation energy for carbide formation and therefore an activity gradient for elemental transport always exists. This elemental transport from metallic alloys to graphite may pose an important challenge as transport could accelerate an alloys degradation and has the potential of creating solid debri in the salt coolant. Pyrolytic boron nitride coatings on graphite were tested in this dissertation and were shown to have excellent performance in a fluoride salt based coolant while also greatly reducing the ability of graphite to interact with corrosion products from a metal

alloy. Additionally, the production of these pyrolytic boron nitride coatings have the potential to be easily implemented in the production of graphite based materials used in MSR designs.

6.1 Future Work

6.1.1 Further Evaluation of PyBN Coatings on Graphite

The main concern of using a PyBN coating on graphite materials in an MSR is the neutron poisoning effect of boron-10. To produce PyBN coatings on graphite, a CVD growth method is used along with the appropriate precursor gases. Precursor gases are likely produced using naturally occurring boron which contains approximately 20% boron-10 and 80% boron-11 [122]. The neutron absorption cross-sections for thermal neutrons for these two isotopes is approximately 3835 barns and 0.0055 barns for boron-10 and boron-11, respectively [123]. The overall neutron cross section for natural boron is then the weighted averaged of the individual cross-sections such that natural boron has a thermal neutron cross-section of approximately 770 barns. This cross-section is likely too large to overcome with simply changes to an MSR design.

However, enriched boron-11 products are readily available as byproducts from the enrichment of boron-10 in purities greater than 99%. The products are available in several forms, including $B^{11}F_3$ and boron-oxide. Both of which can be converted to $B^{11}Cl_3$ which is one of the most popular precursor gases used in the production of PyBN. At 99% enrichment of boron-11, the thermal neutron absorption cross-section then becomes approximately 40 barns. With the cross section dramatically lowered, neutronic calculations could be performed in order to see how higher fuel enrichments might be able to combat the addition of a PyBN coating to graphite materials.

6.1.2 Study of Thermal Gradient Effects

In this dissertation several parameters of the prototypical static isothermal salt exposure test were studied, but a significant parameter missing in these tests is the presence of a thermal gradient. In a reactor system, the salt doesn't sit at a constant temperature as it does in a static isothermal test. The salt flows from the reactor core, where it reaches its highest temperatures through a heat exchanger where it dumps heat to another transfer fluid. As the salt goes through the heat exchanger its temperature drops before it reenters the core to be reheated and the cycle is continued. As mentioned in Section 1.4, the ARE and MSRE programs dedicated an enormous amount of resources to building and evaluating thermal gradient loops so that the effect of the temperature gradient could be studied [24]. While these loops are a challenge to design, operate, and evaluate, not capturing the effect of the thermal gradient may limit the knowledge that can be gained from the prototypical salt exposure test. All reactions, including corrosion reactions, have an associated equilibrium constant to them that dictates how far a reaction can go towards completion. This equilibrium constant is temperature dependent. So, what has been observed in thermal gradient loops is large amounts of degradation in the hot section as the corrosion reactions try to reach equilibrium, but material deposition in the cold section because the salt is now supersaturated with corrosion products [124]. So, future efforts towards investigated materials in the presensce of thermal gradients is likely going to be required to get a more complete picture of materials behavior in molten salt reactor type environments.

6.1.3 Study of Irradiation Effects

Radiation is known to have profound effects on materials used in nuclear reactors including swelling, increased hardness, embrittlement, and environmentally induced cracking [125]. Metallic alloys and other materials used in an MSR are projected to be exposed to higher

temperatures and higher irradiation doses than materials used in current reactor systems so understanding how irradiation effects materials, including how it affects corrosion, in molten salts is going to be critical. Recent studies have primarily focused on how irradiation affects the mechanical properties of alloys. For example several researchers have studied how alloy properties are affected by ion irradiation [126-128], but fewer studies exist on how irradiation may affect the corrosion behavior of alloys in molten salt.

Some recent work has attempted to use He^{+} ion pre-irradiation and salt exposure to understand the effect of irradiation on corrosion, but the use of short range ion irradiations may severely limit the information coming from these studies [129, 130]. Ions have a limited penetration range in alloys on the order of only 1-2 μm depending on the incident energy. But, the effects of corrosion in molten salts are typically on the order of several microns so it's difficult to attribute changes to corrosion directly to the ion irradiation. Of the more recent irradiation work on corrosion effects, in-situ irradiation and corrosion experiments performed by Zhou et al. [131] appear to be the most promising approach to investigating how irradiation may change the corrosion behavior of alloys also being subjected to molten salt corrosion.

In Zhou et al's work, model alloys were used to seal a salt chamber that was positioned inside a proton accelerator so that the sample could be irradiated with protons with a high enough energy to penetrate all the way through the sample while the backside of the sample is also being exposed to a molten salt [131]. In the model alloys it was observed that irradiation could prove to be beneficial to corrosion based on a "self-healing" mechanism were interstitial atoms created during irradiation fill in the vacancies created from corrosion; however, model alloys can only reveal a limited number of insights so tests on true engineering alloys like stainless steel need to be

performed. The University of Wisconsin-Madison is perfectly poised for such experiments using the Ion Beam Laboratory and experimental equipment designed by the author.

References

[1] Energy and The Environment Explained: Greenhouse Gases and The Climate, in: Energy Explained, eia.gov.
[2] Energy and The Environment Explained: Where Greenhouse Gases Come From, in, eia.gov.
[3] A Technology Roadmap for Generation IV Nuclear Energy Systems, U.S. DOE Nuclear Energy Research Advisory Committee and The Generation IV International Forum, (2002).
[4] Technology Roadmap Update for Generation IV Nuclear Energy Systems, OECD Nuclear Energy Agency for the Generation IV International Forum, (2014).
[5] J. Serp, M. Allibert, O. Beneš, S. Delpech, O. Feynberg, V. Ghetta, D. Heuer, D. Holcomb, V. Ignatiev, J.L. Kloosterman, L. Luzzi, E. Merle-Lucotte, J. Uhlíř, R. Yoshioka, D. Zhimin, The molten salt reactor (MSR) in generation IV: Overview and perspectives, Progress in Nuclear Energy, 77 (2014) 308-319.
[6] N. Touran, Molten Salt Reactors, in, whatisnuclear.com.
[7] W.B. Cottrell, H.E. Hungerford, J.K. Leslie, J.L. Meem, Operation of The Aircraft Reactor Experiment - ORNL 1845, in, Oak Ridge National Laboratory, Tennessee, 1955.
[8] E.S. Bettis, R.W. Schroeder, G.A. Cristy, H.W. Savage, R.G. Affel, L.F. Hemphill, The Aircraft Reactor Experiment-Design and Construction, Nuclear Science and Engineering, 2 (1957) 804-825.
[9] M.W. Rosenthal, P.R. Kasten, R.B. Briggs, Molten-Salt Reactors—History, Status, and Potential, Nuclear Technology, 8 (1970) 107-117.
[10] Report of the Fluid Fuel Reactors Task Force, United States Atomic Energy Commision, TID-8507 (1959).
[11] W.R. Grimes, Molten-Salt Reactor Chemistry, Nuclear Application & Technology, 8 (1970) 137-155.
[12] MSR Technology Primer, in, https://egeneration.org/msr-primer/, 2017.
[13] P.N. Haubenreich, J.R. Engel, Experience with the Molten-Salt Reactor Experiment, Nuclear Applications & Technology, 8 (1970) 118-136.
[14] M.W. Rosenthal, R.B. Briggs, P.N. Haubenreich, Molten-Salt Reactor Program Semiannual Progress Report for Period Ending August 31, 1972, Oak Ridge National Laboratory, ORNL-4832 (1972).
[15] B.M. Elsheikh, Safety assessment of molten salt reactors in comparison with light water reactors, Journal of Radiation Research and Applied Sciences, 6 (2013) 63-70.
[16] D.A. Jones, Principles and Prevention of Corrosion, Prentice Hall, 1996.
[17] D.J. Young, High Temperature Oxidation and Corrosion of Metals, Elsevier, 2016.
[18] K. Sridharan, T.R. Allen, 12 - Corrosion in Molten Salts, in: F. Lantelme, H. Groult (Eds.) Molten Salts Chemistry, Elsevier, Oxford, 2013, pp. 241-267.
[19] A. Roine, HSC Chemistry 7 v. 7.00, in, Outotec Research Oy, 2009.
[20] B.C. Kelleher, Purification and Chemical Control of Molten Li₂BeF₄ for a Fluoride Salt Cooled Reactor, in, The University of Wisconsin - Madison, Ann Arbor, 2015, pp. 283.

[21] I.N. Ozeryanaya, Corrosion of metals by molten salts in heat-treatment processes, Metal Science and Heat Treatment, 27 (1985) 184-188.
[22] L.C. Olson, Materials corrosion in molten lithium fluoride-sodium fluoride-potassium fluoride eutectic salt, in, The University of Wisconsin - Madison, Ann Arbor, 2009, pp. 260.
[23] J.W. Koger, A.P. Litman, MASS TRANSFER BETWEEN HASTELLOY N AND HAYNES ALLOY NO. 25 IN A MOLTEN SODIUM FLUOROBORATE MIXTURE, in, United States, 1971, pp. Medium: ED; Size: Pages: 28.
[24] G.M. Adamson, R.S. Crouse, W.D. Manly, INTERIM REPORT ON CORROSION BY ZIRCONIUM-BASE FLUORIDES, in, United States, 1961, pp. Medium: ED; Size: Pages: 60.
[25] K. Britsch, M. Anderson, P. Brooks, K. Sridharan, Natural circulation FLiBe loop overview, International Journal of Heat and Mass Transfer, 134 (2019) 970-983.
[26] S.S. Raiman, G. Muralidharan, R.T. Mayes, J.M. Kurley Iii, Compatibility studies of cladding candidates and advanced low-Cr superalloys in molten NaCl-MgCl₂, in, United States, 2019.
[27] H. Ai, J. Hou, X.-X. Ye, C.L. Zeng, H. Sun, X. Li, G. Yu, X. Zhou, J.-Q. Wang, Influence of graphite-alloy interactions on corrosion of Ni-Mo-Cr alloy in molten fluorides, Journal of Nuclear Materials, 503 (2018) 116-123.
[28] H. Sun, X. Ding, H. Ai, G. Lei, X. Yang, J.-Q. Wang, Interaction mechanisms of a Hastelloy N-316L stainless steel couple in molten LiF-NaF-KF salt, Corrosion Science, 164 (2020) 108317.
[29] Q. Dai, X.-X. Ye, H. Ai, S. Chen, L. Jiang, J. Liang, K. Yu, B. Leng, Z. Li, X. Zhou, Corrosion of Incoloy 800H alloys with nickel cladding in FLiNaK salts at 850 °C, Corrosion Science, 133 (2018) 349-357.
[30] W.H. Doniger, C. Falconer, M. Elbakhshwan, K. Britsch, A. Couet, K. Sridharan, Investigation of impurity driven corrosion behavior in molten 2LiF-BeF2 salt, Corrosion Science, 174 (2020) 108823.
[31] C. Falconer, W.H. Doniger, L. Bailly-Salins, E. Buxton, M. Elbakhshwan, K. Sridharan, A. Couet, Non-galvanic mass transport in molten fluoride salt isothermal corrosion cells, Corrosion Science, 177 (2020) 108955.
[32] K.J. Chan, P.M. Singh, Corrosion Behavior of Pre-Carburized Hastelloy N, Haynes 244, Haynes 230, and Incoloy 800H in Molten FLiNaK, Nuclear Technology, 206 (2020) 1751-1768.
[33] G. Zheng, Corrosion Behavior of Alloys in Molten Fluoride Salts, in, The University of Wisconsin - Madison, Ann Arbor, 2015, pp. 187.
[34] S.S. Raiman, S. Lee, Aggregation and data analysis of corrosion studies in molten chloride and fluoride salts, Journal of Nuclear Materials, 511 (2018) 523-535.
[35] J.H. Shaffer, PREPARATION AND HANDLING OF SALT MIXTURES FOR THE MOLTEN SALT REACTOR EXPERIMENT, in, United States, 1971, pp. Medium: ED; Size: Pages: 41.
[36] S. Delpech, C. Cabet, C. Slim, G.S. Picard, Molten fluorides for nuclear applications, Materials Today, 13 (2010) 34-41.
[37] J. Qiu, B. Leng, H. Liu, D.D. Macdonald, A. Wu, Y. Jia, W. Xue, G. Yu, X. Zhou, Effect of SO42− on the corrosion of 316L stainless steel in molten FLiNaK salt, Corrosion Science, 144 (2018) 224-229.
[38] Y. Zhu, J. Qiu, J. Hou, W. Liu, H. Chen, H. Ai, G. Yu, J. Wang, X. Zhou, Effects of SO42− ions on the corrosion of GH3535 weld joint in FLiNaK molten salt, Journal of Nuclear Materials, 492 (2017) 122-127.

[39] H. Xu, Q. Liu, B. Leng, W. Zhang, X.-X. Ye, F. Han, X. Li, R. Liu, J. Wang, Non-uniform corrosion of UNS N10003 alloy induced by trace SO42- in molten FLiNaK salt, Corrosion Science, 192 (2021) 109802.
[40] D.F. Williams, L.M. Toth, K.T. Clarno, Assessment of Candidate Molten Salt Coolants for the Advanced High-Temperature Reactor (AHTR), in, 2006.
[41] Q. Liu, H. Sun, H. Yin, L. Guo, J. Qiu, J. Lin, Z. Tang, Corrosion behaviour of 316H stainless steel in molten FLiNaK eutectic salt containing graphite particles, Corrosion Science, 160 (2019) 108174.
[42] C. Knosalla, M. Lau, L. Schmies, W. Lippmann, A. Hurtado, Investigation on the Corrosion Behavior of Nickel-Base Alloys in Molten Chlorides for Sensible Heat Energy Applications, Advanced Engineering Materials, 22 (2020) 2000099.
[43] Q. Liu, B. Leng, J. Qiu, H. Yin, J. Lin, Z. Tang, Effect of graphite particles in molten LiF-NaF-KF eutectic salt on corrosion behaviour of GH3535 alloy, Corrosion Science, 168 (2020) 108581.
[44] J.R. Keiser, X. He, D. Sulejmanovic, J.N. Qu, K.R. Robb, K. Oldinski, Material Selection And Corrosion Studies Of Candidate Bearing Materials For Use In Molten Chloride Salts, Journal of Solar Energy Engineering, (2022) 1-12.
[45] V. Pavlík, M. Boča, A. Kityk, Accelerated corrosion testing in molten fluoride salts: Effect of additives and the crucible material, Corrosion Science, 195 (2022) 110011.
[46] L.C. Olson, R.E. Fuentes, M.J. Martinez-Rodriguez, J.W. Ambrosek, K. Sridharan, M.H. Anderson, B.L. Garcia-Diaz, J. Gray, T.R. Allen, Impact of Corrosion Test Container Material in Molten Fluorides, Journal of Solar Energy Engineering, 137 (2015).
[47] C. Falconer, M. Elbakhshwan, W. Doniger, M. Weinstein, K. Sridharan, A. Couet, Activity gradient driven mass transport in molten fluoride salt medium, npj Materials Degradation, 6 (2022) 29.
[48] R.S. Sellers, W.-J. Cheng, B.C. Kelleher, M.H. Anderson, K. Sridharan, C.-J. Wang, T.R. Allen, Corrosion of 316L Stainless Steel Alloy and Hastelloy-N Superalloy in Molten Eutectic LiF-NaF-KF Salt and Interaction with Graphite, Nuclear Technology, 188 (2014) 192-199.
[49] J. Qiu, A. Wu, Y. Li, Y. Xu, R. Scarlat, D.D. Macdonald, Galvanic corrosion of Type 316L stainless steel and Graphite in molten fluoride salt, Corrosion Science, 170 (2020) 108677.
[50] W.H. Doniger, Corrosion and Electrochemistry Studies for Molten Salt Reactor Alloy Development, in, The University of Wisconsin - Madison, Ann Arbor, 2022, pp. 249.
[51] P. Chakraborty, R.H. Banerjee, R. Tewari, V. Kain, Molten Salt Compatibility of a Ni–Cr-Mo-Ti Alloy Developed Indigenously for the Indian MSBR, Transactions of the Indian Institute of Metals, 75 (2022) 1075-1082.
[52] L.C. Olson, J.W. Ambrosek, K. Sridharan, M.H. Anderson, T.R. Allen, Materials corrosion in molten LiF–NaF–KF salt, Journal of Fluorine Chemistry, 130 (2009) 67-73.
[53] B.N. Popov, Corrosion Engineering : Principles and Solved Problems, Elsevier, Amsterdam, NETHERLANDS, THE, 2015.
[54] Y. Wang, H. Liu, C. Zeng, Galvanic corrosion of pure metals in molten fluorides, Journal of Fluorine Chemistry, 165 (2014) 1-6.
[55] Y. Wang, C. Wang, J. Wu, The effect of graphite on the corrosion of Hastelloy N in molten fluorides, Journal of Nuclear Materials, 557 (2021) 153277.
[56] AMETEK, VersaStudio Software Manual, in, USA.
[57] A.K.L. Roy, Galvanic corrosion study of container materials using zero resistance ammeter, in, United States, 1997.

[58] J. Liu, X. Huang, Y. Ren, L.M. Wong, H. Liu, S. Wang, Galvanic corrosion protection of Al-alloy in contact with carbon fibre reinforced polymer through plasma electrolytic oxidation treatment, Scientific Reports, 12 (2022) 4532.
[59] J.A. Von Fraunhofer, P.J. Staheli, Corrosion of Dental Amalgam, Nature, 240 (1972) 304-306.
[60] H. Peng, M. Shen, C. Wang, T. Su, Y. Zuo, L. Xie, Electrochemical investigation of the stable chromium species in molten FLINAK, RSC Advances, 5 (2015) 76689-76695.
[61] H. Peng, M. Shen, C. Wang, Y. Zuo, L. Xie, Electrochemcial Investigation on the Stable Iron Species in Molten FLINAK, Insights Anal Electrochem, 2 (2016).
[62] Y. Wang, J. Zhang, Electrochemical Properties of CrF₂ in FLiNaK Molten Salt and the New Analytical Methods for their Determination, Journal of The Electrochemical Society, 167 (2020) 086503.
[63] H. Ai, Y. Liu, M. Shen, H. Liu, Y. Chen, X. Yang, H. Liu, Y. Qian, J. Wang, Dissolved valence state of iron fluorides and their effect on Ni-based alloy in FLiNaK salt, Corrosion Science, 192 (2021) 109794.
[64] R.B. Snyder, K. Natesan, T.F. Kassner, Analysis of carbon transport in the EBR-II and FFTF primary sodium systems, in, United States, 1976.
[65] J. Sannier, J. Paidassi, J. Dixmier, D. Leclercq, O. Konovaltschikoff, Decarburation des aciers ferritiques dans le sodium en circulation entre 475 et 550°c, Journal of Nuclear Materials, 55 (1975) 169-176.
[66] High-Temperature Characteristics of Stainless Steels, American Iron and Steel Institute, A Designers' Handbook Series No. 9004.
[67] A.A. Frigo, Heat-shield design for glovebox applications, in: Conference: 1998 Annual Conference and Exposition of the American Glovebox Society, Orlando, FL (US), 07/13/1998--07/15/1998; Other Information: PBD: 10 Jul 1998, United States, 1998, pp. Medium: P; Size: 20 pages.
[68] Parker O-Ring Handbook, Parker Hannifin Corporation, 2007.
[69] J.A. Bearden, X-Ray Wavelengths, Reviews of Modern Physics, 39 (1967) 78-124.
[70] L. Bailly-Salins, Modeling the High-Temperature Corrosion of Zirconium Alloy Fuel Cladding and of High Manganese Stainless Steel Exhaust Valves Using Finite Elements in MOOSE, in: Nuclear Engineering and Engineering Physics, University of Wisconsin-Madison, 2021.
[71] J. William D. Callister, D.G. Rethwisch, Materials Science and Engineering: An Introduction, 8th ed., John Wiley & Sons, Inc., 2009.
[72] A.D. Warren, I.J. Griffiths, R.L. Harniman, P.E.J. Flewitt, T.B. Scott, The role of ferrite in Type 316H austenitic stainless steels on the susceptibility to creep cavitation, Materials Science and Engineering: A, 635 (2015) 59-69.
[73] J.W. Elmer, S.M. Allen, T.W. Eagar, Microstructural development during solidification of stainless steel alloys, Metallurgical Transactions A, 20 (1989) 2117-2131.
[74] L.P. Stoter, Thermal ageing effects in AISI type 316 stainless steel, Journal of Materials Science, 16 (1981) 1039-1051.
[75] H. Ebling, M.A. Scheil, Time-Temperature-Sensitization (TTS) Diagrams for Types 347, 304L, and 316L Stainless Steels, in, 1965.
[76] B. Weiss, R. Stickler, Phase instabilities during high temperature exposure of 316 austenitic stainless steel, Metallurgical and Materials Transactions B, 3 (1972) 851-866.

[77] A.S. Lima, A.M. Nascimento, H.F.G. Abreu, P. de Lima-Neto, Sensitization evaluation of the austenitic stainless steel AISI 304L, 316L, 321 and 347, Journal of Materials Science, 40 (2005) 139-144.
[78] G. Zheng, L. He, D. Carpenter, K. Sridharan, Corrosion-induced microstructural developments in 316 stainless steel during exposure to molten Li2BeF4(FLiBe) salt, Journal of Nuclear Materials, 482 (2016) 147-155.
[79] S. Ren, Y. Chen, X.-X. Ye, L. Jiang, S. Yan, J. Liang, X. Yang, B. Leng, Z. Li, Z. Chen, Z. Dai, Corrosion behavior of carburized 316 stainless steel in molten chloride salts, Solar Energy, 223 (2021) 1-10.
[80] G. Zheng, B. Kelleher, G. Cao, M. Anderson, T. Allen, K. Sridharan, Corrosion of 316 stainless steel in high temperature molten Li2BeF4 (FLiBe) salt, Journal of Nuclear Materials, 461 (2015) 143-150.
[81] G. Zheng, B. Kelleher, L. He, G. Cao, M. Anderson, T. Allen, K. Sridharan, High-Temperature Corrosion of UNS N10003 in Molten Li2BeF4 (FLiBe) Salt, Corrosion 71 (2015) 1257-1266.
[82] F.-Y. Ouyang, C.-H. Chang, J.-J. Kai, Long-term corrosion behaviors of Hastelloy-N and Hastelloy-B3 in moisture-containing molten FLiNaK salt environments, Journal of Nuclear Materials, 446 (2014) 81-89.
[83] B.C. Kelleher, K.P. Dolan, P. Brooks, M.H. Anderson, K. Sridharan, Batch-Scale Hydrofluorination of Li27BeF4 to Support Molten Salt Reactor Development, Journal of Nuclear Engineering and Radiation Science, 1 (2015).
[84] C.M. Blood, Solubility and stability of structural metal difluorides in molten fluoride mixtures, in, United States, 1964, pp. Medium: ED; Size: Pages: 54.
[85] R.D. Scheele, A.M. Casella, Assessment of the Use of Nitrogen Trifluoride for Purifying Coolant and Heat Transfer Salts in the Fluoride Salt-Cooled High-Temperature Reactor, in, United States, 2010.
[86] Safe Handling of Hydrogen Fluoride and Hydrofluoric Acid, in, University of Wisconsin-Madison: Environment, Health, and Safety Department, 2017.
[87] Airgas, Safety Data Sheet: Hydrogen Fluoride, in, Airgas USA, LLC, Radnor, PA, 2018.
[88] Airgas, Safety Data Sheet: Hydrogen, in, Airgas USA, LLC, Radnor, PA, 2020.
[89] G. Zong, Z.-B. Zhang, J.-H. Sun, J.-C. Xiao, Preparation of high-purity molten FLiNaK salt by the hydrofluorination process, Journal of Fluorine Chemistry, 197 (2017) 134-141.
[90] C.F. Baes, The Chemistry and Thermodynamics of Molten Salt Reactor Fuels, in: Nuclear Metallurgy, 1969, pp. 617-644.
[91] PanHEA Database v. 2021, in, CompuTherm, LLC.
[92] PanNickel Database v. 2021, in, CompuTherm, LLC.
[93] Britannica, Tin, in: Encyclopedia Britannica, 2021.
[94] Pandat v. 2020, in, Computherm, LLC, 2020.
[95] M. Elbakhshwan, W. Doniger, C. Falconer, M. Moorehead, C. Parkin, C. Zhang, K. Sridharan, A. Couet, Corrosion and Thermal Stability of CrMnFeNi High Entropy Alloy in Molten FLiBe Salt, Scientific Reports, 9 (2019) 18993.
[96] M. Weinstein, C. Falconer, W. Doniger, L. Bailly-Salins, R. David, K. Sridharan, A. Couet, Environmental degradation of electroplated nickel and copper coated SS316H in molten FLiNaK salt, Corrosion Science, 191 (2021) 109735.
[97] J.W. Koger, A.P. Litman, Compatibility of Molybdenum-Base Alloy TZM with LiF-BeF2-ThF4-UF4 (68-20-11.7-03. mole %) at 1100 ºC, ORNL-TM-2724

(1969).
[98] L. Olson, K. Sridharan, M. Anderson, T. Allen, Nickel-plating for active metal dissolution resistance in molten fluoride salts, Journal of Nuclear Materials, 411 (2011) 51-59.
[99] G. Muralidharan, D.F. Wilson, M.L. Santella, D.E. Holcomb, Cladding Alloys for Fluoride Salt Compatibility Final Report, in, United States, 2011.
[100] S. Stumpf, A. Seibert, T. Gouder, F. Huber, T. Wiss, J. Römer, Development of fuel-model interfaces: Investigations by XPS, TEM, SEM and AFM, Journal of Nuclear Materials, 385 (2009) 208-211.
[101] XPSPEAK 4.1, in, 2000.
[102] J.B. Nelson, D.P. Riley, An experimental investigation of extrapolation methods in the derivation of accurate unit-cell dimensions of crystals, Proceedings of the Physical Society, 57 (1945) 160-177.
[103] A.F. Guillermet, An assessment of the Fe□Mo system, Calphad, 6 (1982) 127-140.
[104] A.C. Poulose, S. Veeranarayanan, M.S. Mohamed, R.R. Aburto, T. Mitcham, R.R. Bouchard, P.M. Ajayan, Y. Sakamoto, T. Maekawa, D.S. Kumar, Multifunctional Cu2−xTe Nanocubes Mediated Combination Therapy for Multi-Drug Resistant MDA MB 453, Scientific Reports, 6 (2016) 35961.
[105] Š. Meškinis, A. Vasiliauskas, K. Viskontas, M. Andrulevičius, A. Guobienė, S. Tamulevičius, Hydrogen-Free Diamond Like Carbon Films with Embedded Cu Nanoparticles: Structure, Composition and Reverse Saturable Absorption Effect, Materials (Basel, Switzerland), 13 (2020).
[106] Y. Wang, B. Goh, K. Sridharan, A. Couet, In Situ Corrosion Monitoring of the T91 Alloy in a Molten Chloride Salt Using a Miniaturized Electrochemical Probe for High-Throughput Applications, Analytical Chemistry, 94 (2022) 4012-4020.
[107] A.F. Smith, The Diffusion of Chromium in Type 316 Stainless Steel, Metal Science, 9 (1975) 375-378.
[108] A. Lugovskoy, M. Zinigrad, D. Aurbach, Electrochemical Determination of Diffusion Coefficients of Iron (II) Ions in Chloride Melts at 700-750°C, Israel Journal of Chemistry, 47 (2007) 409-414.
[109] W.H. Doniger, K. Sridharan, Application of voltammetry for quantitative analysis of chromium in molten 2LiF-BeF2 (FLiBe) salt, Journal of Electroanalytical Chemistry, 838 (2019) 73-81.
[110] V. Linnenbom, M. Tetenbaum, C. Cheek, Tracer Diffusion of Iron in Stainless Steel, Journal of Applied Physics, 26 (1955) 932-936.
[111] J. Růžičková, B. Million, Self-diffusion of the components in the F.C.C. phase of binary solid solutions of the Fe□Ni□Cr system, Materials Science and Engineering, 50 (1981) 59-64.
[112] S.R. Shatynski, The thermochemistry of transition metal carbides, Oxidation of Metals, 13 (1979) 105-118.
[113] A.L. Qualls, B.R. Betzler, N.R. Brown, J.J. Carbajo, M.S. Greenwood, R. Hale, T.J. Harrison, J.J. Powers, K.R. Robb, J. Terrell, A.J. Wysocki, J.C. Gehin, A. Worrall, Preconceptual design of a fluoride high temperature salt-cooled engineering demonstration reactor: Motivation and overview, Annals of Nuclear Energy, 107 (2017) 144-155.
[114] X.W. Zhou, C.H. Tang, Current status and future development of coated fuel particles for high temperature gas-cooled reactors, Progress in Nuclear Energy, 53 (2011) 182-188.

[115] P.A. Demkowicz, TRISO Fuel Part I: Background, Fabrication, and Irradiation Performance, in: Conference: CNSC Seminar, Virtual, 05/03/2021 - 05/06/2021, United States, 2021, pp. Medium: ED.
[116] P.A. Demkowicz, B. Liu, J.D. Hunn, Coated particle fuel: Historical perspectives and current progress, Journal of Nuclear Materials, 515 (2019) 434-450.
[117] C. Andreades, A. Cisneros, J.K. Choi, A. Chong, M. Fratoni, S. Hong, L. Huddar, K. Huff, D. Krumwiede, M. Laufer, M. Munk, R. Scarlat, N. Zweibaum, E. Greenspan, P. Peterson, Technical Description of the "Mark 1" Pebble-Bed Fluoride-Salt-Cooled High-Temperature Reactor (PB-FHR) Power Plant, 2014.
[118] C. Andreades, A.T. Cisneros, J.K. Choi, A.Y.K. Chong, M. Fratoni, S. Hong, L.R. Huddar, K.D. Huff, J. Kendrick, D.L. Krumwiede, M.R. Laufer, M. Munk, R.O. Scarlat, N. Zweibau, E. Greenspan, X. Wang, P. Peterson, Design Summary of the Mark-I Pebble-Bed, Fluoride Salt–Cooled, High-Temperature Reactor Commercial Power Plant, Nuclear Technology, 195 (2016) 223-238.
[119] R.T. Paine, C.K. Narula, Synthetic Routes to Boron Nitride, Chemical Reviews, 90 (1990) 73-91.
[120] J. Green, Introduction of Pyrolytic Boron Nitride (PBN), in, Precise Ceramics, https://www.preciseceramic.com/blog/introduction-of-pyrolytic-boron-nitride-pbn/

[121] O. Hod, Graphite and Hexagonal Boron-Nitride have the Same Interlayer Distance. Why?, Journal of Chemical Theory and Computation, 8 (2012) 1360-1369.
[122] K.S. Krane, Introductory Nuclear Physics, John Wiley & Sons, 1988.
[123] Neutron scattering lengths and cross sections, in: A. Munter (Ed.), NIST Center for Neutron Research, https://www.ncnr.nist.gov/resources/n-lengths/.
[124] J.W. KOGER, Fluoride Salt Corrosion and Mass Transfer in High Temperature Dynamic Systems, Corrosion, 29 (1973) 115-122.
[125] G.S. Was, Fundametals of Radiation Materials Science, Springer, 2007.
[126] K. Liu, J. Lin, L.-m. Bao, H.-x. Xu, L. Xu, Z. Liu, J.-r. Zeng, S.-l. Long, L.-l. Cao, J.-j. Li, L. yan, X.-l. Li, G.-l. Zhang, Y. Li, Dose rate effect on micro-structure and hardness of Hastelloy-N irradiated by Xe ions, Journal of Nuclear Science and Technology, 52 (2015) 829-836.
[127] J. Gao, H. Huang, J. Liu, R. Liu, Q. Lei, Y. Li, Synergistic effects on microstructural evolution and hardening of the Hastelloy N alloy under subsequent He and Xe ion irradiation, Journal of Applied Physics, 123 (2018) 205901.
[128] Z. Zhu, H. Huang, J. Liu, J. Gao, Z. Zhu, Xenon ion irradiation induced hardening in inconel 617 containing experiment and numerical calculation, Journal of Nuclear Materials, 525 (2019) 32-39.
[129] H. Zhu, R. Holmes, T. Hanley, J. Davis, K. Short, L. Edwards, Z. Li, Effects of bubbles on high-temperature corrosion of helium ion-irradiated Ni-based alloy in fluoride molten salt, Corrosion Science, 125 (2017) 184-193.
[130] G. Lei, C. Li, Z. Jiang, H. Huang, Irradiation accelerated fluoride molten salt corrosion of nickel-based UNS N10003 alloy revealed by X-ray absorption fine structure, Corrosion Science, 165 (2020) 108408.
[131] W. Zhou, Y. Yang, G. Zheng, K.B. Woller, P.W. Stahle, A.M. Minor, M.P. Short, Proton irradiation-decelerated intergranular corrosion of Ni-Cr alloys in molten salt, Nature Communications, 11 (2020) 3430.

Appendix A

Mechanical Basis for Corrosion Cell Lifting Rods

As shown in Figure 3-3, the lifting assembly for lowering a corrosion cell into the glovebox furnace uses three lifting rods so that the corrosion cell can be inserted between the rods and rested on the bottom plate. Because, a typical corrosion test temperature used in this dissertation was 700 ºC it was important to design the lifting rods such that they would not fail at 700 ºC after several thousands of hours. As a basis on the design it was assumed that the mass of a corrosion cell along with the bottom plate would never exceed 25 lbs (11.34 kg). In a worst case scenario the entire mass would have to be supported by a single lifting rod such that the force in newtons on the lifting rod is:

$$F = ma \qquad \text{Equation A-1}$$

Where a is the acceleration due to gravity, 9.8 m/s^2, and m is the mass in kg. So, the maximum force on a lifting rod is approximately 111 N. According to Figure A-1, stainless steel 316 has a creep-rate of approximately 1% in 100,000 hrs if a stress of approximately 25 MPa is applied and stress is calculated as:

$$\sigma = \frac{F}{A} \qquad \text{Equation A-2}$$

Where σ is given in MPa if F is newtons and area, A, is in mm^2. Rearranging Equation A-2 to calculate for the minimum area if a stress of 25 MPa is applied with a force of 111 N yields a cross-sectional area of 4.4 mm^2 or a circular rod with a diameter of 2.4 mm. Taking a factor of safety of 2.5, and the diameter of the rod should be a minimum of 6 mm (0.24 inches). Because threaded rod's load bearing area is not the diameter of the threads, but the minor diameter of the core of the rod, a 5/16" (minor diameter of 0.252 inches) diameter threaded rod was selected for the lifting rods. Future designs of the lifting assembly used even larger rods just to take an even higher factor of safety into account for heavier experiments.

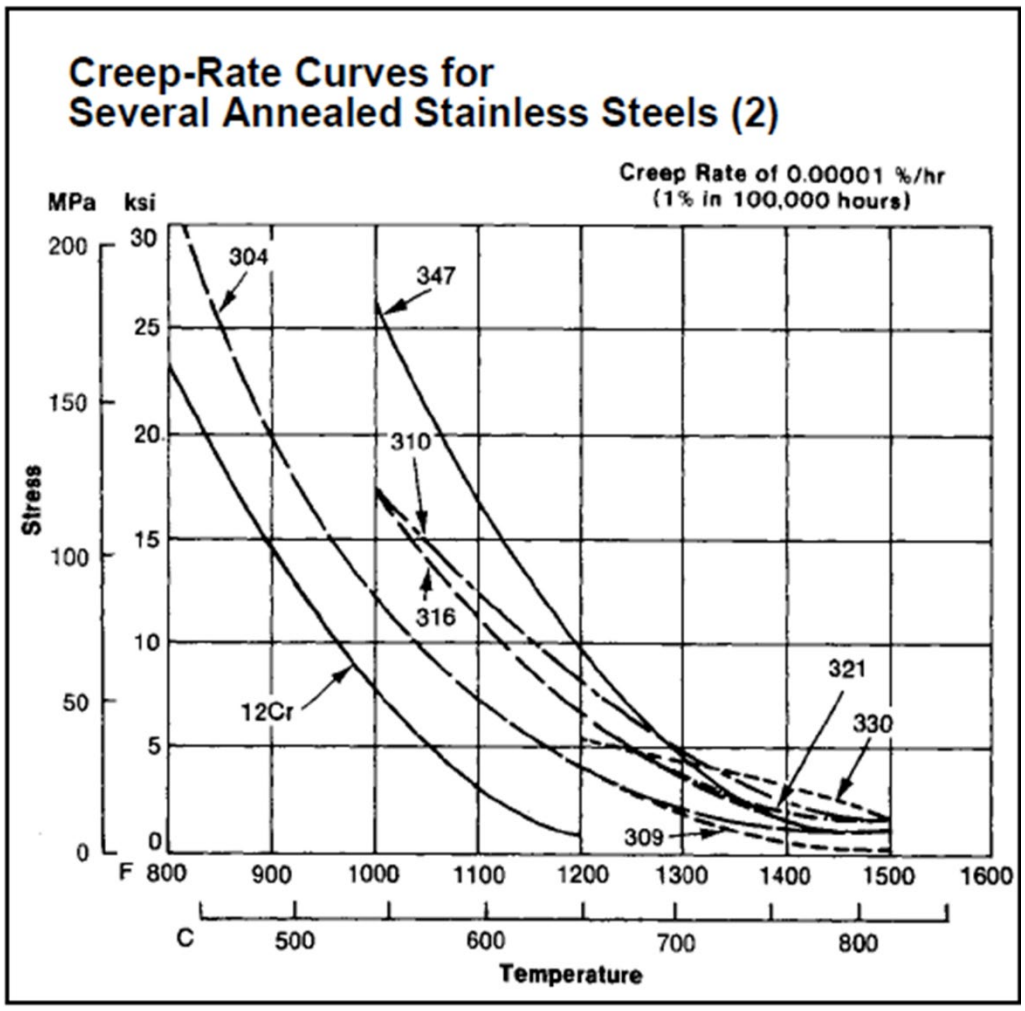

Figure A-1: Creep rate curve of 1% in 100,000 hrs for annealed stainless steels [66].

Appendix B:

Heat Shield Calculations for Glovebox Furnace

Determining the number of planar heat shields required for the corrosion lifting assembly in Figure 3-3 essentially followed the example shown in the Argonne report by Frigo, A.A. [67].

Step 1: Choose the desired outer shield temperature.

The shields separating the heated furnace zone from the rest of well are meant to drop the temperature in the cell to protect the silicon O-ring so the outer shield temperature was desired to be below 200 ºC.

Step 2: Determine characteristic length.

For circular planar shields this is the ratio of the shield diameter to the perimeter. For a circle this reduces to the diameter divided by 4. Now for the diameter of the shield this is limited by the furnace well's inside diameter which is 6.64" (0.169 m). At a corrosion test temperature of 700 ºC there needs to be a small gap between the well and heat shield so it can be lifted out. A gap of 0.04" on both sides of the heat shield was desired, so the heat shield could have a final diameter of 6.56" (0.167 m) at 700 ºC. Due to thermal expansion the heat shield then has to be slightly smaller at room temperature. The final diameter of a circle due to thermal expansion is given by:

$$D_f = D_o[1 + \alpha(T_f - T_o)] \qquad \text{Equation B-1}$$

Where D_o is the room temperature diameter, α is the linear expansion coefficient (for stainless steel 316 this is approximately 16e-6 m/m/ºC [71]), T_f and T_o are the final temperature and room temperature, respectively. So calculating for D_o if the final temperature is 700 ºC gives a diameter of approximately 6.5" (0.165 m).

So, now the characteristic length is then 6.5" divided by 4 or 1.63" (0.04 m).

Step 3: Determine Q_c from Natural Convection Heat Transfer graph

These graphs are provided in the Argonne report [67]. Surface temperature of 200 ºC was chosen in step 1. The heat shields are planar so the Horizontal top curve is used with a characteristic length of 0.04 m. Reading the graph and Q_c is approximately 1150 W/m^2.

Step 4: Determine Q_R from Radiation Heat Transfer graph

Again this is provided in the report. For this the emissivity of the shield material is needed. Values for several materials and finished surfaces are provided in the report. For polished stainless steel the emissivity ranges from 0.17-0.3. So choose 0.3 to be conservative and with the 200 ºC surface temperature a value of Q_R equal to approximately 700 W/m^2 is found.

Step 5: Add Q_C and Q_R to get the total heat flux Q_T

So, from steps 3 and 4, $Q_T = 1150 + 700 = 1850$ W/m^2

Step 6: Determine the temperature factor (A, B, C, ….)

With a surface temperature of 200 ºC and a furnace temperature of 700 ºC the temperature factor is E

Step 7: Find number of shields from the Heat Transfer through Shield Assembly graph

This graph is again provided in the Argonne report. Reading from the graph using a Q_T=1850 W/m^2 and a temperature factor of E, it was determined that a minimum of 5 heat shields was required.

To provide some factor of safety, the number of shields was doubled to 10 since it did not alter the design of the lifting assembly significantly.

Appendix C:

Cr Depletion Depth from GDOES Analysis

GDOES analysis provides information on the concentration of elements in a sample as a function of depth. In Figure C-1, the Cr profile from one of the 316H samples is shown. In the first 2-5 microns the concentration of Cr is clearly depleted due to Cr dissolution in FLiNaK. To determine the depletion depth, first the original bulk concentration is needed. Though GDOES is calibrated for stainless steel analysis, the actual data collected is used to determine what the original concentration is. It can be observed that beyond 15 µm the concentration of Cr is constant and this is likely the original bulk average concentration of Cr.

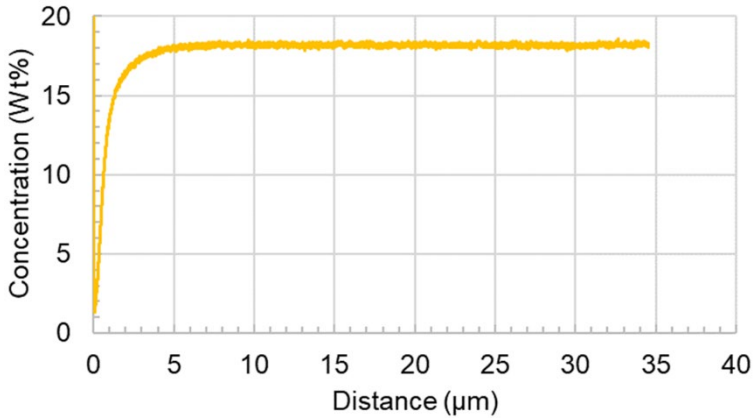

Figure C-1: Cr concentration profile from a 316H sample after FLiNaK exposure

Step 1: Original bulk average concentration of Cr

Average the Cr concentration over a constant region in the Cr profile. In this case the the final 10 µm of Cr concentration was averaged.

Averaged Cr concentration: 18.2 ± 0.09 wt%

Step 2: Choose a criteria for considering when the concentration has returned to the original Cr concentration.

This criteria is a bit arbitrary and there is no set guide for this in the literature. Here the idea of the 95% empirical rule was borrowed. So, the Cr concentration would be considered returned to bulk when the concentration was back within a 2σ range of the bulk average.

A zoomed in plot of the Cr profile is shown in Figure C-2 with the average, upper 2σ, and lower 2σ concentrations shown.

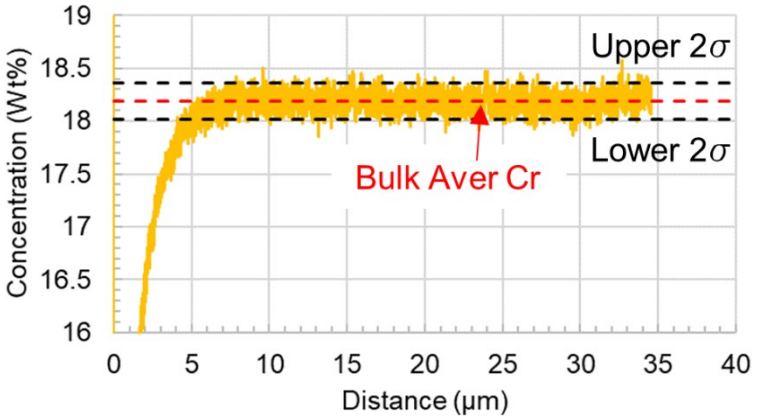

Figure C-2: Cr profile with average and 2σ bounds shown.

Step 3: Determine the depth when Cr returns to bulk average concentration

As seen in the zoomed in profile in Figure C-2, the GDOES data is somewhat noisy so again this can be arbitrary. Here the first point that the concentration of Cr fell within the the 2σ bounds was used as the depletion depth.

So depletion depth was equal to 4 μm

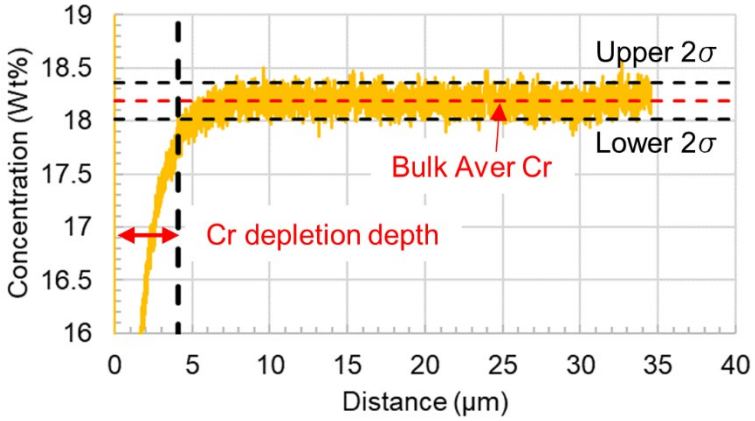

Figure C-3: Cr depletion depth determination

Appendix D:

Additional Activity Plots for Cr and Fe in Material X

As a reminder. For modeling activity gradients between dissimilar materials in Chapter 5, the activity of Cr and Fe in 316SST at 700 ºC (0.55 and 0.72, respectively) was used as a threshold for determining the threshold concentration of Cr and Fe in material X where X is Ni-201, TZM, Cu, Au, Co, Pt, W, or Ag. The activity gradient for elemental transport is hypothesized to increase with increasing threshold concentration. Note that regions of nearly constant activity indicate phase separation and as the weight % of Cr of Fe increases the phase fraction is changing. The lever rule could be used to determine phase fraction.

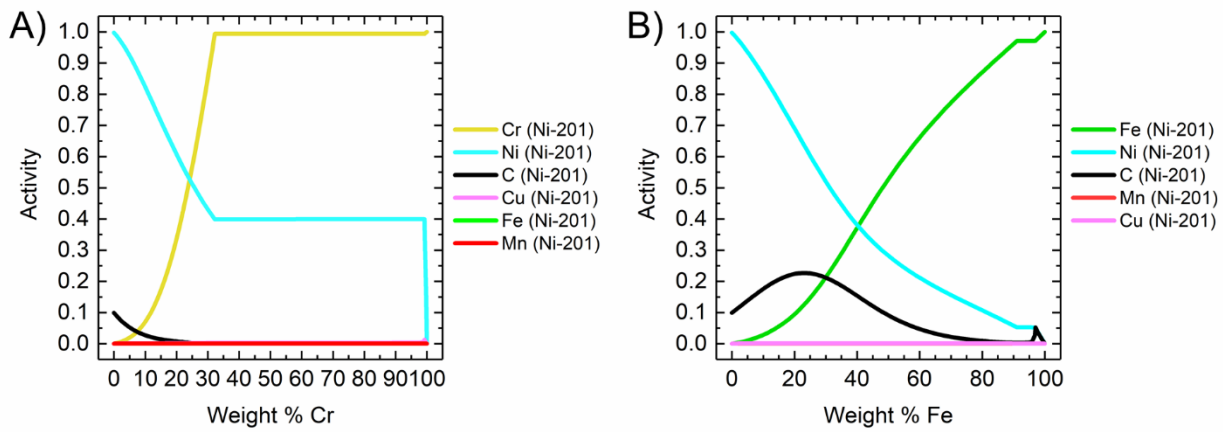

Figure D-1: Activity of Cr and Fe as functions of increasing weight % in Ni-201. a) Cr, b) Fe.

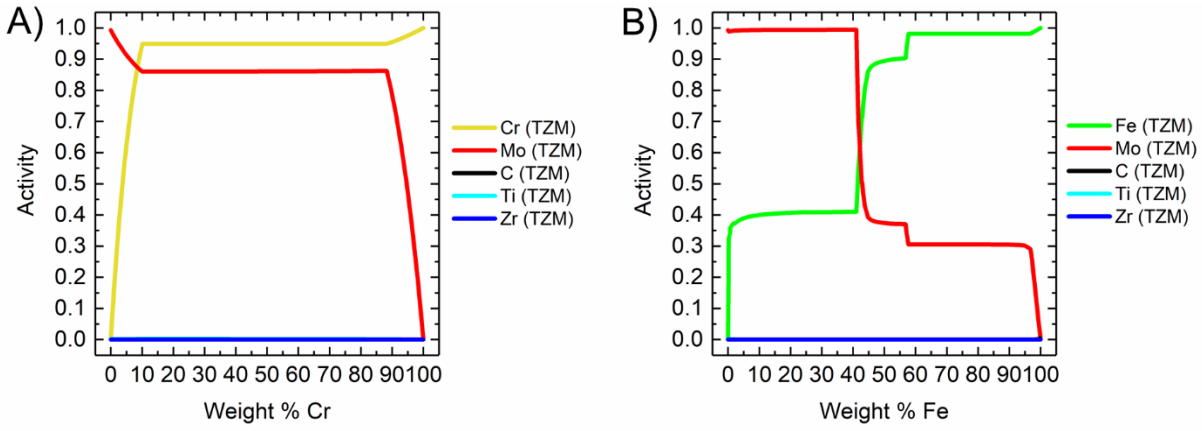

Figure D-2: Activity of Cr and Fe as functions of increasing weight % in TZM. a) Cr, b) Fe.

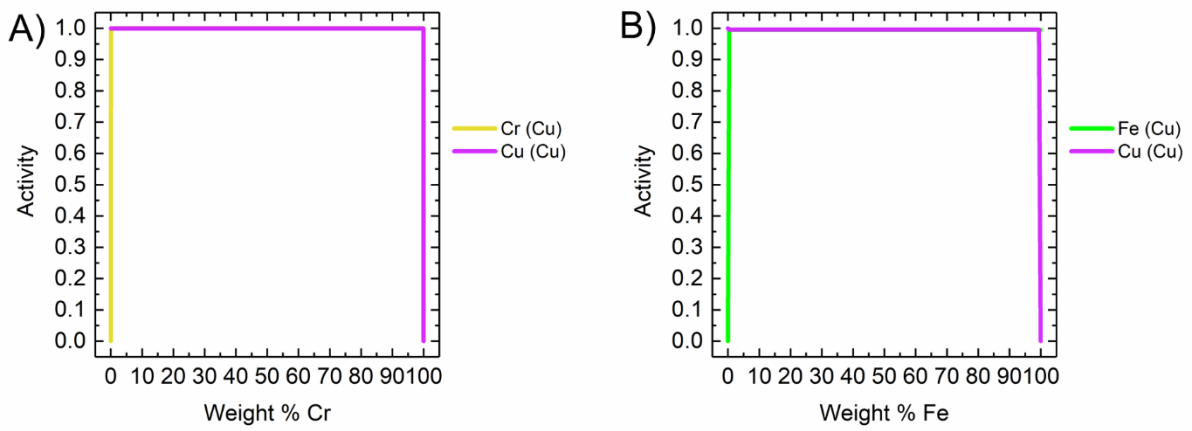

Figure D-3: Activity of Cr and Fe as functions of increasing weight % in Cu. a) Cr, b) Fe.

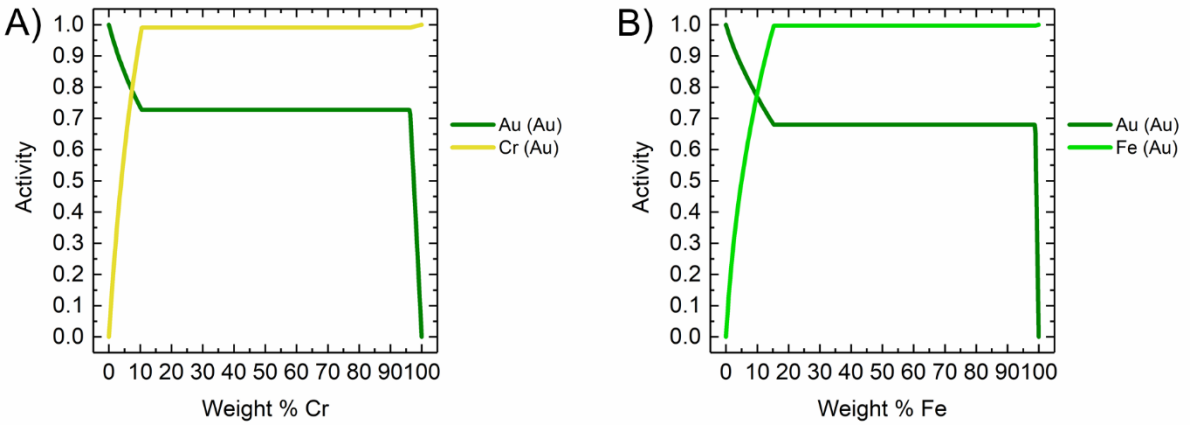

Figure D-4: Activity of Cr and Fe as functions of increasing weight % in Au. a) Cr, b) Fe.

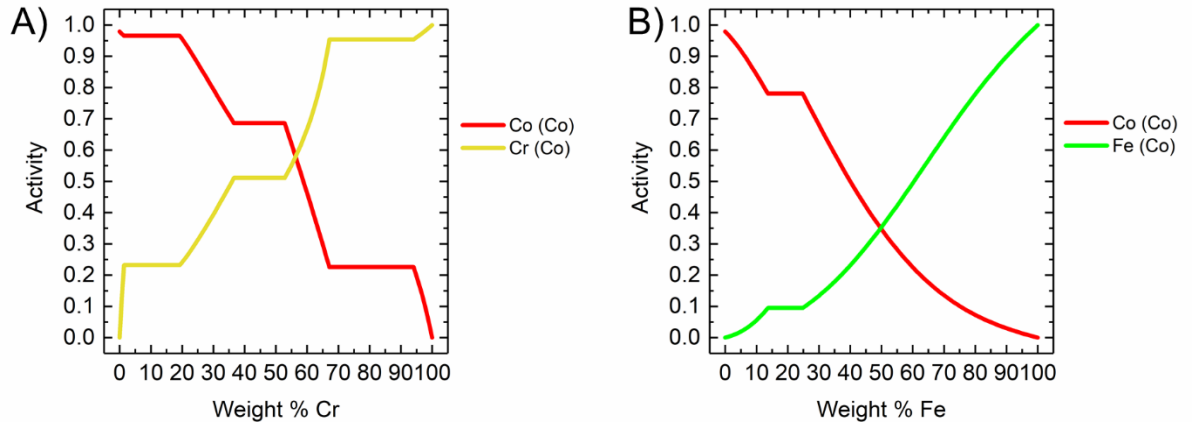

Figure D-5: Activity of Cr and Fe as functions of increasing weight % in Co. a) Cr, b) Fe.

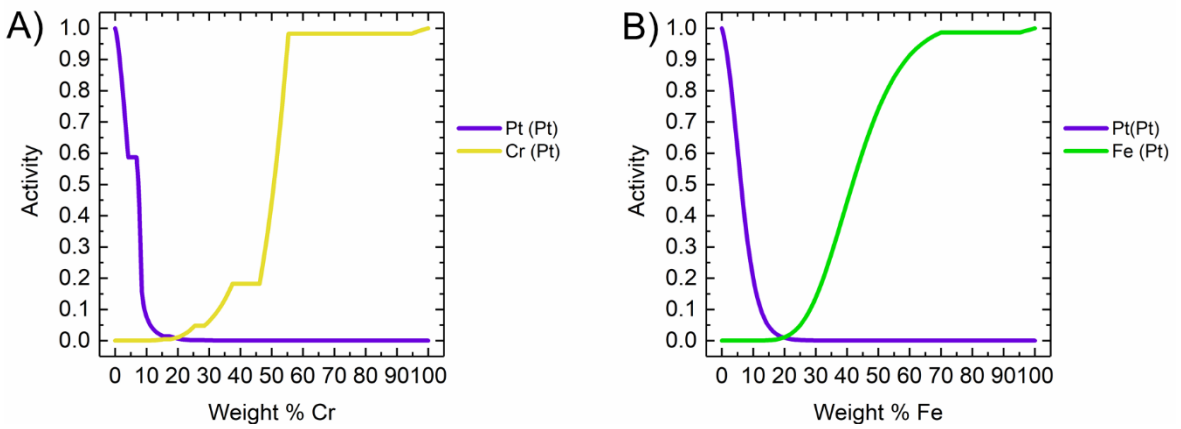

Figure D-6: Activity of Cr and Fe as functions of increasing weight % in Pt. a) Cr, b) Fe.

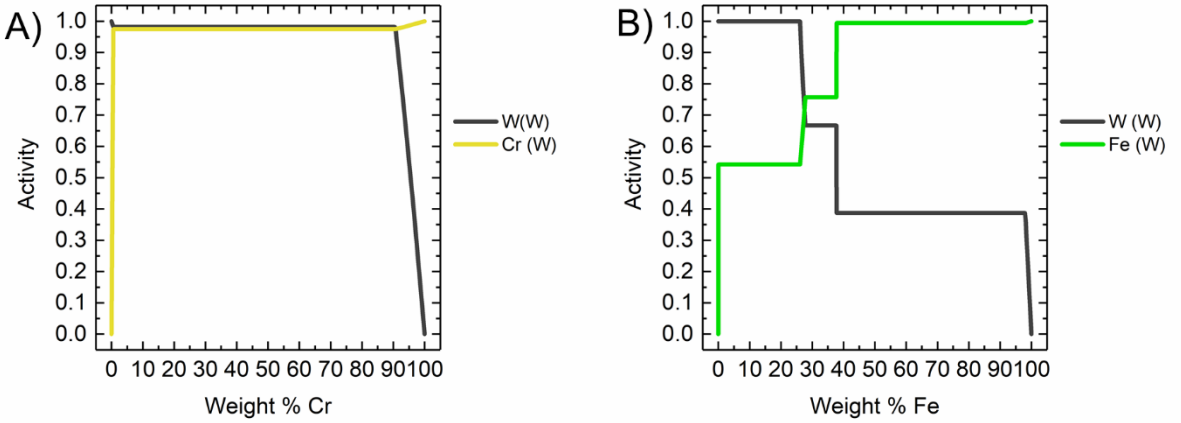

Figure D-7: Activity of Cr and Fe as functions of increasing weight % in W. a) Cr, b) Fe.

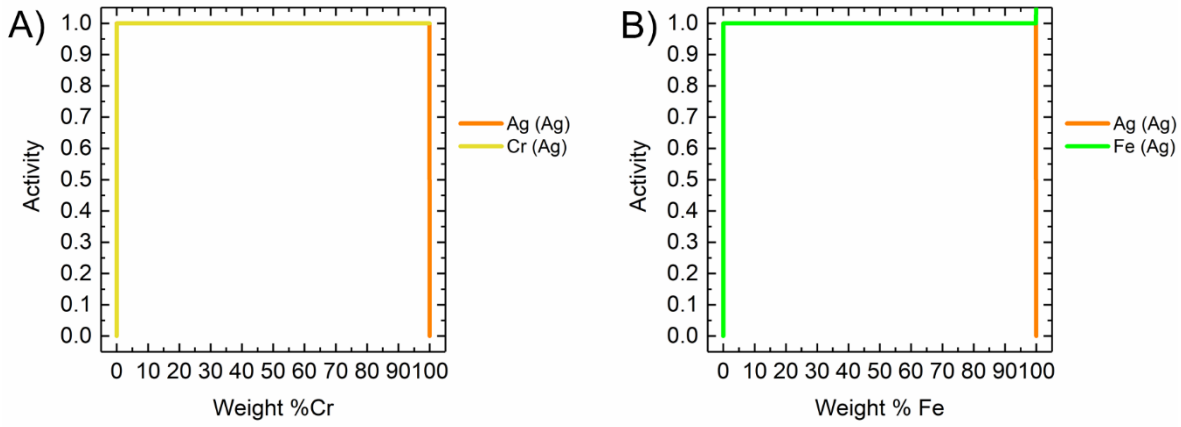

Figure D-8: Activity of Cr and Fe as functions of increasing weight % in Ag. a) Cr, b) Fe.

Appendix E:

Copper Sample SEM/EDS Cross-Section Data

As mentioned in Section 5.2.3 the copper cross-sections showed no sign of elemental transport or corrosion products originating from the 316SST crucibles used to test the copper samples. As seen in Figure E-1, no matter the electrical configuration only pure Cu is observed in the line scan taken along the cross-sections of the copper samples. This data was not included in the main text as it can also be observed that I did not do a great job at polishing the samples. I mean look at the scratches. Welcome to the dissertation easter egg where I break the forth wall and just talk from the heart. There was no way I wanted readers to see this in the main text. Especially when it only shows pure Cu. Which is what was hypothesized based on the activity calculations so it's good to confirm, but nevertheless a boring result. Anyways, thanks for taking an interest in my work, I really hope you were able to find something informative and perhaps inspirational to continue your own work!

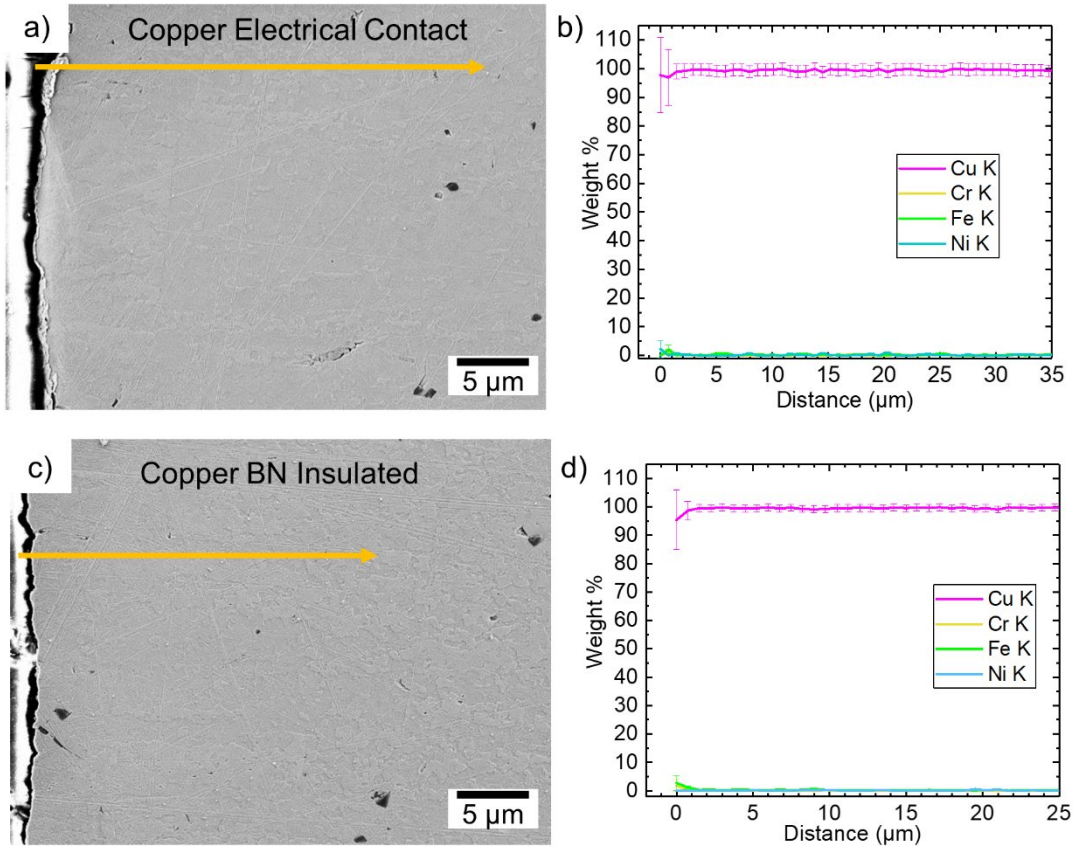

Figure E-1: Cross-section SEM/EDS characterization of the copper sample tested in electrical contact with a 316SST crucible (a,b) and the copper sample tested in electrical isolation from the 316SST crucible (c,d).

Appendix F:

Room Temperature ZRA Measurement: Copper Coil and 304SST Wire

As mentioned in 5.3.2, a ZRA measurement at room temperature was performed to check that the VersaSTAT 3F potentiostat was properly connected for ZRA measurements in FLiNaK. The room temperature measurement was performed on an exact copy of the copper coil 304SST wire couple made for the high temperature FLiNaK measurements. As seen in Figure F-1, over a 1 hour long ZRA measurement the potentiostat is able to record a current value that doesn't decay towards 0 µA which suggests that the potentiostat is setup correctly during the high temperature measurements providing some assurance that 0 µA/cm^2 measurements in FLiNaK are real results.

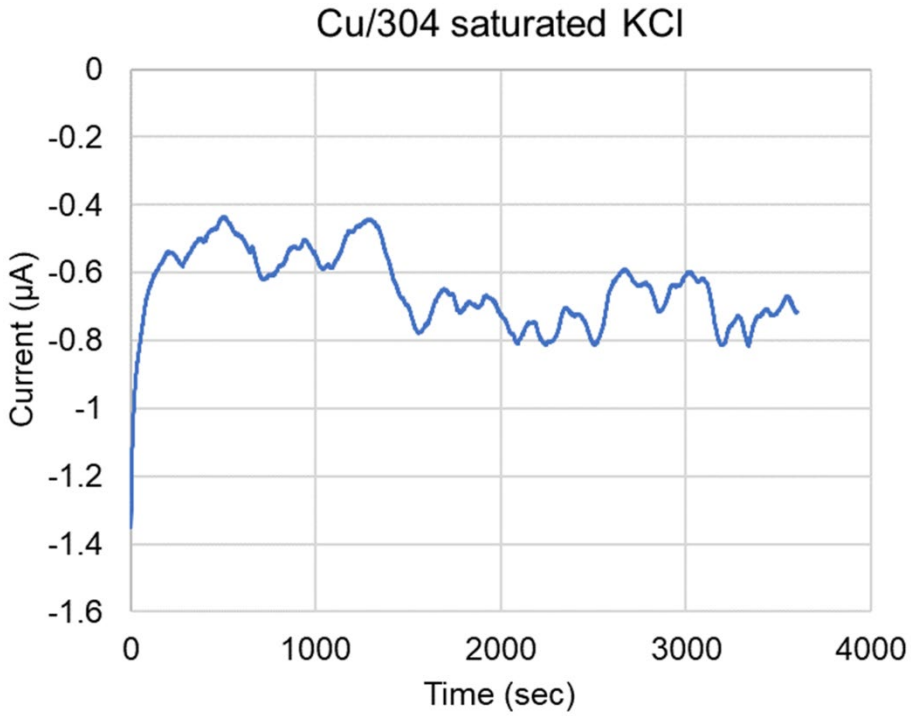

Figure F-1: ZRA measurement between coupled copper and 304SST in a saturated KCl solution at room temperature